Galaxy evolution in clusters and groups up to z 3

Anton Afanasyev

To cite this version:

Anton Afanasyev. Galaxy evolution in clusters and groups up to z 3. Astrophysics [astro-ph]. Université Paris Cité, 2022. English. NNT : 2022UNIP7029 . tel-04190325

HAL Id: tel-04190325
https://theses.hal.science/tel-04190325v1

Submitted on 29 Aug 2023

Université Paris Cité
École Doctorale N°127 Astronomie et Astrophysiqe d’Île-de-France
Laboratoire d’Astroparticule et Cosmologie

Galaxy evolution in clusters and groups up to z ~ 3

Par Anton Afanasyev

Thèse de doctorat de Physique de l’Univers

Dirigée par Simona Mei

Présentée et soutenue publiquement le 29 Septembre 2022

Devant un jury composé de :

Ignacio Trujillo	Chercheur	Institut d’astrophysique des Canaries	Rapporteur
Arjen van der Wel	Professeur	Université de Gand	Rapporteur
Simona Mei	Professeure	Université Paris Cité	Directrice de thèse
Daniele Steer	Professeure	Université Paris Cité	Présidente
Christofer Conselice	Professeur	Université de Manchester	Membre
Emmanuelle Daddi	Chercheur	CEA, Université Paris-Saclay	Membre
Igor Chilingarian	Chercheur	Harvard-Smithsonian CfA	Membre

Titre: L’évolution des galaxies dans les amas et les groupes jusqu’à z ~ 3

Résumé: L’un des principaux défis de l’astrophysique extragalactique actuelle est de comprendre comment la formation et l’évolution des galaxies sont influencées par l’environnement. Les amas de galaxies sont des structures densément peuplées contenant les galaxies les plus massives qui existent. Cependant, la majorité numérique des galaxies dans l’Univers habite des groupes de galaxies moins densément peuplés et le champ. Comprendre les détails de la façon dont les propriétés des galaxies changent à l’intérieur de ces structures, plus particulièrement, comment l’extinction de la formation d’étoiles et la croissance de la taille se produisent, peut aider à comprendre les différents processus sous-jacents dans ces différents environnements.

La thèse se compose de deux blocs quelque peu séparés.

Le premier bloc est consacré à l’étude de l’évolution et du rôle des effets environnementaux sur les galaxies naines dans l’Univers Local. Je réalise une étude de cas de KDG64, un objet du groupe M81 avec une classification transitoire entre galaxie ultra-diffuse, sphéroïdale naine et elliptique naine. Cet objet s’avère être un bon représentant de la vaste population de galaxies de faible masse éteintes qui sont numériquement dominantes à la fois dans les amas et les groupes. Ici, l’histoire de la formation stellaire de KDG64, sa cinématique, les propriétés du halo de matière noire sont estimées et des conclusions sur l’histoire de son extinction sont faites. Le destin de cette petite galaxie peut être repré sentatif de ce qui arrive à la majorité des systèmes stellaires de faible masse dans l’univers. J’étudie également un échantillon de galaxies naines étendues dont la formation d’étoiles s’est récemment éteinte dans l’amas de Coma, et j’étudie l’effet de la pression dynamique sur les galaxies naines. Je conclus qu’une grande fraction de la population de galaxies naines dans les amas pourrait avoir été formée par ce canal.

Le deuxième bloc est consacré à l’étude de l’évolution de la taille des galaxies dans les amas à $1.5 < z < 3$. Le but est de mesurer comment la taille des galaxies dans l’environnement des amas dépend de la masse de la galaxie, de sa morphologie et du taux de formation d’étoiles. La conclusion est qu’à ces décalages vers le rouge, nous voyons beaucoup de galaxies elliptiques à formation d’étoiles, dont certaines passent par la phase de compaction. On constate également que les galaxies de type précoce non formées d’étoiles sont significativement plus grandes que celles du champ. L’évolution de la taille de ces galaxies entre $z = 1$ et $z = 2$ est plus lente dans les amas que dans le champ. Ce bloc démontre également une fonction améliorée pour la relation masse-taille dans les amas qui prend en compte les objets de plus faible masse.

Mots clefs: *galaxies naines, cinématique des galaxies, amas de galaxies, évolution des galaxies, galaxies de type précoce, taille des galaxies, matière noire, modélisation dynamique, pression dynamique, galaxies après la flambée de formation d’étoiles*

Université Paris Cité
Laboratoire d’Astroparticule et Cosmologie

Galaxy evolution in clusters and groups up to z ~ 3

Presented by Anton Afanasyev

PhD thesis in Physics of the Universe

Supervised by Simona Mei

September 2022

Ph.D. Thesis Committee

Ignacio Trujillo	Researcher	Instituto de Astrofísica de Canarias	Referee
Arjen van der Wel	Professor	Ghent University	Referee
Simona Mei	Professor	Université Paris Cité	Supervisor
Daniele Steer	Professor	Université Paris Cité	President
Christofer Conselice	Professor	The University of Manchester	Member
Emmanuelle Daddi	Researcher	CEA, Université Paris-Saclay	Member
Igor Chilingarian	Researcher	Harvard-Smithsonian CfA	Member

Title : Galaxy evolution in clusters and groups up to $z \sim 3$

Abstract: One of the major challenges in the current extragalactic astrophysics is understanding the ways galaxy formation and evolution are influenced by the environment. Galaxy clusters are densely populated structures containing the most massive galaxies in existence. However the numerical majority of galaxies in the Universe inhabit less densely populated galaxy groups and the field. Understanding the details of how galaxy properties change inside this structures, most notably, how quenching and size growth occur, can help understand different underlying processes in these different environments.

The thesis consists of two somewhat separate blocks.

The first block is dedicated to studying the evolution and the role of environmental effects on dwarf galaxies in the Local Universe. I perform a case-study of KDG64, an object in M81 group with a transitional classification between ultra-diffuse galaxy, dwarf spheroidal and dwarf elliptical. This object is found to be a good representative of the vast population of quenched low-mass galaxies that are numerically dominant both in clusters and groups. Here, KDG64 star formation history, kinematics, dark matter halo properties are estimated and conclusions about its quenching history are made. The fate of this small galaxy may be representative of what happens to a majority of low-mass stellar systems in the universe. Also I study a sample of recently quenched extended dwarf galaxies in the Coma cluster, and study the effect of ram pressure stripping on dwarf galaxies. I conclude that a large fraction of the dwarf galaxy population in clusters might have been formed through this channel.

The second block is dedicated to studying size evolution of galaxies in the clusters at $1.5<z<3$. The goal is to measure how galaxy size in the cluster environment depends on galaxy mass, its morphology and star-formation rate. The conclusion is that at these redshifts we see a lot of star-forming elliptical galaxies some of which pass through compaction phase. Also the non-starforming early-type galaxies are found to be significantly larger compared to the field. The size evolution of these galaxies between $z=1$ and $z=2$ is slower in clusters than in the field. This block also demonstrates an improved function for the mass-size relation in the clusters that takes into account lower mass objects.

Mots clefs: *dwarf galaxies, kinematics of galaxies, galaxy clusters, galaxy evolution, early-type galaxies, galaxy size, dark matter, dynamical modelling, ram pressure, post-starburst galaxies*

Contents

List of Figures

List of Tables

RÉSUMÉ

La présente thèse est consacrée à l'étude de l'évolution des galaxies. Il s'agit d'une branche de l'astrophysique qui permet de retracer les changements qui se produisent à l'échelle cosmologique par des moyens observationnels. Comme pour l'évolution d'autres types de systèmes, l'évolution des galaxies produit une riche diversité d'objets individuels structurés en de nombreuses classes régies par des processus physiques clés. L'objectif scientifique général de cette branche est de décoder ces processus clés à partir de l'observation de la population diverse des galaxies. L'apprentissage de l'ensemble des mécanismes qui régissent l'évolution des galaxies est essentiel pour comprendre les tendances globales de l'Univers et les prévoir dans le futur.

L'évolution des galaxies peut être étudiée à l'aide de multiples paramètres. Les plus importants qui influencent la vie d'une galaxie sont sa structure et son activité de formation d'étoiles. Je me concentre ici sur la question de savoir pourquoi et quand les galaxies actuellement sans formation d'étoiles (ci-après "passives") ont cessé de former des étoiles. Il existe de nombreux processus suggérés qui peuvent arrêter la formation d'étoiles dans les galaxies, et il est important d'évaluer les circonstances où un mécanisme donné fonctionne le mieux. Dans cette thèse, j'accorderai une attention particulière à la pression dynamique (c'est-à-dire la pression exercée par le gaz extragalactique sur une galaxie qui le traverse) dans les amas proches, car on pense qu'ils influencent puissamment l'évolution de la population naine.

La structure et l'évolution des galaxies peuvent être quantifiées par des relations d'échelle (c'est-à-dire la distribution des galaxies dans des espaces de paramètres à 2 et 3 dimensions). Elles représentent une méthode viable pour caractériser différents sous-groupes de populations de galaxies, et pour identifier les mécanismes physiques qui conduisent à la séparation des galaxies dans ces sous-groupes. Parfois, des galaxies morphologiquement différentes peuvent se trouver dans le même sous-groupe dans d'autres espaces de paramètres.

Ma thèse de doctorat porte sur les effets de l'environnement sur l'arrêt de la formation d'étoiles et le changement de la morphologie des galaxies, en particulier sur les différences entre les environnements à haute, moyenne et faible densité (amas, groupes et champ, respectivement).

Tout d'abord, j'étudie l'interconnexion entre les différentes classes morphologiques de galaxies passives naines, car elles constituent un milieu parfait pour évaluer les effets de l'environnement sur la formation d'étoiles et la morphologie. Je quantifie les différences entre les galaxies passives de faible masse en groupe et en amas. Deuxièmement, j'étend l'étude des différences entre les amas et l'environnement moyen à $z = 2$ où j'étudie l'évolution de la taille des galaxies dans les amas et la compare avec le champ.

Les galaxies naines elliptiques et lenticulaires étendues sont communes dans les amas de galaxies et les groupes riches. Un environnement moins dense est dominé par des galaxies sphéroïdales naines (dSph) étendues de manière similaire mais moins massives. Récemment, une population supplémentaire de type précoce de galaxies ultra-diffuses (UDG) encore plus grandes a été identifiée, suscitant une discussion sur les connexions morphologiques

et évolutives potentielles entre les trois classifications. On ne sait toujours pas quelles sont les origines des UDGs et si elles présentent des différences intrinsèques par rapport aux autres galaxies passives naines. J'essaie ici de répondre partiellement à cette question en examinant un objet situé à l'intersection de trois classes morphologiques, une grande galaxie dSph dans le groupe M 81, KDG 64 (UGC 5442). Cette galaxie est l'une des plus grandes galaxies dSph dans le volume local, et la seule du groupe M 81 proche qui se prête bien aux observations spectroscopiques à lumière intégrée. Dans cette thèse, je présente les premières mesures de cinématique stellaire résolue spatialement à partir de spectres profonds à lumière intégrée de KDG 64. A partir de ces données, je déduis les propriétés de la population stellaire en utilisant l'ajustement du spectre complet et l'ajustement de la distribution d'énergie spectrale, et je trouve une population stellaire vieille, pauvre en métaux et sans étoiles jeunes. J'estime également les paramètres du halo de matière noire en utilisant la modélisation dynamique de Jeans. Les données ne permettent pas d'établir la forme du halo de matière noire, mais je trouve une fraction de masse de matière noire cohérente de $\sim 90\%$ dans le rayon de demi-lumière (R_e). Je ne trouve également aucune rotation le long des axes majeurs et mineurs. Si elle était placée à la distance de l'amas de Coma, KDG 64 aurait passé les critères morphologiques *soft* de l'UDG. Ces propriétés et la position de KDG 64 sur le Plan Fondamental indiquent qu'elle est un analogue local des petits UDGs trouvés en abondance dans les amas de Coma et de la Vierge et qu'elle est probablement un objet transitionnel dSph-UDG. Sa trajectoire évolutive ne peut être établie de manière unique à partir des données existantes, mais j'interprete les données en supposant que la rétroaction des supernovae et le chauffage dynamique par les forces de marée ont joué des rôles clés dans la formation de KDG 64.

Les chemins évolutifs peu contraignants des galaxies ultra-diffuses peuvent également être étudiés en identifiant les jeunes UDG et les analogues elliptiques naines peuplées d'étoiles massives et brillantes (galaxies post-starbustes, PSG). Dans ce cas, la forte luminosité de surface permet d'obtenir des spectres avec un rapport signal/bruit plus élevé. Grâce à l'exploration de données, 11 galaxies de ce type ont été identifiées dans les amas de galaxies Coma et Abell 2147. Elles ont une faible masse ($2 \times 10^8 < M_* < 2 \times 10^9 M_\odot$), un grand rayon de demi-lumière ($2 < R_e < 5$ kpc) et aucune formation d'étoiles en cours. Toutes les galaxies ont des queues de matière dépourvue de pression dynamique, avec des signes de formation d'étoiles actuelle ou récente. Aucune de ces queues ne s'éloigne directement du centre de l'amas. Leurs vitesses radiales particulières élevées ($500 \ldots 2000$ km/s) et leurs positions dans le diagramme caustique $\Delta v_r - d_{\mathrm{proj}}$ de l'amas de Coma suggèrent qu'elles ont des orbites non radiales et qu'elles sont entrées dans la partie interne de l'amas pour la première fois. Des observations spectroscopiques profondes ont révélé des disques stellaires avec une rotation significative jusqu'à $2.5\ R_e$ contenant 70–95% de matière noire en masse. Une grande fraction des étoiles du disque (10 à 40 %) s'est formée lors d'explosions stellaires intenses il y a 180 à 970 millions d'années, probablement déclenchées par la pression dynamique. Les gradients globaux observés de l'âge stellaire et l'anisotropie des vitesses élevées corroborent ce scénario. La modélisation de l'évolution passive de la population stellaire ainsi que le gonflement cinématique montrent que dans les 10 Gyrs à venir, 9 des 11 galaxies se transformeront en galaxies ultra-diffuses, et les deux autres en elliptiques naines. Si l'on suppose que le taux de chute des galaxies est constant, 44 des galaxies ultra-diffuses actuelles les plus lumineuses de l'amas de Coma doivent s'être formées via l'extraction par pression dynamique de progéniteurs discoïdes formateurs d'étoiles. La modélisation des galaxies spirales naines riches en gaz du sondage Little THINGS montre que si elles tombaient sur l'amas de Coma, elles imiteraient les trajectoires évolutives des PSG observées.

Afin d'étudier l'effet de l'environnement à des décalages vers le rouge plus élevés, j'étudie la relation masse-taille des galaxies dans 15 amas confirmés par spectroscopie à $1.3 < z < 2.8$ provenant de l'étude Clusters Around Radio-Loud AGN. Ces amas couvrent une masse stellaire totale dans la gamme $11.3 < \log(M_*^c/M_\odot) < 12.6$ (masse approximative du halo dans la gamme $13.6 < \log(M_h^c/M_\odot) < 14.6$). Ma principale conclusion est que les galaxies passives de type précoce (ci-après ETG) avec une masse $\log(M/M_\odot) > 10.5$ sont systématiquement ($\gtrsim 3\sigma$) plus grandes que les galaxies de champ. L'évolution de la taille moyenne des ETG passives avec le décalage vers le rouge est plus lente à $1 < z < 2$ par rapport au champ. La relation masse-taille des ETG passives montre une tendance à s'aplatir à $9.6 < \log(M/M_\odot) < 10.5$, où la taille moyenne est $\log(R_e/\mathrm{kpc}) = 0.05 \pm 0.22$, ce qui est largement cohérent avec les tailles des galaxies du champ. Les galaxies d'amas les plus brillantes se situent dans la même relation masse-taille que les satellites. La moitié des galaxies actives de type précoce, qui représentent 30% de notre échantillon de galaxies de type précoce, suivent la relation masse-taille des galaxies actives du champ, et l'autre moitié la relation masse-taille des galaxies passives du champ. Ces dernières galaxies sont très probablement passées par une fusion récente ou une interaction entre galaxies voisines, et s'éteindraient très probablement à une époque ultérieure, augmentant ainsi la fraction de galaxies passives de type précoce dans les amas. Une grande population de galaxies compactes n'a pas été trouvée (une seule), contrairement aux objets observés dans le champ à ces décalages vers le rouge. La taille des galaxies peut être augmentée par divers mécanismes tels que des fusions mineures, ou une rétroaction du trou noir central. Cependant, des modèles semi-analytiques montrent que la différence de taille moyenne que nous observons entre les ETGs passives dans les amas et dans le champ est trop importante pour être expliquée par un quelconque mécanisme physiquement sensé en supposant que les galaxies se forment avec la même taille. Au redshift $z < 1$, d'autres équipes n'ont pas observé de différence dans la taille moyenne des ETG passives dans les amas et le champ. Ce changement de $z \sim 2$ à $z \sim 1$ pourrait être attribué au "biais du progéniteur", c'est-à-dire au mélange des populations d'ETG du champ et des amas pendant l'accrétion cosmologique, qui conduit à l'homogénéisation des populations de galaxies à plus faible decalage vers le rouge.

Ces résultats établissent un cadre pour des études ultérieures de l'évolution des galaxies. Comme démontré dans ce travail, l'utilisation des méthodes spectrophotométriques, structurelles et dynamiques que j'ai développées dans le cadre de ma thèse de doctorat permettra des études plus complètes de l'évolution des galaxies. Plusieurs nouveaux projets potentiels sur les amas à la fois à $z = 0$ et $z = 2$ pourraient être basés directement sur les résultats de cette thèse.

ABSTRACT

The present thesis is dedicated to studying the evolution of galaxies. It is a branch of astrophysics that allows to trace changes happening on a cosmological scale by observational means. Like with the evolution of other types of systems, the evolution of galaxies produces a rich diversity of individual objects structured in many classes governed by key physical processes. The general scientific goal of this branch is to decode these key processes from observing the diverse galaxy population. Learning the ensemble of mechanisms driving galaxy evolution is essential to understand the global trends in the Universe and to predict them into the future.

The evolution of galaxies can be studied using multiple parameters. The most significant ones that influence the life of any galaxy are its structure and star formation activity. Here I focus on the question why and when did currently non star-forming galaxies (hereafter passive) stop forming stars. There are many suggested processes that can halt star formation in galaxies, and it is important to assess the circumstances where a given mechanism works best. In this thesis, I will give special attention to ram pressure (i.e. pressure exerted by the extragalactic gas on a galaxy moving through it) in nearby clusters, as they are thought to powerfully influence the evolution of the dwarf population.

The structure and evolution of galaxies can be quantified by scaling relations (i.e. distribution of galaxies in 2- and 3-dimensional parameter spaces). They represent a viable method to characterize different sub-groups of galaxy populations, and to pinpoint the physical mechanisms that lead to the separation of galaxies in these subgroups. Sometimes, morphologically different galaxies might lie in the same subgroup in other parameter spaces.

My Ph.D. thesis focuses on the effects of environment on stopping star formation and changing galaxy morphology, in particular on differences between high-, medium- and low-density environments (clusters, groups and field, respectively).

Firstly, I study the interconnection between the different morphological classes of dwarf passive galaxies, as they provide a perfect medium to asses the effects of environment on star formation and morphology. I quantify the differences between group and cluster low mass passive galaxies. Secondly, I extend the study of differences between clusters and average environment to $z = 2$ where I study the evolution of galaxy sizes in clusters and compare it with the field.

Faint extended dwarf elliptical and lenticular galaxies are common in galaxy clusters and rich groups. More sparse environment is dominated by similarly extended but less massive dwarf spheroidal galaxies (dSph). Recently, an additional early-type population of even larger ultra-diffuse galaxies (UDGs) has been identified, sparking a discussion on the potential morphological and evolutionary connections between the three classifications. It remains unclear what are the origins of UDGs and if they have any intrinsic differences compared to other dwarf passive galaxies. Here I try to partially answer this question by examining an object lying at the intersection of three morphological classes, a large dSph galaxy in the M 81 group, KDG 64 (UGC 5442). This galaxy is the one of the largest dSph

galaxies in the local volume, and the only one in the nearby M 81 group well suited for the integrated light spectroscopic observations. In this thesis I present the first measurements of spatially resolved stellar kinematics from deep integrated-light spectra of KDG 64. From these data I infer stellar population properties using full-spectrum fitting and fitting the spectral energy distribution, and find an old, metal-poor stellar population with no young stars. I also estimate dark matter halo parameters using Jeans dynamical modelling. The data do not allow to establish the shape of the dark matter halo, but I find a consistent dark matter mass fraction of $\sim 90\%$ within the half-light radius (R_e). I also find no rotation along both major and minor axes. If put at the Coma cluster distance, KDG 64 would have passed the "soft" UDG morphological criteria. These properties and the position of KDG 64 on the Fundamental Plane indicate that it is a local analogue of small UDGs found in abundance in Coma and Virgo clusters and is likely a transitional dSph-UDG object. Its evolutionary path cannot be uniquely established from the existing data, but I argue that supernovae feedback and tidal heating played key roles in shaping KDG 64.

The poorly constrained evolutionary paths of the ultra-diffuse galaxies can also be studied by identifying young UDG and dwarf elliptical analogs populated with bright, massive stars (post-starburst galaxies, PSG). In this case, the high surface brightness allows to obtain spectra with higher signal-to-noise ratio. Using data mining, 11 such galaxies were identified in the Coma and Abell 2147 galaxy clusters, having low-mass ($2 \times 10^8 < M_* < 2 \times 10^9 M_\odot$), large half-light radii ($2 < R_e < 5$ kpc) and no current star formation. All galaxies happen to have tails of ram-pressure-stripped material with signs of current or recent star formation there. None of the tails point directly away from the cluster center. Their high peculiar radial velocities ($500 \ldots 2000$ km/s) and positions in the $\Delta v_r - d_{\mathrm{proj}}$ caustic diagram of the Coma cluster suggest that they have non-radial orbits and that they have entered the inner part of the cluster for the first time. Deep spectroscopic observations revealed stellar discs with significant rotation up to $2.5\ R_e$ containing 70–95% dark matter by mass. A large fraction of the disk stars (10–40%) formed in intense star bursts 180–970 Myr ago, likely triggered by ram pressure. Observed global gradients of stellar age and high velocity anisotropy corroborate this scenario. The modelling of passive evolution of the stellar population as well as kinematical puffing-up shows that in the next 10 Gyr 9 of the 11 galaxies will transform into ultra-diffuse galaxies, and other two into dwarf ellipticals. If a constant rate of galaxy infall is assumed, 44 ± 16 % of the most luminous present-day ultra-diffuse galaxies in the Coma cluster must have formed via ram pressure stripping of disky star-forming progenitors. The modelling of gas-rich dwarf spiral galaxies from Little THINGS survey shows that if they were to fall onto the Coma cluster, they would mimic the evolutionary paths of the observed PSG.

To inquire the effect of environment at higher redshifts, I study the galaxy mass-size relation in 15 spectroscopically confirmed clusters at $1.3 < z < 2.8$ from the Clusters Around Radio-Loud AGN survey. These clusters span a total stellar mass in the range $11.3 < \log(M_*^c/M_\odot) < 12.6$ (approximate halo mass in the range $13.6 < \log(M_h^c/M_\odot) < 14.6$). My main finding is that cluster passive early-type galaxies (hereafter ETG) with mass $\log(M/M_\odot) > 10.5$ are systematically ($\gtrsim 3\sigma$) larger then field galaxies. The passive ETG average size evolution with redshift is slower at $1 < z < 2$ when compared to the field. The passive ETG mass-size relation show a tendency to flatten at $9.6 < \log(M/M_\odot) < 10.5$, where the average size is $\log(R_e/\mathrm{kpc}) = 0.05 \pm 0.22$, which is broadly consistent with galaxy sizes in the field. Brightest cluster galaxies lie on the same mass-size relation as the satellites. Half of the active early-type galaxies, which are 30% of our early-type galaxy sample, follow the field active galaxy mass-size relation, and the other half the field passive galaxy mass-size relation. These latter galaxies most probably went through a recent merger or neighbour galaxy interaction, and would most probably quench at a later epoch and increase the fraction of passive early-type galaxies in clusters. A large population of compact galaxies was not found (only one), contrary to the observed objects in the field at these redshifts. Galaxy sizes can be enlarged by various mechanisms such as minor mergers, or feedback from the central black hole. However, semi-analytical models show that the difference in average size that we observe between passive ETGs in clusters and field is too large to be explained by any physically sensible mechanism under assumption that galaxies form having the same size. At redshift $z < 1$, other teams did not observe any difference in the average size of passive ETG in clusters and the field. This change from $z \sim 2$ to $z \sim 1$ could be attributed to the "progenitor bias" i.e. mixing of field and cluster ETG population during cosmological accretion, which leads to the homogenization of the galaxy populations at lower redshift.

These results set up a framework for further studies of galaxy evolution. As demonstrated in this work, using the spectrophotometric, the structural and dynamical methods that I developed in the context of my Ph.D. thesis will allow more comprehensive studies of galaxy evolution. Several potential new projects in clusters both at $z = 0$ and $z = 2$ could be based directly on the results of this thesis.

Chapter 1

Galaxy formation and evolution

The huge belt of hazy light spanning across the entire sky is known in all cultures on Earth. In Europe, this belt is commonly known as the Milky Way, owing its name to the Greek legend about Heracles. The original Greek version of the name ($\Gamma\alpha\lambda\alpha\xi\acute{\iota}\alpha\varsigma$ $\kappa\acute{\upsilon}\kappa\lambda o\varsigma$) gave birth to a widely used synonym - *the Galaxy*. Our Galaxy unites hundreds of billions of stars and spans up to a hundred thousand light years or 30000 parsec (pc) in diameter. These vast expanses had been causing genuine interest in whether the observable Universe equals the Galaxy, or something lies beyond. Following the brave assumption of Giordano Bruno that the other stars might be similar to our Sun in hosting habitable planets, some scholars of XVIII century (including Immanuel Kant and Thomas Wright) proposed that there could be other galaxies beyond Milky Way, and that some observed nebulæ are in fact distant stellar systems. This hypothesis has been discussed throughout XIX century by such figures as William Herschel and Lord Rosse but was not universally accepted until Edwin Hubble measured the distance to several nebulæ (Hubble, 1925, 1926a, 1929).

1.1 Galaxies

Colloquially, the galaxies are described as mere conglomerations of stars bound by the common gravity. While indeed being the easiest element to detect, stars comprise only a fraction of the matter existing in galaxies. The ever present companion of the stars is interstellar gas that comes in three forms (H_2, HI, HII), and that is constantly in interaction with stars during their life cycle. Gas also often contains interstellar dust that has different aggregate form but in general is located where the gas is. The common gravity potential in the galaxy is however produced not only by the joint mass of the stars and gas, but is dominated by the other unseen component called dark matter (DM, Rubin et al., 1980). Finally, centers of the galaxies are usually inhabited by the massive black holes (BH, Wolfe & Burbidge, 1970) that influence the dynamics of the inner parts of the galaxies and are capable of producing intensive emission in all wavelengths (active galactic nuclei (AGN), Seyfert, 1943).

The most simple parameter one can obtain from a galaxy is its brightness, or in astronomical terms, magnitude. The magnitudes are usually measured in wide chunks of the spectrum called bands (e.g. B-band covers wavelength range $\sim 3900 - 5100$ Å). The apparent magnitude can be linked to the physical properties of a galaxies by normalizing it to a fixed distance of 10 pc - this is called absolute magnitude. Galaxies generally have absolute magnitudes in range $-12 > M_B > -23$, and galaxies with $M_B > -18$ are generally considered dwarfs (Reaves, 1956).

The distribution of the light (in a certain band) across the galaxy is described by surface brightness (μ) commonly measured in mag/arcsec^2. A threshold of $\mu = 25$ mag/arcsec^2 was historically used to determine the visible boundary of galaxies in the era of the photographic plates (the exact value was linked to the plate sensitivity). The major axis diameter of the area brighter than $\mu = 25$ mag/arcsec^2 was treated as galaxy size D$_{25}$ (Redman, 1936). However some galaxies (including a few in this thesis) have surface brightness $\mu > 25$ mag/arcsec^2 at all points of observation (formally making their D$_{25} = 0$), despite still being galaxies by any other account. This caveat was partially solved by the introduction of the Holmberg radius (Holmberg, 1958) with the use of more sensitive plates allowing to reach $\mu_H = 26.5$ mag/arcsec^2. Another class of size proxies emerged later, describing the radius $R_{\%}$ that contains a given percentage of the galaxy luminosity. The commonly used radii from that class are R_{50}, R_{80} and R_{90}. R_{50} containing exactly half of the galaxy luminosity is by far the most popular in the contemporary literature (for better or for worse) and is usually called the effective radius R_e.

The stellar population of a galaxy is often described by its average age and the content of elements heavier than helium (metallicity, [Fe/H]). Also, these two parameters are used to estimate a M/L_* ratio, i.e. how much light does given stellar population produce per unit mass. The properties of dark matter can be constrained from a galaxy rotation velocity and depend on the chosen model for the DM halo, but generally include its central density and scale radius (often defined as R_{200}, a radius containing the average density 200 times the critical density of the Universe).

Galaxies do exist in various types of environment. The large-scale structure of the universe resembles a foam, where galaxies are located in the walls of the bubbles forming it (de Lapparent et al., 1986). The regions with highest galaxy density are located in the nodes of this foamy structure and are called galaxy clusters. They contain up to several thousand galaxies (Godwin et al., 1983) within a few megaparsec (Mpc) radius (e.g., Kubo et al., 2007) and can have total masses up to a few times 10^{15} $M_\odot$ at current epoch (Marriage et al., 2011). However, clusters are numerically rare, and far more galaxies reside in the groups, containing at most a few dozen non-dwarf galaxies. Even more galaxies inhabit the sparsely populated walls of the bubbles, the so called filaments and sheets, where only a few galaxies with stellar mass $M_* > 10^9$ $M_\odot$ are present within 1 Mpc distance (e.g. the Local Sheet, Tully et al., 2016). Finally, the interiors of these large-scale bubbles are called voids, where the galaxy density is very low, with individual galaxies separated by up to 2 Mpc (Pustilnik et al., 2019). As an example, the Milky Way is located in a sheet. The Local group and the neighbouring groups all have 2-5 large galaxies and form a thin structure that is 0.5 Mpc thick and more than 5 Mpc wide (Tully et al., 2008).

1.2 Evolution

A definition of biological evolution states that it is a change in the heritable characteristics of the organisms over successive generations. This process has resulted in a great variety of eukaryotic species on Earth nearing 10 million as of now (Mora et al., 2011). Surprisingly, this rich diversity rests on a number of universal basic elements, e.g. specific molecules of DNA and RNA, contained by all eukaryotic cells (Koonin & Novozhilov, 2017). Such a picture when a diverse set of objects appears, having several universally shared traits, is observed in many fields of scientific knowledge. Sometimes the process whereby this diverse set is created is colloquially called evolution by analogy to the diversification of biological species species (e.g. chemical evolution, geological/planetary evolution, stellar population evolution etc.). Interestingly, these so-called "evolutions" are often linked, e.g. it is currently believed that biological evolution is likely to proceed to the multi-cellular stage only if it occurs on a celestial body with a specific set of parameters (see e.g. Kopparapu et al., 2013; Kaltenegger, 2017).

Stellar evolution is by far the one most resembling biological evolution, because stars do change generations (get "born" and "die") and inherit chemical composition from their original gas cloud (Souto et al., 2019), however no star is an ancestor or a descendant of any other. The processes occurring with galaxies through their lifetime do not strictly match the definition of biological evolution, since the generations of galaxies do not change with time and they do not inherit traits. The evolution of galaxies is thus comprised of (i) evolution of their stellar population and (ii) change of global galactic properties with time. However, the diversity in galaxy appearance and observed parameters is so large that galaxy population looks very similar to a biological ecosystem. For that reason and having made the clarification above, I consider calling the multitude of processes happening with galaxies through cosmic time as *galaxy evolution*.

The evolution of galaxies studies some of the most basic structures in the Universe. Galaxies first appeared as large associations of gravitationally bound matter that span kiloparsec ($\sim 3 \times 10^{19}$ m) scales (Press & Schechter, 1974; White & Rees, 1978; White & Frenk, 1991) soon after the epoch of reionization and has existed ever since (Mutch et al., 2016). Two crucial parameters of a galaxy usually determine its state of being at any time: its structure (including morphology and size) and the star formation rate (Kennicutt, 1998). The other parameters such as kinematics, age and chemical composition of stars, and properties of the central black hole also allow to deduce valuable information about the galaxy. In this chapter, I will describe the physical foundations of these processes and the ways they affect the galaxies.

1.3 Morphological transformations

The morphological classification of galaxies (i.e. their differentiation by shape) was first introduced by Hubble (1922) and then developed (Hubble, 1926b). This picture included so-called early type galaxies (ETG): elliptical (E) and lenticular (S0) and late-type galaxies (LTG): spiral with (SB) or without bar (S) and irregular (Irr). The ellipticals were classified depending on ellipticity of their isophotes (E0-E7, circular to the most elongated ones), and spirals were classified by the extension and prominence of their spiral arms (Sa-Sc, from small and tight to large and open spirals). This classification was enhanced by de Vaucouleurs (1959) who added late Sd and Sm classes as well as dwarf spheroidal (dSph) systems. Since then many more new classes have been added to the classification, such as: dwarf ellipticals (Sandage & Binggeli, 1984), giant low surface brightness galaxies (Bothun et al., 1987), compact ellipticals (Wirth & Gallagher, 1984), ultra-compact dwarfs (Drinkwater et al., 2000), ultra-faint dwarfs (Simon & Geha, 2007), ultra-diffuse galaxies (van Dokkum et al., 2015a), and some more.

Though initial Hubble classification was not intended as evolutionary (see Hubble, 1927), it is clear that some morphological transformations do occur in galaxy lifetime. Hence the question arises, what is the relation between morphological classes? Is it a matter of description, or the differences are indeed evolutionary?

For example, low-luminosity early-type galaxies with no current star formation are the numerically dominant population in galaxy clusters (Sandage & Binggeli, 1984; Ferguson & Sandage, 1988). These galaxies are commonly called dwarf ellipticals (dE) or dwarf lenticulars (dS0) and typically have stellar masses $M_* \sim 10^8 - 10^9 M_\odot$ and effective radii $0.5 - 2$ kpc. Galaxy groups, on the other hand, are numerically dominated by yet fainter dwarf spheroidal galaxies (dSph) similar to dE in half-light radius ($r_e \sim 0.5 - 2$ kpc) and morphology but with $10 - 100$ times fewer stars (Grebel et al., 2003). Sandage & Binggeli (1984) found extended low-surface brightness galaxies with larger radii ($r_e = 1.5 - 4.5$ kpc) and stellar masses similar or smaller than dEs. van Dokkum et al. (2015a) proposed that these ultra-diffuse galaxies (UDGs) constitute a distinct galaxy class. UDGs were found in large quantities first in the Coma cluster and later in other clusters and groups (Muñoz et al., 2015; Mihos et al., 2015; Janssens et al., 2017; Wittmann et al., 2017; Zaritsky et al., 2021).

How these morphological classes relate to each other and the evolutionary processes leading to their structural differences remain uncertain (Conselice, 2018). UDGs are the most puzzling because they share characteristics with both dE and dSph (e.g., Chilingarian et al., 2019; Chamba et al., 2020). Understanding the origin of UDGs is a crucial step in our studies of the evolutionary history of early-type dwarf galaxies.

Another good example is late- to early-type transformation at high and intermediate redshift. The dependence between galaxy morphology and the environment it resides in was first discovered at $z = 0$ (Dressler, 1980; Postman & Geller, 1984) and then at higher redshifts (Couch & Sharples, 1987; Dressler et al., 1997; Tasca et al., 2009). It is thought and observed that at very early epochs LTGs dominate in all environments (van der Wel et al., 2014), however this already changes by $z = 2$ where many ETGs are observed (Whitaker et al., 2010; Chang et al., 2013; Noordeh et al., 2021). This transformation is also connected to the environment since first large ETG populations appear in galaxy clusters or protoclusters (Thomas et al., 2005).

1.4 Quenching

One of the important parameters that determines the state of a galaxy is a rate at which it forms stars (SFR). However, a sizeable fraction of the galaxies in the universe forms stars at trace rates close to 0. These objects are colloquially called passive, and those where star formation occurs - active. The star formation intensity is usually determined through specific star formation rate (sSFR), which is defined as $sSFR = SFR/M_{*}$ yr^{-1}. For a galaxy to be considered passive at $z = 0$, its sSFR should be below a threshold value $sSFR_{crit} \sim 10^{-11.5}$ yr^{-1} (Damen et al., 2009). This value increases with redshift, up to $sSFR_{crit} \sim 10^{-9.5}$ yr^{-1} at $z \sim 2$ (Whitaker et al., 2014; Leja et al., 2019). The suppression of star formation in a galaxy below the critical level marks one of the most significant events in its life, and is called quenching (Faber et al., 2007). A logical assumption is that all currently passive galaxies has gone through quenching and all galaxies were star-forming at some larger redshift, since their stars must have been formed (Bell et al., 2004). The knowledge when and how this happened (if at all) for a given galaxy or for their population might provide valuable clues to the history of galaxy evolution.

I shall start with the latter question: how does quenching happen, i.e. which physical processes make further star formation impossible? Quenching might occur via different channels: currently there are half a dozen proposed quenching mechanisms that work under certain conditions.

The more obvious way to quench the galaxy is to simply wait until it exhausts all reserves of gas due to continuing star formation. Since for a common spiral galaxy with $M_B \sim -20 \ldots -21$ the gas depletion time is $\tau \sim 2 \times 10^9$ years (Bigiel et al., 2008), the galaxy will stop forming stars in 2 Gyr in case no external gas falls onto it. The gas exhaustion might be facilitated by a bar (Gavazzi et al., 2015; Khoperskov et al., 2018) or by the interactions that often happen in dense environments (so-called harassment, Moore et al., 1996). Dense environments are also effective in cutting off the external gas supply due to high temperature and pressure of the intracluster gas (strangulation, Balogh & Morris, 2000; Fujita, 2004; van den Bosch et al., 2008; Peng et al., 2015).

The other important type of quenching that happens in dense environments (especially in clusters) is ram pressure stripping (Gunn & Gott, 1972). Similarly to removal of the external gas reservoir, it is caused by the hot intracluster gas. When a galaxy travels through this gas at orbital speeds ~ 1000 km/s, the force of ram pressure $F \sim \rho v^2$ can overcome the gravitational force that bounds galaxy's own gas, leading to its removal. This process always happens outside-in: outer parts get quenched first since the gravitational potential there is weaker. Ram pressure is more effective at high speeds relative to the ICM, and at low galaxy masses (since the overall gravitational potential is weaker).

The gravitational potential governs another mechanism of quenching that is exclusive for the dwarf galaxies: supernovae (SN) feedback (Dekel & Silk, 1986). It is based on the fact that SN type-II, that appear few Myr after the first stars were formed, generate strong outflows of gas reaching several hundred km/s. This speed is often sufficient for gas to leave the gravitational potential of the host galaxy forever. A single supernova influences only its immediate vicinity (several dozen parsec), however after many SN bursts the gas will become depleted across much larger spaces. This quenching mechanism works better in low-mass galaxies, some studies (Su et al., 2018) show that for ultra-faint dwarf galaxy even one strong hypernova is enough to severely disrupt star formation. SN feedback is currently thought to be the main driver of quenching in the low mass systems with $M_* < 10^8 M_\odot$

Another way to quench the galaxy is feedback from an active galactic nucleus (AGN, Springel et al., 2005). The exact physical mechanisms of AGN quenching are still unclear, but the dominating paradigm is that strong AGN emission and outflows may prevent cool external gas from accreting on the galaxy (Bower et al., 2006; Khalatyan et al., 2008; Dubois et al., 2010). This process plays an important role in galaxy simulations (Dubois et al., 2013; Weinberger et al., 2017), but the observational studies of this phenomenon are less conclusive (Schawinski et al., 2007; Fabian, 2012; Le Fèvre et al., 2019; Silk & Nusser, 2010; Cresci et al., 2015; Combes, 2017; Smirnova-Pinchukova et al., 2022).

Finally, when two galaxies of comparable mass ($M_{big}/M_{small} < 3-4$) merge, and at least one has gas prior to the collision, quenching ensues after the coalescence. This happens because a) the star formation rate is enhanced pre-merger by tidal interaction; b) such merging destroys the gas disk that subsequently falls closer to the center, building a star-forming ring (i.e. Cortijo-Ferrero et al., 2017) with extremely high SFR. Due to this process almost all gas gets consumed by star formation.

Next, one has to take into account the epoch when a galaxy was quenched. The average star formation density in $M_\odot$ per year per $1\mathrm{Mpc}^3$ has peaked around $z \sim 2$ (Madau et al., 1998; Madau & Dickinson, 2014) and has been decreasing since. However, this average value is dominated by the field, i.e. the low-density environment. The high-density environment shows earlier peak (Elbaz et al., 2007; Estrada-Carpenter et al., 2020) often with starbursts (Wang et al., 2016). Galaxies that are already passive are observed in clusters up to $z = 3-4$ (i.e. Gobat et al., 2012; Glazebrook et al., 2017; Merlin et al., 2019), which means that quenching in clusters started very early in the history of the Universe. This observation is compounded by the discoveries of galaxies with extremely old stellar population (Trujillo et al., 2014; Ferré-Mateu et al., 2017) and no traces of more recent star formation. At the same time, quenching is actively happening in the local Universe (i.e. Boselli et al., 2016) in all environment. Most of the currently passive galaxies should have been quenched at some point between these epochs and there are indications that this process did not happen uniformly (Tal et al., 2014; Fumagalli et al., 2014). The questions requiring answers are: when was the “optimal” quenching time for each morphological type, how this is connected to the environment, and how these quenching trends will evolve into the future.

Under current scientific consensus there is no universal mechanism that could explain all instances of quenching. The quenching mechanism, its duration and epoch can vary drastically depending on circumstance. It turns out that very process of star formation is a fragile thing that can be disrupted by various mechanisms (as described above), and both high-mass and low-mass star-forming systems are susceptible. Given the fragility of the star formation, it is remarkable that among the Local Universe galaxies with $M > 10^{10} M_\odot$ the star forming spiral galaxies are numerically prevalent. The study of quenching mechanisms and epochs is essential to understand how galaxies transform from star-forming into passive, and what fate awaits those that did not yet experience this process.

There is also a bit of confusion in the literature between, e.g. early-type galaxies and passive galaxies, since some researchers use these terms as interchangeable. In the present thesis I will strictly follow the notion that early-/late-type separation defines only the morphological state of a galaxy, and passive/active separation defines only the state of its star formation.

The relation between morphology and quenching has long been debated in the community (Martig et al., 2009). There has been observational evidence for morphology driven quenching (Bell et al., 2012; Whitaker et al., 2017; Lu et al., 2021) especially at high galaxy masses, quenching induced morphological changes (Grishin et al., 2021), and both morphology and star-formation changing together (Bruce et al., 2012), possibly due to a third factor (Davies et al., 2020). Currently the causal connection seems complicated with bulge-dominated morphology being an amplifying prerequisite, but not the trigger for quenching (Bell et al., 2012; Fang et al., 2013) and it appears that local conditions for each galaxy (e.g. environment) also have significant impact on this causal link (Kawinwanichakij et al., 2017).

1.5 Scaling relations

The evolution of galaxy parameters can be studied most easily through so-called scaling relations. Each relation displays galaxy population in certain parameter space, and for each galaxy one can model its path across this space if some crucial event in its life occurs.

One of the most basic discovered scaling relation was that between the luminosity and the velocity dispersion ($L \sim \sigma^4$) in the elliptical galaxies (Faber & Jackson, 1976). Soon a similar relation for the spiral galaxies was found by Tully & Fisher (1977) with luminosity related to the rotation velocity ($L \sim v^\beta$, $\beta = 3 - 4$ depending on photometric band). For the elliptical galaxies, a further extension was proposed by Djorgovski & Davis (1987) by adding a third parameter (effective radius), so that galaxies line up in a plane (thus this relation is called Fundamental Plane). The Tully-Fisher relation was in turn modified to link the rotation velocity with the baryonic mass (stars and gas) of a galaxy as $M_{bar} \sim v_{rot}^4$ (Baryonic Tully-Fisher relation McGaugh et al., 2000). These four relations represent the connection between kinematical and physical properties of strongly rotating and weakly rotating galaxies, allowing one to infer physical parameters just from measured kinematics.

The important piece of information that one can obtain about a galaxy is its size. There are many options to define or estimate the size of a galaxy. The most popular options are isophotal diameter D_{25}, Petrosian radius r_{petro} (Petrosian, 1976) and effective radius R_e, though all three do not actually represent the true size, but rather a proxy of how large galaxy is. Presently R_e is by far the most popular size proxy in the literature, typically used together with approximating the light distribution of a galaxy (or one of its components) by a Sérsic profile (Sersic, 1968). The profile is described as:

$$I(R) = I_0 \exp\left[-b_n \left(\frac{R}{R_e}\right)^{1/n}\right],$$

where R_e is the effective radius, n is called Sérsic index, and b_n is a normalization coefficient depending only on n.

With that, the use of the effective radius as a size proxy brings some inherent limitations and perplexities. A detailed description of the R_e caveats is provided in Graham (2019). I shall reiterate here that the single-Sérsic fitting of the objects, where more than one physical component is suspected to be present (e.g. S0 galaxies), might yield misleading values of structural parameters (R_e and Sérsic n). None the less, in some cases (e.g. galaxy studies at $z = 1.5$) one has to resort to single-component fitting, since even the *Hubble Space Telescope* imaging does not provide enough resolution to confidently fit an observed galaxy by two Sérsic profiles. Another noticeable R_e caveat is described in Chamba et al. (2020), where dwarf galaxies with different light concentrations (and hence different effective radii) are shown to have similar radii of threshold surface density (e.g. $M_* = 1\ M_\odot/\mathrm{pc}^2$). I shall bring the attention of the reader that in this manuscript, the word size is used as a synonym for the effective radius R_e – this is a conscious simplification to match the terminology widely used in the literature (i.e. the mass-size relation, which is actually based on the effective radius). One must remember that these are not the same and the effective radius is only a proxy (often not the best one) for the galaxy size.

Other famous scaling relations reflect dependence between color and magnitude (Sandage, 1972; Chilingarian & Zolotukhin, 2012), mass of the central black hole and the bulge (Kormendy & Ho, 2013), dark matter halo mass and stellar mass (Moster et al., 2010) etc. In this work however I will specifically focus on the mass-size relation in the intermediate redshift clusters as a metric for galaxy evolution.

In the local Universe and up to $z = 3$ the most massive galaxies are also among the largest (Kauffmann et al., 2003; Gadotti, 2009; Poggianti et al., 2013; Huertas-Company et al., 2013b; Fernández Lorenzo et al., 2013; Delaye et al., 2014; Belli et al., 2014; van Dokkum et al., 2015b). For example, local elliptical galaxies follow a rather tight relation with intrinsic scatter less than 0.3 dex (Nair et al., 2011; Bernardi et al., 2011b,a, 2014). This dependence is called galaxy mass-size relation (MSR) and provides an insight on the past and present evolution of galaxies.

The first results on the mass-size and size-luminosity relation at $z = 1$ and beyond to $z = 3$ were reported by Trujillo et al. (2004, 2006); McIntosh et al. (2005) who initially did not find strong size differences for massive ($M_* > 2 - 3 \times 10^{10}\ M_\odot$) galaxies at $2 < z < 3$ compared to $z = 0$, but later claimed that galaxies at $z = 2.5$ are on average two times smaller. Later results (Trujillo et al., 2011; Mosleh et al., 2011; Dutton et al., 2011; Szomoru et al., 2012) confirmed that the stellar mass-size relation was already in place at least at $z = 1$, but its normalization increased at low redshift.

The arrival of the new data, such as the Cosmic Assembly Near-infrared Deep Extragalactic Legacy Survey (CANDELS; PI: S. Faber, H. Ferguson; Koekemoer et al., 2011; Grogin et al., 2011), and new observational techniques, such as strong lensing (Yang et al., 2021), confirmed this view. van der Wel et al. (2012, 2014) measured the MSR redshift evolution for both passive and star-forming galaxies in the field in the redshift range $z = 0 - 3$. They demonstrated that the slope of the MSR does not evolve for both populations. However, galaxies become more compact with increasing redshift, which was explained by Carollo et al. (2013) by the fact that the Universe was more dense in earlier times, and the galaxy density evolves approximately as the density of the Universe.

The shape of the MSR is consistent with a scenario in which galaxy growth is dominated by star formation due to cold gas accretion up to a certain mass (which is redshift- and size-dependent, corresponding approximately to $M = 10^{11} M_{\odot}$ at $z = 2$ and $R_e = 1$ Kpc) and by galaxy mergers at higher masses (e.g., Shankar et al., 2013; van Dokkum et al., 2015b; Zanisi et al., 2020) In fact, hierarchical models could explain the fast size growth of giant elliptical galaxies only by sequential minor dry mergers since $z = 2$ (Naab et al., 2009; Trujillo et al., 2011; Newman et al., 2012; van Dokkum et al., 2015b). On the other hand, spiral galaxies do not require minor mergers, since their growth can be attributed to cold gas accretion (Dekel et al., 2009).

It is less clear though if galaxies in clusters and in the field evolved in the same way. Semi-analytical models predict a moderate to strong environmental dependence in the local Universe (Shankar et al., 2014). However, observational results are contradictory. Several works have shown that this relation is independent from environment (e.g., Guo et al., 2009; Weinmann et al., 2009; Cappellari, 2013; Huertas-Company et al., 2013b; Mosleh et al., 2018). Others found that cluster early-type galaxies (ETG) are smaller than those in the field (e.g. Poggianti et al., 2013), however they included a large fraction of S0 galaxies which appear to have smaller radii then elliptical galaxies at fixed stellar mass (Bernardi et al., 2013; Huertas-Company et al., 2013a), and different environmental relations (Erwin et al., 2012; Sil'chenko et al., 2018). On the other hand, Huang et al. (2018) found that massive galaxies in clusters are as much as 20%-40% larger than in the field with deep observations with the Hyper Suprime-Cam (see also Yoon et al., 2017). Cebrián & Trujillo (2014) found that both early- and late-type galaxies are slightly larger in the field, with the difference being the most pronounced at low masses ($\log(M/M_{\odot}) \lesssim 10.3$).

For spiral galaxies, the environmental dependence of the MSR is even more pronounced: its scatter is much larger (Maltby et al., 2010; Cappellari, 2013; Lange et al., 2015, though Cebrián & Trujillo (2014) found slightly lower scatter in clusters for late-type galaxies) and disks are smaller in clusters (Kuchner et al., 2017; Demers et al., 2019). This means that dense environments either destroy disks or inhibit their growth, for example through tidal interactions, ram-pressure, and/or strangulation (Boselli & Gavazzi, 2006).

1.6 Scientific problems

The environmental effects on galaxy evolution are rather strong: the three major groups of phenomena listed above tend to have pronounced differences in clusters and the field. Thus studying the role of environment is crucial in painting a coherent picture of galaxy evolution. The morphological transformations are also interesting, especially given that they are often correlated with quenching, but it is not always clear if there is a causal connection. In this general field, there are several more specific questions to be answered that motivated my research.

Firstly, the status of recently identified class of low-mass extended ultra-diffuse galaxies (van Dokkum et al., 2015a) among other types of dwarf (and non-dwarf) galaxies is currently under heated debate. It is not clear whether they form a physically distinct galaxy class (van Dokkum et al., 2015a; Danieli et al., 2019; Forbes et al., 2020; Brook et al., 2021;

Danieli et al., 2022; Villaume et al., 2022) or represent a "diffuse version" of other dwarf galaxy classes (Conselice, 2018; Chilingarian et al., 2019; Bogdán, 2020; Chamba et al., 2020; Kadowaki et al., 2021; Jones et al., 2021; Jackson et al., 2021). The clarification of this problem requires detailed studies of not only UDGs, but also dwarf elliptical and dwarf spheroidal galaxies to understand their similarities and differences, e.g. stellar population properties, kinematics, dark matter content, globular cluster systems, environment etc. The homogeneous spectrophotometric survey of dwarf galaxies belonging to all three classes would certainly help understand the position of UDGs in relation to other dwarfs, but such a survey needs some preparatory work. Thus, I performed a pilot study of a transitional dSph-UDG object in M 81 group to meet the following goals:

- Inquire whether the ground based integrated light spectral observations of such faint objects are sufficient to recover their kinematics and stellar population. The positive outcome would be the basis of a larger survey covering ~ 100 galaxies of dSph, UDG and dE/dS0 classes.
- Develop and test a dynamical modelling algorithm that allows to estimate the parameters of the dark matter halo (and possibly compare different halo models).
- Understand the evolutionary differences between similar objects in group and cluster environment.

Secondly, the evolutionary path of the ultra-diffuse galaxies is also unclear. The last point from the list above clearly requires better understanding of the processes leading to UDG formation in clusters. Specifically one might wonder how to form such diffuse and extended quiescent galaxies. Several channels have been proposed to date, e.g. "failed galaxies" (Yozin & Bekki, 2015), galaxy mergers (Baushev, 2018), collisions (Silk, 2019) and interactions (Bennet et al., 2018), stellar feedback (Chan et al., 2018a), tidal heating (Carleton et al., 2021) and ram-pressure (Jiang et al., 2019; Grishin et al., 2021). However it appears that no single mechanism can explain the entire UDG population alone. Here I studied one of the potential UDG formation channels in clusters, namely ram-pressure driven quenching of dIrr and dwarf spiral galaxies. This was done by analyzing the stellar population and kinematics of recently quenched post-starburst dwarf galaxies in Coma cluster. The goals of this study were:

- Demonstrate that ram-pressure stripping is indeed a viable channel of UDG formation, i.e. that some observed post-starburst galaxies will transform into UDGs.
- Estimate the efficiency of this channel, i.e. how many present day UDGs were formed like that.

Thirdly, the topic of galaxy evolution in clusters could be extended to higher redshifts. It is important to know how cluster galaxies were different from field galaxies at $z = 2$, when did these differences appear, and why. In the local Universe, the galaxy sizes in clusters and in the field are generally consistent, bot for passive early-type galaxies and for active late-type galaxies (Huertas-Company et al., 2013a,b; Bernardi et al., 2014), even if some works find some environmental dependence, with cluster galaxies being larger (Cebrián & Trujillo, 2014). At higher redshift $0.86 < z < 1.34$, ETG/passive galaxy sizes in clusters and in the field are mostly similar (e.g., Rettura et al., 2010; Huertas-Company et al., 2013a; Marsan et al., 2019; Kelkar et al., 2015; Matharu et al., 2019). Matharu et al. (2019) also provided a model scenario demonstrating that if the ETG sizes were different in clusters and field, they could be homogenized by the infall of the field galaxies into the clusters already by $z = 1$. At $z \gtrsim 1.3$ some works (Delaye et al., 2014; Mei et al., 2015; Matharu et al., 2019) pointed out that cluster galaxies have higher average sizes than the field, when the mass-size relation is taken into account.

With the access to the new CARLA data covering clusters at $1.3 < z < 2.8$ the following questions arose:

- What are the fractions of passive/star-forming and early-/late-type galaxies in these clusters. This question was addressed in a paper lead by Simona Mei (Mei et al., 2022) for which I mainly helped in the galaxy-star separation and final catalog characterization. I will not describe in detail this paper in this thesis, but only the elements that are important for the second questions below that I lead.
- What is the mass-size relation in these clusters, and how the galaxy size in clusters relates to the size in the field.

The body of this thesis is split into three chapters. Each chapter is dedicated to one of the three problems noted above in corresponding order. It is my earnest hope, that combined they provide a valuable advance in understanding the role of environment in galaxy evolution.

Chapter 2

Dwarf quiescent evolution

Ultra-diffuse galaxies represent a unique class of very diffuse objects that could serve as a perfect testing ground for theories of galaxy evolution and galaxy structure. However, their low surface brightness makes the spectroscopical studies difficult (Grishin et al., 2021), and there exists only a handful measurements of stellar population parameters and stellar velocity dispersions for such objects (Beasley et al., 2016; van Dokkum et al., 2016; Danieli et al., 2019; Chilingarian et al., 2019; van Dokkum et al., 2019; Gannon et al., 2020, 2021). The internal dynamics and dark matter content of UDGs remain poorly constrained.

The nearest known genuine UDG is 13 Mpc distant (Monelli & Trujillo, 2019). At that distance only the brightest RGB stars are detectable, using HST, thus detailed stellar population analysis is impossible. Finding UDG-like candidates in the nearest groups would help us understand UDG formation and evolution. The largest quiescent dwarf galaxy in the Local Group, Fornax dSph, clearly cannot be considered as a UDG, because of its relatively small 700 pc effective radius and high (~ 23 mag arcsec^{-2}) average surface brightness (Zaritsky et al., 2006).

The nearby M 81 group has 4 dwarf quiescent galaxies with $r_e \geq 1$ kpc but one (F8D1, Caldwell et al., 1998) is located behind Galactic cirrus, another (IKN, Karachentsev et al., 2004) lies close to a 9-th mag star, and a third (KDG 61, Makarova et al., 2010) is located very near M 81 with projected foreground star-forming regions and likely experiences tidal disturbance. The remaining dSph, KDG 64, is an excellent candidate for deep integrated-light spectroscopy. KDG 64 is one of the largest known dSph, and it borders the UDG and dE regimes in size and surface brightness.

KDG 64 is interesting exactly because it borders multiple dwarf galaxy sub-classes. Its distance of 3.73 Mpc (Tully et al., 2016) enables HST photometry of individual stars but precludes obtaining individual stellar spectra. KDG 64's angular size, surface density and distance places sufficient stars located within a spectrograph slit to measure the average stellar velocity dispersion (σ) along the line of sight. The stochastic influence of individual stellar velocities is expected to be insignificant (Dubath et al., 1992).

My intent in this chapter is to measure stellar population properties and kinematics in the dwarf spheroidal galaxy KDG 64. The kinematics are used to assess the properties of the dark matter halo of this galaxy through an adapted Jeans dynamical modelling algorithm. I performed the spectral analysis, aperture photometry and photometry with *Galfit*, as well as dynamical modelling. I would like to thank Igor Chilingarian for managing the observations and reducing the spectral data, Kirill Grishin for the the Binospec mask design and advice on full specrtum fitting, and Dmitry Makarov for performing star counts on archival HST ACS images. This chapter has been submitted to the journal Astronomy & Astrophysics as a paper (the draft is in the appendix). I thank Igor Chilingarian for help writing the text of this chapter and the paper, and the other co-authors for their valuable comments on the text.

2.1 Sample

The observations were performed with Binospec, a multi-object spectrograph at the 6.5-m telesope of the MMT observatory (Fabricant et al., 2019). This spectrograph has been demonstrated to suit well for the observations of low surface brightness targets due to a high throughput in the blue channel (i.e. Chilingarian et al., 2019). The spectra were obtained under an institutional observing time proposal (Harvard & Smithsonian Center for Astrophysics, PI: Chilingarian) on two consecutive nights: November 6&7, 2018 in a service mode using Binospec's 1000 gpm gratings with wavelength coverage 3,760 Å – 5,300 Å and $R = 3,750 - 4,900$ ($\sigma_{\rm inst} = 34 - 26$ km s^{-1}). The total integration time of 3h 20 min was split into 20 min-long exposures. The observations were conducted with seeing 0.9–1.3 arcsec and good transparency during dark time. The observing team took arc lamp and internal flat field frames at night time and high signal-to-noise sky flats during the day to characterize the spectral resolution across the field and wavelength range.

Kirill Grishin designed a single slit mask with three primary slits for KDG 64: two 50 arcsec-long slits along the major axis and one 20 arcsec-long slit along the minor axis. The major and minor axis slits are tilted by 35 deg and 55 deg to the direction of the dispersion, respectively. To prevent spectra from overlapping, the second major axis slit begins 28.5 arcsec from the galaxy centre. A background galaxy located near the geometric centre of KDG 64 was excluded. The mask PA value was set to +165 deg (see Fig. 2.2).

The data were reduced by Igor Chilingarian with the Binospec pipeline[1] (Kansky et al., 2019) that produces flux calibrated, sky-subtracted, rectified, and wavelength calibrated 2D long-slit images (plus flux error frames) for each slitlet. The image scale is 0.24 arscec pix^{-1} along the slit and the wavelength sampling is 0.38 Å pix^{-1}. We used non-local sky subtraction (i.e. a global sky model computed from all "empty" regions in all slits in the mask) optimized for low surface brightness targets.

The source has been previously observed with space- and ground-based telescopes. For the photometry I used the following publicly available archival data:

1. HST Advanced Camera for Surveys (ACS) images (obtained for a TRGB distance measurement) that resolve KDG 64 into individual stars (PID 9884, PI: Armandroff) in the *F606W* and *F814W* (Cousins Ic) bands;

---

[1] https://bitbucket.org/chil_sai/binospec/src

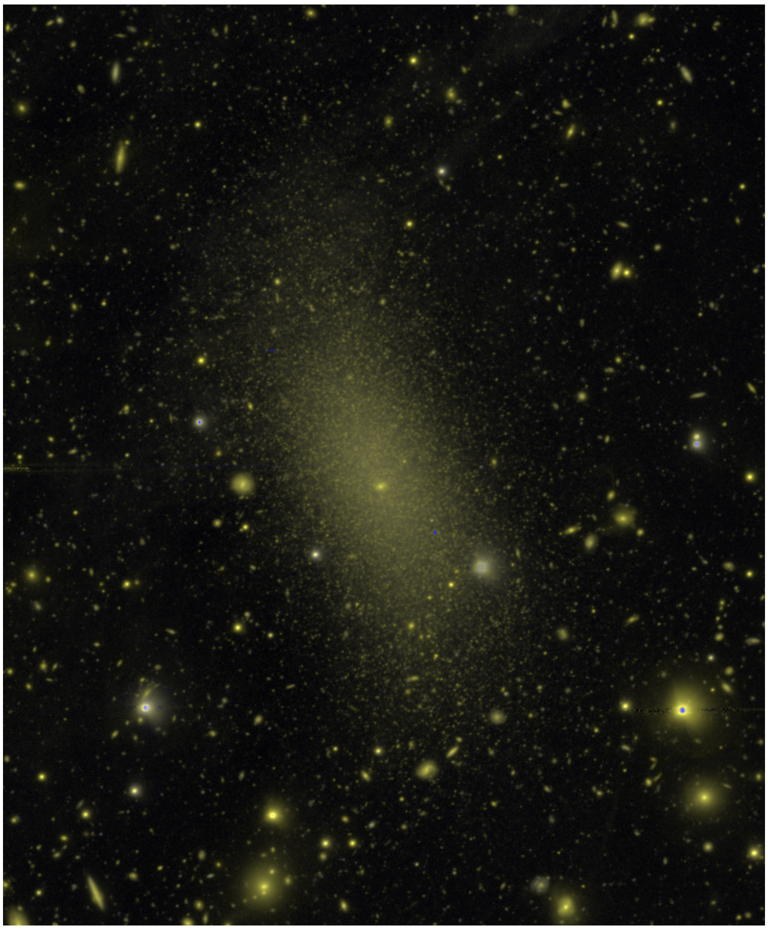

Figure 2.1: A Subaru/HSC color-composite (g- and i-band) image of KDG 64. Source: Subaru HSC Legacy Archive.

2. R-, B- and V-band images from the 2.1m KPNO telescope (PID 0117) for low-resolution 2-D surface photometry (300 s exposure time per band and 0.3 arcsec pix^{-1} scale);
3. GALEX images in NUV and FUV bands;
4. Spitzer Space Telescope *IRAC1* 3.6 μm and *IRAC2* 4.5 μm images.

2.2 Methods

2.2.1 Full spectrum fitting

I analysed the global properties of the KDG 64 stellar populations by modelling the integrated spectrum from the inner 12 arcsec of the major axis slitlet (Fig. 2.3) and the multi-wavelength spectral energy distribution. I used the NBursts+phot technique (Chilingarian & Katkov, 2012) that computes the position of a local minimum of the $(1 - w_{phot})\chi^2_{spec} + w_{phot}\chi^2_{phot}$ statistic. Here χ^2_{spec} and χ^2_{phot} are the χ^2 statistics for a spectrum and an SED

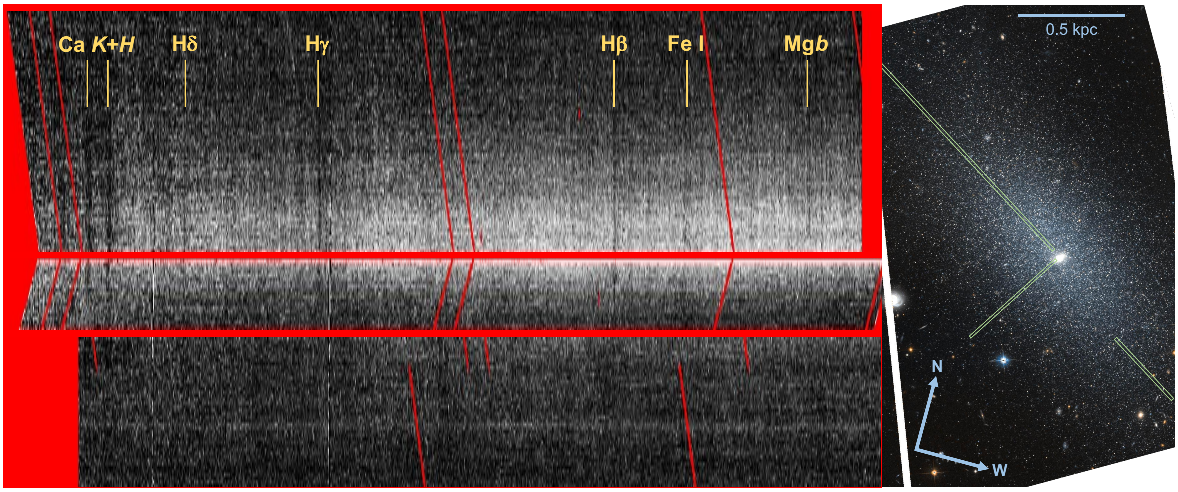

Figure 2.2: **Left:** long slit spectra along galaxy major and minor axes. **Right:** slit positions overlaid on an HST false-color (*F606W/F814W*) image.

respectively, and w_{phot} is the statistical weight of the residuals in the SED fitting. I modelled the optical spectrum from spectral templates interpolated to the specific values of stellar age and metallicity, convolved with the Gaussian line of sight velocity distribution (LOSVD) and multiplied by a polynomial continuum. I constructed a broadband spectral energy distribution (SED) by performing aperture photometry on GALEX (NUV and FUV bands), HST (*F606W* and *F814W* bands), KPNO (B, V, R bands) and Spitzer Space Telescope (*IRAC1* $3.6\ \mu m$ and *IRAC2* $4.5\ \mu m$) images. The PSF of each image was accounted for to carefully subtract the foreground and background contaminants (i.e. bright stars and galaxies detected in the *HST* image).

For modelling the global stellar populations, I used MILES (Vazdekis et al., 2010) simple stellar population (SSP) models computed for PADOVA isochrones (Girardi et al., 2000). The broadband SED is modelled using PEGASE.2-based low-resolution templates (Fioc & Rocca-Volmerange, 1997, 1999). The spectrum is degraded to a spectral resolution of 2.3 Å. I simultaneously modelled the observed optical spectrum integrated in the inner 12 arcsec bin and spectral energy distribution from UV to NIR (since further out the S/N of the spectrum is too low to estimate stellar population parameters). The flux in each band was extracted from an image within the elliptical isophote ($b/a = 0.5$) aligned with the major axis of 100 arcsec($\sim 1.4\ R_e$) excluding the background galaxy near the centre of KDG 64 as well as several other background/foreground contaminants. To account for potential flux calibration errors in both the observed spectrum and MILES SSPs, I included a 15th order polynomial continuum in the fitting procedure.

To measure internal kinematics, I also analysed a full-resolution long-slit spectrum using the NBURSTS technique (Chilingarian et al., 2007b,a), which implements a full spectrum fitting approach in the pixel space using a grid of intermediate-spectral resolution ($R = 10,000$) simple stellar population (SSP) models computed with the PEGASE.HR evolutionary synthesis package (Le Borgne et al., 2004). I convolved SSPs with the Binospec spectral line-spread function determined from the analysis of sky flats. As Chilingarian et al. (2008a) demonstrated, the NBURSTS algorithm can recover stellar velocity dispersions

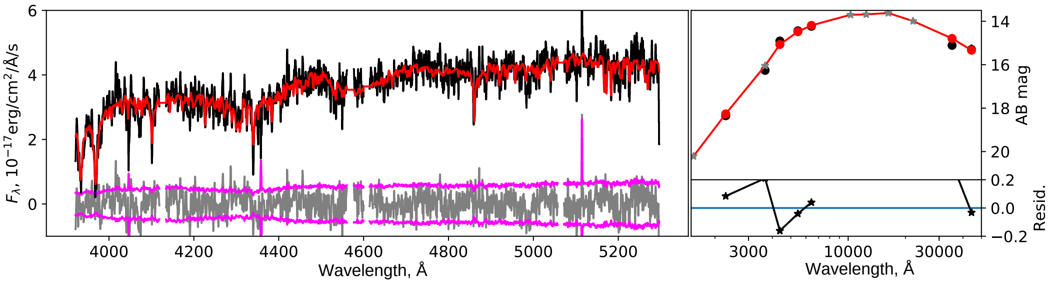

Figure 2.3: A Binospec spectrum of KDG 64 binned within 12 arcsec along the major axis on one side from the galaxy centre in F_λ units (left panel, black); an observed SED in AB magnitudes (right panel, black); the best-fitting model spectra and SED (red), flux uncertainties (purple) and residuals (grey line and black asterisks). The SED fitting residuals are shown in the bottom-right panel.

(σ) down to $\sigma_{\text{inst}}/2$ at a signal-to-noise ratio of 5 per pixel. I used the restframe wavelength range between 3900Å and 5200–5400Å for the fitting procedure. See Chilingarian et al. (2008b); Chilingarian (2009) for a detailed discussion regarding sensitivity, systematics, and limitations of the NBursts full spectrum fitting. I allowed a 15th order multiplicative polynomial continuum correction and a constant additive term to account for uncertainties in subtracting scattered light. The polynomial order (N_{poly}) is chosen to adapt to the fluctuations that have $\lambda_{fluct} \sim 200$Å scale (so $N_{poly} \approx 2 \times \frac{\lambda_{max}-\lambda_{min}}{\lambda_{fluct}}$), and odd orders of continuum consistently yield lower χ^2 than adjacent even orders.

For the reduced long-slit spectra, the median signal-to-noise ratio (SNR) per pixel in the wavelength range from 4,800–5,000 Å reached its maximum value of 1.65 in the brightest pixel of the major axis, the closest to the galaxy centre. To reliably measure stellar velocity dispersion of 15 km s^{-1} for old (10 Gyr) metal-poor ([Fe/H]=-1.5) stellar population, I binned the Binospec dataset along the slit to increase the SNR per spatial bin. I ended up with a total of 15 spatial bins along the major axis and 4 bins along the minor axis for radial velocity measurements (SNR=4) and 5 spatial bins along one side of the major axis (SNR=7) for velocity dispersion measurements. I could not measure the velocity dispersion along the minor axis due to the 1.8X spectral resolution degradation caused by the large tilt of the slit to the direction of dispersion. The velocity dispersion uncertainty estimate using a script from Chilingarian & Grishin (2020) yields an uncertainty of $\sim$ 6 km/s for the utilized setup, meaning that measured velocity dispersions are *not* upper limits with high significance. Thanks to the sufficient ($>$ 2x the data) resolution of the PEGASE.HR models and a well measured line spread function (LSF) of the Binospec spectrograph, the S/N=7 was sufficient to adequately measure the velocity dispersion.

2.2.2 Structural parameters and Dynamical modelling

For dynamical modelling one needs a global luminosity distribution that is difficult to construct from HST frames with conventional 2D-photometry packages (like Galfit or Sextractor) due to the presence of resolved stars. I therefore decided to determine the structural

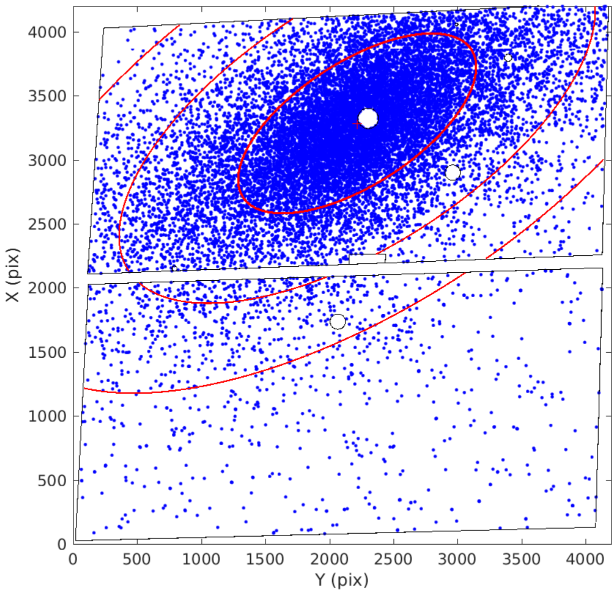

Figure 2.4: A map of the stars lying above the completeness limit (blue dots) in HST/ACS F814W image (the parallelogram-shaped chip boundaries are also displayed) . The best-fitting Sérsic profile elliptical iso-lines are overplotted in red. The white circle in the top chip shows masked region corresponding to a background galaxy.

parameters of KDG 64 from the magnitude-limited star counts normalized by the surface brightness profile obtained from seeing-limited ground-based images.

Dmitry Makarov used the DOLPHOT software package (Dolphin, 2000, 2016) for crowded field photometry to identify the resolved stars in the HST/ACS *F606W* and *F814W* images and to perform PSF photometry. Only the stars with good quality photometry were included in the final catalogue, following the DOLPHOT recipe and parameters. He chose only the stars lying above the completeness limit $m_{F606W} < 26.85$ mag and $m_{F814W} < 25.35$ mag. The spatial distribution of stars has been fitted with a single-Sérsic model using maximum likelihood. The centre coordinates, axial ratio, positional angle, effective radius, global normalization, and Sérsic index were set as free parameters. Also he accounted for foreground contamination following (Makarova et al., 2010) which gives a total of 30-40 stars from our Galaxy. Despite that, the distribution of stars required an additional constant background component at a level of $\sim$ 190 stars which may be an effect of contamination from M 81, M 82, and NGC 3077 The results of the star count decomposition are provided in Figures 2.4 and 2.5.

I performed a 2-D photometric decomposition of ground-based photometric data using Galfit (Peng et al., 2010). The model takes centre coordinates, Sérsic index, effective radius, positional angle, axis ratio and total magnitude as free parameters. All of the fitted parameters except effective radius and PA are close to those obtained from star counts. The divergence in R_e and PA might be explained by the presence of a galactic cirrus at the northern edge of KDG 64 that skews the 2-D photometric data. I used the central sur-

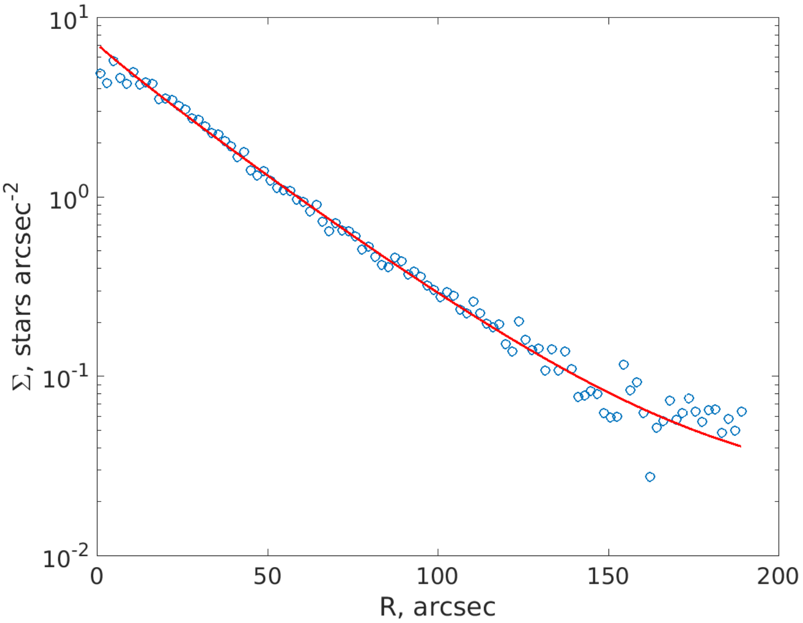

Figure 2.5: The stellar surface density profile (circles) fit by a Sersic profile (red line).

face brightness from 2D decomposition as a normalization to convert the surface density profile of the detected stars into surface brightness profile while keeping all the structural parameters from star counts, as this method better tracks the mass distribution in KDG 64.

I base my dynamical modelling algorithm on the JAM routine (Cappellari, 2008) which has been used extensively to model galactic kinematics in nearby and intermediate-redshift galaxies. It solves the Jeans (Jeans, 1922) equations assuming axial symmetry. To estimate dynamical mass-to-light ratio and mass of dark matter in KDG 64, I followed a procedure described in Afanasiev et al. (2018) without the central black hole component. From the $M_{BH} - M_{\rm bulge}$ scaling relation (Kormendy & Ho, 2013), massive central black hole is unlikely to be present in the centre of dwarf spheroidal galaxy (expected black hole mass $< 10^{4.5} M_{\odot}$), while low central velocity dispersion in KDG 64 rules out the presence of a black hole with $M > 10^{6}\ M_{\odot}$. Currently there is no consensus on the presence of massive black holes in dwarf spheroidals. Most kinematical studies do not find black holes more massive than $10^{5}\ M_{\odot}$ (e.g. Lora et al., 2009), however there is an evidence that some dwarf spheroidals might host supermassive black holes (Bustamante-Rosell et al., 2021). I decided to omit the black hole modelling in this case mainly because it adds an additional variable to the model while the spatial resolution of the kinematics does not allow to probe the black hole kinematic influence with sensible precision (this would likely require kinematics measures for individual stars).

The basic JAM code does not allow a non-self-consistent (that is “mass follows light”) as a default. The code however can be modified to handle the dark matter halo as a separate component influencing only the overall galaxy potential. I used a self-customised version of this code, which allows to handle a dark matter halo separately from the stars. I used two dark matter profiles to model KDG 64, a Burkert halo (Burkert, 1995) and a NFW halo (Navarro et al., 1997). These options allowed to model either cored or cusped dark matter

Table 2.1: Structural parameters of KDG 64 measured using star counts in HST ACS F814W image (left) and using Galfit analysis of 2.1m KPNO R-band deep images.

Method	Star counts	2D decomposition
R$_e$, pc	960 ± 25	1125 ± 20
R$_e$, arcsec	53.1 ± 1.4	62.2 ± 1.1
n	1.06 ± 0.05	1.07 ± 0.01
b/a	0.45 ± 0.01	0.49 ± 0.02
PA, deg	17.4 ± 1.2	28.1 ± 0.5

distribution and compare the goodness of fit for the kinematic data between the two options. Each of these two DM profiles is described by two free parameters and the other properties can be analytically derived. For the Burkert halo I used ρ_0 and r_s, and for Navarro-Frenk-White (NFW) profile I took M_{total} and R_s. I also calculated the total halo mass for the Burkert profile and the dark matter fraction within the effective radius R_e for both profiles to compare the halo parameters with each other and with the results from Chilingarian et al. (2019). With this approach I fixed the stellar mass-to-light ratio at the value determined from the stellar population, $M/L_{*,R} = 1.3\ (M/L)_\odot$ computed using PEGASE.2 models for the stellar population properties of KDG 64. I modelled only spherically-symmetric dark matter halos; oblate or prolate dark matter distributions were outside the scope of this study.

I obtained the galaxy stellar potential from the surface brightness profile using the Multiple Gaussian Expansion (MGE) method (Cappellari, 2002). For dynamical modelling I converted the dark matter profile into multiple Gaussians by fitting 1D dark matter density profiles with the MGE_FIT_1D procedure from Cappellari (2002) and reprojecting the resulting Gaussians in 3D. I added the Gaussians describing the dark matter and the stellar population potentials to obtain the final potential. I ran JAM over a parameter grid of anisotropy β_z (0 to 0.9), and inclination i from edge-on (90°) to the minimum allowed by the galaxy ellipticity (64°) in 6° steps. The grid also included two dark matter halo parameters (central density ρ_0 and scale radius r_s for Burkert halos; halo mass M_{200} and concentration c for NFW halos). I also calculated the halo mass for the Burkert halo (uniquely derived from each pair $\{\rho_0, r_s\}$) for comparison with the NFW halo mass. The concentration c for the NFW profile is capped at $c = 4$, because for lower c values it was not always possible to perform a MGE expansion. The dark matter density was truncated to 0 at R_{200} for both profiles to prevent the divergence of the multiple Gaussian expansion procedure.

2.3 Results

I obtained structural properties of KDG 64 (R_e, n, b/a) from star counts yielding best-fitting values $R_e = 53.1 \pm 1.4$ arcsec, $n = 1.06 \pm 0.05$, $b/a = 0.45 \pm 0.01$. The light distribution is very close to exponential. Assuming a TRGB-estimated distance modulus of 27.86 ± 0.01 mag (Tully et al., 2016), I estimated its physical size as $R_e = 960 \pm 25$ pc, placing it among the largest galaxies of the dSph type. For M 81, the adopted TRGB distance modulus

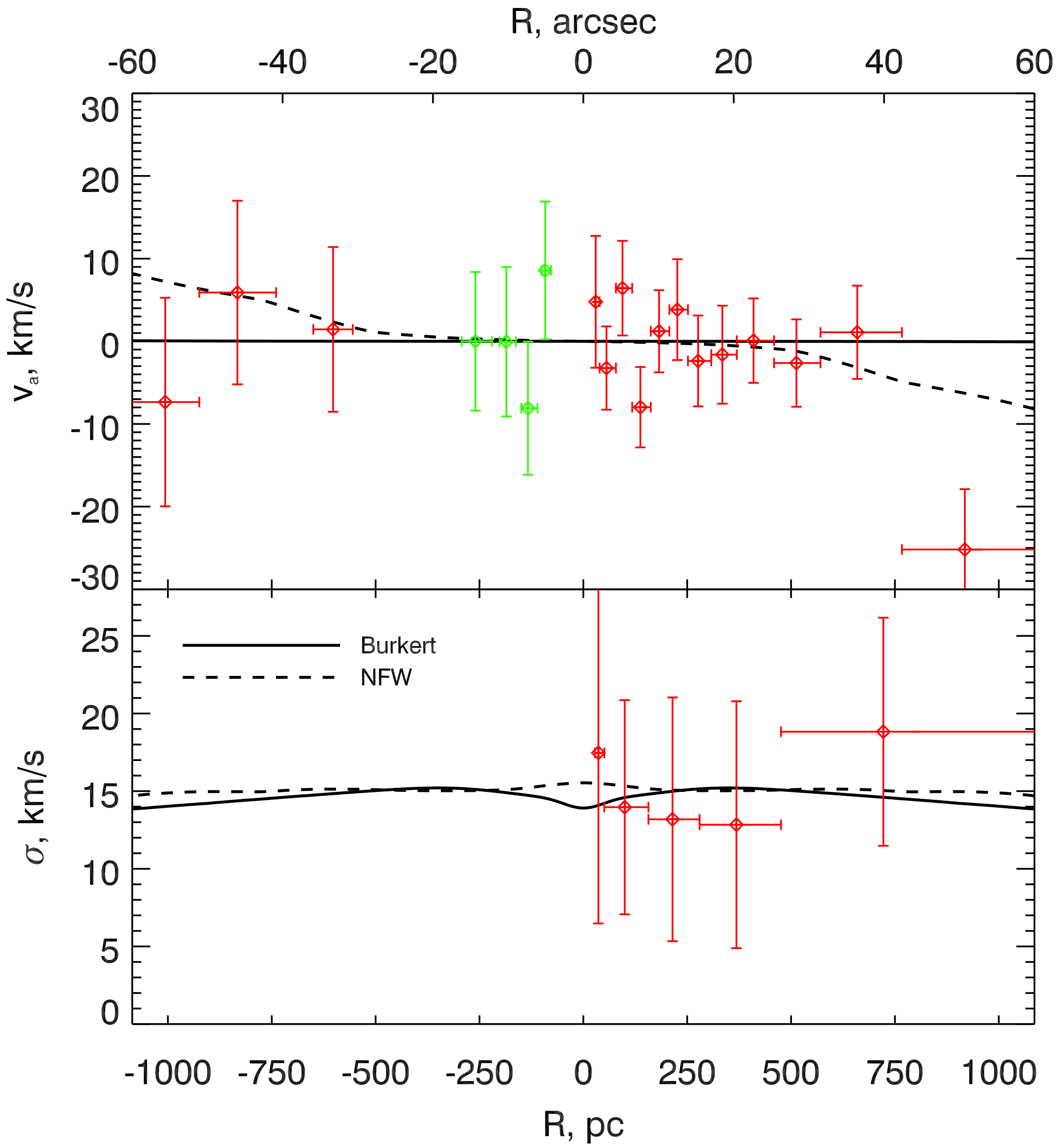

Figure 2.6: Resolved kinematics profiles (red and green v_r data points for minor and major axes respectively) and best-fitting Jeans dynamical models (black lines) with Burkert and NFW dark matter halo profiles.

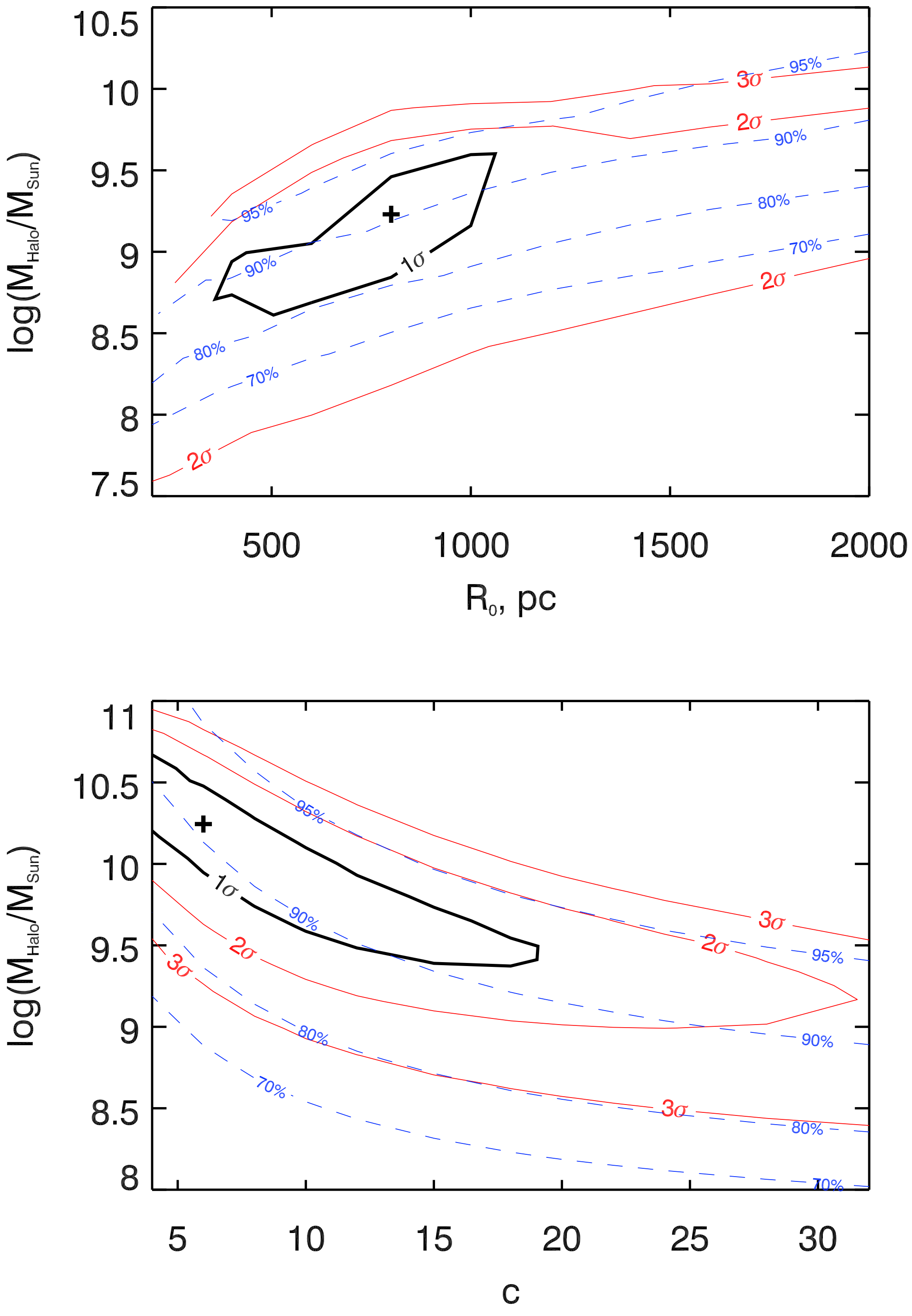

Figure 2.7: **Top:** The confidence levels for the parameters of the Burkert DM profile (red). **Bottom:** Same for the NFW DM profile. The blue dashed lines show the percentage of the dark matter inside 1 R_e for KDG 64 depending on the DM halo parameters.

Table 2.2: Internal kinematics and stellar population properties of KDG 64 derived from Binospec data.

Slit	Major axis	Minor axis
S/N, Å^{-1}	25	10
$v_{\rm los}$, km s^{-1}	-18.4 ± 3.4	-18 ± 6.0
$v_{\rm rot}$, km s^{-1}	< 2.0	< 6.0
σ, km s^{-1}	16.8 ± 1.9	17 (fixed)
Age, Gyr	10.9 ± 1.0	11.0 (fixed)
[Fe/H], dex	-1.33 ± 0.26	-1.33 (fixed)

Table 2.3: Best-fitting parameters of the dynamical models and their 1-σ uncertainties.

DM Halo	Burkert	NFW
log(M$_{200}$/M$_\odot$)	$9.2^{+0.3}_{-0.5}$	$10.2^{+0.4}_{-0.7}$
R$_{200}$, kpc	24^{+6}_{-8}	52 ± 20
R$_0$, kpc or R$_s$, kpc	0.8 ± 0.35	8.8^{+9}_{-7}
log(ρ_0), M$_\odot$ pc^{-3} or c	-1.0 ± 0.25	6^{+12}_{-2}
DM within R$_e$, per cent	90^{+4}_{-8}	91^{+3}_{-4}
β_z	0.8 ± 0.1	0.75 ± 0.1
Inclination, deg	72 ± 6	72 ± 6

is $d = 27.79$ mag (Tully et al., 2016). I calculated the full 3D distance between M 81 and KDG 64 of $r = 160 \pm 20$ kpc (smaller than the 230 kpc assumed in Makarova et al., 2010). The KDG 64 and M 81 heliocentric velocities differ by $\sim$ 20 km s^{-1} suggesting that the orbit of KDG 64 around M 81 lies nearly in the plane of the sky, in agreement with Makarova et al. (2010). Unfortunately it was difficult to assess if KDG 64 is located closer to the pericentre or the apocentre of its orbit.

The mean stellar age obtained from the SED supplemented full-spectrum fitting is 10 Gyr, the metallicity is [Fe/H]$= -1.3$ dex, corresponding to a stellar mass to light ratio $M/L_{\rm R,*} = 1.29 \pm 0.11$ $(M_\odot/L_{\odot,\rm R})$. The SED clearly indicates the lack of young or intermediate stellar populations with ages 5 Gyr or younger.

The vertical anisotropy β_z is rather high, with the best fitting values falling in the range $0.6 - 0.7$ for both DM halos; the best-fitting inclination to the line of sight is $i = 70$ deg. This means that the shape of KDG 64 is a very oblate spheroid, well represented by a thick disc and not a thin disc geometry.

Cored (Burkert, Burkert, 1995) and cusped (NFW Navarro et al., 1997) dark matter distributions fit equally well ($\Delta\chi^2 \approx 0.2$), preventing me from probing the shape of the DM distribution (Fig. 2.6). The best-fitting halo total masses differ by an order of magnitude ($\log(M_{\rm Burkert}/M_\odot) = 9.2$ vs $\log(M_{\rm NFW}/M_\odot) = 10.2$). However, the dark matter fraction inside the effective radius is the same for both halo profiles, slightly more than 90 per cent (see iso-lines in Fig. 2.7 and Table 2.3). This result is also consistent with the $M/L_{dyn,R} = 11$ obtained under mass follows light assumption using un-modified Cappellari (2008) code.

2.4 Conclusion

I demonstrated that one can obtain spectra of low-surface brightness dwarf spheroidal galaxies beyond the Local group of sufficient quality to determine reliable stellar populations and to make spatially resolved kinematic measurements. I am able to perform Jeans dynamical modelling and to estimate dark matter halo parameters. The stellar population parameters of KDG 64 were well measured and consistent between different studies, so I had a good reference for the stellar age and metallicity allowing to study kinematics more precisely.

KDG 64 is located 97.5 arcmin $= 106$ kpc in projected distance from the M 81 center. Even without taking into account the line of sight distance difference, I could estimate the maximum tidal disturbance from M 81. Karachentsev et al. (2002) derive M 81's group total dynamical mass as $\sim 1.6 \times 10^{12} M_{\odot}$, so the mass of the M 81 dark matter halo can be estimated at about 2 times smaller, in agreement with Oehm et al. (2017). An initially spherical galaxy 106 kpc from M 81 would have been distorted into an ellipsoid with expected axis ratio $a/b \approx 1.16 \pm 0.05$ in the M 81 direction (assuming Δr_e is $\sim \frac{2Mr_e^3}{md^3}$). This estimate follows from a tidal force formula for a constant density object. It is a strong assumption for a galaxy, however the decreasing stellar density and the presence of the dark matter around KDG 64 would counteract, and the precise tidal effect can be modelled in an N-body simulation, which falls beyond the scope of the thesis. Anyway, this estimate is way smaller than $a/b = 2.2$ obtained from the KDG 64 photometric analysis. Additionally, KDG 64's isophotes are extended along the line perpendicular to the direction towards M 81. It is therefore unlikely that KDG 64's elliptical shape stems from its current tidal interaction with M 81.

Using the 3D distance $d = 160$ kpc I could constrain the sphere of KDG 64's gravitational influence from the Jacobi radius (see Binney & Tremaine, 2008):

$$R_j = d \times \left(\frac{M_{KDG\ 64}}{3M_{M81}} \right)^{1/3} = 24\ \mathrm{kpc}. \tag{2.1}$$

Interestingly, the best-fitting value for R_{200} of the Burkert dark matter halo is ~ 25 kpc suggesting that the dark matter halos of KDG 64 and M 81 are in equilibrium. Thus, if KDG 64's dark matter halo is being stripped by its host, the process is gradual and should not lead to halo truncation (see also Borukhovetskaya et al., 2022).

KDG 64 exhibits no rotation along the major axis up to 20 arcsec (~ 360 pc, or $1/3$ R$_e$), and beyond that radius the presence of the rotation is questionable. The minor axis also does not exhibit rotation, consistent with the initial assumption of axial symmetry. The dispersion profile is flat, suggesting the dark matter halo dominates the potential at all radii. Low rotation and strong dispersion support is typical of dwarf spheroidals (Walker et al., 2009) as well as UDGs (Chilingarian et al., 2019, Ruiz-Lara et al., 2018, van Dokkum et al., 2019).

The κ-space Fundamental plane (Bender et al., 1992) is an important kinematics metric for a dispersion supported virialized galaxy. This is a modification of the original Fundamental Plane (Djorgovski & Davis, 1987) with the rotated axes (see Figure 2.8). The

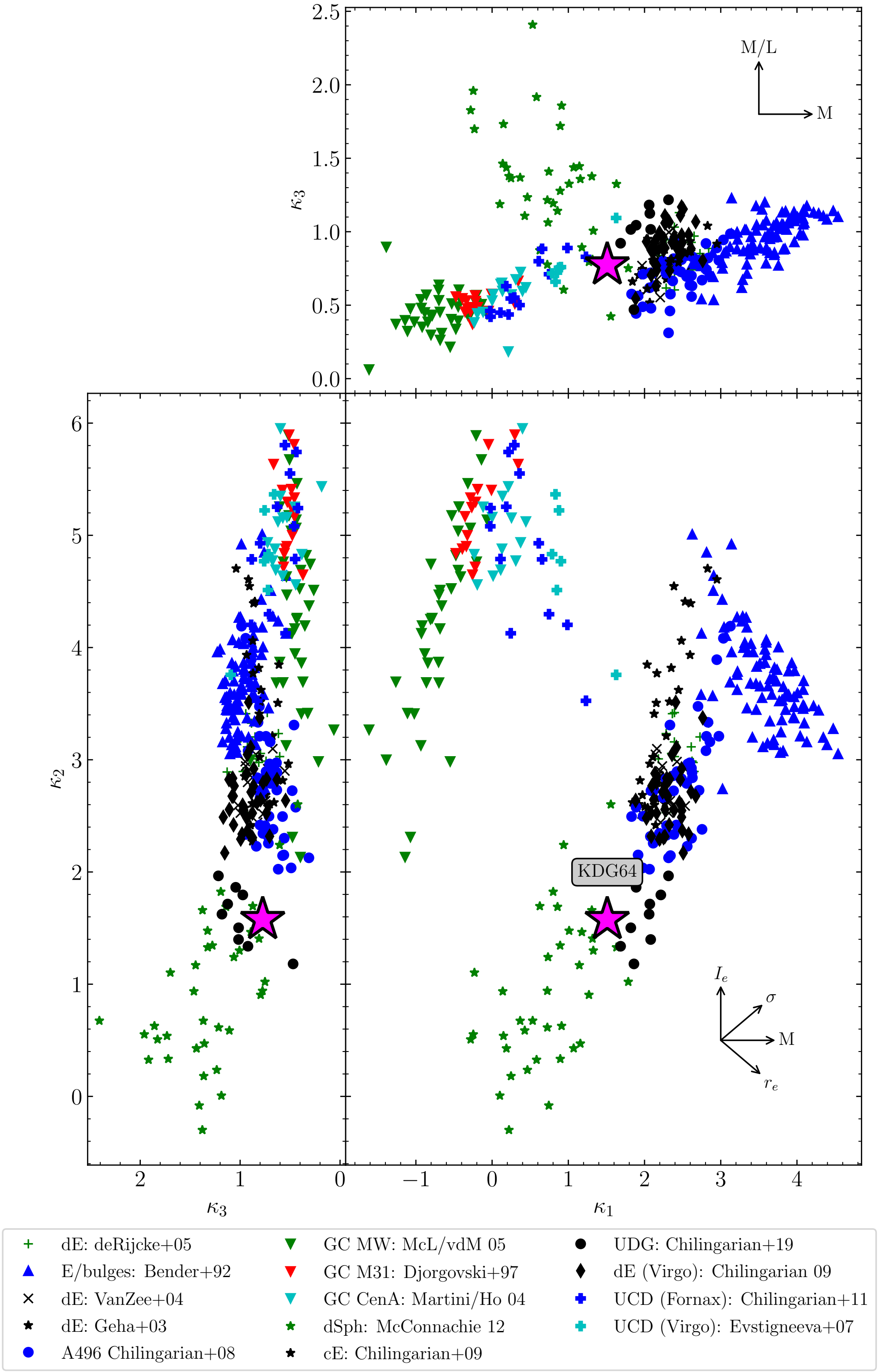

Figure 2.8: The κ-space view of the FP. The position of KDG 64 is marked by a pink star. The sources of data in the literature compilation are shown in the legend.

κ-parameters are defined as: $\kappa_1 = (\log\sigma_0 + \log R_e)/\sqrt{2}$ (a measure of $M_{\rm dyn}$); $\kappa_2 = (\log\sigma_0 + 2\log I_e - \log R_e)/\sqrt{6}$ (compactness); $\kappa_3 = (\log\sigma_0 - \log I_e - \log R_e)/\sqrt{3}$ (a measure of $(M/L)_{\rm dyn}$). KDG 64's position in the $\kappa_1 - \kappa_3$ projection is at the very edge of the 'classical' dSph locus (green stars). It lies comfortably on the trend relation set by globular clusters, UCDs, UDGs and bigger dE and giant elliptical galaxies, while most of the displayed dSph do not. The other two projections also show KDG 64 skewing to the UDG locus. These metrics clearly display KDG 64's transitional nature between dSphs and UDGs. The dark matter fraction within $1r_e$ of just above 90 per cent is comparable to the values found in Chilingarian et al. (2019) for small Coma UDGs. Walker et al. (2009) show that the dark matter fraction in dwarf spheroidal galaxies is stable to the choice of dark matter profile. This is also true for KDG 64. The 800 pc core size is similar to that of large dSphs (e.g Amorisco et al., 2013).

One potential caveat that is indeed present in the kinematics interpretation is the assumption that KDG 64 is oblate in shape. Prolate shapes are considered similarly plausible for dSph and ultra-diffuse galaxies (Burkert, 2017). Indeed, the major axis kinematics of KDG 64 does not demonstrate rotation up to ~ 750 pc or $3/4\ R_e$, which is often a sign of a prolate shape. However, the assumption of a prolate rotating galaxy does not match the data where the observed minor axis rotation is consistent with 0. It is also worth noting that in Grishin et al. (2021) some diffuse galaxies were observed to have no rotation up to $\sim 1\ R_e$, but velocities approaching v_{rot} beyond $1.5\ R_e$, which is consistent with oblate shape and high anisotropy (see e.g. Dehnen & Gerhard, 1993). Another option is that KDG 64 represents a bar-like structure that rotates in the sky plane (rotation axis roughly matches the line of sight), but unfortunately it is possible to neither confirm nor refute this hypothesis due to slow expected proper motions of the stars (10^{-6} arcsec/yr). In summary, it is difficult to establish the true shape of KDG 64 using the existing data, and an addition of prolate morphology to JAM modelling would be an interesting future development. For this study however, I decided to stick to the oblate hypothesis to be able to estimate the dark matter properties.

The structural parameters of KDG 64 also resemble those of smaller UDGs in the Coma cluster (Koda et al., 2015; Yagi et al., 2016 where the UDG selection criteria were $R_e > 0.7$ kpc and $\langle\mu_{e,r}\rangle > 24.0$ mag arcsec^{-2}). KDG 64 has $R_e \sim 0.95 \pm 0.1$ kpc and $\langle\mu_{e,r}\rangle = 23.89 \pm 0.05$ mag, so if placed inside Coma cluster and accounting for corresponding cosmological dimming ($\langle\mu_e\rangle$ becomes 24.01), KDG 64 would have narrowly passed the Yagi et al. (2016) UDG selection criteria. KDG 64 has a rather elongated shape, so if deprojected, its surface brightness would be even fainter. Yagi et al. (2016) catalog contains 204 galaxies (out of total 854) with R_e smaller than KDG 64, and 101 of them have $b/a < 0.5$. From a morphological perspective KDG 64 is similar to the small UDGs in the Coma cluster. These three similarities motivate the claim that KDG 64 is one of the closest UDG analogs in the Local Universe. It could act as a calibration object for integrated light studies of more distant galaxies.

The HST ACS data showed no detectable young stellar population. The full-spectrum plus SED fitting results, and especially the GALEX FUV and NUV fluxes support this conclusion. Makarova et al. (2010) found a slight enhancement of the star formation mostly about $1.5 - 2.5$ Gyr ago and an indication of very small fraction (less than 2 per-cent) of stars

$\sim$500 Myr old. These intermediate age stellar populations account for about 10 per cent of the total mass. Girardi et al. (2010) reports 7 to 9 per cent of population younger than 3 Gyr (with less than 1 per cent younger than 1 Gyr) based on the AGB to RGB star ratio. Weisz et al. (2011) indicate a more protracted star formation history, with only a half of KDG 64 stellar mass in place 6 Gyr ago, and 18 per cent of the stellar mass formed during the last 2 Gyr. This result is inconsistent with our results from full-spectrum fitting and SED analysis. Lianou et al. (2010) do not infer age, giving only the metallicity which varies between -1.72 dex and -1.39 dex depending on the chosen normalization and isochrone. CMD-based results from Milky Way dSphs (Tolstoy et al., 2009) suggest that many of them went through multiple phases of moderate star formation after the buildup of the bulk of their stellar mass $\sim$ 10 Gyr ago. These events typically make up about 10 per cent of the stellar mass, and happen once in 3-5 Gyr.

The best-fitting model for the stellar distribution was found to be Sèrsic + constant background. This background could be attributed to either M 81 + M 82 + NGC 3077 peripheral stars, or excess foreground stars in our Galaxy. In both cases, this background could contain some young stars that might shift the age statistic derived from CMD slightly towards younger ages, and the number of young stars detected in Makarova et al. (2010) is generally comparable to this background value.

Boyce et al. (2001) have detected an HI spur extending from the main cloud around NGC 3077 to KDG 64. However it is mostly located at the radial velocity of NGC 3077, which is about 200 kpc farther than KDG 64. This association with HI is most likely a projection effect, hence KDG 64 does not have any neutral gas.

The neighbours of KDG 64 in the M 81 group with comparable structural properties are KDG 61, DDO 78, DDO 71 (KDG 63), IKN (Karachentsev et al., 2004), and F8D1 (Caldwell et al., 1998). Their M_V ranges from -11.5 mag (IKN) to -13.9 mag (KDG 61), and they are on the bright end of the dSph luminosity distribution. These galaxies all have low surface brightnesses, around $\langle \mu_{e,r} \rangle = 24.4$ mag arcsec^{-2} for KDG 61 and $\langle \mu_{e,r} \rangle \approx 25$ mag arcsec^{-2} for the remaining three galaxies. IKN hosts an unusually rich system of globular clusters (Karachentsev et al., 2006) similarly to Fornax dSph (Buonanno et al., 1998), but its study is severely hampered by a 9 mag foreground star projecting directly on the northern part of the galaxy. Lianou et al. (2010) studied stellar populations of all the galaxies mentioned above as well as KDG 64 with archival HST data. They found that the galaxies are generally similar in their metallicities, ages and star formation histories, thus forming a cohesive population of dwarf M 81 satellites. Future integrated light spectroscopic studies of these objects will help understand the origin and evolution of UDG and dSph galaxy classes.

The evolutionary path of dwarf spheroidal galaxies is still a matter of debate as no single mechanism explains the diversity of their properties (Mayer et al., 2001, 2007; Read & Gilmore, 2005). Here I use KDG 64 properties as a case study for the main dSph formation theories. AGN in dSph have not been discovered to date, but according to well-established scaling between central black holes and their host galaxies (Ferrarese & Merritt, 2000; Gebhardt et al., 2000; Häring & Rix, 2004), they are expected to be in the intermediate-mass range (2 to $5 \times 10^4 M_\odot$), which will not provide enough energy output to quench star formation in the entire galaxy even if the AGN accretes at the Eddington limit. The starvation and strangulation mechanisms are also unlikely to play a major role, for their ineffectiveness in the low mass regime allows dwarf galaxies to form stars in the absence of an external gas reservoir for time periods comparable to Hubble time.

X-ray data from the XMM telescope archive[2] do not demonstrate that M 81 has a massive halo of hot circumgalactic gas. It is well established that ram-pressure quenching is not as efficient in groups as in clusters. In a low-density environment ram pressure is weaker – it may not strip the gas from a dwarf galaxy but instead shield it from UV emission keeping star formation in place (Hausammann et al., 2019). However, some models show that in the group environment ram pressure could act together with tidal heating to completely quench a dwarf spheroidal satellite (Mayer et al., 2006).

Supernovae (SN) feedback (Dekel & Silk, 1986) is widely considered the most common quenching mechanism in the low-mass stellar systems. In the absence of external forces, SN feedback is theorized to “fire” only once in the low mass galaxies, as the gas ejected by SN remnants is expelled forever from a galaxy potential far into the IGM. While SN feedback provides a good explanation for the old and metal poor stellar population, it doesn’t explain the lack of rotation in KDG 64. Dynamical modelling suggests KDG 64 is a very oblate spheroid that does not rotate. However, if it was formed from a star forming disky dIrr progenitor via SN feedback, some residual rotation should have been preserved after the quenching.

It is also puzzling that KDG 64 does not contain globular clusters (GCs) or a central star cluster (the central object shown in Fig. 2.2 is a background galaxy), while some morphologically similar galaxies contain many globular clusters (Fornax, IKN), and over half of all dwarf elliptical galaxies are nucleated (Grant et al., 2005). The majority of Milky Way dSphs do not have any GCs, however they are typically way smaller than KDG 64. Evidently, there exists some mechanism to remove them completely, and SN feedback is not expected to influence globular clusters.

I suspect that ram-pressure stripping, SN feedback and disc heating by M 81 tides all could have played a role in KDG 64 evolution. The old homogeneous stellar population and high orbital anisotropy suggest that KDG 64 should have spent most of its lifetime at moderate distance from M 81, where tidal forces are not strong enough to significantly deform the dSph satellite or strip its DM halo, but where tidal forces significantly contribute to the kinematical heating of the stellar component. As a result the stars gradually shift to the eccentric orbits, and the galaxy transitions from being rotation-supported to pressure-supported. Globular clusters are also shown to be influenced by tides that puff up the GC distribution (Carleton et al., 2021), easing their subsequent detachment. It is possible that the galaxy is initially quenched by SN feedback, and starts to be tidally heated soon afterwards. This tidal evolution has been shown to be important in the models of the Local Group dSphs (Peñarrubia et al., 2008).

---

[2] `https://nxsa.esac.esa.int/nxsa-web/search`

CHAPTER 3

ENVIRONMENT AND POST-STARBURST GALAXIES

Understanding the evolution of the dwarf galaxy population in galaxy clusters is of paramount importance both for the study of galaxy clusters in the cosmological framework and the evolution of individual galaxies in different environments. Specifically, this statement is true for the recently emerged ultra-diffuse galaxy (UDG) class (van Dokkum et al., 2015a; Koda et al., 2015; Yagi et al., 2016), that poses questions to the galaxy evolution theories. Initially some UDGs were thought to be "failed galaxies" (Yozin & Bekki, 2015): massive dark matter halos that formed few stars following rapid gas loss at an early evolutionary stage. This gas loss could arise from the cluster environment, including ram pressure stripping by hot intracluster gas (Gunn & Gott, 1972) and tidal interactions (Moore et al., 1996) or from internal processes such as supernovae (SN) driven winds (Dekel & Silk, 1986). Gas loss from a low-mass star-forming galaxy will quench star formation, allowing the galaxy to evolve into a quiescent early-type system. Recent observations (Ruiz-Lara et al., 2018) and simulations (Carleton et al., 2019; Jiang et al., 2019) suggest that a dwarf galaxy can be puffed up by SN feedback or tidal interactions and transformed into a UDG. It is unclear whether UDGs and dEs belong to the same family (Conselice, 2018; Chilingarian et al., 2019) and share similar evolutionary paths or if they represent different galaxy types with different formation scenarios (e.g. Baushev, 2018).

In the previous chapter, I proposed to overcome the inherent difficulty of an in-depth UDG study by finding the UDG analogs in the Local Volume, i.e. nearby galaxy groups. However, this is not the only available option. Assuming UDGs were once star-forming, one could try to find recently quenched low-mass galaxies (Poggianti et al., 2004), still containing young stars, that presumably will passively evolve into dEs or UDGs later through cosmic time. The higher surface brightness of such post-starburst galaxies (PSG, Henry & Lavery, 1987) enables detailed spectrosopic study of both kinematics and stellar population parameters. Thus one could hypothesize an evolutionary link between the well-studied starburst and post-starburst dwarf galaxies and UDGs.

I would like to bring the reader's attention to the difference between "post-starburst" and "recently quenched" galaxies, which sometimes get mixed together in studies. The term "post-starburst" means (or implies) that a galaxy experienced an elevated rate of star-formation before returning to normal or quenching, while quenching might not have been preceded by a starburst. In other words, not all post-starburst galaxies are quenched (Miller & Owen, 2001), and not all recently quenched galaxies are post-starburst. However, the objects studied in this chapter satisfy both definitions, so the difference is weakly pronounced.

In this chapter I attempt to develop the understanding of the environmental effects in galaxy evolution on a sample of low-mass recently quenched galaxies in Coma and Abell 2147 clusters. Similarly to the previous chapter, I performed photometric analysis and detailed dynamical modelling including dark matter, as well as population statistics calculation. These efforts were part of the study recently published in Nature Astronomy (Grishin et al., 2021), where I am one of three authors who contributed equally. I would like to greatly thank the other two main authors: Kirill Grishin who analyzed the spectra, developed the advanced stellar population models for recently quenched post-starburst galaxies and modelled the passive evolution of the stellar population and disk expansion, and Igor Chilingarian who first identified the sample, proposed and executed the observations, reduced the spectral data and generally managed the project. I thank Kirill Grishin and Igor Chilingarian for help writing the text of this chapter and the paper and the other co-authors for their valuable comments on the text.

3.1 Sample

Data mining the multi-wavelength Reference Catalog of Spectral Energy Distribution of galaxies (RCSED, Chilingarian et al., 2017) revealed 12 blue non-starforming galaxies (mean stellar age < 1.5 billion years) with half-light radii R_e between 2.0 kpc and 5.2 kpc. The RCSED galaxies are part of the main galaxy sample from the 7th Data Release of the Sloan Digital Sky Survey (Abazajian et al., 2009), and form a nearly complete magnitude-limited sample within the SDSS footprint. Nine galaxies reside in the Coma cluster (Figure 3.1), two are Abell 2147 cluster ($d = 156$ Mpc) members (Figure 3.2), and one is a group member. Four of the nine Coma cluster members were previously classified as "blue k+a" post-starburst galaxies (PSGs, Poggianti et al., 2004) based on their integrated-light spectra. However, a recent starburst is needed to properly reproduce the spectra and colours of the remaining galaxies, so they are also PSGs. Two Coma galaxies (GMP 4060 and GMP 2923) are known to exhibit (Yagi et al., 2010) spectacular tails of material stripped by the ram pressure of the hot intracluster medium (Gunn & Gott, 1972) with Hα emission suggesting current star formation. Their discs, unlike most other galaxies in the the Subaru SuprimeCam Hα survey of the Coma cluster, are not starforming. Young stars are UV-bright and expose a 250 kpc long tail in the most massive galaxy in the sample, GMP 2640 (Smith et al., 2010). Visual inspection of Subaru HyperSupremeCam images revealed filamentary tails in both Abell 2147 members (Figure 3.2). Deep broad-band and Hα images of the remaining Coma galaxies also expose faint low-contrast structures near them (Figure 3.3) that are likely the leftovers of ram-pressure-stripped tails significantly dimmed because of stellar evolution.

Blue extended PSGs were selected from the RCSED database by applying two sets of selection criteria. One of them has a stricter stellar age limit, and another one limits the integrated $g - r$ colour with slightly more relaxed stellar age restriction. This allows to

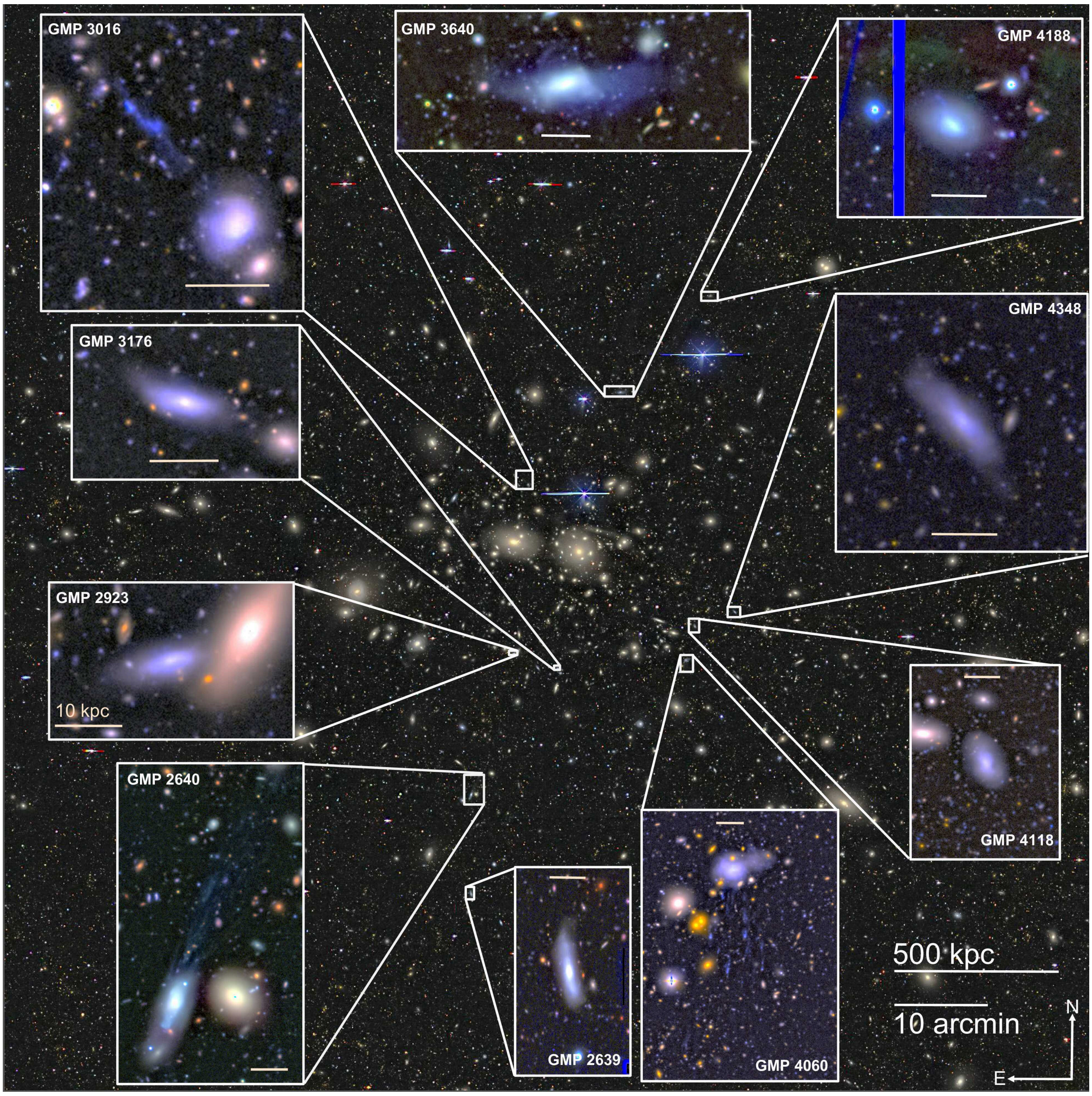

Figure 3.1: Positions of Coma cluster members selected from RCSED and one additional galaxy, GMP 3016. The insets showing zoomed-in galaxy images were constructed from Subaru and Canada-France-Hawaii Telescope (CFHT) optical data in the $u*$, B, V and R bands. A scale bar corresponding to 10 kpc is shown inside each inset.

minimize the loss of possible objects of interest because of the age-metallicity degeneracy that affects the results of the full spectrum fitting of a large galaxy sample using simple stellar population models: the reported overestimated intermediate stellar age (2–3 Gyr) is compensated by the underestimated stellar metallicity, and this degeneracy can be resolved by using broad-band colours. The first set of selection criteria includes:

- $F_{H\alpha}/\Delta F_{H\alpha} < 5$ AND $F_{[\mathrm{OIII}]} < 2\times10^{-16} erg/cm^2/s$ to select galaxies without prominent emission lines.
- Mean stellar populations younger than 1 Gyr. If a spectrum of a galaxy has low

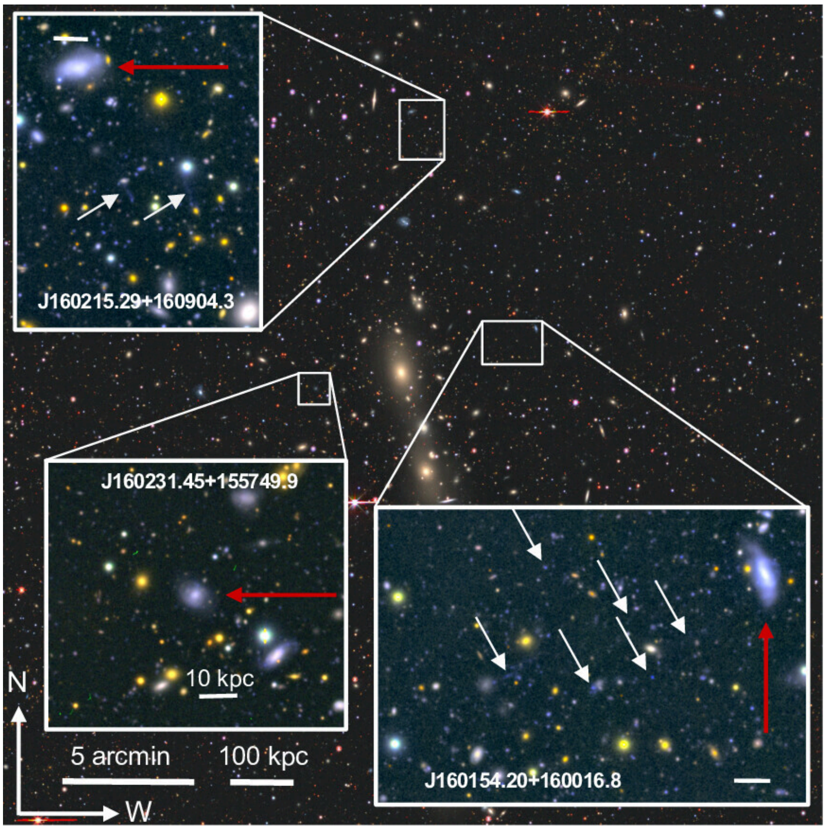

Figure 3.2: Positions of the two Abell 2147 cluster members selected from RCSED and an additional photometrically selected PSG, J160231.45+155749.9. The insets showing zoomed-in images for individual galaxies (marked by red arrows) are constructed from g, r, and i broadband Subaru HSC images. The two galaxies from the main sample exhibit tails of stripped material. The positions of clumps in the tails are marked with white arrows.

signal-to-noise ratio (SNR), its age may shift to the higher values with lower values of metallicity due to age-metallicity degeneracy. To take into account this fact the criteria were supplemented by joining with boolean OR a metallicity condition: $[\mathrm{Z/H}] < -1.3$ dex.

- Galaxies with spectral SNR > 4 reported by SDSS, which is typically underestimated by 30–35%. This criterion rejects spectra with unreliable signal.
- There is no template mismatch, $\chi^2_{\mathrm{ssp}} < 1$
- The extended objects were selected by setting the difference between 3-arcsec fiber magnitude and integral magnitude greater than 0.5 mag in the r band. This criterion selects galaxies with $R_e > 1.5$ kpc at the Coma cluster distance.
- Blue integrated colour $g - r < 0.55$ mag
- Low redshift $0.015 < z < 0.06$

The second filter includes the following conditions:

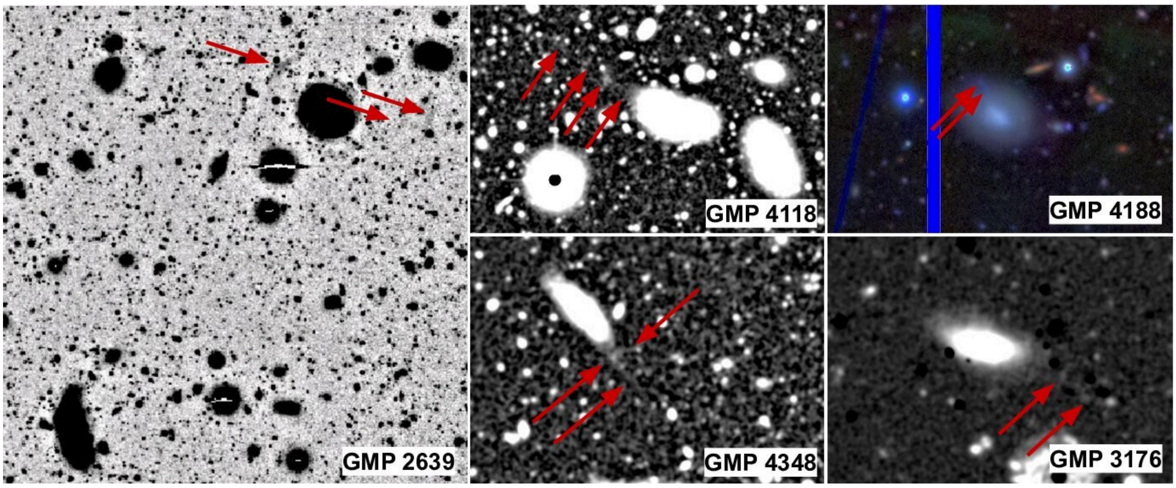

Figure 3.3: Low-contrast filaments suspected to be ram-pressure-stripped tails for five Coma galaxies. For GMP 2639 I show an inverted Rc-band image binned with a 4×4 pix window. For GMP 4118 and GMP 4348 I show H_α images without continuum subtraction convolved with a 2-D Gaussian kernel having FWHM in range $5\ldots7$ pix depending on S/N of input images. For GMP 3176 I show a difference between B and Rc Subaru frames. A spot at the end of the short filament in GMP 4188 pointed by an arrow is a bright Hα source.

- $\mathrm{F_{H\alpha}}/\Delta\mathrm{F_{H\alpha}} < 10$ AND $F_{H\alpha} < 2.5{\times}10^{-16} erg/cm^2/s$ AND $F_{\mathrm{[OIII]}} < 2.0{\times}10^{-16} erg/cm^2/s$
- Mean stellar populations younger than 2 Gyr.
- $\chi^2_{ssp} < 1$
- Difference between 3-arcsec fiber magnitude and integral magnitude greater than 0.5 mag in the r band.
- Blue integrated colour $g - r < 0.4$ mag
- Low redshift $0.015 < z < 0.06$

The joined list of galaxies that meet at least one set of criteria was compiled after rejecting galaxies with unreliable photometry and spectral line flux measurements, leaving 12 galaxies in total. All belong to the SDSS main galaxy sample so that these 12 galaxies form a nearly complete magnitude limited sample within the SDSS DR7 footprint. Nine galaxies are Coma cluster members, 2 galaxies are Abell 2147 cluster members, and the remaining galaxy is a group member (Saulder et al., 2016). In this study I considered only 11 cluster galaxies, because the remaining object does not possess deep high-quality optical imaging data that can be used to assess its structural properties.

Five additional galaxies were also considered as a supplementary sample. These include GMP 3016, the remaining known Coma cluster member with Hα detected in the tail but not in the main disc (Yagi et al., 2010). GMP 3016 is 0.03 mag below the SDSS magnitude limit and would have been excluded by the original selection criteria. Four additional galaxies without SDSS spectra were also included, three fainter UDGs in the Coma cluster with mean stellar ages < 2 Gyr (Chilingarian et al., 2019) and one photometrically selected faint PSG in Abell 2147.

3.2 Methods

3.2.1 Spectroscopic observations and data reduction.

The 11 low-mass PSGs in the Coma and Abell 2147 clusters were observed using the high-throughput multi-object Binospec spectrograph (Fabricant et al., 2019) operated at the 6.5-m MMT and reduced the data using the Binospec data reduction pipeline (Kansky et al., 2019) optimized for extended low-surface brightness objects. All runs were executed using the 1000 line mm^{-1} grating with a 1 arcsec-wide slitlets with the central wavelength of 4400–4500 Å that yielded the overall wavelength coverage of 3760 Å to 5300 Å. This configuration provided an instrumental resolution of $\sigma_{\mathrm{inst}} \sim 26 \ldots 34$ km/s. The exposure times were 2h-2h 20m per galaxy. Additionally, GMP 3640 was observed using the GMOS-N spectrograph operated at the 8 m Gemini-North telescope with the 3h 25m exposure time and effective spectral resolution $\sigma_{\mathrm{inst}} \sim 45$ km/s. More details on the observations are available in Grishin et al. (2021).

3.2.2 Stellar population properties and kinematics

For all PSGs Kirill Grishin simultaneously fit Binospec spectra and broadband fluxes from the far-ultraviolet ($\lambda = 0.17$ μm) to the near-infrared (λ=4.5 μm) extracted from the same region against a grid of PEGASE.HR-based PSG stellar population models using the NBURSTS+PHOT technique (Chilingarian & Katkov, 2012). These stellar population models (Grishin et al., 2019) assume a constant star formation, followed by a starburst and the subsequent shut-off of the star formation. The best-fitting solution yields four parameters: (i) the truncation age (i.e. end of ram pressure stripping); (ii) the fraction of gas consumed from a primordial reservoir before truncation, which is linked to the final stellar metallicity; (iii) the mass fraction of stars born in the final starburst; and (iv) a coefficient for galactic winds. In addition, he obtained radial velocity (V_R) and velocity dispersion of stars (σ), use adaptive binning along the slit to reach sufficient signal-to-noise ratio to reliably measure internal kinematics (7–10 per pixel depending on the object). The spectral resolution (R$\sim$10000) of the model exceeds Binospec's (R$\sim$4000) making it possible to measure velocity dispersion down to 10 km/s (Chilingarian & Grishin, 2020). The details on the stellar population models can be found in Grishin et al. (2019) and on its applications to the full-spectrum fitting in Grishin et al. (2021)

3.2.3 Structural parameters and deep Subaru images.

For Coma cluster galaxies I used deep Rc-band Subaru Suprime-Cam (Miyazaki et al., 2002) images (1470 – 7980 s exposure time) to determine structural parameters. For Abell 2147 only raw archival Subaru Hyper Supreme-Cam (Miyazaki et al., 2018) images were available, so I reduced and co-added them. Using GALFIT (Peng et al., 2010) I model each galaxy with a double Sérsic profile convolved with the point-spread-function (PSF) obtained from Gaussian fits to non-saturated stars. I use uncertainty frames obtained from reduced, sky subtracted Subaru images for the fitting procedure, adding sky background as a constant value obtained from the sky variation analysis. I derive the deprojected effective radius for each galaxy as follows. I construct the deprojected model image of the galaxy using the parameters of the Sérsic components from the fit results, changing the axis ratio to 1. I then measure the radius enclosing exactly half the total flux of the deprojected image. This method can be used for these galaxies since they are expected to have no gas, and hence no dust, so the attenuation is negligible.

I also inspected Subaru Suprime-Cam B-band, V-band, Rc-band, and Hα images downloaded from the Japanese Virtual Observatory. Rc-band images of GMP 3176 revealed a filamentary structure 70 kpc to the west from the galaxy main body. Another galaxy, GMP 3640 has three bright filaments, emerging from its main body. Several galaxies show clumps or other irregularities in their central parts. GMP 4060 and GMP 3640 exhibit the most noticeable disturbances. However, they are substantially less significant in the Rc band compared to the bluer bands (V and B) and, therefore, they are likely caused by different stellar population properties (i.e. younger stellar age) rather than variations in the stellar mass density which would significantly affect the gravitational potential. For Abell 2147 I retrieved raw Hyper Supreme-Cam data in the g, r, and i bands with the total exposure times of 3720, 240, and 2160 sec correspondingly from the Subaru archive and reduced them using the Hyper Suprime-Cam pipeline. In g-band images both Abell 2147 galaxies reveal faint tails with a complex filametary structure reaching 70 kpc in length. Both these tails point roughly towards the cluster centre. The brightest filaments of these tails are also detected in the r and i bands.

3.2.4 Dynamical modelling.

The dynamical modelling algorithm is generally similar to the procedure described in Chapter 3. Here I will state the points specific for this study. I obtained the structural parameters from the deep R-band Subaru data, and I used two-component Sérsic model for all the galaxies, which turned out to be a better fit in all cases. The stellar mass-to-light ratio M/L_* was fixed to the best-fitting value from the stellar population analysis that included a recent starburst.

The dark matter was added to the dynamical model independently from the stars for the main galaxy sample, however here I use only Burkert (Burkert, 1995) dark matter profile to decrease calculation time. This method was applied to all the galaxies in the main sample because it is more physically motivated than the traditionally used “mass follows light” approach. It also better reproduces the observed kinematics of the studied galaxies. The “mass follows light” approach implies that the mass and luminosity profiles of a galaxy have the same shape and differ only by a constant factor M/L_{dyn}, which becomes a free parameter of the fitting procedure instead of the parameters of the dark matter halo. I use this approach for the additional galaxy sample, because the lower quality of spectra prevents me from reliably determining the dark matter halo parameters. The kinematic disturbances in three galaxies, GMP 4060, GMP 2640 and GMP 4188 are unlikely to be of a dynamical origin.

The grids of dynamical models had the following steps: 0.1 for β_z, 0.25 for $\log\rho_0$, 0.2 kpc for r_s, and 6° for inclination. This spacing allows to confidently locate the position of the χ^2 minimum, but does not yield statistical uncertainties for these parameters.

3.2.5 UDG number statistics.

This part was done jointly with Kirill Grishin and Igor Chilingarian during several brainstorm sessions.

We assessed the importance of the ram pressure stripping scenario to other UDG formation channels. We note here that our estimates are applied to the passive UDGs only since the star-forming (often called "blue") UDGs require a different method. We statistically estimated how many present-day UDGs correspond to each PSG in our primary sample of 9 Coma cluster galaxies and compared the result to the observed number of UDGs in the Coma cluster. We modelled the surface brightness evolution from the reconstructed SFH and calculatde the two epochs: (i) t_{SDSS} when a galaxy becomes too faint to be included in the SDSS spectroscopic sample ($m_{R,\mathrm{tot}} > 17.77$ mag) and (ii) t_{UDG} when it dims enough to be classified as a UDG. UDG classification has a surface brightness cutoff of $\langle\mu_R\rangle_{\mathrm{eff}} > 24$ mag/arcsec^2. Statistically speaking, a given PSG will correspond to the number of UDG estimated as $N_{\mathrm{UDG}} = (t_{\mathrm{SDSS}} - 100\mathrm{Myr})/(10\mathrm{Gyr} - t_{\mathrm{UDG}})$ if $t_{\mathrm{UDG}} < 10$ Gyr. At 100 Myr emission lines disappear from a PSG spectrum, and 10 Gyr is the reference passive evolution time. At the end we co-added N_{UDG} for all 9 galaxies in the primary sample. We found that only 7 galaxies reach the UDG regime within 10 Gyr. The total number of expected UDGs from these 7 progenitors is 19.34$\pm$7.00. This estimate was made assuming a constant rate of infall of galaxies on a cluster. Simulations (Lisker et al., 2013) show that during the first 2–3 Gyr of the cluster formation epoch, the infall rate might have been upto twice as high as now. This may only increase our estimate of UDGs formed via the ram pressure stripping channel. The uncertainty was estimated by assuming the Poisson process of the galaxy infall and propagating stellar population parameter statistical errors and the estimated 10% systematic errors for the effective radii (Alabi et al., 2020) and truncation ages (Chilingarian & Asa'd, 2018).

We also estimated the total number of present-day UDGs in a complete magnitude limited sample (Koda et al., 2015; Yagi et al., 2016) with sufficient stellar mass so that 100 Myr after star formation quenching they would be bright enough to meet the SDSS spectroscopic selection. Our initial PSG selection criteria included a minimum 0.5 mag difference between the 3-arcsec fiber magnitude and the total magnitude. This corresponds to a lower R_e limit of $\approx$1.5 kpc for galaxies at the distance of the Coma cluster. During passive evolution, these galaxies will expand by $\approx$25%, so we only count the present-day UDGs having $R_e > 1.875$ kpc. To estimate the stellar mass we need to assume an SFH in a present-day UDG, which we could not infer directly from the available data. The most extreme case would be an instantaneous starburst modelled by a simple stellar population. Such a SFH leads to the minimal possible stellar mass cutoff and, hence, the largest number of UDGs passing the selection. For a 10 Gyr age, there are 90 galaxies in UDG sample (Yagi et al., 2016) which could satisfy the selection criteria for our PSGs in the past at some moment during their lifetime. Our lower limit of of UDGs is therefore 21±7 %, which could be explained by the ram pressure stripping formation scenario.

For a more realistic estimate we considered a typical observed SFH for our PSGs: a truncated constant SFR started 13.0 Gyr with 30% of the total stellar mass formed in the final starburst 10 Gyr ago. This corresponds to the median mass fraction we found in the PSG analysis. The number of UDGs that could possibly satisfy our selection criteria decreased to 44, increasing the importance of the ram-pressure-stripping UDG formation channel to 44±17 %. This fraction would increase even more if we take UDG SFHs with a lower final starburst fraction.

3.3 Results

In the primary sample of 11 PSGs, the truncation ages range from 180 Myr to 970 Myr. In 9 of the 11 galaxies the mass fraction of stars born in the ram pressure-induced starburst lies between 10% and 40%. The fraction of consumed gas for all 11 galaxies is higher than 60%, reaching 90–96% in six cases, corresponding to mass-weighted stellar metallicities of $-1.04\cdots-0.62$ dex. The estimated truncation ages for the seven galaxies with bright tails (including GMP 3016) are younger ($180\ldots500$ Myr) than for the remaining five, whose tails faded close to the limit of detectability. Deriving mass-to-light ratios from the best-fitting stellar population parameters, I estimate the total stellar masses of the PSGs to be in the range 5.1×$10^8 M_\odot$ (GMP 3176) to 2.36×$10^9 M_\odot$ (GMP 2640). Therefore, despite their large sizes these are all dwarf galaxies.

Young stars boost the surface brightness and allow to measure stellar kinematics (V_R and σ) to radii as large as 2.5 R_e (Figure 3.4), substantially further than for other low-mass galaxies beyond the Local Group. All 11 galaxies from the primary sample have $V_R/\sigma > 1$ in their outer parts suggesting that they are rotationally supported systems; GMP 3016 has a nearly face-on orientation. The absence of observed UDGs with such a pronounced degree of rotational support can be explained by the lack of observations to a comparably large radius and also because the stellar rotation in the inner part of a disc slows down over time due to disc expansion. If we restrict the field of view on the low-mass PSGs to the $0.5\ldots1.0$ R_e typically reached for faint dEs (Chilingarian, 2009) and UDGs (Chilingarian et al., 2019), only 6 have rotational velocities exceeding 10 km/s.

All galaxies from the main sample exhibit some sort of regular rotation within R_e. GMP 4060, GMP 2640 and GMP 4188 have noticeable kinematical disturbances localised in the area of significant morphological irregularities. Detailed analysis of high-resolution HST images for the brightest galaxy in the sample, GMP 2640, revealed a large number of luminous star clusters in its central part whose asymmetric distributions on the sides of the slit causes the non-uniform slit illumination and, hence, affects the radial velocity measurements. Disturbances of kinematics profiles of GMP 4060 and GMP 4188 are also of the same origin. I note that some simulations suggest that the ram pressure stripping by itself can lead to the displacement of the dark matter cusp in a low-mass galaxy (Smith et al., 2012), which will cause a slight lopsidedness in a galaxy with a stellar mass close to the least massive representatives of the studied sample.

I fit axisymmetric Jeans anisotropic models (Cappellari, 2008) to the stellar kinematics and structural properties assuming that each galaxy resides in a spherical dark matter halo. In all cases, the modelling yielded significant dark matter fractions, from 70% to 95% of the total mass within 1 R_e, and moderately anisotropic orbits, similar to those of UDGs (Chilingarian et al., 2019). However, the data are of far higher quality for the diffuse PSGs. The gravitational potential in these objects is rapidly changed by the removal of a substantial fraction of the gas by ram pressure on a timescale of $30\ldots70$ Myr, significantly shorter than typical dynamical times in galaxies ($200\ldots350$ Myr). The rapid gravitational potential change transforms quasi-circular stellar orbits to rosette-like (Safarzadeh & Scannapieco, 2017) orbits even in a massive dark matter halo. The stellar density decreases and its radial profile becomes shallower, the orbital radial anisotropy increases, manifested by a rotational velocity drop in the galaxy central regions. The disc expansion due to slow stellar mass loss during slow passive evolution ($5\ldots10$ Gyr) can be neglected when a galaxy has a massive dark matter halo. However, numerical simulations (Tremmel et al., 2020) suggest that a dark matter halo will be gradually stripped by tidal interactions with other galaxy cluster members during flybys, which would cause the overall stellar disc expansion by about 25% over 10 Gyr.

Assuming passive evolution, based on best-fitting stellar population parameters and a slow disc expansion, the internal properties (luminosity, surface brightness, luminosity- and mass-weighted stellar metallicities) for the sample galaxies can be predicted up-to 10 Gyr from now (Figure 3.5-3.6). The Faber–Jackson (Faber & Jackson, 1976) relation connecting stellar velocity dispersion to total luminosity and the luminosity–metallicity relation predict that low-mass PSGs will settle in the locus of known UDGs (7 Coma galaxies and 2 Abell 2147 galaxies) and dEs/dS0s (2 Coma galaxies) in 3–10 Gyr. The luminosity-weighted stellar metallicity will decrease over time because the contrast of the final ram pressure-induced starburst over an underlying metal-poor population will diminish. Stellar velocity dispersion will also decrease following the expansion of a galaxy driven by the slow mass loss due to stellar evolution. The disc expansion will lead to the decrease of the average stellar surface density in the disc by 40–50% without substantial disc thickening. In addition, the stellar volume density also decreases because of the slow stellar mass loss reaching 20% over 10 Gyr. These two factors combined will lower the stellar velocity dispersion by $\sim 35\%$ because σ is proportional to the square root of the local stellar density. The same 9 “future UDGs” will also settle in the UDG locus in the $\langle \mu_{Rc} \rangle$ - R_e diagram (Fig. 3.6) presenting their global structural properties (Kormendy, 1977).

3.4 Conclusion

Because the considered PSG sample in the Coma cluster is complete and because all galaxies were likely formed via ram pressure stripping, the observed UDG fraction formed through this evolutionary channel can be estimated. I compare the surface brightness evolution of low-mass PSGs to a complete photometric sample of Coma UDGs (Yagi et al., 2016). The

No.	Name	RA	Dec	v_r	σ_*	DM($< R_e$)	β_z	$\log \rho_0$	r_s	R_{200}	M_{200}	M^*	M_{Rc}	$\langle \mu_{Rc} \rangle$	R_e
		deg	deg	km/s	km/s	%	$1 - \sigma_z^2/\sigma_r^2$	$M_\odot \mathrm{kpc}^{-3}$	kpc	kpc	$10^8 M_\odot$	$10^8 M_\odot$	mag	$\frac{\mathrm{mag}}{\mathrm{arcsec}^2}$	kpc
1	GMP 4348	194.57587	27.84848	7524±1	51±2	85±8	0.3±0.05	-0.5	1.2	57.8	213	6.0	-18.21	22.45	2.73
2	GMP 3176	194.94282	27.74625	9690±2	46±4	88±5	0.4±0.1	-0.5	1.0	48.2	123	5.1	-17.75	22.51	2.21
3	GMP 2639	195.12170	27.33322	8449±1	43±2	84±3	0.4±0.05	-0.8	1.0	37.2	56	7.9	-18.69	23.34	4.99
4	GMP 4118	194.65901	27.82258	5350±3	33±7	80±10	0.5±0.15	-1.2	1.5	39.6	66	5.8	-17.88	22.79	2.98
5	GMP 4060	194.67746	27.76050	8683±1	26±2	87±15	0.0±0.15	-1.2	2.0	60.4	141	5.8	-18.43	22.32	3.09
6	GMP 2923	195.03358	27.77332	8665±1	40±1	69±9	0.6±0.1	-1.0	1.5	47.1	112	8.0	-18.33	21.78	2.14
7	GMP 2640	195.12180	27.51484	7304±1	78±2	90±4	0.7±0.05	-0.4	2.2	181.4	1445	23.6	-19.59	21.31	3.06
8	GMP 3640	194.81245	28.25101	7446±1	37±2	87±10	0.5±0.1	-0.8	1.5	56.1	186	9.2	-18.68	22.47	3.74
9	GMP 4188	194.63453	28.37797	5863±1	41±2	80±9	0.4±0.15	-1.5	2.1	54.3	195	6.1	-18.06	22.68	2.69
10	J160154.20	240.47583	16.00467	11506±1	52±2	96±2	0.6±0.05	-0.8	2.0	85.3	407	9.4	-18.81	22.33	2.85
11	J160215.29	240.56369	16.15119	12478±2	44±5	95±19	0.5±0.1	-1.0	1.2	37.6	58	7.4	-18.54	23.23	3.77
					Additional sample										
12	GMP 3016	195.00431	28.08188	7702±2	31±5	83±7	0.6±0.1	n/a	n/a	n/a	n/a	3.1	-17.34	22.86	2.17
13	GMP 2673	195.10945	27.45978	6915±4	41±8	82±6	0.8±0.2	n/a	n/a	n/a	n/a	3.1	-17.04	24.33	3.70
14	GMP 2552	195.16098	27.47647	7885±3	52±5	96±1	0.0±0.15	n/a	n/a	n/a	n/a	1.3	-16.13	23.80	1.90
15	J160231.45	240.63104	15.96387	11270±5	39±12	87±15	0.0±0.2	n/a	n/a	n/a	n/a	3.2	-17.25	23.29	2.20
16	GMP 2662	195.11375	27.43855	7360±6	54±12	94±2	0.6±0.1	n/a	n/a	n/a	n/a	0.7	-15.74	23.63	1.66

Table 3.1: Internal dynamics, dark matter contents and structural parameters of diffuse post-starburst galaxies. Columns: GMP (Godwin et al., 1983) designations for Coma cluster galaxies and IAU-style RA for Abell 2147 members (Name). Positions on the sky (RA, Dec), radial velocities (v_r) and stellar velocity dispersions (σ_*) obtained from the full spectrum fitting. Dynamical parameters: dark matter contribution to total mass within R_e (DM), the orbital anisotropy parameter (β_z), logarithm of the central density ($\log \rho_0$) and radial scale (r_s) of the dark matter halo (for the main galaxy sample), radius (R_{200}), where the dark matter density reaches the value 200 times greater than the critical density, dark matter halo mass (M_{200}) inside R_{200}, absolute magnitude, mean surface brightness in the Rc band within the effective radius and effective radii (M_{Rc}, $\langle \mu_{Rc} \rangle$, R_e).

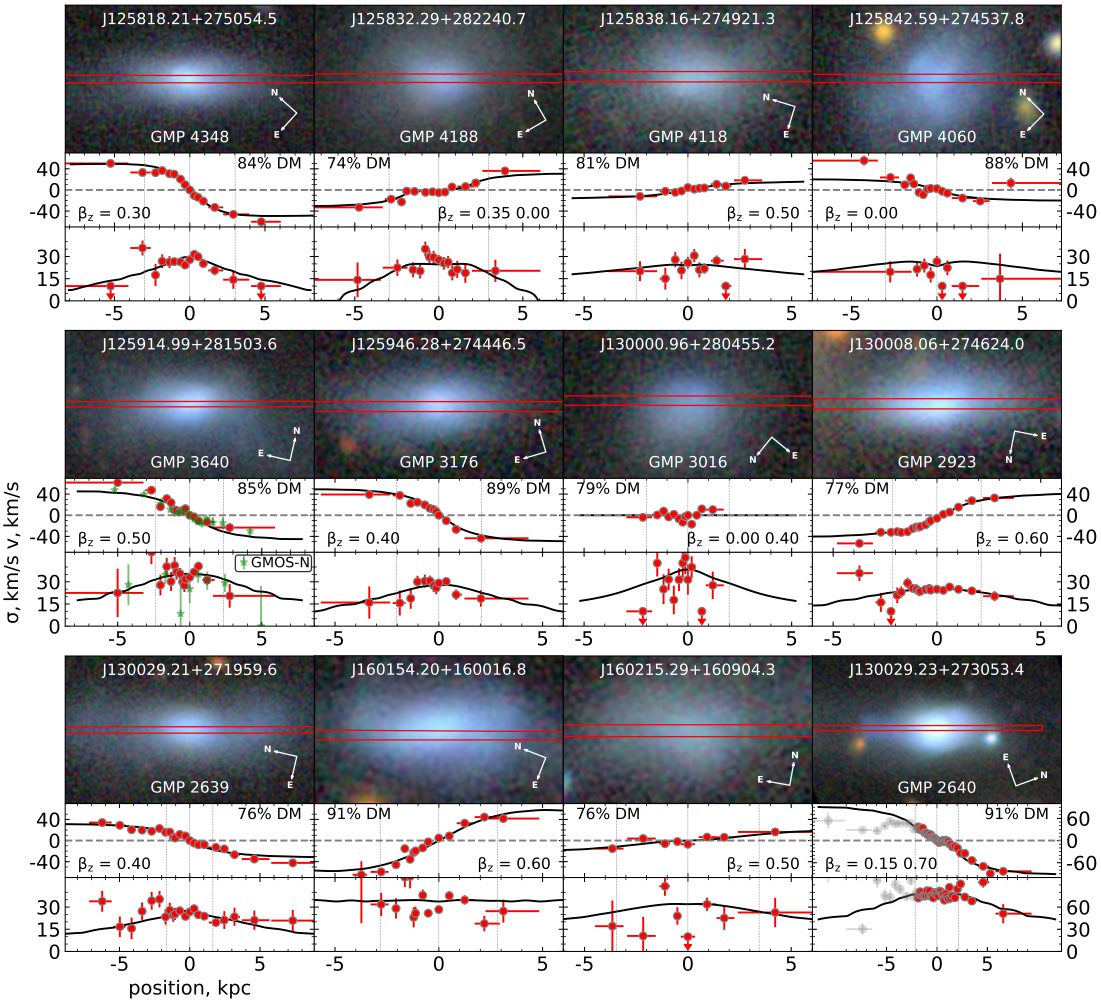

Figure 3.4: Top panel for each galaxy: an optical colour image with an over-plotted slit position; middle panel: stellar radial velocity v; bottom panel: stellar velocity dispersion σ. Black lines show the best-fitting Jeans models for stellar kinematics. The estimated dark matter contribution within $1R_e$ (indicated by vertical dashed lines) and the anisotropy parameter β_z are shown in the upper and lower corners of each v panel. For 8 out of 9 galaxies σ and v profiles are shown in the same scale. For the most massive galaxy, GMP 2640 the scale of these profiles is decreased. This galaxy also has a clump of young stars whose dynamics cannot be explained in the framework of axisymmetric modelling – the data points corresponding to this clump are greyed out.

reconstructed SFHs followed by passive evolution and slow stellar disc expansion allow to estimate how long each PSG will remain above the SDSS magnitude limit ($m_r < 17.77$ mag) after star formation quenching, and if (or when) its surface brightness drops below the adopted UDG threshold ($\langle\mu_{e,R}\rangle > 24.0$ mag arcsec^{-2}). The ratio of the duration of the UDG phase to the duration of the SDSS spectroscopic phase gives a statistical estimate of the number of UDGs corresponding to each PSG in the sample. The estimate is that in the next 10 Gyr, 7 of the 9 low-mass Coma PSGs (not counting GMP 3016) combined correspond to 19.3±7.0 “future” UDGs with $\langle\mu_{e,R}\rangle > 24.0$ mag. The remaining 2 galaxies will evolve into dEs/dS0s with higher surface brightnesses. To estimate the number of present-day Coma cluster UDGs which could have met the SDSS spectroscopic surface brightness and magnitude selection criteria any time in the past, one needs to make an assumption about their SFHs. With the extreme assumption of an instantaneous starburst 12 Gyr ago represented by a simple stellar population, 90 UDGs are expected, with 21±7% formed via ram pressure stripping. Assuming a scenario similar to what happened to the sample under study but 10 Gyr ago (constant star formation and a final starburst that formed 30% of the stellar mass), the result 44 UDGs and a fraction of 44±16 % formed by ram pressure stripping.

All nine low-mass Coma PSGs have high peculiar radial velocities ($500 \ldots 2000$ km/s) and move on non-radial orbits like many jellyfish galaxies (Jaffé et al., 2018). Their positions in the $\Delta v_r - d_{\mathrm{proj}}$ caustic diagram of the Coma cluster are consistent with the hypothesis that they have entered the inner part of the cluster for the first time. They have never crossed the dense cluster centre and are unlikely to ever do so, allowing them to survive for an extended period in a dense cluster environment. Observations (Vulcani et al., 2020) and simulations (Jiang et al., 2019; Jackson et al., 2021) confirm that ram pressure efficiently strips galaxies on tangential orbits, but the longer stripping timescales increase the efficiency of star formation triggered by ram pressure-induced gas compression (Cramer et al., 2020). During such a starburst a galaxy may reach its maximum lifetime surface brightness. GMP 4188, GMP 4118, and J160215.29 are examples of systems on non-radial orbits with lower stellar mass and low surface brightness, which barely made it into the SDSS.

For a galaxy infalling on a radial orbit, the ram pressure-induced starburst produces fewer stars due to rapid gas removal, and the stripped tail will be longer, fainter and harder to detect. Qualitatively, it can be assumed that for a galaxy infalling towards the cluster centre, the ram pressure becomes sufficient to ignite a starburst when it reaches some critical pressure value (P_{SB}); and then when it reaches $P_S = P_{SB} + \Delta P; \Delta P \ll P_{SB}$, the galaxy is stripped completely. The mass of stars formed should depend on the time needed to gain ΔP. ΔP will be gained much faster if a galaxy approaches the cluster core on a purely radial orbit with a pericentral distance close to zero than if it approaches on an orbit with a similar eccentricity ($e \sim 1$) but with a larger pericentral distance just sufficient to strip the galaxy completely. In the former case, the radial density gradient and the radial component of the orbital velocity $v_{r,\mathrm{orb}}$ work together because $P \propto \rho v_{\mathrm{orb}}^2$ and $v_{\mathrm{orb}} \approx v_{r,\mathrm{orb}}$. The large fraction of rapidly removed gas would also strongly increase the orbital anisotropy and decrease the observed stellar rotational velocity. The galaxies on radial orbits will fade and evolve into the UDG regime more quickly, but their low surface brightnesses will reduce their chances of inclusion in the SDSS spectroscopic sample anytime during their lifetime. Fainter and smaller GMP 3016, GMP 2673, GMP 2662 (Chilingarian et al., 2019), and J160231.45+155749.9 illustrate such a fainter continuation of the UDG evolutionary sequence. Such galaxies will also be harder to distinguish from those formed via different proposed UDG formation channels, whichoften produce non-rotating spheroidal stellar systems (Yozin & Bekki, 2015).

Were the late-type UDG progenitors normal-sized dwarf galaxies prior to falling onto the cluster that expanded due to ram pressure stripping? Or were they pre-processed by tidal interactions and supernovae feedback that had puffed them up first, followed by ram

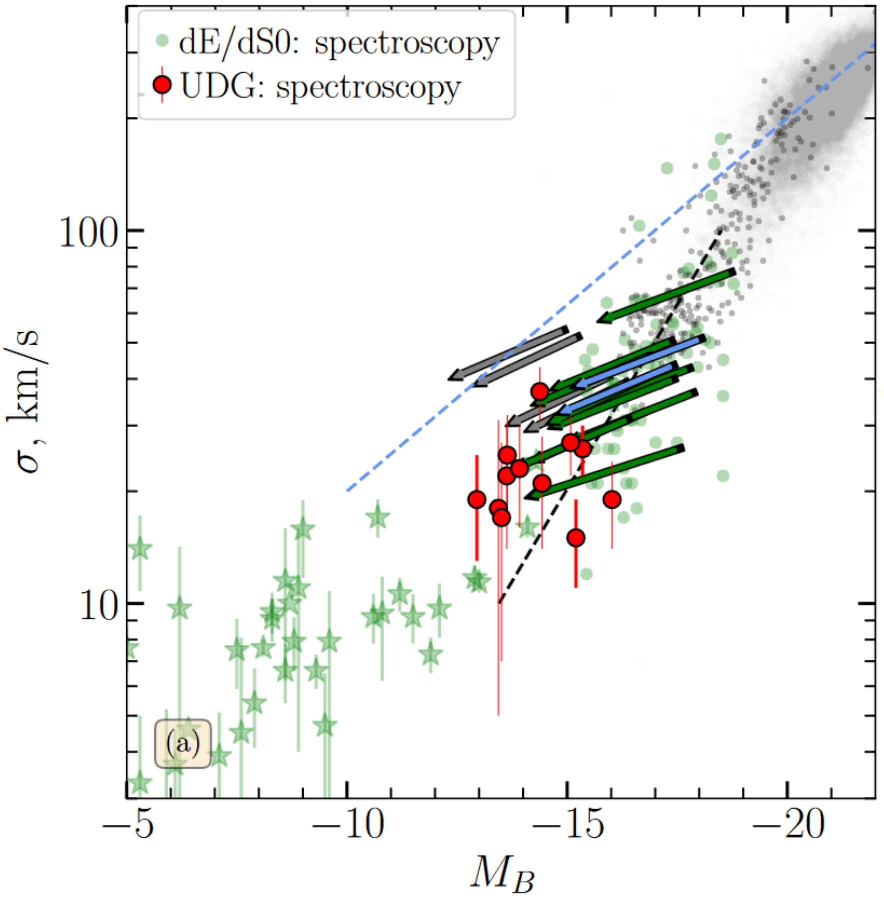

Figure 3.5: Predicted passive evolution of low-mass PSGs from their SFHs during the next 10 Gyr on the Faber–Jackson $\sigma - M_B$ relation. I show the primary targets from the Coma and Abell 2147 clusters and additional PSGs galaxies not included in the statistical calculations by green, cyan and grey arrows respectively. Each arrow starts at the currently observed position of a galaxy and points to its expected location in 10 Gyr. The $L \sim \sigma^4$ and the $L \sim \sigma^{2.5}$ best-fitting linear correlations (Graham & Soria, 2019) for giant and dwarf galaxies are shown. All PSGs but two will move into the UDG locus in the next 10 Gyr. The two remaining galaxies, GMP 2640 and GMP 2923 will settle in dE region. The literature sample includes dEs (Chilingarian et al., 2008b; Chilingarian, 2009; Binggeli & Jerjen, 1998), photometric (Alabi et al., 2020; van Dokkum et al., 2015b; Yagi et al., 2016) and spectroscopic (Gu et al., 2018; Ruiz-Lara et al., 2018; Chilingarian et al., 2019; Gannon et al., 2020, 2021) samples of UDGs, Local Group dwarf spheroidal galaxies (McConnachie, 2012), Local Volume dwarf late-type galaxies from *Little Things* (Hunter et al., 2012), a sample of giant early-type galaxies (Bender et al., 1992) complemented by a selection of Coma cluster early-type galaxies (grey dots) and elliptical galaxies at $z < 0.2$ (grey shaded region) from RCSED.

pressure stripping that quenched them without increasing their size? Simulations (Safarzadeh & Scannapieco, 2017) suggest that a stellar disc of a low-mass gas-rich (gas fraction 70%) galaxy sitting in a $M_{200} = 10^{11} M_\odot$ dark matter halo (slightly more massive than stud-

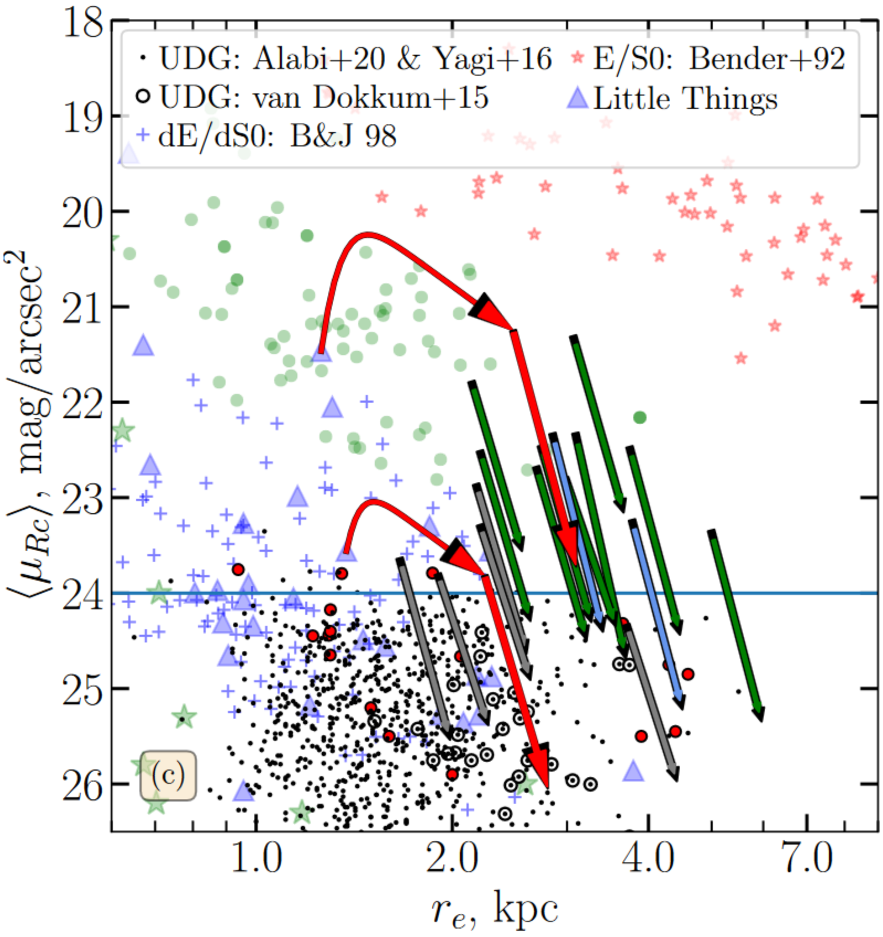

Figure 3.6: Predicted passive evolution of low-mass PSGs from their SFHs during the next 10 Gyr on the mean surface brightness – effective radius $\langle\mu_{Rc}\rangle$ - R_e relation. The points are same as in Fig. 3.5. A cyan solid line at $\langle\mu_{Rc}\rangle = 24.0$ mag/arcsec^2 denotes the UDG surface brightness cut. The red tracks display evolutionary models of the two *Little Things* objects, NGC 4214 and DDO 168 if they were ram pressure stripped: (i) a ram pressure induced starburst and disc expansion (curved tracks) followed by (ii) slow passive evolution (straight tracks).

ied PSGs) would expand by a factor of ∼1.5 due to ram pressure stripping alone while the stellar mass loss would remain negligible. On the other hand, the "Little Things" survey (Hunter et al., 2012) of local dwarf late-type galaxies includes 9 of 37 objects with regular kinematics having $R_e > 1$ kpc, high gas fractions, and dark halo masses in the range of $10^{10.2} \ldots 10^{10.7} M_\odot$ (Oh et al., 2015). If they fell onto a cluster, they would first become brighter because of the ram pressure induced starburst, but later, when stripped, would expand to $R_e = 1.5 \ldots 5$ kpc and fade as a result of passive evolution, finally ending up in the UDG locus of the $\langle\mu_e\rangle - R_e$ diagram as shown by red tracks for the two examples in Fig. 3.6. Their largely undisturbed morphology and kinematics along with sparse environment suggest that they are "normal" low-mass discs, which did not undergo significant pre-processing, hence, corroborating the scenario that ram pressure stripping alone can transform many dwarf spiral and irregular galaxies into UDGs by causing both quenching and disc expansion. Because the radial distribution of neutral gas in gas-rich dwarfs is usually much shallower than stellar density profiles (Hunter et al., 2012), the ram pressure induced star formation could further grow R_e by stronger stellar surface density increase in the outer parts of the disc compared to the inner regions. A search in RCSED for low-mass ($M_* < 3 \times 10^9 M_\odot$) extended ($R_e > 2$ kpc) star-forming galaxies within 5 Mpc from the Coma cluster centre reveals about 50 objects with the morphologies resembling those of "Little Things" dwarfs, which might become the progenitors of a new generation of PSGs and then UDGs, should they fall onto the Coma cluster core in the future.

Chapter 4

CARLA clusters

To better understand and confirm which evolutionary physical processes led to the environmental effects observed in the local Universe, it is essential to study the dependence of galaxy size growth on environment through cosmic time. One of the most obvious ways to do it is to study the mass-size relation (MSR) of galaxies in clusters and in the field at different redshifts. Here I point out that the word "size" in this chapter always refers to the effective radius R_e. It is true that these two quantities are not the same physically, and the effective radius also depends strongly on the light concentration in the galaxy image. However, it is widely used as a size proxy for distant galaxies where other, more precise size proxies can not be adequately measured. The detailed discussion on the meaning of galaxy size is provided in Chapter 1.

The relation between galaxy size and mass is different for late- and early-type galaxies (LTG and ETG) due to their different structure. Late type galaxies are mostly spirals, and their size depends weakly on galaxy mass (e.g., van der Wel et al., 2014), which means that more massive LTGs have higher stellar densities. ETG sizes demonstrate similar behaviour only up to $\log M/M_\odot \sim 10.3$ (Kormendy, 1977), and more massive early-type galaxies have a clearly defined mass-size dependence. This mass-size relation of massive ETGs have been extensively studied, because its existence suggests the presence of some universal mechanisms in the formation and/or evolution of early-type galaxies. The consensus scenario for the origin of the massive ETG mass-size relation is a series of numerous dry minor mergers and/or tidal disruption of satellites (e.g., Naab et al., 2009; Dekel et al., 2009; Oser et al., 2012; Lapi et al., 2018). van Dokkum et al. (2010) (see Fig. 8 and Eq. 6-7) demonstrated that any physical process depositing mass at $r > R_e$ would result in a relation $R_e \propto M$ for exponential density profile and $R_e \propto M^{1.8}$ for de Vaucouleurs profile, translating into a linear dependence in the mass-size plane. Minor mergers are very effective in puffing up the outskirts of an ETG and do not cause significant mass growth (Bezanson et al., 2009; Hopkins et al., 2009). At the same time this hypothesis does not require exotic ways of rapidly changing the galaxy potential like pushing large quantities of gas to the galaxy periphery by quasar activity (e.g., Fan et al., 2008, 2010). The size history of ETGs is thus a reflection of the minor merger history, which has important implications in the cosmological theories (Bower et al., 2006; Toft et al., 2012; Brooks & Christensen, 2016; Rey & Starkenburg, 2022). On the other hand, the number of minor mergers experienced by a given early-type galaxy might be different depending on its environment (Somerville & Davé, 2015). Thus the studies of the mass-size relation relative to the environment are of utmost importance.

The studies of the mass-size-environment dependence have yielded varying results, especially for quiescent ETG, which are the main focus of the present Chapter. One of the main reasons for such a variety in conclusions stems from slightly varying sample properties (i.e. mass range, size definition, environment selection, etc.), so here I try to unite these studies mentioning their most important features.

No difference was found at $0.4 \lesssim z \lesssim 2$ between galaxies in the field and moderately dense environments (e.g., Rettura et al., 2010; Huertas-Company et al., 2013a; Kelkar et al., 2015) for $\log(M/M_{\odot}) \sim 10.5 - 11.8$. At $z = 2$, Allen et al. (2015) report larger cluster star-forming galaxies compared to the field, while quiescent galaxies do not show such a difference, being only slightly larger in clusters (in the mass range $\log(M/M_{\odot}) \sim 9 - 11.5$). This notion is supported by Saracco et al. (2017) at $\log(M/M_{\odot}) \sim 10.3 - 11.3$, who have found no environmental effect on the $z = 1.3$ elliptical MSR, noting that cluster ellipticals tend to be more massive. Mowla et al. (2019) and Marsan et al. (2019) focused on high-mass ($\log(M/M_{\odot} > 11.3)$) passive galaxies, whose MSR was found to be consistent with the lower-mass galaxy MSR and to show strong evolution with redshift.

Others found larger quiescent galaxy sizes in clusters at both high (Delaye et al., 2014, $\log(M/M_{\odot}) \sim 10.5 - 11.5$) and low (Mei et al., 2015, $\log(M/M_{\odot}) \sim 9.5 - 10.5$) mass. At $z = 1.4$ Chan et al. (2018b) found that passive cluster galaxies ($\log(M/M_{\odot}) \sim 10.2 - 11.5$) are about 30% larger than in the field. Noordeh et al. (2021) also found larger cluster quiescent galaxy sizes for $\log(M/M_{\odot} > 10.3)$ with Sérsic $n > 2$ at $z = 2$.

Smaller sizes in clusters were reported by Raichoor et al., 2012 ($\log(M/M_{\odot}) \sim 10 - 11.5$) in low statistical significant samples. Sazonova et al. (2020) found that $z = 1.5$ bulge-dominated cluster galaxies with $\log(M/M_{\odot} < 10.5)$ are significantly more compact than the field counterparts. (Matharu et al., 2019) reported slightly smaller cluster passive galaxy sizes at $0.86 < z < 1$ for $\log(M/M_{\odot} > 10)$.

There is also some evidence that the MSR flattens out at low masses ($\log(M/M_{\odot}) \lesssim 10.3$) in the local Universe Bernardi et al. (2011a), and up to $z \sim 1$ (Nedkova et al., 2021), as predicted by models (Shankar et al., 2014). The picture complicates even further if size is quantified by the the half-mass radius instead of the half-light radius. In fact, the average galaxy concentration also depends both on environment and redshift (Szomoru et al., 2013; Mosleh et al., 2017; Suess et al., 2019).

Finally, several studies found high percentages of compact post-starburst (Barro et al., 2013; Maltby et al., 2018; Socolovsky et al., 2019; Matharu et al., 2020; Wilkinson et al., 2021) and massive compact galaxies (Lu et al., 2019; Gu et al., 2020; Tadaki et al., 2020) in dense environments at $z = 1.5 - 2$.

Several works (i.e. Cebrián & Trujillo, 2014; Delaye et al., 2014) hinted at the hypothesis that the redshift evolution of galaxy size in clusters might be different from that in the field, while Matharu et al. (2019) found that this difference likely diminished already by $z \sim 1$.

In this chapter, I extended MSR studies in an unique sample of galaxy clusters at redhift

$1.3 \lesssim z \lesssim 2.8$ from the CARLA (Clusters Around Radio-Loud AGN (Wylezalek et al., 2013, 2014) survey. It contains 15 most prominent galaxy overdensities followed up by *HST* F140W imaging and G141 grism spectroscopy. The cluster total stellar mass spans the range $11.3 < \log(M_*^c/M_\odot) < 12.6$, which corresponds to an approximate halo mass in the range $13.6 < \log(M_h^c/M_\odot) < 14.6$ (Mei et al., 2022, submitted to A&A). The aim of this chapter was to take advantage of the available high-quality data to test several hypotheses about cluster galaxies at $1.3 < z < 2$. I wanted to contribute to the following open problems: (i) Estimate how the galaxy size in clusters compares to the field (i.e. larger or more compact galaxies). (ii) Assess the evolution of this cluster-to-field size ratio with redshift. (iii) Given the relatively low mass measurement threshold, assess the MSR flattening towards the low masses.

This part of my thesis is part of a larger in-depth study of the CARLA clusters, performed by Simona Mei, Nina Hatch, Stefania Amodeo and myself within the larger CARLA collaboration. Many interesting results, including the sample selection of the 15 most promising overdensities, are contained in a companion paper, Mei et al. (2022), where I am also a co-author. I will be referencing this companion article as M22 throughout the thesis. This chapter will be published as a paper to be submitted to the journal Astronomy & Astrophysics (the draft is in the appendix). I thank Simona Mei for help writing the text of this chapter and the paper. I also thank other co-authors for their valuable comments on the text.

4.1 Sample

4.1.1 CARLA cluster candidates

CARLA is a 408h Warm *Spitzer*/IRAC survey of galaxy overdensities around 420 radio-loud AGN (RLAGN). The AGN were selected across the full sky and in the redshift range of $1.3 < z < 3.2$. Approximately half of them are radio loud quasars (RLQs) and the other half are radio galaxies (HzRGs). With the aim to detect galaxy cluster candidates, Wylezalek et al. (2013) selected galaxies at $z > 1.3$ around the AGN, using a color selection in the IRAC channel 1 ($\lambda = 3.6\ \mu$m; IRAC1, hereafter) and channel 2 ($\lambda = 4.5\ \mu$m; IRAC2, hereafter). They found that 92% of the selected RLAGN reside in dense environments, with the majority (55%) of them being overdense at a $> 2\sigma$ level, and 10% of them at a $> 5\sigma$ level, with respect to a field sample in the *Spitzer* UKIDSS Ultra Deep Survey (SpUDS, Rieke et al., 2004).

From their IRAC luminosity function, Wylezalek et al. (2014) showed that CARLA overdensity galaxies have probably quenched faster and earlier compared to field galaxies. Some of the CARLA northern overdensities were also observed in either deep *z*-band or deep *i*-band, with Gemini/GMOS, VLT/ISAAC and WHT/ACAM (P.I. Hatch (see below); Cooke et al., 2015). These observations permitted us to estimate galaxy star formation rate histories, and to deduce that, on average, the star formation of galaxies in these targets had been rapidly quenched (Cooke et al., 2015).

The twenty highest CARLA *Spitzer* overdensities candidates were followed by a *Hub-*

ble Space Telescope Wide Field Camera 3 (*HST*/WFC3) observations (P.I. Stern (see below); Noirot et al., 2016, 2018), and sixteen of them were spectroscopically confirmed at $1.4 < z < 2.8$, together with seven spectroscopically confirmed serendipitous structures at $0.9 < z < 2.1$ (Noirot et al., 2018). The structure members were confirmed as line-emitters in Hα, Hβ, [OII], and/or [OIII], depending on the redshift, and have star formation estimates from the line fluxes (Noirot et al., 2018). The galaxy star-formation (for stellar mass $\gtrsim 10^{10} M_{\odot}$) is below the star-forming *main sequence* (MS) of field galaxies at similar redshift. Star-forming galaxies are mostly found within the central regions (Noirot et al., 2018).

Mei et al. (2022) (M22) performed an in-depth study of the morphology, quiescence and merger incidence of CARLA clusters. They found that the galaxy morphology-density and passive-density relations are already in place at $z \sim 3$ and 2, respectively. The cluster ETG and passive fractions depend on local environment and mildly on galaxy mass. Cluster merger fractions are significantly higher than in the CANDELS fields, as predicted from previous studies to explain high quiescent fractions at $z \lesssim 1.5$. Their findings confirm that all the spectroscopically confirmed CARLA overdensities have properties consistent with clusters and proto-clusters.

I briefly describe the observations used in this study below. More details on the *Spitzer* IRAC, *HST*/WFC3 and ground-based observations, data reduction and results can be found in Wylezalek et al. (2013, 2014), Noirot et al. (2016, 2018), and Cooke et al. (2015), respectively.

4.1.2 Spitzer Observations

All CARLA clusters were observed with *Spitzer* IRAC1 and IRAC2 (Cycle 7 and 8 snapshot program; P.I.: D. Stern), with total exposure times of 800 s/1000 s in IRAC1 and 2000 s/2100 s in IRAC2, for clusters at $z < 2/z > 2$, which provided a similar depth in both channels. The IRAC cameras have 256×256 InSb detector arrays with a pixel size of 1.22 arcsec and a field of view of 5.2×5.2 arcmin. Wylezalek et al. (2013) performed the data calibration and mapping with the MOPEX package (Makovoz & Khan, 2005) and detected sources with SExtractor (Bertin & Arnouts, 1996), using the IRAC-optimized SExtractor parameters from Lacy et al. (2005). The final *Spitzer* IRAC1 and IRAC2 mosaic has a pixel size of 0.61 arcsec, after taking into account dithering and sub-pixelation. The 95% completeness limit is obtained at IRAC1=22.6 mag and IRAC2=22.9 mag.

4.1.3 HST Observations

The *HST*/WFC3 imaging and grism spectroscopy were obtained with the dedicated *HST* follow-up program (Program ID: 13740; P.I.: D. Stern). The program consisted of F140W band (hereafter H_{140}) imaging (with a field of view of $2 \times 2.3\ \mathrm{arcmin}^2$ at a resolution of $0.06\ \mathrm{arsec\ pix}^{-1}$, after taking into account dithering), and G141 grism spectroscopy (with a throughput > 10% in the wavelength range of $1.08\ \mu\mathrm{m} < \lambda < 1.70\ \mu\mathrm{m}$ and spectral resolution $R = \lambda/\Delta\lambda = 130$). This grism was chosen in order to permit the identification of strong emission lines at our target redshift, such as Hα, Hβ, [OII] and [OIII]. Noirot et al. (2016, 2018) performed the data reduction using the `aXe` (Kümmel et al., 2009) pipeline, by combining the individual exposures, and removing cosmic ray and sky signal. They performed the source detection with SExtractor (Bertin & Arnouts, 1996), and extracted two-dimensional spectra for each field, based on the positions and sizes of the sources. The redshifts and emission line fluxes were determined using the python version of `mpfit` and are published in Noirot et al. (2018). Our HST image 5σ magnitude limit within an aperture of radius 0.17 arcsec is $H_{140} = 27.1$ mag.

4.1.4 Ground-based optical observations

Ground-based optical imaging in i or z-band is available for nine of the CARLA clusters (Cooke et al., 2015). Seven clusters were observed in September 2013 - December 2014 using ACAM at 4.2m William Hershel telescope (P.I. Hatch). ACAM has a circular field of view, 8.3 arcmin in diameter with a pixel scale 0.25 arcsec pixel^{-1}. Two other clusters were observed between February and April 2014 with GMOS-S (at Gemini South telescope) using the EEV detectors. The field of view of GMOS-S is 5.5×5.5 arcmin with a pixel scale of 0.146 arcsec pixel^{-1}. Exposure times were calculated depending on the actual seeing, in order to reach a consistent depth across all fields. The reduction of the *i*-band images was performed with the publicly available THELI software (Erben et al., 2005; Schirmer, 2013). For the photometric calibration M22 used either available Sloan Digital Sky Survey photometry or standard stars observed before and after the cluster observations. More details on these observations and image reduction can be found in Cooke et al. (2015). CARLA J2039-2514 has archival imaging observations with VLT/ISAAC (run ID 69.A-0234) in the *z*-band with 4800s exposure time (see also Noirot et al., 2016).

Full details on these observations and the image processing can be found in (Cooke et al., 2015), and the summary of the optical imaging used in this thesis is shown in Table 4.1: instrument, bandpass, exposure time, seeing, and the 5σ magnitude limit.

4.1.5 Galaxy sample selection

Our sample selection is described in detail in M22. Our selection aims at optimizing the sample completeness and purity. Observations of most of the CARLA clusters and protoclusters include three (H_{140}, IRAC1 , IRAC2) to five bandpasses (ground based *i*-band and *z*-band , H_{140}, IRAC1, IRAC2), and M22 could not perform a precise photometric redshift analysis from their spectral energy distribution. Instead, they selected galaxies in color and given spatial regions where they expected a small outlier contamination.

M22 selected galaxies with $(\mathrm{IRAC1} - \mathrm{IRAC2}) > -0.1$, $\mathrm{IRAC1} < 22.6$ mag, from which

Table 4.1: CARLA confirmed cluster sample ground-based observations from Cooke et al. (2015). For more details on these observations, please refer to Cooke et al. (2015). When it is not specified the imaging was taken in the *i*-band. One cluster was observed in the *z*-band. The 5 σ magnitude limit is measured in circular regions with radius equal to 2.5 the full width half maximum of the composed images.

Name	z_{clus}	Other name	Instrument	Bandpass	Exp. Time sec.	Seeing arcsec	5σ mag. limit mag
CARLAJ1358+5752	1.368	J1358+5752	*ACAM*	*i*	8400	0.9	24.95
CARLAJ1103+3449	1.442	6CE1100+3505	*ACAM*	*i*	9600	1.1	25.14
CARLAJ2355-0002	1.490	TXS2353-003	*ACAM*	*i*	6000	0.8	24.99
CARLAJ1129+0951	1.528	J1129+0951	*GMOS-S*	*i*	2645	0.4	24.78
CARLAJ1753+6310	1.582	7C1753+6311	*ACAM*	*i*	6000	0.7	25.08
CARLAJ1052+0806	1.646	J1052+0806	*GMOS-S*	*i*	2645	0.6	25.04
CARLAJ1018+0530	1.952	J1018+0530	*ACAM*	*i*	7200	0.8	25.19
CARLAJ2039-2514	1.997	MRC2036-254	*ISAAC*	*z*	4800	0.7	23.20
CARLAJ0800+4029	2.004	J0800+4029	*ACAM*	*i*	6600	0.9	25.16

they obtained a sample $\sim 90\%$ pure and complete of galaxies at $z > 1.3$. To reduce the contamination from outliers with $z > 1.3$, but not at the cluster redshift, they only selected galaxies hosted by the densest cluster regions, in circles of radius of 0.5 arcmin (~ 0.25 Mpc at our redshifts), in which the background contamination is $\lesssim 20\%$ in most clusters. The scale of these regions corresponds to the scale of the dense cluster cores at $z > 1$ (Postman et al., 2005). van der Wel et al. (2012) and Kartaltepe et al. (2015) showed that morphological classification and the measurement of galaxy structural parameters are dependable only for magnitudes brighter than the WFC3/F160W magnitude $H_{160} = 24.5$ mag, and in this study M22 and myself select galaxies brighter than $H_{140} = 24.5$ mag.

Our final sample includes a total of 271 galaxies in fifteen CARLA confirmed clusters and nineteen overdense regions. In fact, three of our clusters are double structures (M22), as predicted by cosmological models for clusters assembling at $z = 1.5 - 3$ (Chiang et al., 2013; Muldrew et al., 2015). Galaxies that were spectroscopically confirmed at a redshift different than the clusters by Noirot et al. (2018) and a recent photo-spectral analysis of CARLAJ1018+0530 by Werner et al. (in preparation) were not considered in this analysis. The details on our galaxy sample selection are in M22.

4.1.6 Galaxy morphological classification and Passive and active galaxy selection

The details on our morphological classification and passive and active galaxy selection are provided in M22. Here I reiterate the main points.

M22 performed a galaxy visual morphological classification using two large morphological class, early-type galaxies (ETG) and late type galaxies (LTG). ETG include spheroid and compact galaxies, and LTG include disks and irregular galaxies. Those correspond to the main morphological class used in the CANDELS survey (Kartaltepe et al., 2015): (1) Disk. These galaxies have a disk even if they don't show clear spiral arms; (2) Spheroid. There galaxies are resolved spheroids and do not show a disk; (3) Irregular. All galaxies that cannot be classified either as Disk or Speroids; (4) Compact/Unresolved. These are compact or unresolved galaxies; (5) Unclassifiable. The sample used in this paper does not include any *Unclassifiable* galaxy.

For clusters that were observed in four bandpasses, M22 identified passive and active galaxies using color-color diagrams, which correspond to the *UVJ* diagrams used in the literature to separate passive from active dusty galaxies up to a redshift z=3.5 (e.g., Labbé et al., 2005; Wuyts et al., 2007; Williams et al., 2009; Whitaker et al., 2011; Fang et al., 2018). The FUV rest-frame can substitute the U-rest frame, and some works show that this can lead to more precise specific star formation rate (sSFR) measurements (Arnouts et al., 2013; Leja et al., 2019).

Passive galaxies were selected by M22 as galaxies with specific star formation rate $\log(\mathrm{sSFR}) < -9.5$, using the CANDELS Santini et al. (2015) sSFR as the reference "true" sSFR for our selection calibration. This selection permitted us to obtain passive samples that are ~80-85% complete and pure, and includes recently quenched galaxies at $\sim 3\sigma$ below the field star formation main sequence.

4.2 Methods

4.2.1 Galaxy photometry and mass measurement

The photometry was performed by Stefania Amodeo and was obtained from a joint analysis of IRAC1, IRAC2, H_{140} and, when available, ground-based *i*-band or *z*-band images, as described in M22. For an efficient source deblending, Amodeo used the T-PHOT software (Merlin et al., 2015, 2016), with the high-resolution *HST* images as priors to derive PSF-matched fluxes in the other lower-resolution bands.

M22 also describe in detail our stellar mass measurements. They measured the CARLA galaxy stellar masses by calibrating our PSF-matched *Spitzer*/IRAC1 magnitudes with galaxy stellar masses from Santini et al. (2015) derived from the Guo et al. (2013) multi-wavelength catalog in the CANDELS WIDE GOODS-S field. The *Spitzer* IRAC1 magnitudes correspond to the rest-frame near-infrared in the redshift range of the CARLA sample, and are not expected to be biased by extinction. M22 found a very good correlation between these magnitudes and the Santini et al. (2015) mass measurements, with scatters of ≈ 0.12 dex at the redshift of the cluster studied in this paper. Adding in quadrature the scatter of the

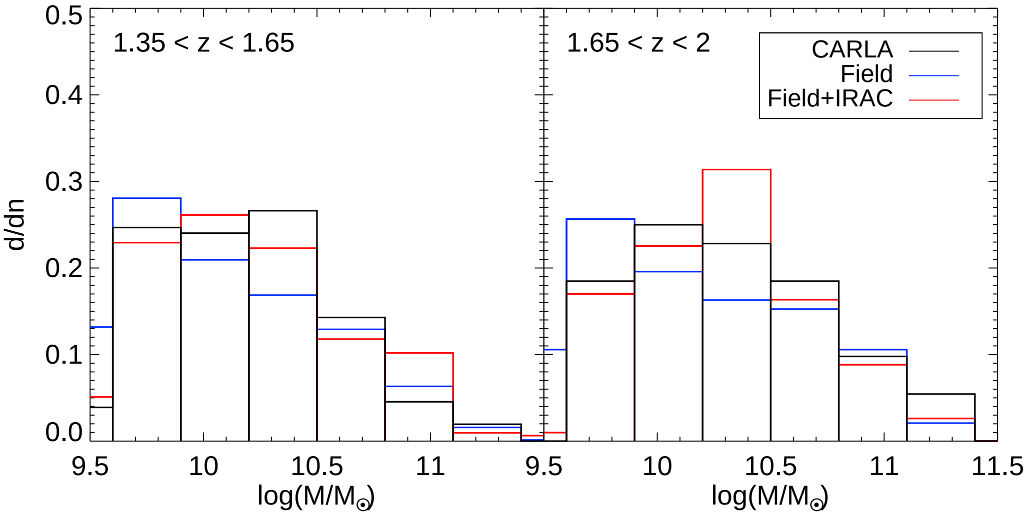

Figure 4.1: The mass distribution of the cluster galaxies compared to the field sample. The black line represents CARLA galaxies, the blue line denotes field galaxies from CANDELS in the corresponding redshift bins, the red line shows the same as blue line after applying *Spitzer* magnitude and color cuts. All histograms are peak-normalized.

relation and uncertainties from Santini et al. (2015), they obtained mass uncertainties in the range $\sim 0.4 - 0.5$ dex, and $\approx 0.2 - 0.3$ dex for masses larger than $\log_{10}(M/M_{\odot}) > 10.5$. Hereafter, I use the symbol M for the galaxy stellar mass. The selected sample has the mass distribution very close to the field studies, which is demonstrated in Figure 4.1. It means there is no bias in our mass-size analysis that can be attributed to the sample mass distribution.

4.2.2 Measurements of galaxy structural properties

I measured galaxy structural parameters using the software GALAPAGOS (Barden et al., 2012), which performs the following main steps: source detection; creation of image and noise cutouts for each detected source; estimation of the local background; fit of the surface brightness profile to a Sérsic profile; compilation of all objects in a final output catalog.

The source detection is based on SExtractor (Bertin & Arnouts, 1996). Following Barden et al. (2012), I ran SExtractor on the H_{140} images in the *cold* and *hot* modes, which are optimized to detect bright and faint objects, respectively. I adopted the same configuration of parameters used for the catalogs released by the Cosmic Assembly Near-IR Deep Extragalactic Legacy Survey (CANDELS, Grogin et al., 2011; Koekemoer et al., 2011), and published by Galametz et al. (2013) and Guo et al. (2013). More specifically, I created a first catalog including all the *cold* sources; then I compared every source detected in the *hot* mode to the first catalog detections, added to the first catalog those whose central position does not lie inside the Kron ellipse of any *cold* source, and discarded the others. Table 4.2 shows the key SExtractor parameters used in our source detection.

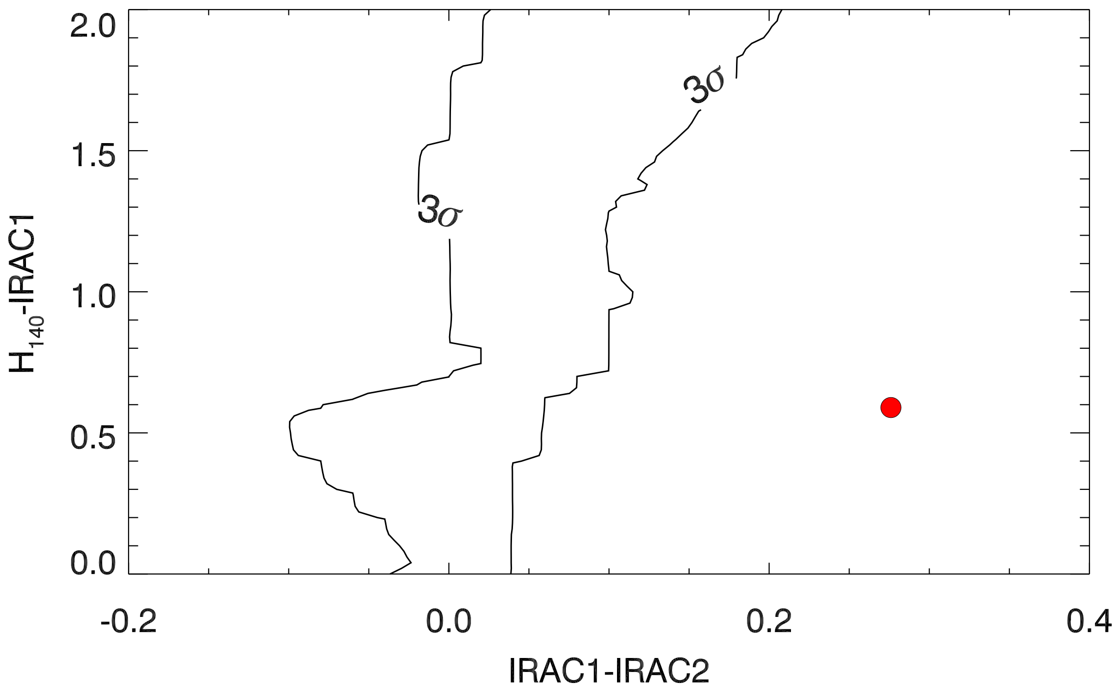

Figure 4.2: A two color diagram to separate stars and galaxies. The 3σ locus of the modelled star distribution is shown by a black contour, the unresolved object from our sample is shown in red, and is most probably extragalactic.

Table 4.2: SExtractor parameters used for source detection in CARLA clusters.

SExtractor	Cold Mode	Hot Mode
DETECT_MINAREA	5.0	10.0
DETECT_THRESH	0.75	0.7
ANALYSIS_THRESH	5.0	0.8
FILTER_NAME	tophat_9.0_9x9	gauss_4.0_7x7
DEBLEND_NTHRESH	16	64
DEBLEND_MINCONT	0.0001	0.001
BACK_SIZE	256	128
BACK_FILTERSIZE	9	5
BACKPHOTO_THICK	100	48

Table 4.3: Constraints on GALFIT parameters.The constraint on magnitude is relative to the measured SExtractor magnitude.

parameter	description	constraints	units
n	Sérsic index	0.2 : 8	
R_e	effective radius	0.3 : 400	pixel
Q	axis ratio	0.0001 : 1	
m	magnitude	-3 : +3	SExtractor mag

The photometric and structural parameter estimation was based on GALFIT (Peng et al., 2002), that fits the surface brightness profile of each detected source to a one-component *Sérsic* model (Sersic, 1968), defined by the following free parameters: the total magnitude m, the half-light radius measured along the major axis (effective radius) R_e, the Sérsic index n, the axis ratio Q (the ratio between the model minor and major axis, b/a), the position angle $P.A.$, and the central position. The software uses the Levenberg-Marquardt algorithm to minimise the residual between a galaxy image and the PSF-convolved model by modifying the free parameters.

I used exactly the same GALFIT configuration as van der Wel et al. (2012, 2014) (Table 4.3). While this CANDELS analysis was not performed in the same observational bandpass as for CARLA, the H_{160} images for the CANDELS "wide" catalog (Koekemoer et al., 2011) have a 5σ magnitude limit of $H_{160} = 27.4$ mag, which is comparable to the CARLA magnitude limit of $H_{140} = 27.1$ mag (both were calculated within an aperture with 0.17 arcsec radius), when the different filter response functions are taken into account. The conversion to physical length-scale in kiloparsec was performed using the angular distance of each cluster, and assuming that all cluster galaxies have the same redshift as the average redshift of the cluster from Noirot et al. (2018).

I manually re-ran GALFIT on the 22 individual galaxies for which either GALAPAGOS did not converge or the resulting values had uncertainties greater than the value itself, or the parameters hit the constraints in either R_e, n or q. In those cases, I tried varying the input parameters to find a stable global minimum of the residuals while keeping the constraints and settings of the procedure from van der Wel et al. (2014). I divided our sample in 3 categories: (i) Galaxies with a good quality fit; (ii) QSO, whose effective radii are uncertain due to saturation in the *HST* image (9 objects); (iii) Unresolved galaxies, where GALFIT converged close to the minimum constraint for the effective radius. I also excluded QSO from the analysis since their real size is unknown.

The unresolved galaxy category consists of only one object with an effective radius $R_e = 0.5$ pix, which is close to the lower limit for the R_e estimate used by van der Wel et al. (2012) ($R_{e,min} = 0.018$ arcsec or 0.3 pix in WFPC3 image). The objects with such effective radii are essentially indistinguishable from point sources due to PSF, so their R_e is an upper limit, and they might be either a bona-fide extragalactic galaxy, or a Milky Way foreground

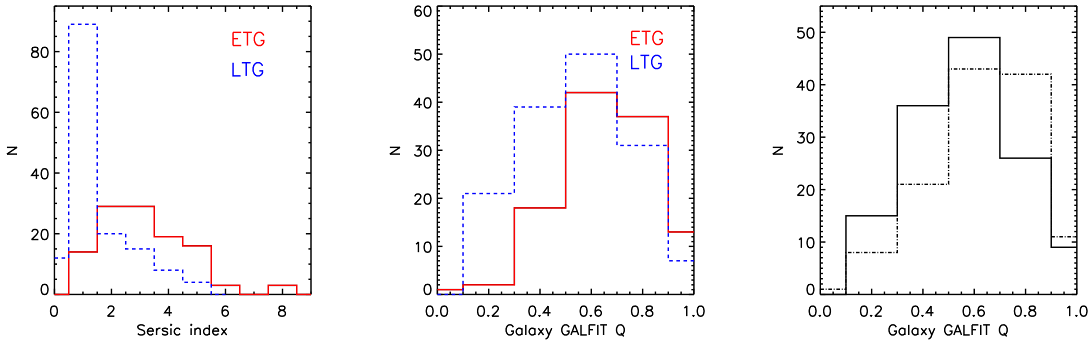

Figure 4.3: CARLA cluster structural parameter distribution for our main morphological classes, ETG (red continuous line), and LTG (blue dashed line). Left: Sérsic index distribution; Middle: GALFIT Q distribution; Right: GALFIT Q distribution for asymmetric (continuous line) and symmetric galaxies (dash-dotted line). The parameters are consistent with the visual morphological classification.

star. This object is not listed in the Gaia EDR3 catalogue as a star (Gaia Collaboration et al., 2020). I used the TRILEGAL model[1] (Girardi et al., 2005) to obtain a sample of simulated stars with magnitudes $IRAC1 < 26$ mag at the source RA and DEC, and with standard settings for the geometry of the thin disk, the thick disk and the halo of the Milky Way, as well as for their stellar population parameters. I built a (H_{140}-IRAC1) vs (IRAC1-IRAC2) diagram (see Fig. 4.2), to identify the locus of the synthetic star colors (see Fig. 4.2). The source does not lie in the star locus and I keep it as a bona-fide extragalactic galaxy.

In Fig. 4.3, Simona Mei compared our GALAPAGOS structural parameters with visual morphology from M22. The median Sérsic index for ETG, and LTG, is ∼3 and ∼1, respectively, consistent with what is expected for ETG de Vaucouleur and LTG exponential profiles. The median Q for early, late, asymmetric and symmetric galaxies is ∼ 0.7, 0.55, 0.7, and 0.55, respectively, with early and symmetric galaxies being rounder, as expected.

4.3 Results

Fig. 4.4 shows each cluster passive and active galaxy mass-size relation, compared to CANDELS (van der Wel et al., 2014). Though both size and mass measurements might have systematic uncertainties, they were calibrated to van der Wel et al. (2014) values so we can directly compare the two distributions. I interpolated van der Wel et al. (2014)'s best-fitting relations at each cluster redshift. While the active and LTG distributions lie on the same active galaxy mass-size relation as van der Wel et al. (2014), the passive and ETG population systematically lie above the van der Wel et al. (2014)'s passive galaxy relation. This is also shown in Fig. 4.5, where I divide the sample in two redshift bins and observe a similar behavior for active and passive galaxies. The relation also indicates a tendency to flatten at

---

[1] http://stev.oapd.inaf.it/cgi-bin/trilegal

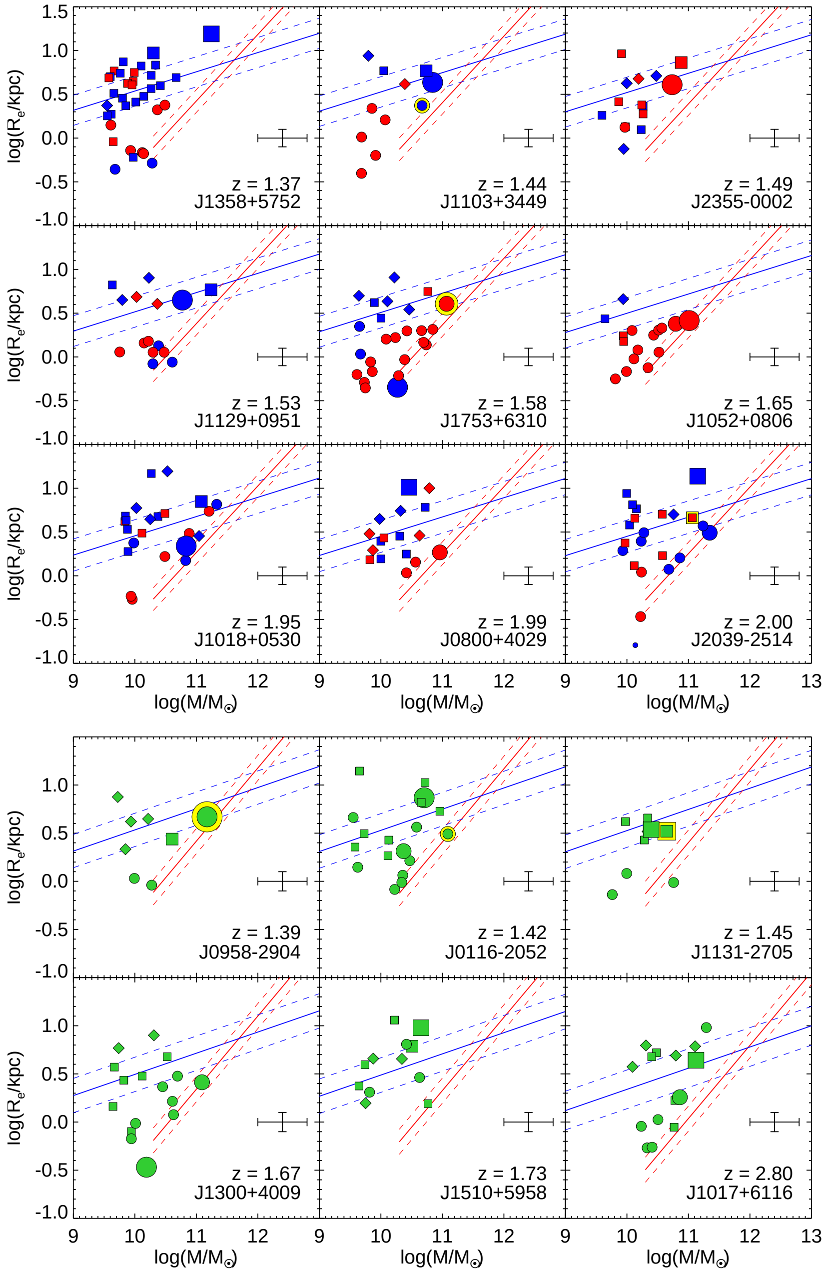

Figure 4.4: The mass-size relations for each cluster. Red and blue colors show passive [$\log(\mathrm{sSFR}) < -9.5$], and active galaxies, respectively. Green symbols show galaxies for which M22 could not separate passive from active galaxies. Circles, squares, and diamonds correspond to ETG, LTG and irregulars, respectively. The largest symbols show the BCG, the second largest indicate the second brightest galaxies. The one compact galaxy is shown by the smaller symbol. A yellow contour around the galaxy symbol indicates a HzRG. The red and blue solid lines are CANDELS van der Wel et al. (2014)'s mass-size relation for passive and active galaxies respectively, interpolated to the redshift of each cluster. The passive galaxy MSR is clipped at $\log(M/M_\odot) = 10.3$ to reflect the fitting range in van der Wel et al. (2014). The dashed lines are 1-σ scatter for these relations. Cluster active and LTG galaxies lie on the van der Wel et al. (2014)'s active galaxy MSR. Cluster passive ETG have systematically larger sizes than van der Wel et al. (2014)'s passive galaxies.

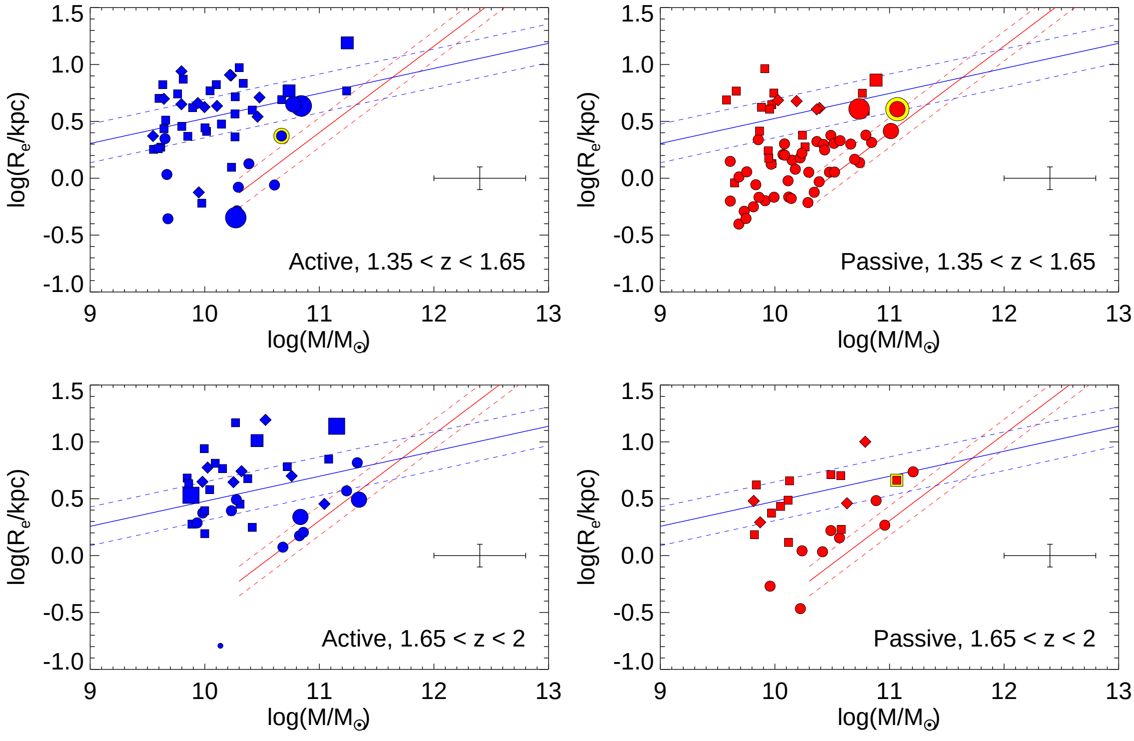

Figure 4.5: The mass-size relation in two redshift bins. The symbols are the same as in Figure 4.4, the van der Wel et al. (2014)'s mass-size relations are shown at the mean redshift of each bin ($z = 1.47$ and $z = 1.8$). Here we show only the passive and active galaxies in two redshift bins, separated by morphology.

$\log(\mathrm{M}) \lesssim 10.5$ for passive galaxies. About $\sim 30\%$ of the cluster ETG are active, and mostly lie on the LTG galaxy MSR. The bulk of these active ETGs is found in just two clusters (J1018+0530 and J2039-2514, both around $z \sim 2$). The cluster Brighter Cluster Galaxies (BCG) and the second brightest are shown with larger symbols, and lie on the same MSR as the satellites. Fig. 4.6 demonstrates MSR separately for LTGs and ETGs, including galaxies with no passive/active separation. Fig. 4.6 also shows a sizeable population of passive LTGs, which mostly lie on the active field relation from van der Wel et al. (2014). This might be the reason why in some clusters (e.g. J2355-0002 and J2039-2514) passive and active galaxy sizes are consistent in Fig. 4.4: such clusters contain a large fraction of passive LTGs, which might be a sign of continuing cluster assembly.

Fig. 4.7 shows the evolution of the passive ETG mass-size relation in clusters in the redshift range $0.7 < z < 2$ as compared to the CANDELS (van der Wel et al., 2014)'s mass-size relation. I added to our sample the passive ETG observations from Strazzullo et al. (2013), Delaye et al. (2014), and Newman et al. (2014), which used analyses similar to ours. When authors published circularized effective radii, defined as $R_{e,circ} = R_e\sqrt{(b/a)}$ (e.g., Delaye et al., 2014), I convert their sizes to the Sérsic profile half-light radii along its major axis. Fig. 4.8 demonstrates the difference between (van der Wel et al., 2014) passive galaxy relation and our data, and the majority of data points lie above the relation.

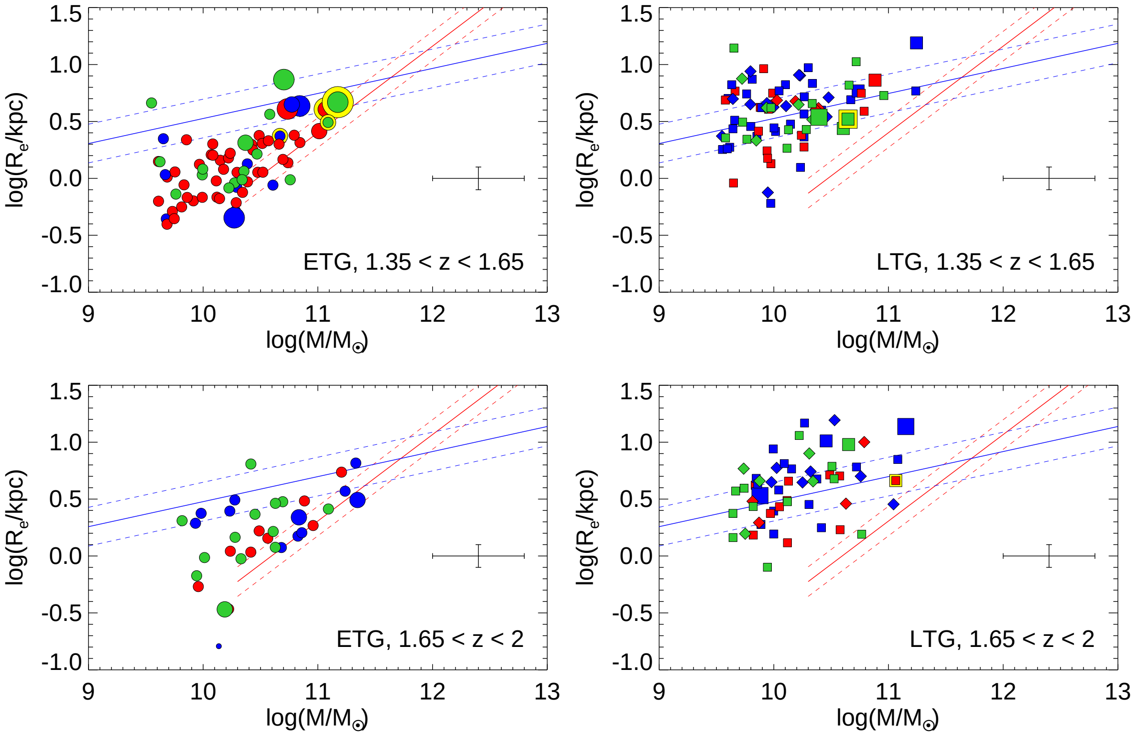

Figure 4.6: The mass-size relation in two redshift bins. The symbols are the same as in Figure 4.4, the van der Wel et al. (2014)'s mass-size relations are shown at the mean redshift of each bin ($z = 1.47$ and $z = 1.8$). In both redshifts bins, cluster active and LTG galaxies lie on the van der Wel et al. (2014)'s active galaxy MSR. Cluster passive ETG have systematically larger sizes than van der Wel et al. (2014)'s passive galaxies.

Fig 4.9 shows the redshift evolution of the mass-normalized radius $R_{10.7}$, defined as (van der Wel et al., 2014) :

$$R_e(\mathrm{kpc}) = R_{10.7}(\mathrm{kpc}) \left(\frac{M}{5 \times 10^{10} M_\odot} \right)^\beta \tag{4.1}$$

Here β is a slope parameter (changing slightly between $0.71 - 0.76$) which we adopt for corresponding redshifts from van der Wel et al. (2014). For this figure, I only consider galaxies with $\log \left(M/M_\odot \right) > 10.5$ in all the clusters for a homogeneous sample comparison. At lower mass it is known that the mass-size relation is also predicted (Shankar et al., 2013) and observed (Graham et al., 2006; Lange et al., 2015; Li et al., 2018; Hamadouche et al., 2022) to flatten at least up to $z = 2$ (Nedkova et al., 2021) and I do not have enough statistics to quantify this flattening in our data at the same level of uncertainty as in the field. For the field reference I use Bernardi et al. (2014) for $z = 0$ (large black circle) and van der Wel et al. (2014) for the other redshift bins (small black circles). For van der Wel et al. (2014) field sample I took only the passive galaxies with $\log \left(M/M_\odot \right) > 10.5$ in the corresponding photometric redshift bins. All the points are calculated as a median size ($R_{10.7}$) of a Monte Carlo simulation (1000 runs) of each sample (redshift bin or set of clusters). The point uncertainties were computed in the same procedure as the standard deviation of the median size for each sample. The fit uncertainties were also computed using a 1000 runs Monte Carlo simulation of the data points. The last point at $z = 2.75$ was not included in the fit of the field data since it breaks the linear relation.

While the cluster mass-size relation of cluster and field passive ETG is mostly similar in the local Universe (e.g., Huertas-Company et al., 2013a), cluster ETG sizes are systematically higher than field passive galaxies at $\log\left(M/M_\odot\right) > 10.5$ and $z > 1$ and their evolution is slower in the range $1 \lesssim z \lesssim 2$. This is quantified by the fit to the redshift evolution of the cluster $R_{10.7}$ for galaxy mass $\log\left(M/M_\odot\right) > 10.5$:

$$\log(R_{10.7}) = (-0.16 \pm 0.02)\ (z-1) + (0.44 \pm 0.01) \tag{4.2}$$

compared to the evolution in the field from van der Wel et al. (2014):

$$\log(R_{10.7}) = (-0.29 \pm 0.04)\ (z-1) + (0.33 \pm 0.02) \tag{4.3}$$

For galaxies with $\log\left(M/M_\odot\right) > 10.5$, at $1 < z < 2$, cluster passive ETG are on average $\gtrsim 1\sigma$ larger than the field. At $z = 1.5$ the cluster passive ETG are ~40% larger than those in the field, and at $z = 2$ they are larger by ~120%. The passive ETG fraction in clusters is $\sim 60 \pm 10\%$, compared to $\sim 28 \pm 2\%$ in CANDELS.

In the range $9.6 < \log\left(M/M_\odot\right) < 10.5$, where I observe a flattening of the MSR, the average cluster passive ETG size is $\log(R_e) = 0.05 \pm 0.22$.

4.4 Conclusion

4.4.1 Galaxy sizes are larger in clusters than in the field

I observe higher passive ETG sizes in CARLA clusters ($1.4 \leq z \leq 2.8$) compared to field CANDELS's passive ETG (van der Wel et al., 2014). Larger passive early-type galaxy sizes in clusters at $z > 1$ were also observed by Delaye et al. (2014); Strazzullo et al. (2013); Newman et al. (2014). From these combined results, I obtain the evolution of the mass-normalized radius $R_{10.7}$ as a function of redshift, which shows that passive ETG with $\log\left(M/M_\odot\right) > 10.5$ and $z > 1$ are systematically larger than field passive ETG galaxies. Their mass growth at $1 \lesssim z \lesssim 2$ is slower than in the field.

At redshift $0.86 < z < 1.34$, Matharu et al. (2019) finds that cluster quiescent galaxies with $\log\left(M/M_\odot\right) \gtrsim 10$ are 0.08 ± 0.04 dex (~ 20 %) more compact than the field, within 1σ from the field MSR, which has an intrinsic scatter $\sigma_{\log(R_e)} = 0.13$ dex. They used a toy model to show that these galaxies will in part merge with the cluster brightest galaxies and in part tidally destroyed, and new, larger, galaxies will be accreted in clusters from the field, maintaining a similar MSR in field and clusters in the redshift range $0 < z \lesssim 1$. The model considers that galaxies in groups and filaments constantly fall onto the cluster larger haloes

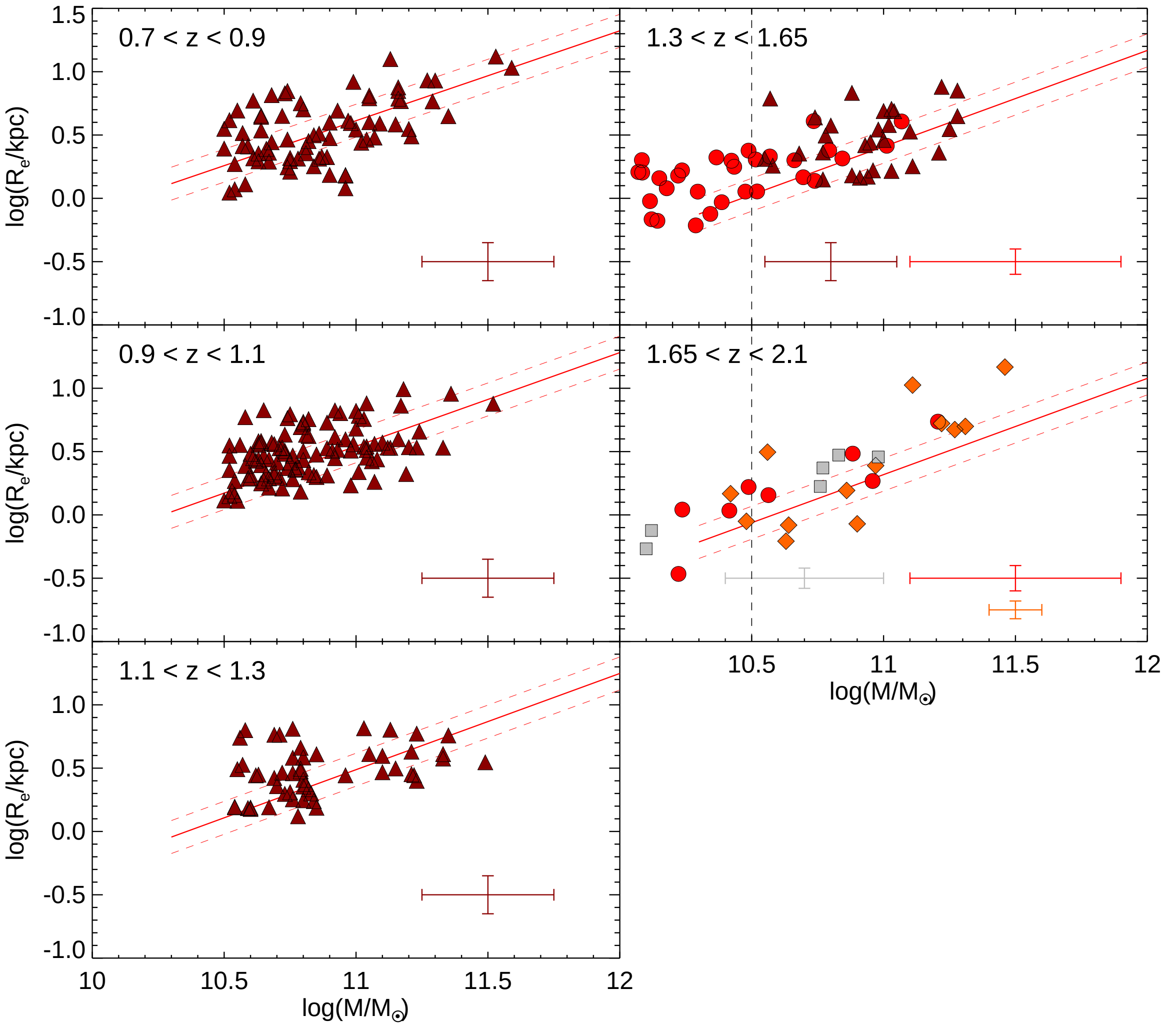

Figure 4.7: The evolution of the cluster passive ETG mass-size relation. The red circles are our sample. The brown triangles, grey squares and orange diamonds are observations from Delaye et al. (2014), Strazzullo et al. (2013), and Newman et al. (2014), respectively. The red line is the van der Wel et al. (2014) CANDELS passive galaxy relation.

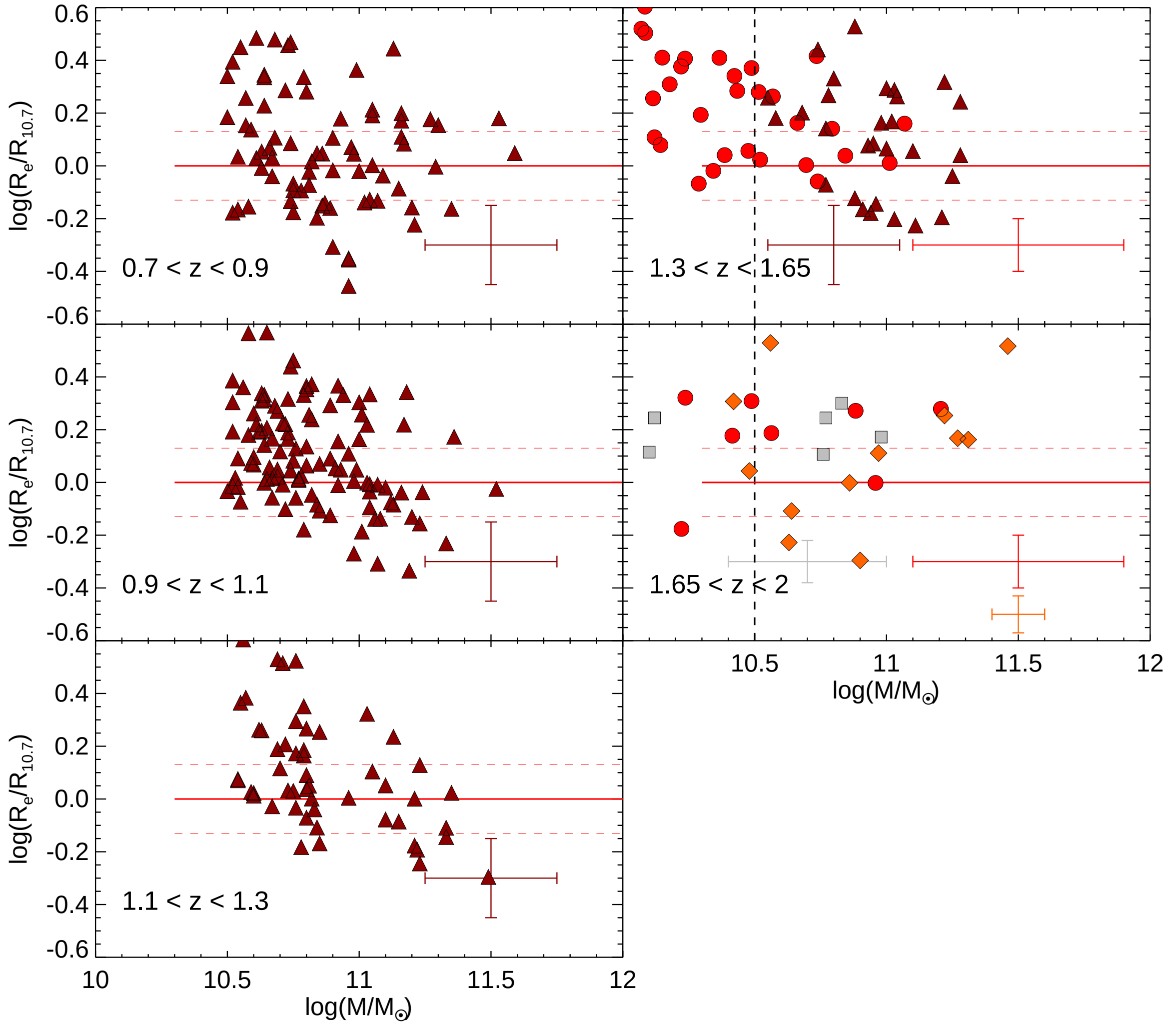

Figure 4.8: The evolution of the cluster passive ETG mass-size relation, normalized to the field relation. The symbols are the same as in Fig. 4.7. Cluster passive ETG are systematically larger than CANDELS galaxies.

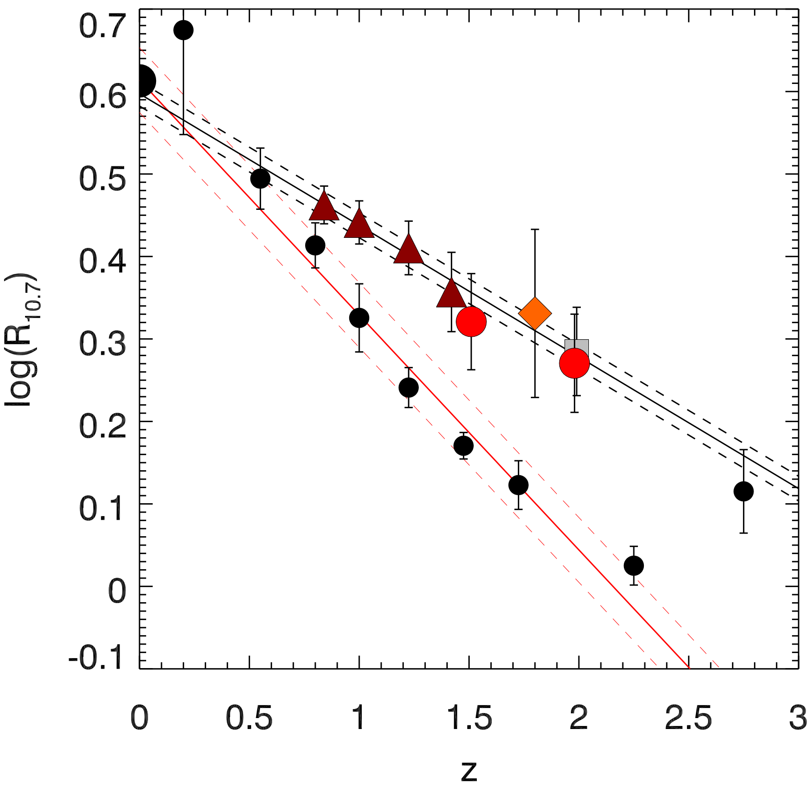

Figure 4.9: The evolution of passive ETG mass-normalized radius $R_{10.7}$ (see text) with redshift. The brown triangles, grey squares and orange diamonds show observations from Delaye et al. (2014), Strazzullo et al. (2013), and Newman et al. (2014), respectively. The black circles are field ETG sizes taken from Bernardi et al. (2014) for $z = 0$, and from van der Wel et al. (2014) for the other redshifts.

with the flow of the cosmic time (progenitor bias; van Dokkum & Franx, 1996; Saglia et al., 2010).

Because of this accretion, new passive members are added to the original early type passive population. The new passive objects can form either through environmental quenching by ram-pressure (Gunn & Gott, 1972), harassment (Moore et al., 1996) or strangulation (van den Bosch et al., 2008), or they can infall already being quenched prior to the entry to the cluster, by group preprocessing (Fujita, 2004). In the first case predominantly late-type disky galaxies are mostly transformed into lenticulars and dwarf ellipticals. In the second case, galaxies preprocessed in the group environment are larger. A part of the size growth in the clusters can be attributed to the addition of the group elliptical galaxies and lenticular galaxies that mix with the native cluster ETG population and homogenizes the size distribution to that of the field. This is further compounded by results by Matharu et al. (2020), that can be explained by the accretion of old compact ETGs onto BCG or their disruption into the intracluster light. The Matharu et al. (2019)'s results at $1 < z < 1.34$ show larger sizes, and are consistent with Delaye et al. (2014)'s results and our findings in this paper.

Field galaxies at $2 \lesssim z \lesssim 3$ (van der Wel et al., 2014; Patel et al., 2017; Marsan et al., 2019) show larger sizes than the extrapolation of the field size evolution at lower redshift (e.g., see the highest redhsift field point in Fig 4.9). This is explained by the transition from the epoch in which galaxy growth is dominated by gas accretion and the epoch in which minor mergers become dominant (Naab et al., 2009). On the other end, cluster galaxies are already larger than field galaxies at $z \sim 2$, then grow more slowly than field galaxies, to reach the same average sizes by $z = 1$ and then evolve to $z \sim 0$ on average in the same way as field galaxies, mainly because of accretion of field larger galaxies and disruption of the cluster more compact galaxies (Matharu et al., 2019).

4.4.2 Star forming ETG

I observe active ETGs (AETG) that follow the passive ETG MSR in four of our five clusters at $z = 1.5 - 2$. The presence of AETG in clusters has been observed at $z \sim 0$ (e.g., Sheen et al., 2016) and up to $z \sim 2$ (Ferreras & Silk, 2000; Mei et al., 2006, 2015; Jaffé et al., 2011; Mansheim et al., 2017). At $1.35 < z < 1.65$ our AETG are $20^{+7}_{-5}\%$ of all ETG, of which $45 \pm 18\%$ ($64^{+16}_{-20}\%$ for 2.5σ) lie within 1σ of the passive MSR. At $1.65 < z < 2.05$ AETG are $55 \pm 13\%$ of all ETG, of which $42 \pm 17\%$ ($58 \pm 17\%$ for 2.5σ) lie within 1σ of the passive MSR.

These galaxies indicate that their morphological transformation happened before quenching (Barro et al., 2013, 2014) or that a recent event triggered the star formation again (e.g. Shapiro et al., 2010; Kaviraj et al., 2011). It is also possible that these objects initially formed as ETG from a monolithic gas cloud collapse, and we still see the residual SF at $z = 2$.

In the local Universe ($z \lesssim 1$), star forming ETG show evidence for recent gas-rich minor merger events or interactions with gas-rich neighbour galaxies, and are thought to become quiescent when the gas acquired during the merger, and which fuels star formation, will have been exhausted (e.g., Lee et al., 2006; Huertas-Company et al., 2010; George & Zingade, 2015; George, 2017). If this is true also at the higher redshifts that I probe, these galaxies have gone through a recent merger or neighbour galaxy interaction, and would most probably quench at a later epoch and increase the fraction of passive ETG in the cluster population. This explains why they follow the passive ETG MSR, and not the active galaxy MSR.

4.4.3 The MSR flattening for log(M) $\leq$ 10.5

Our MSR indicates a tendency to flatten at $\log\left(M/M_{\odot}\right) \lesssim 10.5$. In the range $9.6 < \log\left(M/M_{\odot}\right) < 10.5$, where I observe a average cluster passive ETG size of $\log(R_e) = 0.05{\pm}0.22$. This is a trend observed in passive ETG in clusters and field in the local Universe (e.g., Bernardi et al., 2014; Nedkova et al., 2021) and at $z \lesssim 2$ (e.g., Nedkova et al., 2021) for galaxies in the mass range $7 \lesssim \log(\mathrm{M}) \lesssim 10.5$. It is predicted in semi-analytical models (e.g., Shankar et al., 2013), where it occurs at the transitional mass ($\log(\mathrm{M}) \sim 10.5$) below which galaxy growth is dominated by both disk instabilities and mergers, and above which galaxy growth is due to minor mergers. Our average cluster passive ETG size is ~ 0.2 dex smaller than the average size from Nedkova et al. (2021), and consistent within $\sim 1\sigma$.

CHAPTER 5

CONCLUSION AND PERSPECTIVES

The observations of KDG 64 demonstrate that large group-dwelling dwarf spheroidal galaxies are in fact barely distinguishable from other diffuse low-mass non star-forming stellar systems in groups and clusters. It is not possible to make sweeping conclusions from a single galaxy, but I can argue that at least some of the morphologically similar cluster dwarfs should follow the same evolutionary paths as dwarf spheroidals in groups. The definitive answer requires systematic observations of low mass galaxies in different environments analysed in a homogeneous fashion. This work demonstrates the feasibility of such a program. The developed dynamical modelling algorithm (based on one of the fastest currently available implementations for non-spherical systems) will allow to perform a dark matter census in the local universe, determining DM halo parameters for all nearby passive galaxies and thus refine the stellar-to-dark matter mass relation.

This thesis demonstrates that a comprehensive spectrophotometric study of galaxies including full-spectrum fitting, structural measurements and dynamical modelling allows to conclude a lot about their intrinsic properties and evolution. If a bigger sample is studied, this method can be useful for uncovering the evolution history of different galaxy populations. Currently there exist surveys providing spatially resolved spectroscopy such as MaNGA (Bundy et al., 2015) and CALIFA (Sánchez et al., 2012). Once the developed spectrophotometric approach is properly automated, it can be applied to these surveys, as well as new ones. I am hopeful that I will have the pleasure of participating in some of the outlined perspective projects.

The observations of recently ram-pressure stripped low-mass disc galaxies suggest: (i) that ram pressure stripping is a viable channel of UDG formation and that UDGs formed via this channel *de facto* extend the corresponding dE/dS0 sub-class to lower surface brightnesses and larger sizes; (ii) that ram pressure stripping is responsible for a substantial fraction of large rotating UDGs in galaxy clusters including extreme objects like DF 44 (van Dokkum et al., 2016) and also higher surface brightness, spatially extended, dwarf early-type galaxies; (iii) that ram pressure stripping affects not only morphological appearance but also stellar dynamics by increasing the stellar disc orbital anisotropy; and (iv) that the tangential orbits of UDG progenitors at large pericentral distances lead to higher ram pressure-induced star formation efficiencies, and higher stellar masses and surface densities.

The sample of PSG proved to be just the tip of the iceberg in studying the ram pressure influenced galaxy population. The current selection is based on the SDSS spectroscopic target magnitude limit ($m_r < 17.77$) and the survey footprint. Later considerations showed that (i) for the sake of sample purity several PSG in Coma were not selected because there was some emission present, however these galaxies are good candidates to study ram pressure effects even with some leftover star formation; (ii) the Virgo cluster that was not covered by SDSS contains plenty of galaxies both in process and after ram pressure stripping, and these objects are easier to study in detail due to their location 5 times closer. The possibilities are vast with this kind of targets, and I expect that by observing the signatures of ram pressure stripping it will be possible to (i) estimate the speed of a galaxy through intergalactic medium using the configuration of ram pressure induced starburst observed in some galaxies; (ii) reconstruct the orbit of in the cluster of any such galaxy if the precise distance is known. These two methods combined for a statistically significant sample of galaxies could provide an independent method of measuring the mass distribution in galaxy clusters.

The study of the mass-size relation of galaxies in a sample of 15 spectroscopically confirmed clusters at $1.3 < z < 2.8$ from the CARLA survey (Wylezalek et al., 2013, 2014; Noirot et al., 2018) yielded several important findings.

Our main results are:

- Cluster LTG at $1.4 < z < 2.8$ lie on the same MSR as active field galaxies from van der Wel et al. (2014)'s CANDELS analysis
- Cluster ETG at $1.4 < z < 2.8$ show sizes that are $\gtrsim 1\sigma$ systematically higher than passive field galaxies from van der Wel et al. (2014) CANDELS analysis
- The evolution of cluster passive ETG sizes is slower at $1 < z < 2$ when compared to the field. We fit the average evolution for the mass-normalized radius as:
  $$\log(R_{10.7}) = -0.16\,(z-1) + 0.44 \tag{5.1}$$
  compared to the evolution in the field from van der Wel et al. (2014), which is:
  $$\log(R_{10.7}) = -0.29\,(z-1) + 0.33 \tag{5.2}$$
- Brightest cluster galaxies lie on the same mass-size relation as the satellites
- Half of the active ETG, which are 30% of our ETG sample, follow the field passive galaxy MSR. These galaxies most probably went through a recent merger or neighbour galaxy interaction, and would most probably quench at a later epoch and increase the fraction of passive ETG in the cluster population.

- In in the range $9.6 < \log\left(M/M_{\odot}\right) < 10.5$, Our MSR flattens at $\log\left(M/M_{\odot}\right) < 10.5$, and we measure the average $\log(R_e) = 0.05 \pm 0.22$, which is 0.2 dex smaller, but consistent with galaxy sizes at $z = 0 - 2$ from Nedkova et al. (2021).
- We do not observe a large population of compact galaxies (only one), as it is observed in the field at these redshifts (e.g., Barro et al., 2013).

The predictions from semi-empirical models kindly provided by Francesco Shankar and Hao Fu show that the number of mergers by $z = 2$ is not enough to explain a twofold difference in average sizes, and more work is required to model our observations. A further trend of field and cluster ETG sizes becoming closer by $z = 1$ is likely an effect of progenitor bias, where smaller ETG formed in groups end up in clusters through large-scale structure condensation. The high percentage of both early-type and passive galaxies in the studied clusters means that both morphological transformation and quenching have mostly occurred by $z \sim 2$. The large percentage (roughly 50%) of the active ETG that follow the passive MSR demonstrates that cluster environment at $z \sim 2$ catalyzes morphological transformations and/or quenching, and these objects are especially interesting in future studies of these processes.

BIBLIOGRAPHY

Abazajian K. N., et al., 2009, ApJS, 182, 543

Afanasiev A. V., et al., 2018, MNRAS, 477, 4856

Alabi A. B., Romanowsky A. J., Forbes D. A., Brodie J. P., Okabe N., 2020, MNRAS, 496, 3182

Allen R. J., et al., 2015, ApJ, 806, 3

Amorisco N. C., Agnello A., Evans N. W., 2013, MNRAS, 429, L89

Arnouts S., et al., 2013, A&A, 558, A67

Balogh M. L., Morris S. L., 2000, MNRAS, 318, 703

Barden M., Häußler B., Peng C. Y., McIntosh D. H., Guo Y., 2012, MNRAS, 422, 449

Barro G., et al., 2013, ApJ, 765, 104

Barro G., et al., 2014, ApJ, 791, 52

Baushev A. N., 2018, New Astron., 60, 69

Beasley M. A., Romanowsky A. J., Pota V., Navarro I. M., Martinez Delgado D., Neyer F., Deich A. L., 2016, ApJ, 819, L20

Bell E. F., et al., 2004, ApJ, 608, 752

Bell E. F., et al., 2012, ApJ, 753, 167

Belli S., Newman A. B., Ellis R. S., 2014, ApJ, 783, 117

Bender R., Burstein D., Faber S. M., 1992, ApJ, 399, 462

Bennet P., Sand D. J., Zaritsky D., Crnojević D., Spekkens K., Karunakaran A., 2018, ApJ, 866, L11

Bernardi M., Roche N., Shankar F., Sheth R. K., 2011a, MNRAS, 412, L6

Bernardi M., Roche N., Shankar F., Sheth R. K., 2011b, MNRAS, 412, 684

Bernardi M., Meert A., Sheth R. K., Vikram V., Huertas-Company M., Mei S., Shankar F., 2013, MNRAS, 436, 697

Bernardi M., Meert A., Vikram V., Huertas-Company M., Mei S., Shankar F., Sheth R. K., 2014, MNRAS, 443, 874

Bertin E., Arnouts S., 1996, A&AS, 117, 393

Bezanson R., van Dokkum P. G., Tal T., Marchesini D., Kriek M., Franx M., Coppi P., 2009, ApJ, 697, 1290

Bigiel F., Leroy A., Walter F., Brinks E., de Blok W. J. G., Madore B., Thornley M. D., 2008, AJ, 136, 2846

Binggeli B., Jerjen H., 1998, A&A, 333, 17

Binney J., Tremaine S., 2008, Galactic Dynamics: Second Edition

Bogdán Á., 2020, ApJ, 901, L30

Borukhovetskaya A., Errani R., Navarro J. F., Fattahi A., Santos-Santos I., 2022, MNRAS, 509, 5330

Boselli A., Gavazzi G., 2006, PASP, 118, 517

Boselli A., et al., 2016, A&A, 596, A11

Bothun G. D., Impey C. D., Malin D. F., Mould J. R., 1987, AJ, 94, 23

Bower R. G., Benson A. J., Malbon R., Helly J. C., Frenk C. S., Baugh C. M., Cole S., Lacey C. G., 2006, MNRAS, 370, 645

Boyce P. J., et al., 2001, ApJ, 560, L127

Brook C. B., Di Cintio A., Macciò A. V., Blank M., 2021, ApJ, 919, L1

Brooks A., Christensen C., 2016, in Laurikainen E., Peletier R., Gadotti D., eds, Astrophysics and Space Science Library Vol. 418, Galactic Bulges. p. 317 (`arXiv:1511.04095`), doi:10.1007/978-3-319-19378-6_12

Bruce V. A., et al., 2012, MNRAS, 427, 1666

Bundy K., et al., 2015, ApJ, 798, 7

Buonanno R., Corsi C. E., Zinn R., Pecci F. F., Hardy E., Suntzeff N. B., 1998, ApJ, 501, L33

Burkert A., 1995, ApJ, 447, L25

Burkert A., 2017, ApJ, 838, 93

Bustamante-Rosell M. J., Noyola E., Gebhardt K., Fabricius M. H., Mazzalay X., Thomas J., Zeimann G., 2021, ApJ, 921, 107

Caldwell N., Armandroff T. E., Da Costa G. S., Seitzer P., 1998, AJ, 115, 535

Cappellari M., 2002, MNRAS, 333, 400

Cappellari M., 2008, MNRAS, 390, 71

Cappellari M., 2013, ApJ, 778, L2

Carleton T., Errani R., Cooper M., Kaplinghat M., Peñarrubia J., Guo Y., 2019, MNRAS, 485, 382

Carleton T., Guo Y., Munshi F., Tremmel M., Wright A., 2021, MNRAS, 502, 398

Carollo C. M., et al., 2013, ApJ, 773, 112

Cebrián M., Trujillo I., 2014, MNRAS, 444, 682

Chamba N., Trujillo I., Knapen J. H., 2020, A&A, 633, L3

Chan T. K., Kereš D., Wetzel A., Hopkins P. F., Faucher-Giguère C. A., El-Badry K., Garrison-Kimmel S., Boylan-Kolchin M., 2018a, MNRAS, 478, 906

Chan J. C. C., et al., 2018b, ApJ, 856, 8

Chang Y.-Y., et al., 2013, ApJ, 773, 149

Chiang Y.-K., Overzier R., Gebhardt K., 2013, ApJ, 779, 127

Chilingarian I. V., 2009, MNRAS, 394, 1229

Chilingarian I. V., Asa'd R., 2018, ApJ, 858, 63

Chilingarian I. V., Grishin K. A., 2020, PASP, 132, 064503

Chilingarian I. V., Katkov I. Y., 2012, in Tuffs R. J., Popescu C. C., eds, IAU Symposium Vol. 284, The Spectral Energy Distribution of Galaxies - SED 2011. pp 26–28 (`arXiv:1112.5191`), doi:10.1017/S1743921312008642

Chilingarian I. V., Zolotukhin I. Y., 2012, MNRAS, 419, 1727

Chilingarian I., Prugniel P., Sil'chenko O., Koleva M., 2007a, in Vazdekis A., R. Peletier R., eds, IAU Symposium Vol. 241, Stellar Populations as Building Blocks of Galaxies. Cambridge University Press, Cambridge, UK, pp 175–176 (`arXiv:0709.3047`)

Chilingarian I. V., Prugniel P., Sil'Chenko O. K., Afanasiev V. L., 2007b, MNRAS, 376, 1033

Chilingarian I. V., Cayatte V., Bergond G., 2008a, MNRAS, 390, 906

Chilingarian I. V., Cayatte V., Durret F., Adami C., Balkowski C., Chemin L., Laganá T. F., Prugniel P., 2008b, A&A, 486, 85

Chilingarian I., Cayatte V., Revaz Y., Dodonov S., Durand D., Durret F., Micol A., Slezak E., 2009, Science, 326, 1379

Chilingarian I. V., Mieske S., Hilker M., Infante L., 2011, MNRAS, 412, 1627

Chilingarian I. V., Zolotukhin I. Y., Katkov I. Y., Melchior A.-L., Rubtsov E. V., Grishin K. A., 2017, ApJS, 228, 14

Chilingarian I. V., Afanasiev A. V., Grishin K. A., Fabricant D., Moran S., 2019, ApJ, 884, 79

Combes F., 2017, Frontiers in Astronomy and Space Sciences, 4, 10

Conselice C. J., 2018, Research Notes of the American Astronomical Society, 2, 43

Cooke E. A., et al., 2015, MNRAS, 452, 2318

Cortijo-Ferrero C., et al., 2017, MNRAS, 467, 3898

Couch W. J., Sharples R. M., 1987, MNRAS, 229, 423

Cramer W. J., Kenney J. D. P., Cortes J. R., Cortes P. C. Vlahakis C., Jáchym P., Pompei E., Rubio M., 2020, ApJ, 901, 95

Cresci G., et al., 2015, ApJ, 799, 82

Damen M., Labbé I., Franx M., van Dokkum P. G., Taylor E. N., Gawiser E. J., 2009, ApJ, 690, 937

Danieli S., van Dokkum P., Conroy C., Abraham R., Romanowsky A. J., 2019, ApJ, 874, L12

Danieli S., et al., 2022, ApJ, 927, L28

Davies J. J., Crain R. A., Oppenheimer B. D., Schaye J., 2020, MNRAS, 491, 4462

Dehnen W., Gerhard O. E., 1993, MNRAS, 261, 311

Dekel A., Silk J., 1986, ApJ, 303, 39

Dekel A., et al., 2009, Nature, 457, 451

Delaye L., et al., 2014, MNRAS, 441, 203

Demers M. L., Parker L. C., Roberts I. D., 2019, MNRAS, 489, 2216

Djorgovski S., Davis M., 1987, ApJ, 313, 59

Djorgovski S. G., Gal R. R., McCarthy J. K., Cohen J. G., de Carvalho R. R., Meylan G., Bendinelli O., Parmeggiani G., 1997, ApJ, 474, L19

Dolphin A. E., 2000, PASP, 112, 1383

Dolphin A., 2016, DOLPHOT: Stellar photometry, Astrophysics Source Code Library, record ascl:1608.013 (ascl:1608.013)

Dressler A., 1980, ApJ, 236, 351

Dressler A., et al., 1997, ApJ, 490, 577

Drinkwater M. J., Jones J. B., Gregg M. D., Phillipps S., 2000, Publ. Astron. Soc. Australia, 17, 227

Dubath P., Meylan G., Mayor M., 1992, ApJ, 400, 510

Dubois Y., Devriendt J., Slyz A., Teyssier R., 2010, MNRAS, 409, 985

Dubois Y., Gavazzi R., Peirani S., Silk J., 2013, MNRAS, 433, 3297

Dutton A. A., et al., 2011, MNRAS, 410, 1660

Elbaz D., et al., 2007, A&A, 468, 33

Erben T., et al., 2005, Astronomische Nachrichten, 326, 432

Erwin P., Gutiérrez L., Beckman J. E., 2012, ApJ, 744, L11

Estrada-Carpenter V., et al., 2020, ApJ, 898, 171

Evstigneeva E. A., Gregg M. D., Drinkwater M. J., Hilker M., 2007, AJ, 133, 1722

Faber S. M., Jackson R. E., 1976, ApJ, 204, 668

Faber S. M., et al., 2007, ApJ, 665, 265

Fabian A. C., 2012, ARA&A, 50, 455

Fabricant D., et al., 2019, PASP, 131, 075004

Fan L., Lapi A., De Zotti G., Danese L., 2008, ApJ, 689, L101

Fan L., Lapi A., Bressan A., Bernardi M., De Zotti G., Danese L., 2010, ApJ, 718, 1460

Fang J. J., Faber S. M., Koo D. C., Dekel A., 2013, ApJ, 776, 63

Fang J. J., et al., 2018, ApJ, 858, 100

Ferguson H. C., Sandage A., 1988, AJ, 96, 1520

Fernández Lorenzo M., Sulentic J., Verdes-Montenegro L., Argudo-Fernández M., 2013, MNRAS, 434, 325

Ferrarese L., Merritt D., 2000, ApJ, 539, L9

Ferré-Mateu A., Trujillo I., Martín-Navarro I., Vazdekis A., Mezcua M., Balcells M., Domínguez L., 2017, MNRAS, 467, 1929

Ferreras I., Silk J., 2000, ApJ, 541, L37

Fioc M., Rocca-Volmerange B., 1997, A&A, 326, 950

Fioc M., Rocca-Volmerange B., 1999, arXiv e-prints, pp astro−ph/9912179

Forbes D. A., Alabi A., Romanowsky A. J., Brodie J. P., Arimoto N., 2020, MNRAS, 492, 4874

Fujita Y., 2004, PASJ, 56, 29

Fumagalli M., et al., 2014, ApJ, 796, 35

Gadotti D. A., 2009, MNRAS, 393, 1531

Gaia Collaboration Brown A. G. A., Vallenari A., Prusti T., de Bruijne J. H. J., Babusiaux C., Biermann M., 2020, arXiv e-prints, p. arXiv:2012.01533

Galametz A., et al., 2013, ApJS, 206, 10

Gannon J. S., Forbes D. A., Romanowsky A. J., Ferré-Mateu A., Couch W. J., Brodie J. P., 2020, MNRAS, 495, 2582

Gannon J. S., et al., 2021, MNRAS, 502, 3144

Gavazzi G., et al., 2015, A&A, 580, A116

Gebhardt K., et al., 2000, ApJ, 539, L13

Geha M., Guhathakurta P., van der Marel R. P., 2003, AJ, 126, 1794

George K., 2017, A&A, 598, A45

George K., Zingade K., 2015, A&A, 583, A103

Girardi L., Bressan A., Bertelli G., Chiosi C., 2000, A&AS, 141, 371

Girardi L., Groenewegen M. A. T., Hatziminaoglou E., da Costa L., 2005, A&A, 436, 895

Girardi L., et al., 2010, ApJ, 724, 1030

Glazebrook K., et al., 2017, Nature, 544, 71

Gobat R., et al., 2012, ApJ, 759, L44

Godwin J. G., Metcalfe N., Peach J. V., 1983, MNRAS, 202, 113

Graham A. W., 2019, Publ. Astron. Soc. Australia, 36, e035

Graham A. W., Soria R., 2019, MNRAS, 484, 794

Graham A. W., Merritt D., Moore B., Diemand J., Terzić B., 2006, AJ, 132, 2711

Grant N. I., Kuipers J. A., Phillipps S., 2005, MNRAS, 363, 1019

Grebel E. K., Gallagher John S. I., Harbeck D., 2003, AJ, 125, 1926

Grishin K. A., Chilingarian I. V., Afanasiev A. V., Katkov I. Y., 2019, arXiv e-prints, p. arXiv:1909.13460

Grishin K. A., Chilingarian I. V., Afanasiev A. V., Fabricant D., Katkov I. Y., Moran S., Yagi M., 2021, Nature Astronomy, 5, 1308

Grogin N. A., et al., 2011, ApJS, 197, 35

Gu M., et al., 2018, ApJ, 859, 37

Gu Y., Fang G., Yuan Q., Lu S., 2020, PASP, 132, 054101

Gunn J. E., Gott III J. R., 1972, ApJ, 176, 1

Guo Y., et al., 2009, MNRAS, 398, 1129

Guo Y., et al., 2013, ApJS, 207, 24

Hamadouche M. L., et al., 2022, MNRAS, 512, 1262

Häring N., Rix H.-W., 2004, ApJ, 604, L89

Hausammann L., Revaz Y., Jablonka P., 2019, A&A, 624, A11

Henry J. P., Lavery R. J., 1987, ApJ, 323, 473

Holmberg E., 1958, Meddelanden fran Lunds Astronomiska Observatorium Serie II, 136, 1

Hopkins P. F., Hernquist L., Cox T. J., Keres D., Wuyts S., 2009, ApJ, 691, 1424

Huang S., et al., 2018, MNRAS, 480, 521

Hubble E. P., 1922, ApJ, 56, 162

Hubble E. P., 1925, ApJ, 62, 409

Hubble E. P., 1926a, ApJ, 63, 236

Hubble E. P., 1926b, ApJ, 64, 321

Hubble E. P., 1927, The Observatory, 50, 276

Hubble E. P., 1929, ApJ, 69, 103

Huertas-Company M., Aguerri J. A. L., Tresse L., Bolzonella M., Koekemoer A. M., Maier C., 2010, A&A, 515, A3

Huertas-Company M., et al., 2013a, MNRAS, 428, 1715

Huertas-Company M., Shankar F., Mei S., Bernardi M., Aguerri J. A. L., Meert A., Vikram V., 2013b, ApJ, 779, 29

Hunter D. A., et al., 2012, AJ, 144, 134

Jackson R. A., et al., 2021, MNRAS, 502, 4262

Jaffé Y. L., Aragón-Salamanca A., De Lucia G., Jablonka P., Rudnick G., Saglia R., Zaritsky D., 2011, MNRAS, 410, 280

Jaffé Y. L., et al., 2018, MNRAS, 476, 4753

Janssens S., Abraham R., Brodie J., Forbes D., Romanowsky A. J., van Dokkum P., 2017, ApJ, 839, L17

Jeans J. H., 1922, MNRAS, 82, 122

Jiang F., Dekel A., Freundlich J., Romanowsky A. J., Dutton A. A., Macciò A. V., Di Cintio A., 2019, MNRAS, 487, 5272

Jones M. G., Bennet P., Mutlu-Pakdil B., Sand D. J., Spekkens K., Crnojević D., Karunakaran A., Zaritsky D., 2021, ApJ, 919, 72

Kadowaki J., Zaritsky D., Donnerstein R. L., RS P., Karunakaran A., Spekkens K., 2021, ApJ, 923, 257

Kaltenegger L., 2017, ARA&A, 55, 433

Kansky J., et al., 2019, PASP, 131, 075005

Karachentsev I. D., et al., 2002, A&A, 383, 125

Karachentsev I. D., Karachentseva V. E., Huchtmeier W. K., Makarov D. I., 2004, AJ, 127, 2031

Karachentsev I. D., et al., 2006, AJ, 131, 1361

Kartaltepe J. S., et al., 2015, ApJS, 221, 11

Kauffmann G., et al., 2003, MNRAS, 341, 33

Kaviraj S., Tan K.-M., Ellis R. S., Silk J., 2011, MNRAS, 411, 2148

Kawinwanichakij L., et al., 2017, ApJ, 847, 134

Kelkar K., Aragón-Salamanca A., Gray M. E., Maltby D., Vulcani B., De Lucia G., Poggianti B. M., Zaritsky D., 2015, MNRAS, 450, 1246

Kennicutt Robert C. J., 1998, ARA&A, 36, 189

Khalatyan A., Cattaneo A., Schramm M., Gottlöber S., Steinmetz M., Wisotzki L., 2008, MNRAS, 387, 13

Khoperskov S., Haywood M., Di Matteo P., Lehnert M. D., Combes F., 2018, A&A, 609, A60

Koda J., Yagi M., Yamanoi H., Komiyama Y., 2015, ApJ, 807, L2

Koekemoer A. M., et al., 2011, ApJS, 197, 36

Koonin E. V., Novozhilov A. S., 2017, Annual Review of Genetics, 51, 45

Kopparapu R. K., et al., 2013, ApJ, 765, 131

Kormendy J., 1977, ApJ, 218, 333

Kormendy J., Ho L. C., 2013, ARA&A, 51, 511

Kubo J. M., Stebbins A., Annis J., Dell'Antonio I. P., Lin H., Khiabanian H., Frieman J. A., 2007, ApJ, 671, 1466

Kuchner U., Ziegler B., Verdugo M., Bamford S., Häußler B., 2017, A&A, 604, A54

Kümmel M., Walsh J. R., Pirzkal N., Kuntschner H., Pasquali A., 2009, PASP, 121, 59

Labbé I., et al., 2005, ApJ, 624, L81

Lacy M., et al., 2005, ApJS, 161, 41

Lange R., et al., 2015, MNRAS, 447, 2603

Lapi A., et al., 2018, ApJ, 857, 22

Le Borgne D., Rocca-Volmerange B., Prugniel P., Lançon A., Fioc M., Soubiran C., 2004, A&A, 425, 881

Le Fèvre O., et al., 2019, A&A, 625, A51

Lee J. H., Lee M. G., Hwang H. S., 2006, ApJ, 650, 148

Leja J., Tacchella S., Conroy C., 2019, ApJ, 880, L9

Li H., et al., 2018, MNRAS, 476, 1765

Lianou S., Grebel E. K., Koch A., 2010, A&A, 521, A43

Lisker T., Weinmann S. M., Janz J., Meyer H. T., 2013, MNRAS, 432, 1162

Lora V., Sánchez-Salcedo F. J., Raga A. C., Esquivel A., 2009, ApJ, 699, L113

Lu S.-Y., Gu Y.-Z., Fang G.-W., Yuan Q.-R., 2019, Research in Astronomy and Astrophysics, 19, 150

Lu S., Fang G., Gu Y., Yuan Q., Cai Z.-Y., Kong X., 2021, ApJ, 913, 81

Madau P., Dickinson M., 2014, ARA&A, 52, 415

Madau P., Pozzetti L., Dickinson M., 1998, ApJ, 498, 106

Makarova L., Koleva M., Makarov D., Prugniel P., 2010, MNRAS, 406, 1152

Makovoz D., Khan I., 2005, in Shopbell P., Britton M., Ebert R., eds, Astronomical Society of the Pacific Conference Series Vol. 347, Astronomical Data Analysis Software and Systems XIV. p. 81

Maltby D. T., et al., 2010, MNRAS, 402, 282

Maltby D. T., Almaini O., Wild V., Hatch N. A., Hartley W. G., Simpson C., Rowlands K., Socolovsky M., 2018, MNRAS, 480, 381

Mansheim A. S., Lemaux B. C., Dawson W. A., Lubin L. M., Wittman D., Schmidt S., 2017, ApJ, 834, 205

Marriage T. A., et al., 2011, ApJ, 737, 61

Marsan Z. C., et al., 2019, ApJ, 871, 201

Martig M., Bournaud F., Teyssier R., Dekel A., 2009, ApJ, 707, 250

Martini P., Ho L. C., 2004, ApJ, 610, 233

Matharu J., et al., 2019, MNRAS, 484, 595

Matharu J., et al., 2020, MNRAS, 493, 6011

Mayer L., Governato F., Colpi M., Moore B., Quinn T., Wadsley J., Stadel J., Lake G., 2001, ApJ, 547, L123

Mayer L., Mastropietro C., Wadsley J., Stadel J., Moore B., 2006, MNRAS, 369, 1021

Mayer L., Kazantzidis S., Mastropietro C., Wadsley J., 2007, Nature, 445, 738

McConnachie A. W., 2012, AJ, 144, 4

McGaugh S. S., Schombert J. M., Bothun G. D., de Blok W. J. G., 2000, ApJ, 533, L99

McIntosh D. H., et al., 2005, ApJ, 632, 191

McLaughlin D. E., van der Marel R. P., 2005, ApJS, 161, 304

Mei S., et al., 2006, ApJ, 639, 81

Mei S., et al., 2015, ApJ, 804, 117

Mei S., et al., 2022, arXiv e-prints, p. arXiv:2209.02078

Merlin E., et al., 2015, A&A, 582, A15

Merlin E., et al., 2016, A&A, 595, A97

Merlin E., et al., 2019, MNRAS, 490, 3309

Mihos J. C., et al., 2015, ApJ, 809, L21

Miller N. A., Owen F. N., 2001, ApJ, 554, L25

Miyazaki S., et al., 2002, PASJ, 54, 833

Miyazaki S., et al., 2018, PASJ, 70, S1

Monelli M., Trujillo I., 2019, ApJ, 880, L11

Moore B., Katz N., Lake G., Dressler A., Oemler A., 1996, Nature, 379, 613

Mora C., Tittensor D. P., Adl S., Simpson A. G. B., Worm B., 2011, PLOS Biology, 9, e1001127

Mosleh M., Williams R. J., Franx M., Kriek M., 2011, ApJ, 727, 5

Mosleh M., Tacchella S., Renzini A., Carollo C. M., Molaeinezhad A., Onodera M., Khosroshahi H. G., Lilly S., 2017, ApJ, 837, 2

Mosleh M., Tavasoli S., Tacchella S., 2018, ApJ, 861, 101

Moster B. P., Somerville R. S., Maulbetsch C., van den Bosch F. C., Macciò A. V., Naab T., Oser L., 2010, ApJ, 710, 903

Mowla L. A., et al., 2019, ApJ, 880, 57

Muñoz R. P., et al., 2015, ApJ, 813, L15

Muldrew S. I., Hatch N. A., Cooke E. A., 2015, MNRAS, 452, 2528

Mutch S. J., Geil P. M., Poole G. B., Angel P. W., Duffy A. R., Mesinger A., Wyithe J. S. B., 2016, MNRAS, 462, 250

Naab T., Johansson P. H., Ostriker J. P., 2009, ApJ, 699, L178

Nair P., van den Bergh S., Abraham R. G., 2011, ApJ, 734, L31

Navarro J. F., Frenk C. S., White S. D. M., 1997, ApJ, 490, 493

Nedkova K. V., et al., 2021, MNRAS, 506, 928

Newman A. B., Ellis R. S., Bundy K., Treu T., 2012, ApJ, 746, 162

Newman A. B., Ellis R. S., Andreon S., Treu T., Raichoor A., Trinchieri G., 2014, ApJ, 788, 51

Noirot G., et al., 2016, ApJ, 830, 90

Noirot G., et al., 2018, ApJ, 859, 38

Noordeh E., Canning R. E. A., Willis J. P., Allen S. W., Mantz A., Stanford S. A., Brammer G., 2021, MNRAS, 507, 5272

Oehm W., Thies I., Kroupa P., 2017, MNRAS, 467, 273

Oh S.-H., et al., 2015, AJ, 149, 180

Oser L., Naab T., Ostriker J. P., Johansson P. H., 2012, ApJ, 744, 63

Patel S. G., Hong Y. X., Quadri R. F., Holden B. P., Williams R. J., 2017, ApJ, 839, 127

Peñarrubia J., Navarro J. F., McConnachie A. W., 2008, ApJ, 673, 226

Peng C. Y., Ho L. C., Impey C. D., Rix H.-W., 2002, AJ, 124, 266

Peng C. Y., Ho L. C., Impey C. D., Rix H.-W., 2010, AJ, 139, 2097

Peng Y., Maiolino R., Cochrane R., 2015, Nature, 521, 192

Petrosian V., 1976, ApJ, 210, L53

Poggianti B. M., Bridges T. J., Komiyama Y., Yagi M., Carter D., Mobasher B., Okamura S., Kashikawa N., 2004, ApJ, 601, 197

Poggianti B. M., et al., 2013, ApJ, 762, 77

Postman M., Geller M. J., 1984, ApJ, 281, 95

Postman M., et al., 2005, ApJ, 623, 721

Press W. H., Schechter P., 1974, ApJ, 187, 425

Pustilnik S. A., Tepliakova A. L., Makarov D. I., 2019, MNRAS, 482, 4329

Raichoor A., et al., 2012, ApJ, 745, 130

Read J. I., Gilmore G., 2005, MNRAS, 356, 107

Reaves G., 1956, AJ, 61, 69

Redman R. O., 1936, MNRAS, 96, 588

Rettura A., et al., 2010, ApJ, 709, 512

Rey M. P., Starkenburg T. K., 2022, MNRAS, 510, 4208

Rieke G. H., et al., 2004, ApJS, 154, 25

Rubin V. C., Ford W. K. J., Thonnard N., 1980, ApJ, 238, 471

Ruiz-Lara T., et al., 2018, MNRAS, 478, 2034

Safarzadeh M., Scannapieco E., 2017, ApJ, 850, 99

Saglia R. P., et al., 2010, A&A, 524, A6

Sánchez S. F., et al., 2012, A&A, 538, A8

Sandage A., 1972, ApJ, 176, 21

Sandage A., Binggeli B., 1984, AJ, 89, 919

Santini P., et al., 2015, ApJ, 801, 97

Saracco P., Gargiulo A., Ciocca F., Marchesini D., 2017, A&A, 597, A122

Saulder C., van Kampen E., Chilingarian I. V., Mieske S., Zeilinger W. W., 2016, A&A, 596, A14

Sazonova E., et al., 2020, ApJ, 899, 85

Schawinski K., Thomas D., Sarzi M., Maraston C., Kaviraj S., Joo S.-J., Yi S. K., Silk J., 2007, MNRAS, 382, 1415

Schirmer M., 2013, ApJS, 209, 21

Sersic J. L., 1968, Atlas de Galaxias Australes

Seyfert C. K., 1943, ApJ, 97, 28

Shankar F., Marulli F., Bernardi M., Mei S., Meert A., Vikram V., 2013, MNRAS, 428, 109

Shankar F., et al., 2014, MNRAS, 439, 3189

Shapiro K. L., et al., 2010, MNRAS, 402, 2140

Sheen Y.-K., Yi S. K., Ree C. H., Jaffé Y., Demarco R., Treister E., 2016, ApJ, 827, 32

Sil'chenko O. K., Kniazev A. Y., Chudakova E. M., 2018, AJ, 156, 118

Silk J., 2019, MNRAS, 488, L24

Silk J., Nusser A., 2010, ApJ, 725, 556

Simon J. D., Geha M., 2007, ApJ, 670, 313

Smirnova-Pinchukova I., et al., 2022, A&A, 659, A125

Smith R. J., et al., 2010, MNRAS, 408, 1417

Smith R., Fellhauer M., Assmann P., 2012, MNRAS, 420, 1990

Socolovsky M., Maltby D. T., Hatch N. A., Almaini O., Wild V., Hartley W. G., Simpson C., Rowlands K., 2019, MNRAS, 482, 1640

Somerville R. S., Davé R., 2015, ARA&A, 53, 51

Souto D., et al., 2019, ApJ, 874, 97

Springel V., Di Matteo T., Hernquist L., 2005, ApJ, 620, L79

Strazzullo V., et al., 2013, ApJ, 772, 118

Su K.-Y., et al., 2018, MNRAS, 480, 1666

Suess K. A., Kriek M., Price S. H., Barro G., 2019, ApJ, 877, 103

Szomoru D., Franx M., van Dokkum P. G., 2012, ApJ, 749, 121

Szomoru D., Franx M., van Dokkum P. G., Trenti M., Illingworth G. D., Labbé I., Oesch P., 2013, ApJ, 763, 73

Tadaki K.-i., et al., 2020, ApJ, 901, 74

Tal T., et al., 2014, ApJ, 789, 164

Tasca L. A. M., et al., 2009, A&A, 503, 379

Thomas D., Maraston C., Bender R., Mendes de Oliveira C., 2005, ApJ, 621, 673

Toft S., Gallazzi A., Zirm A., Wold M., Zibetti S., Grillo C., Man A., 2012, ApJ, 754, 3

Tolstoy E., Hill V., Tosi M., 2009, ARA&A, 47, 371

Tremmel M., Wright A. C., Brooks A. M., Munshi F., Nagai D., Quinn T. R., 2020, MNRAS, 497, 2786

Trujillo I., et al., 2004, ApJ, 604, 521

Trujillo I., et al., 2006, ApJ, 650, 18

Trujillo I., Ferreras I., de La Rosa I. G., 2011, MNRAS, 415, 3903

Trujillo I., Ferré-Mateu A., Balcells M., Vazdekis A., Sánchez-Blázquez P., 2014, ApJ, 780, L20

Tully R. B., Fisher J. R., 1977, A&A, 54, 661

Tully R. B., Shaya E. J., Karachentsev I. D., Courtois H. M., Kocevski D. D., Rizzi L., Peel A., 2008, ApJ, 676, 184

Tully R. B., Courtois H. M., Sorce J. G., 2016, AJ, 152, 50

Vazdekis A., Sánchez-Blázquez P., Falcón-Barroso J., Cenarro A. J., Beasley M. A., Cardiel N., Gorgas J., Peletier R. F., 2010, MNRAS, 404, 1639

Villaume A., et al., 2022, ApJ, 924, 32

Vulcani B., et al., 2020, ApJ, 899, 98

Walker M. G., Mateo M., Olszewski E. W., Peñarrubia J., Evans N. W., Gilmore G., 2009, ApJ, 704, 1274

Wang T., et al., 2016, ApJ, 828, 56

Weinberger R., et al., 2017, MNRAS, 465, 3291

Weinmann S. M., Kauffmann G., van den Bosch F. C., Pasquali A., McIntosh D. H., Mo H., Yang X., Guo Y., 2009, MNRAS, 394, 1213

Weisz D. R., et al., 2011, ApJ, 739, 5

Whitaker K. E., et al., 2010, ApJ, 719, 1715

Whitaker K. E., et al., 2011, ApJ, 735, 86

Whitaker K. E., et al., 2014, ApJ, 795, 104

Whitaker K. E., et al., 2017, ApJ, 838, 19

White S. D. M., Frenk C. S., 1991, ApJ, 379, 52

White S. D. M., Rees M. J., 1978, MNRAS, 183, 341

Wilkinson A., Almaini O., Wild V., Maltby D., Hartley W. G., Simpson C., Rowlands K., 2021, MNRAS, 504, 4533

Williams R. J., Quadri R. F., Franx M., van Dokkum P., Labbé I., 2009, ApJ, 691, 1879

Wirth A., Gallagher J. S. I., 1984, ApJ, 282, 85

Wittmann C., et al., 2017, MNRAS, 470, 1512

Wolfe A. M., Burbidge G. R., 1970, ApJ, 161, 419

Wuyts S., et al., 2007, ApJ, 655, 51

Wylezalek D., et al., 2013, ApJ, 769, 79

Wylezalek D., et al., 2014, ApJ, 786, 17

Yagi M., et al., 2010, AJ, 140, 1814

Yagi M., Koda J., Komiyama Y., Yamanoi H., 2016, ApJS, 225, 11

Yang L., Roberts-Borsani G., Treu T., Birrer S., Morishita T., Bradač M., 2021, MNRAS, 501, 1028

Yoon Y., Im M., Kim J.-W., 2017, ApJ, 834, 73

Yozin C., Bekki K., 2015, MNRAS, 452, 937

Zanisi L., et al., 2020, MNRAS, 492, 1671

Zaritsky D., Gonzalez A. H., Zabludoff A. I., 2006, ApJ, 638, 725

Zaritsky D., Donnerstein R., Karunakaran A., Barbosa C. E., Dey A., Kadowaki J., Spekkens K., Zhang H., 2021, ApJS, 257, 60

de Lapparent V., Geller M. J., Huchra J. P., 1986, ApJ, 302, L1

de Rijcke S., Michielsen D., Dejonghe H., Zeilinger W. W., Hau G. K. T., 2005, A&A, 438, 491

de Vaucouleurs G., 1959, Handbuch der Physik, 53, 275

van Dokkum P. G., Franx M., 1996, MNRAS, 281, 985

van Dokkum P. G., et al., 2010, ApJ, 709, 1018

van Dokkum P. G., Abraham R., Merritt A., Zhang J., Geha M., Conroy C., 2015a, ApJ, 798, L45

van Dokkum P. G., et al., 2015b, ApJ, 813, 23

van Dokkum P., et al., 2016, ApJ, 828, L6

van Dokkum P., et al., 2019, ApJ, 880, 91

van Zee L., Barton E. J., Skillman E. D., 2004, AJ, 128, 2797

van den Bosch F. C., Aquino D., Yang X., Mo H. J., Pasquali A., McIntosh D. H., Weinmann S. M., Kang X., 2008, MNRAS, 387, 79

van der Wel A., et al., 2012, ApJS, 203, 24

van der Wel A., et al., 2014, ApJ, 788, 28

CHAPTER 6

APPENDIX

MNRAS **000**, 1–9 (2022) Preprint 26 July 2022 Compiled using MNRAS LATEX style file v3.0

KDG 64: a large dwarf spheroidal or a small ultra-diffuse satellite of Messier 81

Anton V. Afanasiev,[1,2★] Igor V. Chilingarian,[3,2†] Kirill A. Grishin,[1,2] Dmitry Makarov,[4] Lidia Makarova,[4] Daniel Fabricant,[3] Nelson Caldwell,[3] and Sean Moran[3]
[1] *Université de Paris, CNRS, Astroparticule et Cosmologie, F-75013, Paris, France*
[2] *Sternberg Astronomical Institute, M. V. Lomonosov Moscow State University, Universitetsky prospect 13, Moscow, 119234, Russia*
[3] *Center for Astrophysics — Harvard and Smithsonian, 60 Garden St. MS09, Cambridge, MA 02138, USA*
[4] *Special Astrophysical Observatory of RAS, Nizhnij Arkhyz 369167, Karachai-Cherkessian Republic, Russia*

Accepted —. Received —; in original form 2022-Jun-11

ABSTRACT

Low-mass early-type galaxies, including dwarf spheroidals (dSph) and brighter dwarf ellipticals (dE), dominate the galaxy population in groups and clusters. Recently, an additional early-type population of more extended ultra-diffuse galaxies (UDGs) has been identified, sparking a discussion on the potential morphological and evolutionary connections between the three classifications. Here we present the first measurements of spatially resolved stellar kinematics from deep integrated-light spectra of KDG 64 (UGC 5442), a large dSph galaxy in the M 81 group. From these data we infer stellar population properties and dark matter halo parameters using Jeans dynamical modelling. We find an old, metal-poor stellar population with no young stars and a dark matter mass fraction of $\sim 90\%$ within the half-light radius. These properties and the position of KDG 64 on the Fundamental Plane indicate that it is a local analogue of smaller UDGs in the Coma and Virgo clusters and is probably a transitional dSph-UDG object. Its evolutionary path cannot be uniquely established from the existing data, but we argue that supernovae feedback and tidal heating played key roles in shaping KDG 64.

Key words: galaxies: individual: UGC 5442 – galaxies: dwarf – galaxies: kinematics

1 INTRODUCTION

Low-luminosity early-type galaxies with no current star formation are the numerically dominant population in galaxy clusters (Sandage & Binggeli 1984; Ferguson & Sandage 1988). These galaxies are commonly called dwarf ellipticals (dE) or dwarf lenticulars (dS0) and typically have stellar masses $M_* \sim 10^8 - 10^9 M_\odot$ and effective radii 0.5 – 2 kpc. Galaxy groups, on the other hand, are numerically dominated by yet fainter dwarf spheroidal galaxies (dSph) similar to dE in size (half-light radius $r_e \sim 0.5 - 2$ kpc) and morphology but with 10 – 100 times fewer stars (Grebel et al. 2003). Sandage & Binggeli (1984) found extended low-surface brightness galaxies with larger radii ($r_e = 1.5 -$ 4.5 kpc) and stellar masses similar or smaller than dEs. van Dokkum et al. (2015) proposed that these ultra-diffuse galaxies (UDGs) constitute a distinct galaxy class. UDGs were found in large quantities first in the Coma cluster and later in other clusters and groups (Muñoz et al. 2015; Mihos et al. 2015; Janssens et al. 2017; Wittmann et al. 2017; Zaritsky et al. 2021).

How these morphological classes relate to each other and the evolutionary processes leading to their structural differences remain uncertain (Conselice 2018). UDGs are the most puzzling because they share characteristics with both with dE and dSph (Chilingarian et al. 2019). Understanding the origin of UDGs is a crucial step in our studies of the evolutionary history of early-type dwarf galaxies.

The low UDG surface brightness makes spectroscopy difficult (Grishin et al. 2021), and we have measurements of stellar population parameters and stellar velocity dispersions for only a handful of UDGs (Beasley et al. 2016; van Dokkum et al. 2016; Danieli et al. 2019; Chilingarian et al. 2019; van Dokkum et al. 2019; Gannon et al. 2020, 2021). The internal dynamics and dark matter content of UDGs remain poorly constrained.

The nearest known UDG is 13 Mpc distant (Monelli & Trujillo 2019). At that distance only the brightest RGB stars are detectable, using HST, thus detailed stellar population

---

★ E-mail: anton.afanasiev@voxastro.org
† E-mail: igor.chilingarian@cfa.harvard.edu; chil@sai.msu.ru

analysis is impossible. Finding UDG-like candidates in the nearest groups would help us understand UDG formation and evolution. The largest quiescent dwarf galaxy in the Local Group, Fornax dSph, clearly cannot be considered as a UDG, because of its relatively small 700 pc effective radius and ~ 23 mag arcsec^{-2} average surface brightness (Zaritsky et al. 2006).

The M 81 group has 4 dwarf quiescent galaxies r$_e$ ≥ 1 kpc but one (F8D1, Caldwell et al. 1998) is located behind Galactic cirrus, another (IKN, Karachentsev et al. 2004) lies close to a 9-th mag star, and a third (KDG 61, Makarova et al. 2010) is located very near M 81 with projected foreground star-forming regions and likely tidal disturbance. The remaining dSph, KDG 64, is an excellent candidate for deep integrated-light spectroscopy. KDG 64 is one of the largest known dSph, and it borders the UDG and dE regimes in size and surface brightness.

KDG 64 is interesting because it borders multiple dwarf galaxy sub-classes. Its distance of 3.73 Mpc (Tully et al. 2016) enables HST photometry of individual stars but precludes obtaining individual stellar spectra. KDG 64's angular size, surface density and distance places sufficient stars located within a spectrograph slit to measure the average stellar velocity dispersion (σ) along the line of sight. The stochastic influence of individual stellar velocities is insignificant (Dubath et al. 1992). Our pilot study of KDG 64 demonstrates our ability to measure internal kinematics, to determine the stellar population, and to infer the dark matter content through dynamical modelling. A similar approach can be applied to future studies of dwarf galaxies with a wider range of masses, luminosities, surface brightnesses and dark matter properties.

2 NEW AND ARCHIVAL OBSERVATIONS

We observed KDG 64 with Binospec, a multi-object spectrograph at the 6.5-m MMT (Fabricant et al. 2019). We designed a single slit mask with three primary slits for KDG 64: two 50 arcsec-long slits along the major axis and one 20 arcsec-long slit along the minor axis. The major and minor axis slits are tilted by 35 deg and 55 deg to the direction of the dispersion, respectively. To prevent spectra from overlapping, the second major axis slit begins 28.5 arcsec from the galaxy centre. We excluded a background galaxy located near the geometric centre of KDG 64. The mask PA value was set to +165 deg (see Fig. 1).

The spectra were obtained on two consecutive nights: November 6&7, 2018. We used Binospec's 1000 gpm gratings with wavelength coverage 3,760 Å – 5,300 Å and $R = 3,750 - 4,900$ ($\sigma_{\rm inst} = 34 - 26$ km s^{-1}). The total integration time of 3h 20 min was split into 20 min-long exposures. The observations were conducted with seeing 0.9–1.3 arcsec and good transparency during dark time. We took arc lamp and internal flat field frames at night time and high signal-to-noise sky flats during the day to characterize the spectral resolution across the field and wavelength range.

We reduced the data with the Binospec pipeline[1] (Kansky et al. 2019) that produces flux calibrated, sky-subtracted, rectified, and wavelength calibrated 2D long-slit images (plus flux error frames) for each slitlet. The image scale is 0.24 arscec pix^{-1} along the slit and the wavelength sampling is 0.38 Å pix^{-1}. We used non-local sky subtraction (i.e. a global sky model computed from all "empty" regions in all slits in the mask) optimized for low surface brightness targets.

HST Advanced Camera for Surveys (ACS) archival images (obtained for a TRGB distance measurement) resolve KDG 64 into individual stars (PID 9884, PI: Armandroff) in the *F606W* and *F814W* (Cousins *Ic*) bands. We use archival *R*- and *V*-band images from the 2.1m KPNO telescope (PID 0117) for low-resolution 2-D surface photometry (300 s exposure time per band and 0.3 arcsec pix^{-1} scale). We construct a broadband spectral energy distribution (SED) with aperture photometry from GALEX (NUV and FUV bands), HST (*F606W* and *F814W* bands), KPNO (B, V, R bands) and Spitzer Space Telescope (*IRAC1* 3.6 μm and *IRAC2* 4.5 μm).

3 DATA ANALYSIS METHODS

3.1 Full spectrum fitting

We analyse the global properties of the KDG 64 stellar populations by modelling the integrated spectrum from the inner 12 arcsec of the major axis slitlet (Fig. 2) and the multi-wavelength spectral energy distribution. We use the NBursts+phot technique (Chilingarian & Katkov 2012) that computes the position of a local minimum of the $(1-w_{phot})\chi^2_{spec}+w_{phot}\chi^2_{phot}$ statistic. Here χ^2_{spec} and χ^2_{phot} are the χ^2 statistics for a spectrum and an SED respectively, and w_{phot} is the statistical weight of the residuals in the SED fitting. We model the optical spectrum from spectral templates interpolated to the specific values of stellar age and metallicity, convolved with the Gaussian line of sight velocity distribution (LOSVD) and multiplied by a polynomial continuum.

For global stellar population modelling we use Miles (Vazdekis et al. 2010) simple stellar population (SSP) models computed for Padova isochrones (Girardi et al. 2000). The broadband SED is modelled using pegase.2-based low-resolution templates (Fioc & Rocca-Volmerange 1997, 1999). A spectrum is degraded to a spectral resolution of 2.3 Å. We simultaneously model the observed optical spectrum integrated in the inner 12 arcsec bin and spectral energy distribution from UV to NIR. A flux in each band is extracted from an image within the elliptical isophote ($b/a = 0.5$) aligned with the major axis of 100 arcsec ~ 1.4 r_e excluding the background galaxy near the centre of KDG 64 as well as several other background/foreground contaminants. To account for potential flux calibration errors in both the observed spectrum and Miles SSPs, we include a 15th order polynomial continuum in the fitting procedure.

To measure internal kinematics, we also analyse a full-resolution long-slit spectrum using the NBursts technique (Chilingarian et al. 2007b,a), which implements a full spectrum fitting approach in the pixel space using a grid of intermediate-spectral resolution ($R = 10,000$) simple stellar population (SSP) models computed with the pegase.hr

---

[1] `https://bitbucket.org/chil_sai/binospec/src`

evolutionary synthesis package (Le Borgne et al. 2004). We convolve SSPs with the Binospec spectral line-spread function determined from the analysis of sky flats. As Chilingarian et al. (2008a) demonstrated, the NBursts algorithm can recover stellar velocity dispersions (σ) down to $\sigma_{\text{inst}}/2$ at a signal-to-noise ratio of 5 per pixel. We use the restframe wavelength range between 3900Å and 5200–5400Å for the fitting procedure. See Chilingarian et al. (2008b); Chilingarian (2009) for a detailed discussion regarding sensitivity, systematics, and limitations of the NBursts full spectrum fitting. We allow a 15th order multiplicative polynomial continuum correction and a constant additive term to account for uncertainties in subtracting scattered light.

For the reduced long-slit spectra, the median signal-to-noise ratio (SNR) per pixel in the wavelength range from 4,800–5,000 Å reached its maximum value of 1.65 in the brightest pixel of the major axis, the closest to the galaxy centre. To reliably measure stellar velocity dispersion of 15 km s^{-1} for old (10 Gyr) metal-poor ([Fe/H]=$-$1.5) stellar population (Chilingarian & Grishin 2020), we bin the Binospec dataset along the slit increase the SNR per spatial bin. We end up with a total of 15 spatial bins along the major axis and 4 bins along the minor axis for radial velocity measurements (SNR=4) and 5 spatial bins along one side of the major axis (SNR=7) for velocity dispersion measurements. We can not measure the velocity dispersion along the minor axis due to the 1.8X spectral resolution degradation caused by the large tilt of the slit to the direction of dispersion.

3.2 Star counts and 2-D photometry

We use the DOLPHOT software package (Dolphin 2000, 2016) for crowded field photometry to identify the resolved stars in the HST/ACS *F606W* and *F814W* images and to perform PSF photometry. Only the stars with good quality photometry are included in the final catalogue, following the DOLPHOT recipe and parameters. We choose only the stars lying above the completeness limit $m_{F606W} < 26.85$ mag and $m_{F814W} < 25.35$ mag. The spatial distribution of stars is fit with a single-Sérsic model using maximum likelihood. We set the centre coordinates, axial ratio, positional angle, effective radius, global normalization, and Sérsic index as free parameters. We also account for foreground contamination following (Makarova et al. 2010) which gives a total of 30-40 stars from our galaxy. Despite that, the distribution of stars requires an additional constant background component at a level of $\sim$ 190 stars which may be an effect of contamination from M 81, M 82, and NGC 3077.

For dynamical modelling we need a global luminosity distribution that is difficult to construct from HST frames with conventional 2D-photometry packages (like Galfit or Sextractor) due to the presence of resolved stars. We therefore determine the structural parameters of KDG 64 from the magnitude-limited star counts normalized by the surface brightness profile obtained from seeing-limited ground-based images. We perform a 2-D photometric decomposition of ground-based photometric data using Galfit (Peng et al. 2010). The model takes centre coordinates, Sérsic index, effective radius, positional angle, axis ratio and total magnitude as free parameters. All of the fitted parameters except effective radius and PA are close to those obtained from star counts. The divergence in R_e and PA might be explained by the presence of a galactic cirrus at the northern edge of KDG 64 that skews the 2-D photometric data. We use the central surface brightness from 2D decomposition as a normalization to convert the surface density profile of the detected stars into surface brightness profile while keeping all the structural parameters from star counts, as this method should better track the mass distribution in KDG 64.

3.3 Dynamical modelling

We use the Jeans Anisotropic Modeling (JAM) approach (Cappellari 2008) to estimate dynamical mass-to-light ratio and mass of dark matter in KDG 64. We follow a procedure described in Afanasiev et al. (2018) without the central black hole component. From the $M_{BH}-M_{\text{bulge}}$ scaling relation (Kormendy & Ho 2013), massive central black hole is unlikely to be present in the centre of dwarf spheroidal galaxy (expected black hole mass $< 10^{4.5} M_{\odot}$). Currently there is no consensus on the presence of massive black holes in dwarf spheroidals. Most kinematical studies do not find black holes more massive than 10^5 $M_{\odot}$ (e.g. Lora et al. 2009), however there is an evidence that some dwarf spheroidals might host supermassive black holes (Bustamante-Rosell et al. 2021).

The basic JAM code does not allow a non-self-consistent (that is "mass follows light") as a default, but the code can be easily modified to handle the dark matter halo as a separate component influencing only the overall galaxy potential. We use two dark matter profiles to model KDG 64, a Burkert halo (Burkert 1995) and a NFW halo (Navarro et al. 1997). These options allow us to model either cored or cusped dark matter distribution and compare the goodness of fit for the kinematic data between the two options. Each of these two DM profiles is described by two free parameters and the other properties can be analytically derived. For the Burkert halo we use ρ_0 and r_s, and for NFW profile we take M_{total} and R_s. We also calculate the total halo mass for the Burkert profile and the dark matter fraction within the effective radius R_e for both profiles to compare the halo parameters with each other and with the results from Chilingarian et al. (2019). With this approach we fix the stellar mass-to-light ratio at the value determined from the stellar population, $M/L_{*,R} = 1.3\ (M/L)_{\odot}$ computed using PEGASE.2 models for the stellar population properties of KDG 64. We model only spherically-symmetric dark matter haloes; oblate or prolate dark matter distributions are outside the scope of our study.

The galaxy stellar potential is obtained from the surface brightness profile (see Section 3.2) using the Multiple Gaussian Expansion (MGE) method (Cappellari 2002). For dynamical modelling we convert the dark matter profile into multiple Gaussians by fitting 1D dark matter density profiles with the MGE_FIT_1D procedure from Cappellari (2002) and deprojecting the resulting Gaussians in 3D. We add the Gaussians describing the dark matter and the stellar population potentials to obtain the final potential. We run JAM over a parameter grid of anisotropy β_z (0 to 0.9), and inclination i from edge-on (90°) to the minimum allowed by the galaxy ellipticity (64°) in 6° steps. The grid also includes two dark matter halo parameters (central density ρ_0 and scale radius r_s for Burkert haloes; halo mass M_{200} and concentration c for NFW haloes). We also calculate the halo mass for the Burkert halo (uniquely derived from each pair $\{\rho_0, r_s\}$)

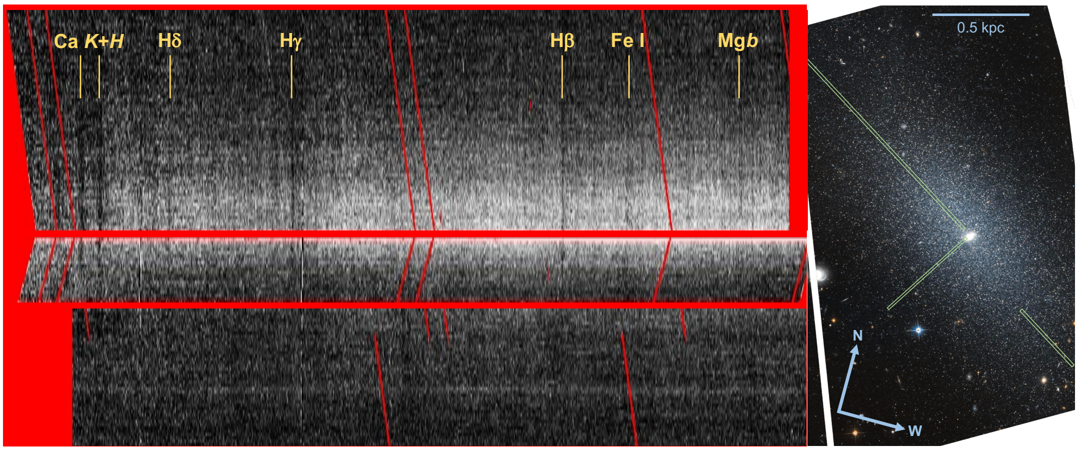

Figure 1. Left: long slit spectra along galaxy major and minor axes. **Right:** slit positions overlaid on an HST false-color (*F606W/F814W*) image.

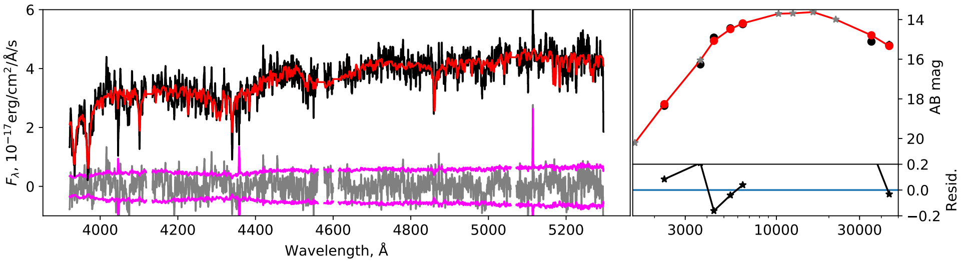

Figure 2. A Binospec spectrum of KDG 64 binned within 12 arcsec along the major axis on one side from the galaxy centre in F_λ units (left panel, black); an observed SED in AB magnitudes (right panel, black); the best-fitting model spectra and SED (red), flux uncertainties (purple) and residuals (grey line and black asterisks). The SED fitting residuals are shown in the bottom-right panel.

Table 1. Structural parameters of KDG 64 measured using star counts in HST ACS F814W image (left) and using Galfit analysis of 2.1m KPNO R-band deep images.

Method	Star counts	2D decomposition
R$_e$, pc	960 ± 25	1125 ± 20
R$_e$, arcsec	53.1 ± 1.4	62.2 ± 1.1
n	1.06 ± 0.05	1.07 ± 0.01
b/a	0.45 ± 0.01	0.49 ± 0.02
PA, deg	17.4 ± 1.2	28.1 ± 0.5

Table 2. Internal kinematics and stellar population properties of KDG 64 derived from Binospec data.

Slit	Major axis	Minor axis
S/N, Å^{-1}	25	10
$v_{\rm los}$, km s^{-1}	−18.4 ± 3.4	−18 ± 6.0
$v_{\rm rot}$, km s^{-1}	< 2.0	< 6.0
σ, km s^{-1}	16.8 ± 1.9	17 (fixed)
Age, Gyr	10.9 ± 1.0	11.0 (fixed)
[Fe/H], dex	−1.33 ± 0.26	−1.33 (fixed)

for comparison with the NFW halo mass. The concentration c for the NFW profile is capped at $c = 4$, because for lower c values it is not always possible to perform a MGE expansion.

4 RESULTS

We obtain structural properties of KDG 64 (R_e, n, b/a) from star counts yielding best-fitting values $R_e = 53.1$ arcsec, $n = 1.06$, $b/a = 0.45$. The light distribution is very close to exponential. Assuming a TRGB-estimated distance modulus of 27.86 mag (Tully et al. 2016), we estimate its physical size as $R_e = 960$ pc, placing it among the largest galaxies of the dSph type. For M 81, the adopted TRGB distance modulus is $d = 27.79$ mag (Tully et al. 2016). We are able to calculate the full 3D distance between M 81 and KDG 64 of $r = 160$ kpc (smaller than the 230 kpc assumed in Makarova et al. 2010). The KDG 64 and M 81 heliocentric velocities differ by 20 km s^{-1} suggesting that the orbit of KDG 64 around M 81 lies nearly in the plane of the sky, in agreement

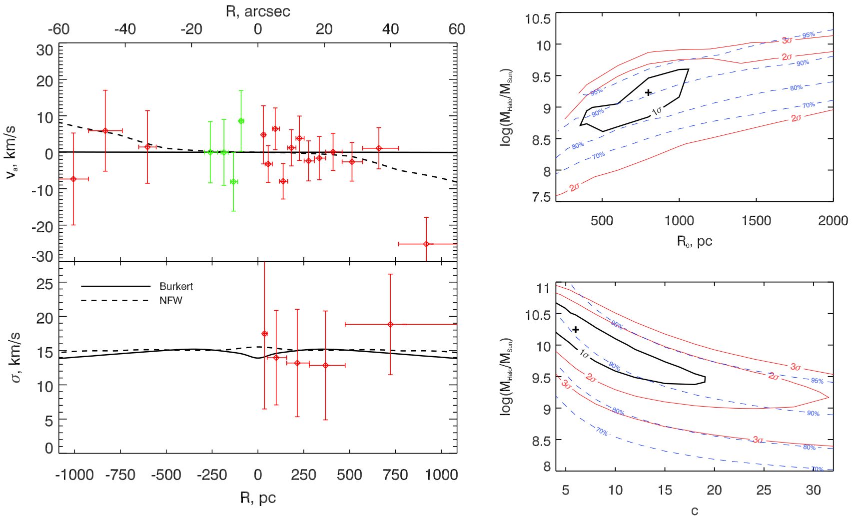

Figure 3. Left: Resolved kinematics profiles (red and green v_r data points for minor and major axes respectively) and best-fitting Jeans dynamical models (black lines) with Burkert and NFW dark matter halo profiles. **Right:** confidence levels for the parameters of Burkert and NFW DM profiles.

Table 3. Best-fitting parameters of the dynamical models and their 1-σ uncertainties.

DM Halo	Burkert	NFW
$\log(\mathrm{M}_{200}/\mathrm{M}_\odot)$	$9.2^{+0.3}_{-0.5}$	$10.2^{+0.4}_{-0.7}$
R_{200}, kpc	24^{+6}_{-8}	52 ± 20
R_0, kpc or R_s, kpc	0.8 ± 0.35	8.8^{+9}_{-7}
$\log(\rho_0)$, $\mathrm{M}_\odot$ pc^{-3} or c	-1.0 ± 0.25	6^{+12}_{-2}
DM within R_e, per cent	90^{+4}_{-8}	91^{+3}_{-4}
β_z	0.8 ± 0.1	0.75 ± 0.1
Inclination, deg	72 ± 6	72 ± 6

with Makarova et al. (2010). Unfortunately it is difficult to assess if KDG 64 is located closer to the pericentre or the apocentre of its orbit.

The mean stellar age obtained from the SED supplemented full-spectrum fitting is 10 Gyr, the metallicity is [Fe/H]= −1.3 dex, corresponding to a stellar mass to light ratio $M/L_{\mathrm{R},*} = 1.29 \pm 0.11$ ($M_\odot/L_{\odot,\mathrm{R}}$). The SED clearly indicates the lack of young or intermediate stellar populations with ages 5 Gyr or younger.

The vertical anisotropy β_z is rather high, with the best fitting values falling in the range 0.6–0.7 for both DM haloes; the best-fitting inclination to the line of sight is $i = 70$ deg. This means that the shape of KDG 64 is a very oblate spheroid, well represented by a thick disc and not a thin disc geometry.

Cored (Burkert) and cusped (NFW) dark matter distributions fit equally well ($\Delta\chi^2 \approx 0.2$), preventing us from probing the shape of the innermost DM distribution. The best-fitting halo total masses differ by an order of magnitude ($\log(M_{\mathrm{Burkert}}/M_\odot) = 9.2$ vs $\log(M_{\mathrm{NFW}}/M_\odot) = 10.2$). However, the dark matter fraction inside the effective radius is the same for both halo profiles, slightly more than 90 per cent (see iso-lines in Fig. 3 and Table 3).

5 DISCUSSION

We demonstrate that we can obtain spectra of low-surface brightness dwarf spheroidal galaxies beyond the Local group of sufficient quality to determine reliable stellar populations and to make spatially resolved kinematic measurements. We are able to perform Jeans dynamical modelling and to estimate dark matter halo parameters. The stellar population parameters of KDG 64 are well measured and consistent between different studies, so we can emphasize kinematics measurements.

KDG 64 is located 97.5 arcmin = 106 kpc in projected distance from M 81. Even without taking into account the line of sight distance difference, we can estimate the maximum tidal disturbance from M 81. Karachentsev et al. (2002) derive M 81's group total dynamical mass as $\sim 1.6 \times 10^{12} M_\odot$, so the mass of the M 81 dark matter halo can be estimated at 2–3 times smaller. An initially spherical galaxy 106 kpc from M 81 would have been distorted into an ellipsoid with expected axis ratio $a/b = 1.16$ in the M 81 direction.This value is much smaller than $a/b = 2.2$ we obtain from the KDG 64 photometric analysis. Additionally, KDG 64's isophotes are extended along the line perpendicular to the direction towards M 81. It is therefore unlikely that KDG 64's elliptical shape stems from its current tidal interaction with M 81.

Using the 3D distance $d = 160$ kpc we can constrain the sphere of KDG 64's gravitational influence from the Jacobi

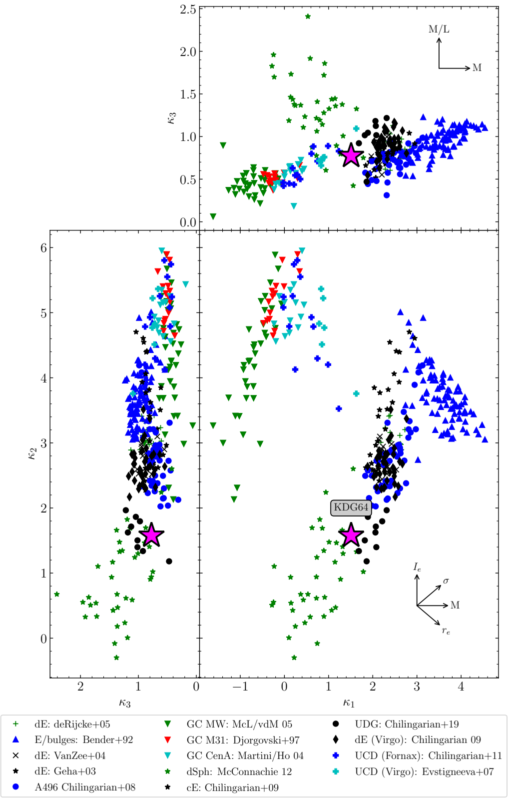

Figure 4. The κ-space view of the FP. The position of KDG 64 is marked by a pink star. The sources of data in the literature compilation are shown in the legend.

radius (see Binney & Tremaine 2008):

$$R_j = d \times \left(\frac{M_{KDG\ 64}}{3M_{M81}}\right)^{1/3} = 24\ \text{kpc}. \quad (1)$$

Interestingly, the best-fitting value for R_{200} of the Burkert dark matter halo is ~ 25 kpc suggesting that the dark matter haloes of KDG 64 and M 81 are in equilibrium. Thus, if KDG 64's dark matter halo is being stripped by its host, the process is gradual and should not lead to halo truncation (see also Borukhovetskaya et al. 2022).

KDG 64 exhibits no rotation along the major axis up to 20 arcsec (~ 360 pc, or 1/3 R$_e$), and beyond that radius the presence of the rotation is questionable. The minor axis also does not exhibit rotation, consistent with our initial assumption of axial symmetry. The dispersion profile is flat, suggesting the dark matter halo dominates the potential at all radii. Low rotation and strong dispersion support is typical of dwarf spheroidals (Walker et al. 2009) as well as UDGs (Chilingarian et al. 2019, Ruiz-Lara et al. 2018, van Dokkum et al. 2019).

The κ-space Fundamental plane (Bender et al. 1992) is an important kinematics metric for a dispersion supported virialized galaxy. This is a modification of the original Fundamental Plane (Djorgovski & Davis 1987) with the rotated axes (see Figure 4). The κ-parameters are defined as: $\kappa_1 = (\log\sigma_0 + \log R_e)/\sqrt{2}$ (a measure of $M_{\rm dyn}$); $\kappa_2 = (\log\sigma_0 + 2\log I_e - \log R_e)/\sqrt{6}$ (compactness); $\kappa_3 = (\log\sigma_0 - \log I_e - \log R_e)/\sqrt{3}$ (a measure of $(M/L)_{\rm dyn}$). KDG 64's position in the $\kappa_1 - \kappa_3$ projection is clearly in the locus of the UDGs (black circles) rather than 'classical' dSphs (green stars). The other two projections also show KDG 64 skewing to the UDG locus. These metrics clearly display KDG 64's transitional nature between dSphs and UDGs, favoring the UDG locus. The dark matter fraction within $1r_e$ of just above 90 per cent is comparable to the values found in Chilingarian et al. (2019) for small Coma UDGs. Walker et al. (2009) show that the dark matter fraction in dwarf spheroidal galaxies is stable to the choice of dark matter profile. This is also true for KDG 64. The 800 pc core size is similar to that of large dSphs (e.g Amorisco et al. 2013).

The structural parameters of KDG 64 also resemble those of smaller UDGs in the Coma cluster (Koda et al. 2015; Yagi et al. 2016 where the UDG selection criteria were $R_e > 0.7$ kpc and $\langle\mu_{e,r}\rangle > 24.0$ mag arcsec^{-2}). KDG 64 has $R_e \sim 0.95$ kpc and $\langle\mu_{e,r}\rangle = 23.89$ mag, so if placed inside Coma cluster and accounting for corresponding cosmological dimming ($\langle\mu_e\rangle$ becomes 24.01), KDG 64 would have barely passed the Yagi et al. (2016) UDG selection criteria. KDG 64 has a rather elongated shape, so if deprojected, its surface brightness would be even fainter. Yagi et al. (2016) catalog contains 204 galaxies (out of total 854) with R_e smaller than KDG 64, and 101 of them have $b/a < 0.5$. From a morphological perspective KDG 64 is similar to the small UDGs in the Coma cluster. These three similarities motivate the claim that KDG 64 is one of the closest UDG analogs in the Local Universe. It could act as a calibration object for integrated light studies of more distant galaxies.

The HST ACS data shows no detectable young stellar population. Our full-spectrum+SED fitting results, and especially the GALEX FUV and NUV fluxes support this conclusion. Makarova et al. (2010) found a slight enhancement of the star formation mostly about 1.5 − 2.5 Gyr ago and an indication of very small fraction (less than 2 percent) of stars ~500 Myr old. These intermediate age stellar populations account for about 10 per cent of the total mass. Girardi et al. (2010) reports 7 to 9 per cent of population younger than 3 Gyr (with less than 1 per cent younger than 1 Gyr) based on the AGB to RGB star ratio. Weisz et al. (2011) indicate a more protracted star formation history, with only a half of KDG 64 stellar mass in place 6 Gyr ago, and 18 per cent of the stellar mass formed during the last 2 Gyr. This result is inconsistent with our results from full-spectrum fitting and SED analysis. Lianou et al. (2010) do not infer age, giving only the metallicity which varies between −1.72 dex and −1.39 dex depending on the chosen normalization and isochrone. CMD-based results from Milky Way dSphs (Tolstoy et al. 2009) suggest that many of them went through multiple phases of moderate star formation after the buildup of the bulk of their stellar mass ~ 10 Gyr ago. These events typically make up about 10 per cent of the stellar mass, and happen once in 3-5 Gyr.

The best-fitting model for the stellar distribution was found to be Sèrsic + constant background. This background could be attributed to either M 81 + M 82 + NGC 3077 peripheral stars, or excess foreground stars in our Galaxy. In both cases, this background could contain some young stars that might shift the age statistic derived from CMD slightly towards younger ages, and the number of young stars detected in Makarova et al. (2010) is generally comparable to this background value.

Boyce et al. (2001) have detected an Hi spur extending from the main cloud around NGC 3077 to KDG 64. However it is mostly located at the radial velocity of NGC 3077, which is about 200 kpc farther than KDG 64. This association with Hi is most likely a projection effect, hence KDG 64 does not have any neutral gas.

The neighbours of KDG 64 in the M 81 group with comparable structural properties are KDG 61, DDO 78, DDO 71 (KDG 63), IKN (Karachentsev et al. 2004), and F8D1 (Caldwell et al. 1998). Their M_V ranges from −11.5 mag (IKN) to −13.9 mag (KDG 61), and they are on the bright end of the dSph luminosity distribution. These galaxies all have low surface brightnesses, around $\langle\mu_{e,r}\rangle = 24.4$ mag arcsec^{-2} for KDG 61 and $\langle\mu_{e,r}\rangle \approx 25$ mag arcsec^{-2} for the remaining three galaxies. IKN hosts an unusually rich system of globular clusters (Karachentsev et al. 2006) similarly to Fornax dSph (Buonanno et al. 1998), but its study is severely hampered by a 9 mag foreground star projecting directly on the northern part of the galaxy. Lianou et al. (2010) studied stellar populations of all the galaxies mentioned above as well as KDG 64 with archival HST data. They found that the galaxies are generally similar in their metallicities, ages and star formation histories, thus forming a cohesive population of dwarf M 81 satellites. Future integrated light spectroscopic studies of these objects will help us understand the origin and evolution of UDG and dSph galaxy classes.

The evolutionary path of dwarf spheroidal galaxies is still a matter of debate as no single mechanism explains the diversity of their properties (Mayer et al. 2001, 2007; Read & Gilmore 2005). Here we use KDG 64 properties as a case study for the main dSph formation theories. AGN in dSph have not been discovered to date, but according to well-established scaling between central black holes and their host galaxies (Ferrarese & Merritt 2000; Gebhardt et al. 2000; Häring & Rix 2004), they are expected to be in the intermediate-mass range (2 to $5 \times 10^4 M_\odot$), which will not provide enough energy output to quench star formation in the entire galaxy even if the AGN accretes at the Eddington limit. The starvation and strangulation mechanisms are also unlikely to play a major role, for their ineffectiveness in the low mass regime allows dwarf galaxies to form stars in the absence of an external gas reservoir for time periods comparable to Hubble time.

X-ray data from the XMM telescope archive[2] do not demonstrate that M 81 has a massive halo of hot circumgalactic gas. It is well established that ram-pressure quenching is not as efficient in groups as in clusters. In a low-density environment ram pressure is weaker – it may not strip the gas from a dwarf galaxy but instead shield it from UV emission keeping star formation in place (Hausammann et al. 2019). However, some models show that in the group environment ram pressure could act together with tidal heating to completely quench a dwarf spheroidal satellite (Mayer et al. 2006).

Supernovae (SN) feedback (Dekel & Silk 1986) is widely considered the most common quenching mechanism in the low-mass stellar systems. In the absence of external forces, SN feedback is theorized to "fire" only once in the low mass galaxies, as the gas ejected by SN remnants is expelled forever from a galaxy potential far into the IGM. While SN feedback provides a good explanation for the old and metal poor stellar population, it doesn't explain the lack of rotation in KDG 64. Dynamical modelling suggests KDG 64 is a very oblate spheroid that does not rotate. However, if it was formed from a star forming discy dIrr progenitor via SN feedback, some residual rotation should have been preserved after the quenching.

It is also puzzling that KDG 64 does not contain globular clusters (GCs) or a central star cluster (the central object shown in Fig. 1 is a background galaxy), while some morphologically similar galaxies contain many globular clusters (Fornax, IKN), and over half of all dwarf elliptical galaxies are nucleated (Grant et al. 2005). The majority of Milky Way dSphs do not have any GCs, however they are typically way smaller than KDG 64. Evidently, there exists some mechanism to remove them completely, and SN feedback is not expected to influence globular clusters.

We suspect that ram-pressure stripping, SN feedback and disc heating by M 81 tides all could have played a role in KDG 64 evolution. The old homogeneous stellar population and high orbital anisotropy suggest that KDG 64 should have spent most of its lifetime at moderate distance from M 81, where tidal forces are not strong enough to significantly deform the dSph satellite or strip its DM halo, but where tidal forces significantly contribute to the kinematical heating of the stellar component. As a result the stars gradually shift to the eccentric orbits, and the galaxy transitions from being rotation-supported to pressure-supported. Globular clusters are also shown to be influenced by tides that puff up the GC distribution (Carleton et al. 2021), easing their subsequent detachment. It is possible that the galaxy is initially quenched by SN feedback, and starts to be tidally heated soon afterwards. This tidal evolution has been shown to be important in the models of the Local Group dSphs (Peñarrubia et al. 2008).

KDG 64 demonstrates that large group-dwelling dwarf spheroidal galaxies are in fact barely distinguishable from other diffuse low-mass non-starforming stellar systems in groups and clusters. It is not possible to make sweeping conclusions from a single galaxy, but we can argue that at least some of the morphologically similar cluster dwarfs should follow the same evolutionary paths as dwarf spheroidals in groups. The definitive answer requires systematic observations of low mass galaxies in different environments analysed in a homogeneous fashion. This work demonstrates the feasibility of such a program.

ACKNOWLEDGEMENTS

AA acknowledges the Université de Paris for funding his PhD research and the Russian Science Foundation (RScF)

---

[2] `https://nxsa.esac.esa.int/nxsa-web/search`

grant No. 22-12-00080 for supporting the development of the dynamical modelling procedures. AA, IC, KG acknowledge the RScF grant No. 19-12-00281 for supporting the analysis of the spectral and photometric data and the Interdisciplinary Scientific and Educational School of Moscow University "Fundamental and Applied Space Research". IC's research is supported by the Telescope Data Center at Smithsonian Astrophysical Observatory. We are grateful to the staff of the MMT Observatory jointly operated by Smithsonian Astrophysical Observatory and the University of Arizona for their support of Binospec operations and service mode observations. We thank F. Combes, G. Mamon, and O. Sil'chenko for fruitful discussions related to this project.

DATA AVAILABILITY

The data underlying this article will be shared on reasonable request to the corresponding author.

REFERENCES

Afanasiev A. V., et al., 2018, MNRAS, 477, 4856
Amorisco N. C., Agnello A., Evans N. W., 2013, MNRAS, 429, L89
Beasley M. A., Romanowsky A. J., Pota V., Navarro I. M., Martinez Delgado D., Neyer F., Deich A. L., 2016, ApJ, 819, L20
Bender R., Burstein D., Faber S. M., 1992, ApJ, 399, 462
Binney J., Tremaine S., 2008, Galactic Dynamics: Second Edition
Borukhovetskaya A., Errani R., Navarro J. F., Fattahi A., Santos-Santos I., 2022, MNRAS, 509, 5330
Boyce P. J., et al., 2001, ApJ, 560, L127
Buonanno R., Corsi C. E., Zinn R., Pecci F. F., Hardy E., Suntzeff N. B., 1998, ApJ, 501, L33
Burkert A., 1995, ApJ, 447, L25
Bustamante-Rosell M. J., Noyola E., Gebhardt K., Fabricius M. H., Mazzalay X., Thomas J., Zeimann G., 2021, ApJ, 921, 107
Caldwell N., Armandroff T. E., Da Costa G. S., Seitzer P., 1998, AJ, 115, 535
Cappellari M., 2002, MNRAS, 333, 400
Cappellari M., 2008, MNRAS, 390, 71
Carleton T., Guo Y., Munshi F., Tremmel M., Wright A., 2021, MNRAS, 502, 398
Chilingarian I. V., 2009, MNRAS, 394, 1229
Chilingarian I. V., Grishin K. A., 2020, PASP, 132, 064503
Chilingarian I. V., Katkov I. Y., 2012, in Tuffs R. J., Popescu C. C., eds, IAU Symposium Vol. 284, The Spectral Energy Distribution of Galaxies - SED 2011. pp 26–28 (`arXiv:1112.5191`), doi:10.1017/S1743921312008642
Chilingarian I., Prugniel P., Sil'chenko O., Koleva M., 2007a, in Vazdekis A., R. Peletier R., eds, IAU Symposium Vol. 241, Stellar Populations as Building Blocks of Galaxies. Cambridge University Press, Cambridge, UK, pp 175–176 (`arXiv:0709.3047`)
Chilingarian I. V., Prugniel P., Sil'Chenko O. K., Afanasiev V. L., 2007b, MNRAS, 376, 1033
Chilingarian I. V., Cayatte V., Bergond G., 2008a, MNRAS, 390, 906
Chilingarian I. V., Cayatte V., Durret F., Adami C., Balkowski C., Chemin L., Laganá T. F., Prugniel P., 2008b, A&A, 486, 85
Chilingarian I., Cayatte V., Revaz Y., Dodonov S., Durand D., Durret F., Micol A., Slezak E., 2009, Science, 326, 1379
Chilingarian I. V., Mieske S., Hilker M., Infante L., 2011, MNRAS, 412, 1627
Chilingarian I. V., Afanasiev A. V., Grishin K. A., Fabricant D., Moran S., 2019, ApJ, 884, 79
Conselice C. J., 2018, Research Notes of the American Astronomical Society, 2, 43
Danieli S., van Dokkum P., Conroy C., Abraham R., Romanowsky A. J., 2019, arXiv e-prints
Dekel A., Silk J., 1986, ApJ, 303, 39
Djorgovski S., Davis M., 1987, ApJ, 313, 59
Djorgovski S. G., Gal R. R., McCarthy J. K., Cohen J. G., de Carvalho R. R., Meylan G., Bendinelli O., Parmeggiani G., 1997, ApJ, 474, L19
Dolphin A. E., 2000, PASP, 112, 1383
Dolphin A., 2016, DOLPHOT: Stellar photometry, Astrophysics Source Code Library, record ascl:1608.013 (ascl:1608.013)
Dubath P., Meylan G., Mayor M., 1992, ApJ, 400, 510
Evstigneeva E. A., Gregg M. D., Drinkwater M. J., Hilker M., 2007, AJ, 133, 1722
Fabricant D., et al., 2019, PASP, 131, 075004
Ferguson H. C., Sandage A., 1988, AJ, 96, 1520
Ferrarese L., Merritt D., 2000, ApJ, 539, L9
Fioc M., Rocca-Volmerange B., 1997, A&A, 326, 950
Fioc M., Rocca-Volmerange B., 1999, arXiv e-prints, pp astro–ph/9912179
Gannon J. S., Forbes D. A., Romanowsky A. J., Ferré-Mateu A., Couch W. J., Brodie J. P., 2020, MNRAS, 495, 2582
Gannon J. S., et al., 2021, MNRAS, 502, 3144
Gebhardt K., et al., 2000, ApJ, 539, L13
Geha M., Guhathakurta P., van der Marel R. P., 2003, AJ, 126, 1794
Girardi L., Bressan A., Bertelli G., Chiosi C., 2000, A&AS, 141, 371
Girardi L., et al., 2010, ApJ, 724, 1030
Grant N. I., Kuipers J. A., Phillipps S., 2005, MNRAS, 363, 1019
Grebel E. K., Gallagher John S. I., Harbeck D., 2003, AJ, 125, 1926
Grishin K. A., Chilingarian I. V., Afanasiev A. V., Fabricant D., Katkov I. Y., Moran S., Yagi M., 2021, Nature Astronomy, 5, 1308
Häring N., Rix H.-W., 2004, ApJ, 604, L89
Hausammann L., Revaz Y., Jablonka P., 2019, A&A, 624, A11
Janssens S., Abraham R., Brodie J., Forbes D., Romanowsky A. J., van Dokkum P., 2017, ApJ, 839, L17
Kansky J., et al., 2019, PASP, 131, 075005
Karachentsev I. D., et al., 2002, A&A, 383, 125
Karachentsev I. D., Karachentseva V. E., Huchtmeier W. K., Makarov D. I., 2004, AJ, 127, 2031
Karachentsev I. D., et al., 2006, AJ, 131, 1361
Koda J., Yagi M., Yamanoi H., Komiyama Y., 2015, ApJ, 807, L2
Kormendy J., Ho L. C., 2013, ARA&A, 51, 511
Le Borgne D., Rocca-Volmerange B., Prugniel P., Lançon A., Fioc M., Soubiran C., 2004, A&A, 425, 881
Lianou S., Grebel E. K., Koch A., 2010, A&A, 521, A43
Lora V., Sánchez-Salcedo F. J., Raga A. C., Esquivel A., 2009, ApJ, 699, L113
Makarova L., Koleva M., Makarov D., Prugniel P., 2010, MNRAS, 406, 1152
Martini P., Ho L. C., 2004, ApJ, 610, 233
Mayer L., Governato F., Colpi M., Moore B., Quinn T., Wadsley J., Stadel J., Lake G., 2001, ApJ, 547, L123
Mayer L., Mastropietro C., Wadsley J., Stadel J., Moore B., 2006, MNRAS, 369, 1021
Mayer L., Kazantzidis S., Mastropietro C., Wadsley J., 2007, Nature, 445, 738
McConnachie A. W., 2012, AJ, 144, 4
McLaughlin D. E., van der Marel R. P., 2005, ApJS, 161, 304

Mihos J. C., et al., 2015, ApJ, 809, L21

Monelli M., Trujillo I., 2019, ApJ, 880, L11

Muñoz R. P., et al., 2015, ApJ, 813, L15

Navarro J. F., Frenk C. S., White S. D. M., 1997, ApJ, 490, 493

Peñarrubia J., Navarro J. F., McConnachie A. W., 2008, ApJ, 673, 226

Peng C. Y., Ho L. C., Impey C. D., Rix H.-W., 2010, AJ, 139, 2097

Read J. I., Gilmore G., 2005, MNRAS, 356, 107

Ruiz-Lara T., et al., 2018, MNRAS, 478, 2034

Sandage A., Binggeli B., 1984, AJ, 89, 919

Tolstoy E., Hill V., Tosi M., 2009, ARA&A, 47, 371

Tully R. B., Courtois H. M., Sorce J. G., 2016, AJ, 152, 50

Vazdekis A., Sánchez-Blázquez P., Falcón-Barroso J., Cenarro A. J., Beasley M. A., Cardiel N., Gorgas J., Peletier R. F., 2010, MNRAS, 404, 1639

Walker M. G., Mateo M., Olszewski E. W., Peñarrubia J., Evans N. W., Gilmore G., 2009, ApJ, 704, 1274

Weisz D. R., et al., 2011, ApJ, 739, 5

Wittmann C., et al., 2017, MNRAS, 470, 1512

Yagi M., Koda J., Komiyama Y., Yamanoi H., 2016, ApJS, 225, 11

Zaritsky D., Gonzalez A. H., Zabludoff A. I., 2006, ApJ, 638, 725

Zaritsky D., Donnerstein R., Karunakaran A., Barbosa C. E., Dey A., Kadowaki J., Spekkens K., Zhang H., 2021, ApJS, 257, 60

de Rijcke S., Michielsen D., Dejonghe H., Zeilinger W. W., Hau G. K. T., 2005, A&A, 438, 491

van Dokkum P. G., Abraham R., Merritt A., Zhang J., Geha M., Conroy C., 2015, ApJ, 798, L45

van Dokkum P., et al., 2016, ApJ, 828, L6

van Dokkum P., et al., 2019, ApJ, 880, 91

van Zee L., Barton E. J., Skillman E. D., 2004, AJ, 128, 2797

This paper has been typeset from a TEX/LATEX file prepared by the author.

Transforming gas-rich low-mass discy galaxies into ultra-diffuse galaxies by ram pressure

Kirill A. Grishin[1,2*], Igor V. Chilingarian[3,1*], Anton V. Afanasiev[4,5,1*], Daniel Fabricant[3], Ivan Yu. Katkov[6,1], Sean Moran[3], Masafumi Yagi[7]

[1]*Sternberg Astronomical Institute, M.V. Lomonosov Moscow State University, 13 Universitetsky prospect, Moscow, 119992, Russia*
[2]*Department of Physics, M.V. Lomonosov Moscow State University, 1 Vorobyovy Gory, Moscow, 119991, Russia*
[3]*Center for Astrophysics – Harvard and Smithsonian, 60 Garden St. MS09, Cambridge MA 02138, USA*
[4]*Université de Paris, CNRS, Astroparticule et Cosmologie, F-75013 Paris, France*
[5]*LERMA, Observatoire de Paris, PSL Research University, CNRS, F-75014 Paris, France*
[6]*New York University Abu Dhabi, 129188, Saadiyat Island, Abu Dhabi, United Arab Emirates*
[7]*Subaru Telescope, National Astronomical Observatory of Japan, 2-21-1 Osawa, Mitaka, Tokyo 181-8588, Japan*
**These authors contributed equally to this work*

Faint extended elliptically-shaped ultra-diffuse galaxies (UDGs) and slightly brighter and more compact dwarf elliptical (dE) and lenticular (dS0) stellar systems are common in galaxy clusters. Their poorly constrained evolutionary paths can be studied by identifying young UDG and dE analogs populated with bright, massive stars. Using data mining we identified 11 such low-mass ($2 \times 10^8 < M_* < 2 \times 10^9 M_\odot$) galaxies with large half-light radii ($2.0 < r_e < 5$ kpc) and recently quenched star formation in the Coma and Abell 2147 galaxy clusters. All galaxies happen to have ram-pressure-stripped tails with signs of current or recent star formation. Deep spectroscopic observations revealed rotating stellar discs containing 70–95% dark matter by mass. A large fraction of the disc stars (10–60%) formed in intense star bursts 180–970 Myr ago, likely triggered by ram pressure. Observed global gradients of stellar age corroborate this scenario. Passive evolution in the next 10 Gyr will transform 9 of the 11 galaxies into UDGs. If we assume a constant rate of galaxy infall, 44±16 % of the most luminous present-day UDGs in Coma must have formed via ram pressure stripping of discy progenitors.

Main

The first systematic studies of the two nearest galaxy clusters (Virgo and Fornax) three decades ago[1,2] revealed large populations of low-luminosity ($L_B \lesssim 3 \times 10^9 L_\odot$) early-type galaxies, including some very extended examples ($r_e > 5\ kpc$). Recently, dozens[3] and then hundreds[4] of similar extended "ultra-diffuse" galaxies (UDGs) were found in the more distant ($d = 99$ Mpc)[5] and populous Coma cluster and also in galaxy groups[6]. These UDGs include several extreme examples with the size but $<1\%$ of the stellar mass of the Milky Way. Initially some UDGs were thought to be "failed galaxies"[7]: massive dark matter halos that formed few stars following rapid gas loss at an early evolutionary stage. This gas loss could arise from the cluster environment, including ram pressure stripping by hot intracluster gas[8] and tidal interactions[9] or from internal processes such as supernovae (SN) driven winds[10]. Gas loss from a low-mass star-forming galaxy will quench star formation, allowing the galaxy to evolve into a quiescent early-type system. Recent observations[11] and simulations[12,13] suggest that a dwarf galaxy can be puffed up by SN feedback or tidal interactions and transformed into a UDG. It is unclear whether UDGs and dEs belong to the same family[14,15] and share similar evolutionary paths or if they represent different galaxy types with different formation scenarios. In-depth observational studies of UDGs are challenging because their surface brightnesses are significantly below that of the night sky. This fundamental limitation can be overcome by identifying recently quenched low-mass galaxies, still containing young stars, that will passively evolve into dEs or UDGs.

Data mining the multi-wavelength Reference Catalog of Spectral Energy Distribution of galaxies (RCSED[16]) revealed 12 blue but non-starforming galaxies (mean stellar age < 1.5 billion years) with half-light radii r_e between 2.0 kpc and 5.2 kpc. The RCSED galaxies are part of the main galaxy sample from the 7th Data Release of the Sloan Digital Sky Survey[17], and form a nearly complete magnitude-limited sample within the SDSS footprint. Nine galaxies reside in the Coma cluster (Figure 1), two are Abell 2147 cluster ($d = 156$ Mpc) members (Figure 2), and one is a group member. Four of the nine Coma cluster members were previously classified as "blue k+a" post-starburst galaxies (PSGs)[18] based on their integrated-light spectra. However, a recent starburst is needed to properly reproduce the spectra and colours of the remaining galaxies, so they are also PSGs. Two Coma galaxies (GMP 4060 and GMP 2923) are known[19] to exhibit spectacular tails of material stripped by the ram pressure of the hot intracluster medium[8] with Hα emission suggesting current star formation. Their discs, unlike most other galaxies in the the Subaru SuprimeCam Hα survey of the Coma cluster, are not starforming. Young stars are UV-bright and expose a 250 kpc long tail in the most massive galaxy in our sample, GMP 2640[20]. Visual inspection of Subaru HyperSupremeCam images revealed filamentary tails in both Abell 2147 members (Figure 2). Deep broad-band and Hα images of the remaining Coma galaxies also expose faint low-contrast structures near them (Extended Data Figure 3) that are likely the leftovers of ram-pressure-stripped tails significantly dimmed because of stellar evolution.

None of the tails point away from the cluster centre suggesting that these galaxies have orbits with significantly tangential shapes. The galaxies with the brightest tails have the youngest mean stellar ages of the 11 PSGs. The lack of star formation in their discs suggests that they could be classified as "post-jellyfish" galaxies. Similar, but typically more massive "jellyfish" systems[21] have active star formation in their discs and tails[22]. Two similar low-mass quenched PSGs with impressive tails, IC 3418[23] and VCC 1249[24] in the nearby Virgo cluster are believed[23] to have been recently transformed by ram pressure stripping from star forming galaxies into quiescent dwarfs. However, at the Coma cluster distance both galaxies would have fallen below the SDSS magnitude limit. Prior to stripping, ram pressure can compress gas and induce a burst of star formation[25,26], consistent with the PSG classification of our galaxies.

Results

We observed the 11 low-mass PSGs in the Coma and Abell 2147 clusters using the high-throughput multi-object Binospec spectrograph[27] operated at the 6.5-m MMT. GMP 3640 was also observed with the 8 m Gemini-North telescope using the GMOS-N spectrograph. We added five additional galaxies to the sample. These include GMP 3016, the remaining known Coma cluster member with Hα detected in the tail but not in the main disc[19]. GMP 3016 is 0.03 mag below the SDSS magnitude limit and would have been excluded by the original selection criteria. We also included four additional galaxies without SDSS spectra, three fainter UDGs in the Coma cluster with mean stellar ages < 2 Gyr[15] and one photometrically selected faint PSG in Abell 2147.

To assess the current properties of PSGs and predict their evolution, we adopted a simple physically motivated scenario for their star formation histories (SFHs). This scenario includes a period of constant star formation rate (SFR) that started 12 Gyr ago and a more recent ram pressure-induced starburst followed by the shutoff of star formation[28].

We simultaneously fit Binospec spectra and broadband fluxes from the far-ultraviolet ($\lambda = 0.17$ μm) to the near-infrared (λ=4.5 μm) extracted from the same region against a grid of PSG stellar population models using the NBURSTS+PHOT technique[29] (see Extended Data Figures 1–

2). The best-fitting solution yields four parameters: (i) the truncation age (i.e. end of ram pressure stripping); (ii) the fraction of gas consumed from a primordial reservoir before truncation, which is linked to the final stellar metallicity; (iii) the mass fraction of stars born in the final starburst; and (iv) a coefficient for galactic winds. In addition, we obtain radial velocity (V_R) and velocity dispersion of stars (σ). In the primary sample of 11 PSGs, the truncation ages range from 180 Myr to 970 Myr. In 9 of the 11 galaxies the mass fraction of stars born in the ram pressure-induced starburst lies between 10% and 40%. The fraction of consumed gas for all 11 galaxies is higher than 60%, reaching 90–96% in six cases, corresponding to mass-weighted stellar metallicities of $-1.04 \cdots -0.62$ dex. The estimated truncation ages for the seven galaxies with bright tails (including GMP 3016) are younger ($180 \ldots 500$ Myr) than for the remaining five, whose tails faded close to the limit of detectability. Deriving mass-to-light ratios from our best-fitting parameters, we estimate the total stellar masses of our PSGs to be in the range $5.1{\times}10^8 M_\odot$ (GMP 3176) to $2.36{\times}10^9 M_\odot$ (GMP 2640). Therefore, despite their large sizes these are all dwarf galaxies. Truncation age profiles (see Extended Data Figure 4) for most galaxies show weak global gradients across the disc superimposed on radially increasing gradients. The radial gradients are more pronounced for denser and more massive galaxies, e.g. GMP 4348, GMP 2640, GMP 3640. The radially increasing gradients correspond to the outside-in star formation quenching expected from the ram pressure stripping. SN feedback would cause inside-out quenching and produce radially decreasing truncation age profiles. Ram pressure strips the disc gradually from one side to the other (excepting in face-on cases), consistent with the observed truncation age gradients across the disc. The gradients across the disc are preserved for hundreds of Myr because the inner regions of all the galaxies in our sample rotate like a solid body.

Young stars boost the surface brightness and allow us to measure stellar kinematics (V_R and σ) to radii as large as 2.5 r_e (Figure 3), substantially further than for other low-mass galaxies beyond the Local Group. All 11 galaxies from the primary sample have $V_R/\sigma > 1$ in their outer parts suggesting that they are rotationally supported systems; GMP 3016 has a nearly face-on orientation. The absence of observed UDGs with such a pronounced degree of rotational support can be explained by the lack of observations to a comparably large radius and also because the stellar rotation in the inner part of a disc slows down over time due to disc expansion. If we restrict our view of the low-mass PSGs to the $0.5 \ldots 1.0$ r_e typically reached for faint dEs[30] and UDGs[15], only 6 have rotational velocities exceeding 10 km/s.

We fit axisymmetric Jeans anisotropic models[31] to the stellar kinematics and structural properties assuming that each galaxy resides in a spherical dark matter halo. In all cases, the modelling yielded significant dark matter fractions, from 70% to 95% of the total mass within $1\ r_e$, and moderately anisotropic orbits, similar to those of UDGs[15]. However, the data are of far higher quality for the diffuse PSGs. The gravitational potential in these objects is rapidly changed by the removal of a substantial fraction of the gas by ram pressure on a timescale of $30 \ldots 70$ Myr, significantly shorter than typical dynamical times in galaxies ($200 \ldots 350$ Myr). The rapid gravitational potential change transforms quasi-circular stellar orbits to rosette-like[32] orbits even in a massive dark matter halo. The stellar density decreases and its radial profile becomes shallower, the orbital radial anisotropy increases, manifested by a rotational velocity drop in the galaxy central regions. The disc expansion due to slow stellar mass loss during slow passive evolution ($5 \ldots 10$ Gyr) can be neglected when a galaxy has a massive dark matter halo. However, numerical simulations[33] suggest that a dark matter halo will be gradually stripped by tidal interactions with other galaxy cluster members during flybys, which would cause the overall stellar disc expansion by about 25% over 10 Gyr.

Assuming passive evolution, based on best-fitting stellar population parameters and a slow disc expansion, we can predict internal properties (luminosity, surface brightness, luminosity- and mass-weighted stellar metallicities) of our galaxies up-to 10 Gyr from now (Figure 4). The Faber–Jackson[34] relation connecting stellar velocity dispersion to total luminosity and the luminosity–metallicity relation, predict that our low-mass PSGs will settle in the locus of known UDGs (7 Coma galaxies and 2 Abell 2147 galaxies) and dEs/dS0s (2 Coma galaxies) in 3–10 Gyr. The luminosity-weighted stellar metallicity will decrease over time because the contrast of the final ram pressure-induced starburst over an underlying metal-poor population will diminish. Stellar velocity dispersion will also decrease following the expansion of a galaxy. The same 9 "future UDGs" will also settle in the UDG locus in the $\langle \mu_{Rc} \rangle$ - r_e diagram presenting their global structural properties[35].

Implications for evolution of ultra-diffuse galaxies

Because our PSG sample in the Coma cluster is complete and because all galaxies were likely formed via ram pressure stripping, we can estimate the observed UDG fraction formed through this evolutionary channel. We compare the surface brightness evolution of low-mass PSGs to a complete photometric sample of Coma UDGs[36]. The reconstructed SFHs followed by passive evolution and slow stellar disc expansion, allow us to estimate how long each PSG will remain above the SDSS magnitude limit ($m_r < 17.77$ mag) after star formation quenching, and if (or when) its surface brightness drops below the adopted UDG threshold ($\langle \mu_{e,R} \rangle > 24.0$ mag arcsec^{-2}). The

5

ratio of the duration of the UDG phase to the duration of the SDSS spectroscopic phase gives us a statistical estimate of the number of UDGs corresponding to each PSG in our sample. We estimate that in the next 10 Gyr, 7 of the 9 low-mass Coma PSGs (not counting GMP 3016) combined correspond to 19.3±7.0 "future" UDGs with $\langle\mu_{e,R}\rangle > 24.0$ mag. The remaining 2 galaxies will evolve into dEs/dS0s with higher surface brightnesses. To estimate the number of present-day Coma cluster UDGs which could have met the SDSS spectroscopic surface brightness and magnitude selection criteria any time in the past, we need to make an assumption about their SFHs. We bound the possibilities with the extreme assumption of an instantaneous starburst 12 Gyr ago represented by a simple stellar population. This produces 90 UDGs, with 21±7% formed via ram pressure stripping. If we assume a scenario suggested by our PSGs but that occurred 10 Gyr ago, constant star formation and a final starburst that formed 30% of the stellar mass, we end up with 44 UDGs and a fraction of 44±16 % formed by ram pressure stripping (see Extended Data Figure 5).

All nine low-mass Coma PSGs have high peculiar radial velocities ($500\ldots2000$ km/s) and move on non-radial orbits like many jellyfish galaxies[37]. Their positions in the $\Delta v_r - d_{\rm proj}$ caustic diagram of the Coma cluster are consistent with the hypothesis that they have entered the inner part of the cluster for the first time. They have never crossed the dense cluster centre and are unlikely to ever do so, allowing them to survive for an extended period in a dense cluster environment. Observations[38] and simulations[13,39] confirm that ram pressure efficiently strips galaxies on tangential orbits, but the longer stripping timescales increase the efficiency of star formation triggered by ram pressure-induced gas compression[40]. During such a starburst a galaxy may reach its maximum lifetime surface brightness. GMP 4188, GMP 4118, and J160215.29+160904.3 are examples of systems on non-radial orbits with lower stellar mass and therefore low surface brightness, which barely made it into the SDSS.

For a galaxy infalling on a radial orbit, the ram pressure-induced starburst produces fewer stars due to rapid gas removal, and the stripped tail will be longer, fainter and harder to detect. Qualitatively, we can assume that for a galaxy infalling towards the cluster centre, the ram pressure becomes sufficient to ignite a starburst when it reaches some critical pressure value (P_{SB}); and then when it reaches $P_S = P_{SB} + \Delta P; \Delta P \ll P_{SB}$, the galaxy is stripped completely. The mass of stars formed should depend on the time needed to gain ΔP. ΔP will be gained much faster if a galaxy approaches the cluster core on a purely radial orbit with a pericentral distance close to zero than if it approaches on an orbit with a similar eccentricity ($e \sim 1$) but with a larger pericentral distance just sufficient to strip the galaxy completely. In the former case, the radial density gradient and the radial component of the orbital velocity $v_{r,\mathrm{orb}}$ work together because $P \propto \rho v_{\mathrm{orb}}^2$ and $v_{\mathrm{orb}} \approx v_{r,\mathrm{orb}}$. The large fraction of rapidly removed gas would also strongly increase the orbital anisotropy and decrease the observed stellar rotational velocity. The galaxies on radial orbits will fade and evolve into the UDG regime more quickly, but their low surface brightnesses will reduce their chances of inclusion in the SDSS spectroscopic sample anytime during their lifetime. Fainter and smaller GMP 3016, GMP 2673, GMP 2662[15], and J160231.45+155749.9 illustrate such a fainter continuation of the UDG evolutionary sequence. Such galaxies will also be harder to distinguish from those formed via different proposed UDG formation channels, which often produce non-rotating spheroidal stellar systems[7].

Were the late-type UDG progenitors normal-sized dwarf galaxies prior to falling onto the cluster that expanded due to ram pressure stripping? Or were they pre-processed by tidal interactions and supernovae feedback that had puffed them up first, followed by ram pressure stripping that quenched them without increasing their size? Simulations[32] suggest that a stellar disc of a low-mass gas-rich (gas fraction 70%) galaxy sitting in a $M_{200} = 10^{11} M_\odot$ dark matter halo (slightly more massive than our PSGs) would expand by a factor of $\sim$1.5 due to ram pressure stripping alone while the stellar mass loss would remain negligible. On the other hand, the "Little Things" survey[41] of local dwarf late-type galaxies includes 9 of 37 objects with regular kinematics having $r_e > 1$ kpc, high gas fractions, and dark halo masses in the range of $10^{10.2} \ldots 10^{10.7} M_\odot$[42]. If they fell onto a cluster, they would first become brighter because of the ram pressure induced starburst, but later, when stripped, would expand to $r_e = 1.5 \ldots 5$ kpc and fade as a result of passive evolution, finally ending up in the UDG locus of the $\langle \mu_e \rangle - r_e$ diagram as shown by red tracks for the two examples in Fig. 4. Their largely undisturbed morphology and kinematics along with sparse environment suggest that they are "normal" low-mass discs, which did not undergo significant pre-processing, hence, corroborating the scenario that ram pressure stripping alone can transform many dwarf spiral and irregular galaxies into UDGs by causing both quenching and disc expansion. Because the radial distribution of neutral gas in gas-rich dwarfs is usually much shallower than stellar density profiles[41], the ram pressure induced star formation could further grow r_e by stronger stellar surface density increase in the outer parts of the disc compared to the inner regions. A search in RCSED for low-mass ($M_* < 3 \times 10^9 M_\odot$) extended ($r_e > 2$ kpc) star-forming galaxies within 5 Mpc from the Coma cluster centre reveals about 50 objects with the morphologies resembling those of "Little Things" dwarfs, which might become the progenitors of a new generation of PSGs and then UDGs, should they fall onto the Coma cluster core in the future.

Our observations of recently ram-pressure stripped low-mass disc galaxies suggest: (i) that ram pressure stripping is a viable channel of UDG formation and that UDGs formed via this channel *de facto* extend the corresponding dE/dS0 sub-class to lower surface brightnesses and larger sizes; (ii) that ram pressure stripping is responsible for a substantial fraction of large rotating UDGs in galaxy clusters including extreme objects like DF 44[43] and also higher surface brightness, spatially extended, dwarf early-type galaxies; (iii) that ram pressure stripping affects not only morphological appearance but also stellar dynamics by increasing the stellar disc orbital anisotropy; and (iv) that the tangential orbits of UDG progenitors at large pericentral distances lead to higher ram pressure-induced star formation efficiencies, and higher stellar masses and surface densities.

Acknowledgements KG, IC, AA, IK acknowledge the Russian Science Foundation (RScF) grants No. 19-12-00281 for supporting the search of UDG progenitors and data analysis of a multi-wavelength spectrophotometric dataset, and No. 17-72-20119 for supporting the development of stellar population models used in the data analysis; and the Interdisciplinary Scientific and Educational School of Moscow University "Fundamental and Applied Space Research". KG acknowledges the support from the Foundation of development of theoretical physics and mathematics "Basis". IC's research is supported by the Telescope Data Center at Smithsonian Astrophysical Observatory. We thank D. Eisenstein, F. Combes, G. Mamon, and O. Sil'chenko for fruitful discussions related to this project. We are grateful to the staff of the MMT Observatory jointly operated by Smithsonian Astrophysical Observatory and the University of Arizona for their support of Binospec operations and service mode observations. This study is based in part on data collected at Subaru Telescope and retrieved from the SuprimeCam and Hyper-SuprimeCam data archive system, which is operated by Subaru Telescope and Astronomy Data Center at National Astronomical Observatory of Japan and on observations obtained at the international Gemini Observatory (proposal GN-2017A-FT-22), a program of NSFs NOIRLab, which is managed by the Association of Universities for Research in Astronomy (AURA) under a cooperative agreement with the National Science Foundation on behalf of the Gemini Observatory partnership: the National Science Foundation (United States), National Research Council (Canada), Agencia Nacional de Investigación y Desarrollo (Chile), Ministerio de Ciencia, Tecnología e Innovación (Argentina), Ministério da Ciência, Tecnologia, Inovações e Comunicações (Brazil), and Korea Astronomy and Space Science Institute (Republic of Korea).

Competing Interests The authors declare that they have no competing financial interests.

Author Contributions K.G. computed stellar population models, prepared Binospec observations, analyzed Binospec data and wrote the manuscript; I.C. formulated PSG search criteria and discovered the galaxies in the RCSED catalog, reduced Binospec data, modified the full spectrum fitting code to analyze them and wrote the manuscript; A.A. performed surface photometry, performed dynamical modelling and wrote the manuscript; D.F. led the development of the Binospec spectrograph and proposed the observational strategy; I.K. jointly with I.C. developed the spectrophotometric fitting code NBURSTS+PHOT and validated the spectroscopic data analysis; S.M. supported preparation and execution of observations; M.Y. provided cutouts of deep Subaru images and did the reduction of archival Subaru data for Abell 2147; I.C., D.F., and S.M. performed Binospec observations during the commissioning and science verification of the instrument; all authors discussed the manuscript.

Correspondence Correspondence and requests for materials should be addressed to Igor Chilingarian (email: igor.chilingarian@cfa.harvard.edu; chil@sai.msu.ru) and Kirill Grishin (email: grishin@voxastro.org).

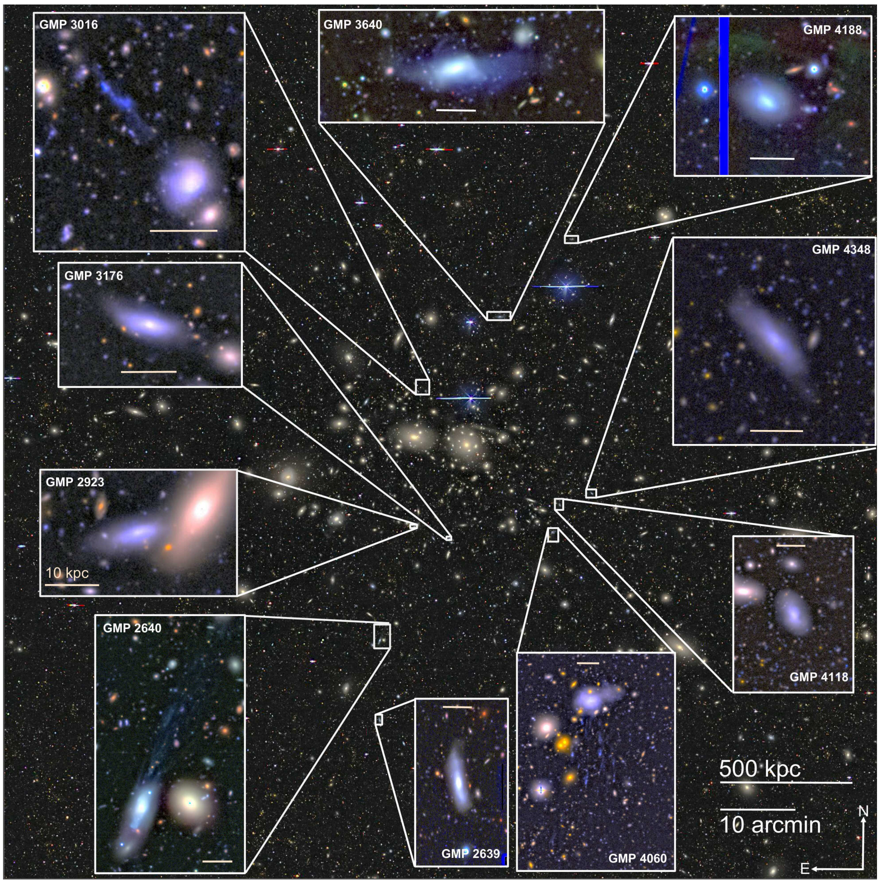

Figure 1: Positions of Coma cluster members selected from RCSED and one additional galaxy, GMP 3016. The insets showing zoomed-in galaxy images were constructed from Subaru and CFHT optical data in the $u*$, B, V and R bands. A scale bar corresponding to 10 kpc is shown inside each inset. In GMP 2640 the image reveals a blue clump of recently formed stars south-east of the centre which was masked for dynamical modelling purposes.

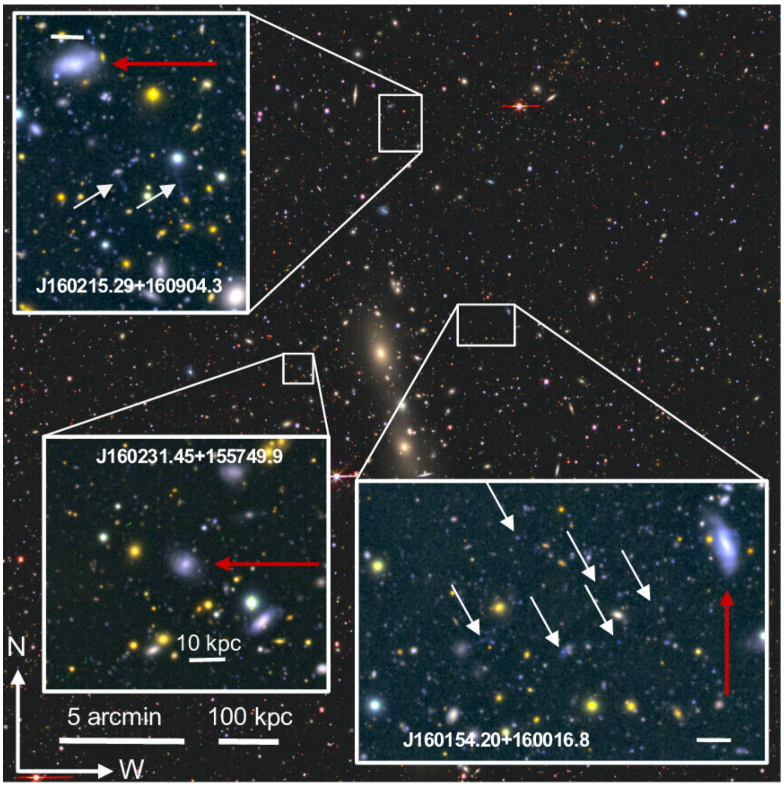

Figure 2: Positions of the two Abell 2147 cluster members selected from RCSED and an additional photometrically selected PSG, J160231.45+155749.9. The insets showing zoomed-in images for individual galaxies (marked by red arrows) are constructed from g, r, and i broadband HSC images. The two galaxies from the main sample exhibit tails of stripped material. We mark the positions of clumps in the tails with white arrows.

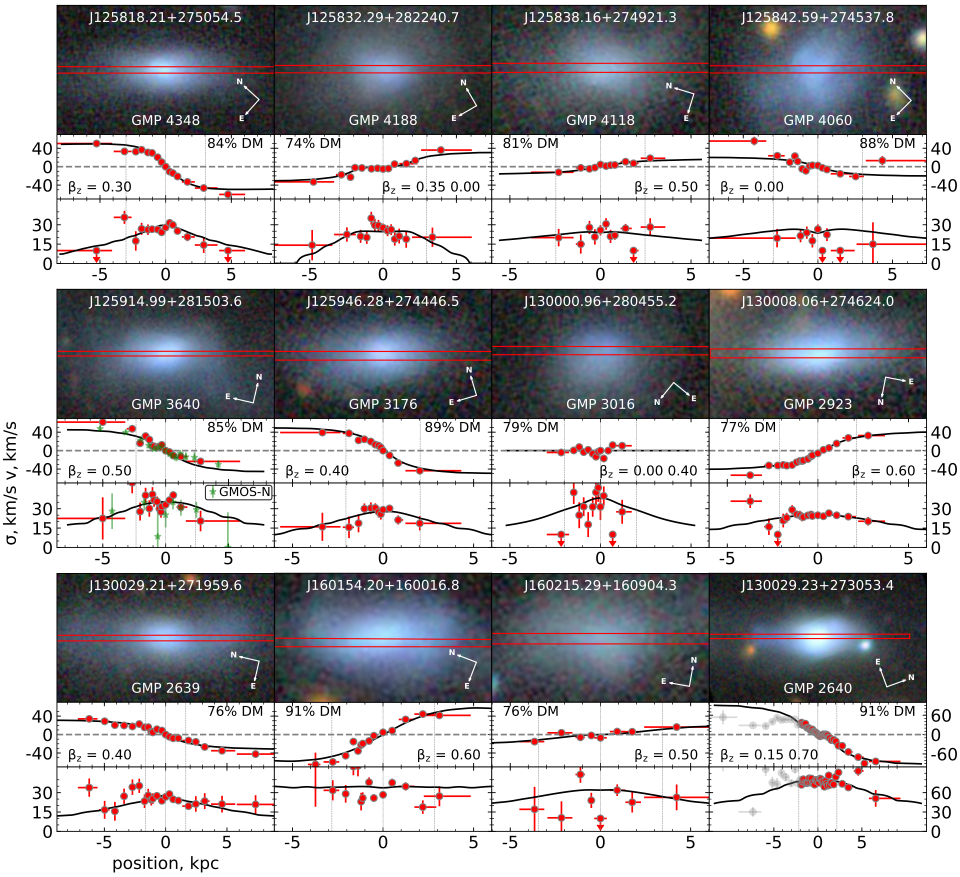

Figure 3: Top panel for each galaxy: an optical colour image with an over-plotted slit position; middle panel: stellar radial velocity v; bottom panel: stellar velocity dispersion σ. Black lines show the best-fitting Jeans models for stellar kinematics. The estimated dark matter contribution within $1r_e$ (indicated by vertical dashed lines) and the anisotropy parameter β_z are shown in the upper and lower corners of each v panel. For 8 out of 9 galaxies σ and v profiles are shown in the same scale. For the most massive galaxy, GMP 2640 the scale of these profiles is decreased. This galaxy also has a clump of young stars whose dynamics cannot be explained in the framework of axisymmetric modelling – the data points corresponding to this clump are greyed out.

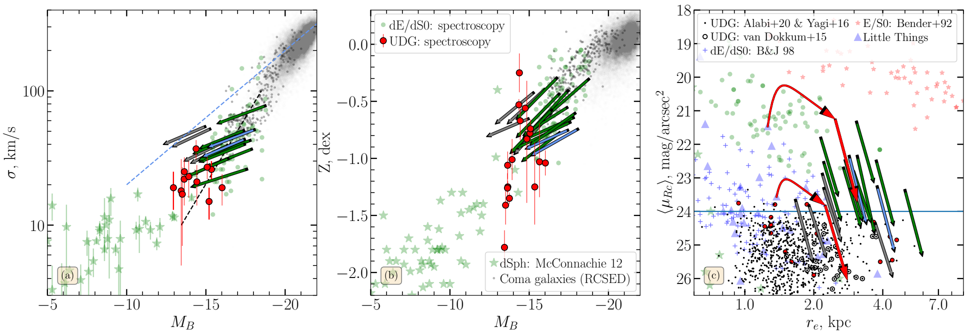

Figure 4: Predicted passive evolution of low-mass PSGs from their SFHs during the next 10 Gyr on the Faber–Jackson $\sigma - M_B$ (panel (a)), metallicity–luminosity $[\mathrm{Fe/H}] - \mathrm{M_B}$ (panel (b)) and mean surface brightness – effective radius $\langle \mu_{Rc} \rangle$ - r_e (panel (c)) relations. We show our primary targets from the Coma and Abell 2147 clusters and additional PSGs galaxies not included in the statistical calculations by green, cyan and grey arrows respectively. Each arrow starts at the currently observed position of a galaxy and points to its expected location in 10 Gyr. On the Faber–Jackson relation we show the $L \sim \sigma^4$ and the $L \sim \sigma^{2.5}$ best-fitting linear correlations[44] for giant and dwarf galaxies. A cyan solid line in the right panel at $\langle \mu_{Rc} \rangle = 24.0$ mag/arcsec^2 denotes the UDG surface brightness cut. All PSGs but two will move into the UDG locus in the next 10 Gyr. The two remaining galaxies, GMP 2640 and GMP 2923 will settle in dE region. The literature sample includes dEs[30,45,46], photometric[36,47,48] and spectroscopic[11,15,49–51] samples of UDGs, Local Group dwarf spheroidal galaxies[52], Local Volume dwarf late-type galaxies from *Little Things*[41], a sample of giant early-type galaxies[53] complemented by a selection of Coma cluster early-type galaxies (grey dots) and elliptical galaxies at $z < 0.2$ (grey shaded region) from RCSED. In panel (c), the red tracks display evolutionary models of the two *Little Things* objects, NGC 4214 and DDO 168 if they were ram pressure stripped: (i) a ram pressure induced starburst and disc expansion (curved tracks) followed by (ii) slow passive evolution (straight tracks).

Table 1: Internal dynamics, and dark matter contents of diffuse post-starburst galaxies.

No.	Name	RA	Dec	v_r	σ_*	DM($< r_e$)	β_z	$\log \rho_0$	r_s	M_{200}	R_{200}
		deg	deg	km/s	km/s	%		$M_\odot$kpc^{-3}	kpc	$10^8 M_\odot$	kpc
1	GMP 4348	194.57587	27.84848	7524±1	51±2	85±8	0.3	-0.5	1.2	213	57.8
2	GMP 3176	194.94282	27.74625	9690±2	46±4	88±5	0.4	-0.5	1.0	123	48.2
3	GMP 2639	195.12170	27.33322	8449±1	43±2	84±3	0.4	-0.8	1.0	56	37.2
4	GMP 4118	194.65901	27.82258	5350±3	33±7	80±10	0.5	-1.2	1.5	66	39.6
5	GMP 4060	194.67746	27.76050	8683±1	26±2	87±15	0.0	-1.2	2.0	141	60.4
6	GMP 2923	195.03358	27.77332	8665±1	40±1	69±9	0.6	-1.0	1.5	112	47.1
7	GMP 2640	195.12180	27.51484	7304±1	78±2	90±4	0.7	-0.4	2.2	1445	181.4
8	GMP 3640	194.81245	28.25101	7446±1	37±2	87±10	0.5	-0.8	1.5	186	56.1
9	GMP 4188	194.63453	28.37797	5863±1	41±2	80±9	0.4	-1.5	2.1	195	54.3
10	J160154.20+160016.8	240.47583	16.00467	11506±1	52±2	96±2	0.6	-0.8	2.0	407	85.3
11	J160215.29+160904.3	240.56369	16.15119	12478±2	44±5	95±19	0.5	-1.0	1.2	58	37.6
Additional sample											
12	GMP 3016	195.00431	28.08188	7702±2	31±5	83±7	0.6	n/a	n/a	n/a	n/a
13	GMP 2673	195.10945	27.45978	6915±4	41±8	82±6	0.8	n/a	n/a	n/a	n/a
14	GMP 2552	195.16098	27.47647	7885±3	52±5	96±1	0.0	n/a	n/a	n/a	n/a
15	J160231.45+155749.9	240.63104	15.96387	11270±5	39±12	87±15	0.0	n/a	n/a	n/a	n/a
16	GMP 2662	195.11375	27.43855	7360±6	54±12	94±2	0.6	n/a	n/a	n/a	n/a

GMP[54] designations for Coma cluster galaxies and IAU-style names for Abell 2147 members (Name). Positions on the sky (RA, Dec), radial velocities (v_r) and stellar velocity dispersions (σ_*) obtained from the full spectrum fitting. Dynamical parameters: dark matter contribution to total mass within r_e (DM),the orbital anisotropy parameter (β_z), logarithm of the central density ($\log \rho_0$) and radial scale (r_s) of the dark matter halo (for the main galaxy sample), dark matter halo mass (M_{200}) inside R_{200}, radius (R_{200}), where the dark matter density reaches the value 200 times greater than the critical density.

Table 2: Structural properties, Stellar population parameters and stellar masses derived from the Binospec spectra and SED modelling of diffuse post-starburst galaxies.

No.	M_{Rc}	$\langle\mu_{Rc}\rangle$	r_e	$t_{\rm trunc}$	Starburst fraction	Gas fraction	λ	$[Z/H]_L$	$[\alpha/Fe]_L$	$[Z/H]_M$	$[\alpha/Fe]_M$	$(M/L)_{Rc}$	M^*
	mag	mag/arcsec^2	kpc	Myr	%	%		dex	dex	dex	dex		$10^8 M_\odot$
1	-18.21	22.45	2.73	825.6±3.0	40±2	98±1	3.7	-0.55±0.01	0.09±0.02	-0.74±0.01	0.09±0.01	0.45±0.02	6.0
2	-17.75	22.51	2.21	233.5±1.2	10±1	99±2	1.5	-0.07±0.04	0.06±0.06	-0.43±0.02	0.07±0.03	0.59±0.01	5.1
3	-18.69	23.34	4.99	779.3±5.5	60±1	83±1	1.5	-0.45±0.01	0.10±0.02	-0.58±0.01	0.09±0.01	0.39±0.01	7.9
4	-17.88	22.79	2.98	563.8±5.8	10±1	99±1	5.1	-0.58±0.05	0.07±0.07	-0.83±0.03	0.09±0.04	0.59±0.01	5.8
5	-18.43	22.32	3.09	413.4±2.7	40±2	47±1	1.5	-0.64±0.01	0.05±0.01	-0.83±0.01	0.06±0.01	0.35±0.01	5.8
6	-18.33	21.78	2.14	182.8±1.1	10±1	96±8	1.5	-0.04±0.06	0.05±0.09	-0.43±0.03	0.07±0.04	0.54±0.02	8.0
7	-19.59	21.31	3.06	351.3±0.5	20±1	98±2	2.5	-0.28±0.03	0.06±0.04	-0.58±0.02	0.07±0.02	0.50±0.02	23.6
8	-18.68	22.47	3.74	517.8±3.7	30±4	98±1	3.7	-0.57±0.02	0.07±0.02	-0.80±0.01	0.08±0.02	0.45±0.03	9.2
9	-18.06	22.68	2.69	400.1±4.9	10±1	55±1	2.5	-0.72±0.02	0.06±0.02	-0.93±0.01	0.09±0.02	0.53±0.01	6.1
10	-18.81	22.33	2.85	498.9±9.9	30±2	98±1	5.1	-0.64±0.01	0.06±0.01	-0.87±0.01	0.07±0.01	0.41±0.01	9.4
11	-18.54	23.23	3.77	969.9±10.9	60±38	78±3	1.5	-0.43±0.12	0.11±0.18	-0.56±0.04	0.10±0.07	0.41±0.21	7.4
Additional sample													
12	-17.34	22.86	2.17	264.7±3.8	10±1	96±2	5.1	-0.53±0.02	0.06±0.03	-0.84±0.01	0.08±0.02	0.51±0.01	3.1
13	-17.04	24.33	3.70	327.2±3.1	5±2	91±1	1.5	-0.25±0.02	0.06±0.03	-0.51±0.01	0.08±0.02	0.69±0.01	3.1
14	-16.13	23.80	1.90	786.7±4.5	20±4	99±1	1.5	-0.22±0.03	0.08±0.04	-0.44±0.01	0.08±0.01	0.64±0.05	1.3
15	-17.25	23.29	2.20	245.8±3.7	5±1	99±1	5.1	-0.51±0.02	0.06±0.03	-0.82±0.01	0.09±0.01	0.59±0.02	3.2
16	-15.74	23.63	1.66	230.0±5.1	10±3	96±8	5.1	-0.51±0.01	0.06±0.01	-0.83±0.01	0.08±0.01	0.50±0.02	0.7

Galaxy number corresponding to the Table 1. Structural parameters: absolute magnitude, mean surface brightness in the Rc band within the effective radius and effective radii ($\langle\mu_{Rc}\rangle, r_e$). Stellar population parameters from the full spectrum fitting: age of truncation ($t_{\rm trunc}$), fraction of stellar mass formed in the final ram-pressure-induced starburst (SB fraction), fraction of gas consumed into stars prior to ram-pressure stripping (Gas fraction), linear coefficient for galactic winds (λ). Parameters computed from the stellar population models: luminosity-weighted metallicities ($[Z/H]_L$), α-enhancements ($[\alpha/Fe]_L$) and their mass weighted equivalents ($[Z/H]_M$, $[\alpha/Fe]_M$)

Methods

PSG selection criteria. We select blue extended PSGs from the RCSED[16] database by applying two sets of selection criteria. One of them has a stricter stellar age limit, and another one limits the integrated $g - r$ colour with slightly more relaxed stellar age restriction. This allows us to minimize the loss of possible objects of interest because of the age-metallicity degeneracy that affects the results of the full spectrum fitting of a large galaxy sample using simple stellar population models: the reported overestimated intermediate stellar age (2–3 Gyr) is compensated by the underestimated stellar metallicity, and this degeneracy can be resolved by using broad-band colours. The first set of selection criteria includes:

- $F_{H\alpha}/\Delta F_{H\alpha} < 5$ AND $F_{\mathrm{[OIII]}} < 2 \times 10^{-16} erg/cm^2/s$ to select galaxies without prominent emission lines.
- Mean stellar populations younger than 1 Gyr. If a spectrum of a galaxy has low signal-to-noise ratio (SNR), its age may shift to the higher values with lower values of metallicity due to age-metallicity degeneracy. To take into account this fact we supplemented our criteria by joining with boolean OR a metallicity condition: $\mathrm{[Z/H]} < -1.3$ dex.
- Galaxies with spectral SNR > 4 reported by SDSS, which is typically underestimated by 30–35%. This criterion rejects spectra with unreliable signal.
- There is no template mismatch, $\chi^2_{\mathrm{ssp}} < 1$
- We select extended objects by setting the difference between 3-arcsec fiber magnitude and integral magnitude greater than 0.5 mag in the r band. This criterion selects galaxies with $r_e > 1.5 kpc$ at the Coma cluster distance.
- Blue integrated colour $g - r < 0.55$ mag
- Low redshift $0.015 < z < 0.06$

This set of criteria returned 7 objects. After visual inspection we rejected one with unreliable $H\alpha$ flux measurements and another one with unreliable integrated photometry in SDSS DR7 bringing its $g - r$ colour below 0.55 mag, when in Dark Energy Camera Legacy Survey (DECaLS[55]) it has $g - r = 0.61$ mag. Finally this filter yielded 5 galaxies.

The second filter includes the following conditions:

- $\mathrm{F_{H\alpha}/\Delta F_{H\alpha}} < 10$ AND $F_{H\alpha} < 2.5\times10^{-16} erg/cm^2/s$ AND $F_{[\mathrm{OIII}]} < 2.0\times10^{-16} erg/cm^2/s$
- Mean stellar populations younger than 2 Gyr.
- $\chi^2_{ssp} < 1$
- Difference between 3-arcsec fiber magnitude and integral magnitude greater than 0.5 mag in the r band.
- Blue integrated colour $g - r < 0.4$ mag
- Low redshift $0.015 < z < 0.06$

These criteria select 10 galaxies. We rejected one object that is apparently interacting with a companion and has incorrect photometric measurements in the SDSS/RCSED, leaving 9 galaxies.

We joined the lists of galaxies selected using both sets of criteria. The two lists have two objects in common, leaving 12 galaxies. All belong to the SDSS main galaxy sample so that these 12 galaxies form a nearly complete magnitude limited sample within the SDSS DR7 footprint. Ten galaxies are Coma cluster members, 2 galaxies are Abell 2147 cluster members, and the remaining galaxy is a group member[5]. In this study we consider only 11 cluster galaxies, because the remaining object does not possess deep high-quality optical imaging data that can be used to assess its structural properties.

We selected additional candidate PSGs without SDSS spectroscopic confirmation as blue 5σ outliers towards fainter near-UV magnitudes from the universal three-dimensional ultraviolet–optical colour–colour–magnitude relation for non-active galaxies[56] with sizes corresponding to $r_e > 1.5$ kpc at the distance of their host cluster (Coma or Abell 2147). This selection returned 5 objects in Coma and 2 in Abell 2147. We placed three Coma and one Abell 2147 candidates in the Binospec slitmasks and all were spectroscopically confirmed as PSGs without current star formation and members of their host clusters.

Spectroscopic observations and data reduction. We obtained spectroscopic observations of 11 PSGs using the 6.5-m MMT. We obtained long-slit spectroscopy for each galaxy with the Binospec[27] multi-object spectrograph and reduced the data using the Binospec data reduction pipeline[57] optimized for extended low-surface brightness objects. Small angular distances between galaxies allow us to observe 2–3 galaxies simultaneously with the same slit mask. For nine galaxies in Coma cluster we designed 4 masks: “Coma 1” (GMP 2640, GMP 2639), “Coma 3” (GMP 4348, GMP 4118, GMP 4060), “Coma A” (GMP 2923, GMP 3176) and “Coma B”

(GMP 4188, GMP 3640). “Coma 1” was observed in two runs: (i) December 14, 2017, during the instrument commissioning and (ii) April 10, 2018. To increase S/N both datasets were combined into one. “Coma 3” was observed on April 7, 2018. “Coma A” was observed in two consecutive nights: 4th and 5th of June 2018 with mean seeing of 1 arcsec. “Coma B” was observed on 8th of June 2018 with 1 arcsec seeing. Both galaxies in Abell 2147 were placed on one “A2147” mask which was observed on the 14th of June 2018. GMP 3016 was observed on 29th of January 2020 as a filler target for another Binospec program. In all runs we used the 1000 line mm^{-1} grating with a 1 arcsec-wide slitlets with the central wavelength of 4400–4500 Å that yielded the overall wavelength coverage of 3760 Å to 5300 Å. This configuration provides an instrumental resolution of $\sigma_{\text{inst}} \sim 26 \ldots 34$ km/s. The total exposure time was 2h 20min for the “Coma 1” mask and 2h for all remaining masks.

We also added optically selected galaxies and UDGs as filler targets to each mask. Spectra of UDGs obtained with these masks were used for dynamical modelling and dark matter contribution estimate[15]. After the analysis of all dwarf galaxy spectra, we created an additional sample that comprised of five galaxies: 3 filler galaxies in Coma cluster and one in A2147 that met our post-starburst selection criteria. The fifth galaxy, GMP 3016, is the only galaxy from study[19] without detected emission inside its 27 mag isophote in the deep R-band Subaru imaging. There is no SDSS spectrum for this galaxy, because its total magnitude is 0.03 mag below the magnitude limit of the SDSS spectroscopic selection. These galaxies have low stellar masses and surface brightnesses and are not included in SDSS spectroscopic sample.

After the reduction of all spectroscopic data using the Binospec data reduction pipeline[57] we obtained sky subtracted, flux calibrated, wavelength calibrated two-dimensional images with error frames for each slitlet. For the sky subtraction we used a global sky model implemented in the pipeline.

Additionally, we observed GMP 3640 using the GMOS-N spectrograph operated at the 8 m Gemini-North telescope on the 24th and 25th of June of 2017 (fast turnaround program *N2017-FT-22*) with the median image quality of 0.7 and 0.9 arcsec for these two nights respectively. We used the B 1200 grating and a 0.75 arcsec slit with the wavelength setup centered at 4500 Å that yields the spectral resolution $\sigma_{\text{inst}} \sim 45$ km/s. The total exposure time was 3h 25min. We reduced the data using our own data reduction pipeline for GMOS data.

Stellar population properties. For all PSGs we simultaneously fit optical spectra and broadband magnitudes. We take ultraviolet fluxes from the catalogs based on deep (23 ksec in near-UV and 18 ksec in far-UV) GALEX imaging data. Mid-infrared magnitudes were obtained by applying

Sextractor[58] to Spitzer IRAC frames available from the Spitzer Heritage Archive combined into super mosaics. Optical broadband fluxes were generally taken from SDSS[17] and DECaLS surveys. We use deep CFHT observations in the u^* band instead of shallow data in SDSS u. We take near-IR magnitudes from UKIDSS LAS DR10 data and CFHT K and J where available. We apply foreground extinction correction and K-correction[59] to all magnitudes.

We use a 4-dimensional MILES-based (for spectra) and PEGASE.2-based (for broad-band SEDs) grid of stellar population models[28] computed for the Kroupa IMF[60] to perform stellar population analysis. We treat the chemical evolution of the stellar population self-consistently using an analytic formulation[61] of the "leaky box" model[62–64]. This model allows a fraction of heavy elements produced in stars to escape via galactic winds with the rate proportional to the current SFR[65,66]. We model the evolution of iron and α-elements separately, accounting for the delayed contribution from SN Ia explosions[67]. We use spatially co-added spectra in one r_e to maximize S/N of optical spectra . As galaxy rotation may smooth spectral details, we correct spectra for the radial velocity profile. We minimize a linear combination of χ^2 values for spectrum and SED with the weight of χ^2_{SED} varying between 0.4 and 0.6 for different galaxies against the two parameters: truncation age and fraction of consumed gas. During this procedure we model observed spectra as a template convolved with the Gaussian LOSVD and multiplied by a polynomial continuum with degree from 9 to 15. Because the spectral resolution of MILES-based models is lower than that of Binospec spectra, we convolve the data with a Gaussian to match the resolution of stellar population models. Then we scan the grid of two remaining parameters: fraction of stellar mass born in the final starburst and galactic winds coefficient λ. We obtain uncertainties for the first two parameters from the covariance matrix resulting from the minimization procedure. For the two remaining parameters we estimate the uncertainties by approximating the χ^2 profile near the minimum by a quadratic function. We provide formal statistical uncertainties in Tables 1–2, but for our galaxies with high SNRs, the systematic errors that originate from the choice of input spectral and SED templates are much higher than statistical ones (10–15% on truncation age and $\sim$0.1 dex on metallicity and α-enhancement). We compare luminosity weighted metallicities computed for the SFHs with the parameters derived from our modelling with the values obtained in other studies in the 3-rd panel of Fig. 4. For this comparison we only use spectroscopic measurements of stellar populations from the literature done using different forms of the full spectrum fitting of intermediate- and high-resolution spectra and exclude those based on SED fitting[68] or line-strength indices[69] and also obtained through excessively wide slits hence reducing the spectral resolution[70]. We also excluded spectroscopic measurements of NGC1052-DF2[71] from our analysis despite on good quality of data and reliable measurements, because distance to this galaxy remains a matter of debate[72,73].

Stellar kinematics. We use the NBURSTS[74] full spectrum fitting technique to measure radial velocity and velocity dispersion profiles. We use adaptive binning along the slit to reach sufficient signal-to-noise ratio to reliably measure internal kinematics (7–10 per pixel depending on the object). We use PEGASE.HR-based models[28] that implement PSG SFHs with self-consistent evolution of stellar metallicity. These models are similar to those used for the stellar population analysis but do not include α-element enhancements. The spectral resolution (R∼10000) of the model exceeds Binospec's (R∼4000) making it possible to measure velocity dispersion down to 10 km/s[75]. All galaxies from the main sample exhibit some sort of regular rotation within r_e. GMP 4060, GMP 2640 and GMP 4188 have noticeable kinematical disturbances localised in the area of significant morphological irregularities. Detailed analysis of high-resolution HST images for the brightest galaxy in our sample, GMP 2640, revealed a large number of luminous star clusters in its central part whose asymmetric distributions on the sides of the slit causes the non-uniform slit illumination and, hence, affects the radial velocity measurements. Disturbances of kinematics profiles of GMP 4060 and GMP 4188 are also of the same origin. We notice that some simulations suggest that the ram pressure stripping by itself can lead to the displacement of the dark matter cusp in a low-mass galaxy[76], which will cause a slight lopsidedness a galaxy with a stellar mass close to the lower end of what we sample in our study.

Structural parameters and deep Subaru images. For Coma cluster galaxies we use deep Rc-band Subaru Suprime-Cam[77] images (1470 – 7980 s exposure time) to determine structural parameters. For Abell 2147 only raw archival Subaru Hyper Supreme-Cam[78] images are available, so we reduced and co-added them. Using GALFIT[79] we model each galaxy with a double Sérsic profile convolved with the point-spread-function (PSF) obtained from Gaussian fits to non-saturated stars. We use uncertainty frames obtained from reduced, sky subtracted Subaru images for the fitting procedure, adding sky background as a constant value obtained from the sky variation analysis. We derive the deprojected effective radius for each galaxy as follows. We construct the deprojected image of the galaxy using the Sérsic components from the fit results, changing the axis ratio to 1. We then measure the radius enclosing exactly half the total flux of the deprojected image.

We also inspected Subaru Suprime-Cam B-band, V-band, Rc-band, and Hα images downloaded from the Japanese Virtual Observatory. Rc-band images of GMP 3176 revealed a filamentary structure 70 kpc to the west from the galaxy main body. Another galaxy, GMP 3640 has three bright filaments, emerging from its main body. Several galaxies show clumps or other irregularities in their central parts. GMP 4060 and GMP 3640 exhibit the most noticeable disturbances. However, they are substantially less significant in the Rc band compared to the bluer bands (V and B) and, therefore, they are likely caused by different stellar population properties (i.e. younger stellar age) rather than variations in the stellar mass density which would significantly affect the gravitational potential. For Abell 2147 we retrieved raw Hyper Supreme-Cam data in the g, r, and i bands with the total exposure times of 3720, 240, and 2160 sec correspondingly from the Subaru archive and reduced them using the Hyper Suprime-Cam pipeline. In g-band images both Abell 2147 galaxies reveal faint tails with a complex filametary structure reaching 70 kpc in length. Both these tails point roughly towards the cluster centre. The brightest filaments of these tails are also detected in the r and i bands.

Dynamical modelling. We base our dynamical modelling algorithm on the JAM routine[31] which has been used extensively to model galactic kinematics in nearby and intermediate-redshift galaxies. It solves the Jeans[80] equations assuming axial symmetry. For each galaxy we construct a suite of dynamical models that correspond to different parameter values. We use a customised version of this code, which allows us to handle a dark matter halo separately from the stars. The main steps are as follows: (i) We use GALFIT to fit the R-band Subaru image of each galaxy using a two-component Sérsic model. (ii) The model image of a galaxy is converted into multiple two-dimensional Gaussians (6–10 per galaxy). The same procedure is applied to a spherical Burkert[81] dark matter density profile, and then the two Gaussian sets are co-added to construct a model of the gravitational potential. The dark matter density profile is truncated at R_{200} to prevent the divergence of the multiple Gaussian expansion procedure. (iii) A set of Gaussians is then supplied to the modelling routine that computes the radial velocity and velocity dispersion profiles convolved with the PSF from observations for a grid of parameter values. We then scan χ^2 values evaluated for each model to find the best values of following parameters: the dark matter central density ρ_0, halo scale radius r_s and stellar vertical anisotropy β_z. We also allow the inclination i to vary between $\arccos(b/a)$ and $90\,\mathrm{deg}$. The stellar mass-to-light ratio M/L_* is fixed to the best-fitting value from the stellar population analysis. We compute grids of dynamical models with the following steps: 0.1 for β_z, 0.25 for $\log \rho_0$, 0.2 kpc for r_s, and 6° for inclination. This spacing allows us to confidently locate the position of the χ^2 minimum, but does not yield statistical uncertainties for these parameters.

We apply this method to all the galaxies in our main sample because it is more physically motivated than the traditionally used "mass follows light" approach. It also better reproduces the observed kinematics of our galaxies. The "mass follows light" approach implies that the mass and luminosity profiles of a galaxy have the same shape and differ only by a constant factor M/L_{dyn}, which becomes an extra free parameter of the fitting procedure. We use this approach for the additional galaxy sample, because the lower quality of spectra prevents us from reliably determining the dark matter halo parameters. As we mentioned above, the kinematic disturbances in three galaxies, GMP 4060, GMP 2640 and GMP 4188 are unlikely to be of a dynamical origin.

Disc expansion due to ram pressure stripping. By selection, the galaxies in our sample already have sizes comparable to rather large UDGs being at the same time substantially more extended than typical gas-rich dwarfs in sparse environments. To estimate the importance of ram pressure stripping as a disc expansion mechanism for "normal" dwarf late-type galaxies infalling on-to a massive galaxy cluster like Coma, we took two galaxies from LITTLE THINGS[41] sample: NGC 4214 having stellar mass comparable to GMP 2640, the most massive galaxy in our sample, and DDO 168 comparable to the smallest galaxy in the additional sample. Because the ram pressure timescale is shorter than the rotation period at r_e by a factor of a few, we estimate the average disc expansion using a formula for the change of the orbital radius in case of the rapid mass loss[82] $r_f/r_i = \frac{\varepsilon}{2\varepsilon-1}$. In this formula, $\varepsilon = M_f/M_i$, M_i is initial total mass inside r_e that includes dark matter[83], stars and gas; M_f is the same without gas. This approach suggests that there is no change in the outer surface brightness profile slope, but in the inner parts the dark matter contribution decreases causing the orbital expansion to a higher degree than in the galaxy's outskirts. This creates a large flat core in the surface brightness profile and also increases r_e.

Our modelling shows that ram pressure stripping is capable in expanding a stellar disc by a factor of 2 and even more and might be solely responsible for transforming compact gas-rich galaxies to quiescent stellar systems with UDG sizes and densities. We model the ram pressure induced starburst with a constant SFH for 60 Myr so that the stellar mass formed in it is 20% of the total final stellar mass, the rest of the gas is stripped. We expect that the disc expansion initiated by ram pressure stripping will continue for 300 Myr, which roughly corresponds to the rotation periods of the galactic discs in our PSGs as well as in NGC 4214 and DDO 168. Both, the starburst and the disc expansion start simultaneously but the expansion lasts longer – these stages correspond to the curved parts of the red tracks with an arrow at the end in Fig. 4. Then the galaxies are left to evolve passively for 10 Gyr with a slow disc expansion due to stellar evolution (straight portions of the tracks in Fig. 4.) At the end of the first stage of the disc expansion, 300 Myr after they entered the cluster DDO 168 and NGC 2414 would resemble GMP 3016 and GMP 2640 respectively.

Slow disc expansion modelling. After a stripping event, the stars evolve, and the most massive of them will die. We assume that the galaxy will stay in the cluster after stripping and the final starburst, and that the gas released as a result of stellar evolution will be gradually stripped and will not form new stars. Therefore, the stellar mass decrease with time, leading to disc expansion.

We estimate the expansion of the disc assuming angular momentum conservation, which gives us the following expression:

$$v(M_{tot}(t_0), r(t_0)) \cdot r(t_0) = v(M_{tot}(t_0 + \delta t), r(t_0 + \delta t)) \cdot r(t_0 + \delta t). \tag{1}$$

For $\delta t \to 0$ we get the exact expression for $\dot{r}$:

$$\dot{r}/r = \frac{\partial M_{tot}}{\partial t} \frac{\partial v}{\partial M_{tot}} / \left(\frac{\partial v}{\partial r} r + v \right) \tag{2}$$

This formula can be expressed in terms of logarithmic derivatives:

$$\dot{r}/r = \alpha(r) \cdot \dot{M}/M; \; \alpha(r) = M_{tot} \frac{\partial v}{\partial M_{tot}} / \left(\frac{\partial v}{\partial r} r + v \right) \tag{3}$$

Applying it to an exponential disc, we find that $\alpha(r)$ is a smooth function with values between 1.3 and 3.0, reaching the maximum (3.0) at $r = 0$ and $r \to \infty$, with the minimum at $2r_e$. The central disc expansion is therefore larger than in the outskirts. Therefore, the slope of light profile will decrease with time and the Sersic index will drop to values seen in ordinary ultra-diffuse galaxies.

The presence of significant amounts of dark matter keeps the relative change of M_{tot} and its derivative $\partial M_{tot}/\partial t$ quite small, driving the full expression for $\dot{r}/r$ to near-zero values. This leads to a decrease of overall disc expansion from 20% with no dark matter case to 3–5% for PSGs with dark matter fractions of 70–90%. This small value cannot affect mean surface brightness by more than 0.1 mag arcsec^{-2}. However, numerical simulations suggest that dark matter haloes of low-mass galaxies can be efficiently stripped by tidal forces during close passages near other cluster members, therefore one would still expect a slow disc expansion over time reaching the same 20–25% over 10 Gyr. Strong tidal interactions, which substantially disturb the galaxy morphology are rare so they generally have little effect on the UDG shapes or leave visible tidal features[84]. The disc expansion will lead to the decrease of the average stellar surface density in the disc by 40–50% without substantial disc thickening. In addition, the stellar volume density also decreases because of the slow stellar mass loss reaching 20% over 10 Gyr. These two factors combined will lower the stellar velocity dispersion by ~35% because σ is proportional to the square root of the local stellar density.

Simulations[33] also show that disc expansion causes the dark matter density decrease by some 40% in the central parts of galaxies what leads to the drop of the circular velocity by 20%, because it is proportional to the square root of combined density of stars and dark matter, which dominates the mass. Combined with the stellar density decrease, this effect reaches ~25%. However, observed stellar rotational velocity is smaller than the circular velocity at a given position in a galaxy due to asymmetric drift (v_a) and to estimate the change of its value we applied the formula 4.228

from Binney & Tremaine[85] under the assumption that during the process of slow expansion the ratios of the different velocity dispersion components do not change. In this case, the change of the asymmetric drift velocity is proportional to σ_R^2/v_c. For 85% of dark matter inside $1\ r_e$ the decrease of stellar rotational velocity will be 25%.

UDG number statistics. We assess the importance of the ram pressure stripping scenario to other UDG formation channels. We statistically estimate how many present-day UDGs correspond to each PSG in our primary sample of 9 Coma cluster galaxies and compare the result to the observed number of UDGs in the Coma cluster. We model the surface brightness evolution from the reconstructed SFH and calculate the two epochs: (i) $t_{\rm SDSS}$ when a galaxy becomes too faint to be included in the SDSS spectroscopic sample ($r_{\rm tot} > 17.77$ mag) and (ii) $t_{\rm UDG}$ when it dims enough to be classified as a UDG. UDG classification has a surface brightness cutoff of $\langle \mu_R \rangle_{\rm eff} > 24$ mag/arcsec^2. Statistically speaking, a given PSG will correspond to the number of UDG estimated as $N_{\rm UDG} = (t_{\rm SDSS} - 100{\rm Myr})/(10{\rm Gyr} - t_{\rm UDG})$ if $t_{\rm UDG} < 10$ Gyr. At 100 Myr emission lines disappear from a PSG spectrum, and 10 Gyr is the reference passive evolution time. At the end we co-add $N_{\rm UDG}$ for all 9 galaxies in the primary sample. We find that only 7 galaxies reach the UDG regime within 10 Gyr. The total number of expected UDGs from these 7 progenitors is 19.34±7.00. This estimate is made assuming a constant rate of infall of galaxies on a cluster. Simulations[86] show that during the first 2–3 Gyr of the cluster formation epoch, the infall rate might be up-to twice as high as now. This may only increase our estimate of UDGs formed via the ram pressure stripping channel. The uncertainty is estimated by assuming the Poisson process of the galaxy infall and propagating stellar population parameter statistical errors and the estimated 10% systematic errors for the effective radii[47] and truncation ages[61].

We now need to estimate the total number of present-day UDGs in a complete magnitude limited sample[4,36] with sufficient stellar mass so that 100 Myr after star formation quenching they would be bright enough to meet the SDSS spectroscopic selection. Our initial PSG selection criteria includes a minimum 0.5 mag difference between the 3-arcsec fiber magnitude and the total magnitude. This corresponds to a lower r_e limit of ≈1.5 kpc for galaxies at the distance of the Coma cluster. During passive evolution, these galaxies will expand by $\approx 25\%$, so we only count the present-day UDGs having $r_e > 1.875$ kpc. To estimate the stellar mass we need to assume an SFH in a present-day UDG, which we cannot infer directly from the available data. The most extreme case would be an instantaneous starburst modelled by a simple stellar population. Such a SFH leads to the minimal possible stellar mass cutoff and, hence, the largest number of UDGs passing the selection. For a 10 Gyr age, there are 90 galaxies in UDG sample[36] which could satisfy the selection criteria for our PSGs in the past at some moment during their lifetime. Our lower limit of of UDGs is therefore 21±7 %, which could be explained by the ram pressure stripping formation scenario.

For a more realistic estimate we consider a typical observed SFH for our PSGs: a truncated constant SFR started 13.0 Gyr with 30% of the total stellar mass formed in the final starburst 10 Gyr ago. This corresponds to the median mass fraction we found in the PSG analysis. The number of UDGs that could possibly satisfy our selection criteria decreases to 44, increasing the importance of the ram-pressure-stripping UDG formation channel to 44±17 %. This fraction would increase even more if we take UDG SFHs with a lower final starburst fraction. In Extended Data Figure 5 we show how the adopted SFH affects the total number of UDGs from the study[36] that satisfy the SDSS spectroscopic selection criteria and our selection criteria anytime during their lifetime. We consider three SFHs, all starting 13 billion years ago with truncation ages of 10, 8 and 5 billion years. In all cases we estimate the number of UDGs as described above. In the case of earlier truncation time, M/L ratio and stellar mass change significantly. Given the SDSS magnitude limit we have a individual magnitude limit of UDG for each scenario of star formation. If a galaxy was bright enough 10 billion years ago to pass the selection criteria, this galaxy can now be very faint, and many galaxies from the sample of present-day UDGs are brighter than this limit. In case of more extended scenario of star formation, the M/L ratio and stellar mass change less, we infer a significant fraction of long-lived old stars. The magnitude limit for UDGs is correspondingly brighter, decreasing the number of UDGs. The most extreme case is a SFH with truncation age of 5 Gyr without a final starburst, i.e. constant SFR from 13 Gyr to 5 Gyr. In this case none of known UDGs pass the SDSS selection criteria.

Data availability. Reduced flux calibrated Binospec spectra co-added within $1r_e$ and thier best-fitting NBURSTS+PHOT spectrophotometric models (see Extended Data Figures 1–2), the spatially resolved profiles of internal kinematics and stellar populations and corresponding axisymmetric Jeans models for every galaxy as are available through ZENODO data repository with the following permanent identifier: `https://doi.org/10.5281/zenodo.5031351`. That package also contains a compilation of data points used in Fig. 4 and a PYTHON procedure to reproduce the figure. Fully reduced Subaru and CFHT images used for the dynamical modelling procedure are available in the corresponding open access data archives (`http://jvo.nao.ac.jp/index-e.html`; `http://www.cadc-ccda.hia-iha.nrc-cnrc.gc.ca/en/`).

1. Sandage, A. & Binggeli, B. Studies of the virgo cluster. iii - a classification system and an illustrated atlas of virgo cluster dwarf galaxies. AJ **89**, 919–931 (1984).

2. Ferguson, H. C. & Sandage, A. Population studies in groups and clusters of galaxies. i - the luminosity function of galaxies in the fornax cluster. AJ **96**, 1520–1533 (1988).

3. van Dokkum, P. G. *et al.* Forty-seven Milky Way-sized, Extremely Diffuse Galaxies in the Coma Cluster. ApJ **798**, L45 (2015).

4. Koda, J., Yagi, M., Yamanoi, H. & Komiyama, Y. Approximately a Thousand Ultra-diffuse Galaxies in the Coma Cluster. ApJ **807**, L2 (2015).

5. Saulder, C., van Kampen, E., Chilingarian, I. V., Mieske, S. & Zeilinger, W. W. The matter distribution in the local universe as derived from galaxy groups in sdss dr12 and 2mrs. A&A **596**, A14 (2016).

6. Román, J. & Trujillo, I. Ultra-diffuse galaxies outside clusters: clues to their formation and evolution. MNRAS **468**, 4039–4047 (2017).

7. Yozin, C. & Bekki, K. The quenching and survival of ultra diffuse galaxies in the Coma cluster. MNRAS **452**, 937–943 (2015).

8. Gunn, J. E. & Gott, J. R., III. On the Infall of Matter Into Clusters of Galaxies and Some Effects on Their Evolution. ApJ **176**, 1 (1972).

9. Moore, B., Katz, N., Lake, G., Dressler, A. & Oemler, A. Galaxy harassment and the evolution of clusters of galaxies. Nature **379**, 613–616 (1996).

10. Dekel, A. & Silk, J. The origin of dwarf galaxies, cold dark matter, and biased galaxy formation. ApJ **303**, 39–55 (1986).

11. Ruiz-Lara, T. *et al.* Spectroscopic characterization of the stellar content of ultra-diffuse galaxies. MNRAS **478**, 2034–2045 (2018).

12. Carleton, T. *et al.* The formation of ultra-diffuse galaxies in cored dark matter haloes through tidal stripping and heating. MNRAS **485**, 382–395 (2019).

13. Jiang, F. *et al.* Formation of ultra-diffuse galaxies in the field and in galaxy groups. MNRAS **487**, 5272–5290 (2019).

14. Conselice, C. J. Ultra-diffuse Galaxies Are a Subset of Cluster Dwarf Elliptical/Spheroidal Galaxies. *Research Notes of the American Astronomical Society* **2**, 43 (2018).

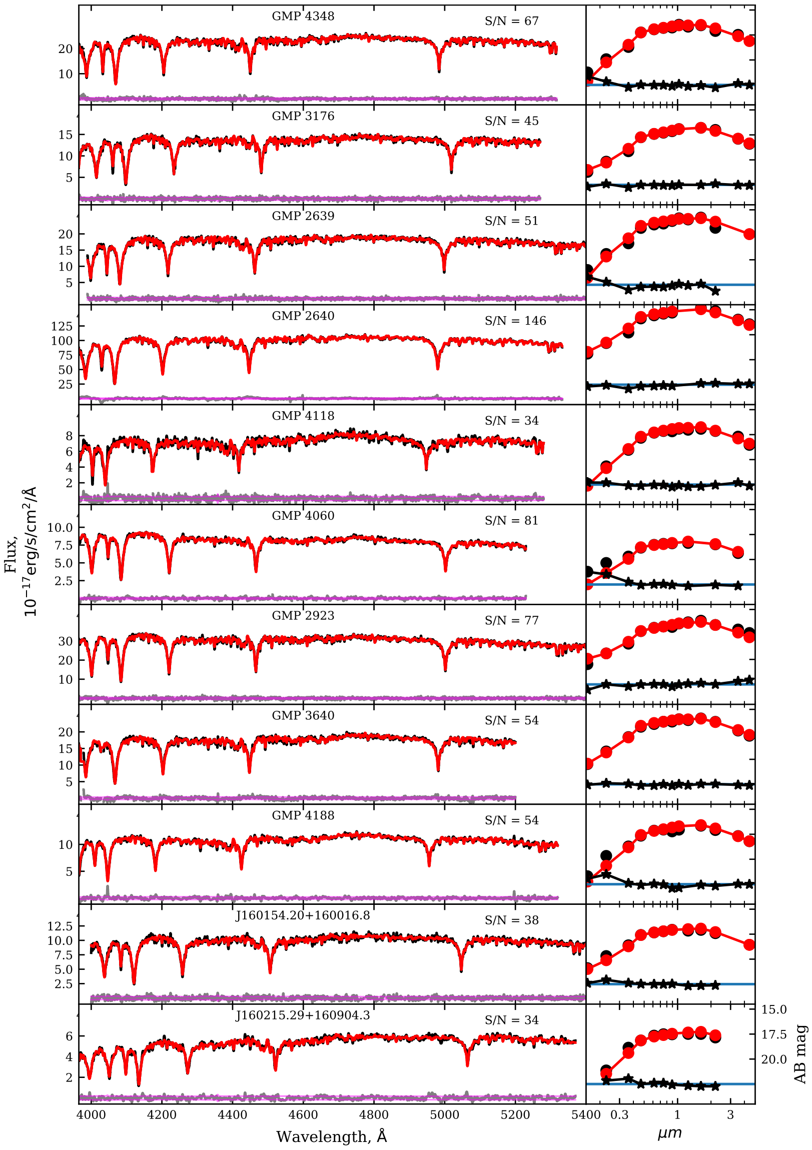

Extended Data Figure 1: Observed data (black) degraded down to correspond template resolution and best-fitting templates (red) for Binospec spectra (left panels) and broad-band SEDs (right panels) for PSGs from the main sample. For the spectra we also show 1σ uncertainty profiles (magenta) and fitting residuals (grey). SED panels show observations and best-fitting models as black and red dots correspondingly. The residuals are shown with black stars around a cyan line representing zero level in the same scale as SEDs. The upper right corner of each spectrum contains a median signal-to-noise ratio for a degraded spectrum per pixel. Main spectral features and broad-band filter bandpasses are marked in the upper row of panels.

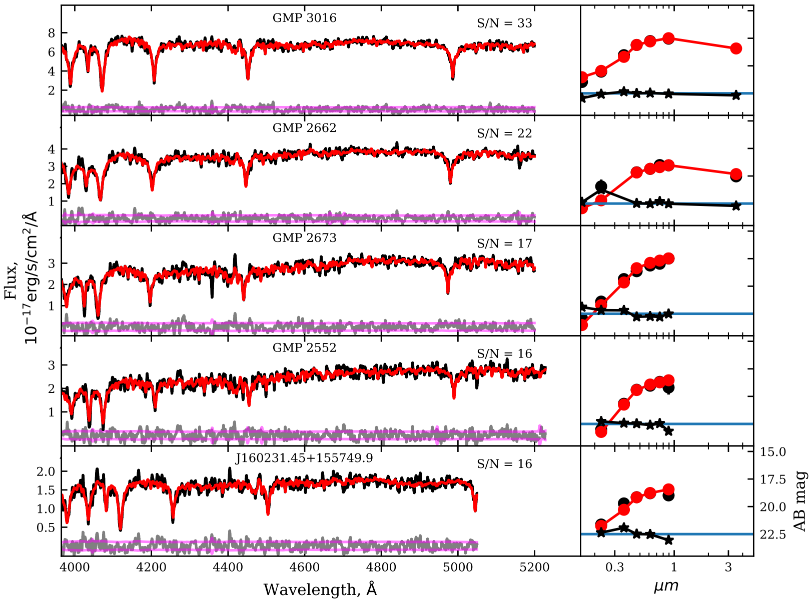

Extended Data Figure 2: The same as Extended Data Figure 1 for the additional galaxy sample.

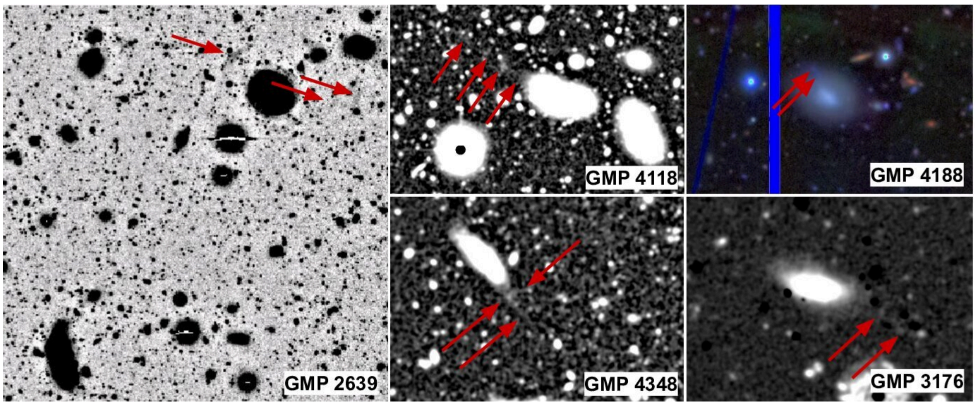

Extended Data Figure 3: Low-contrast filaments suspected to be ram-pressure-stripped tails for five Coma galaxies. For GMP 2639 we show an inverted Rc-band image binned with a 4×4 pix window. For GMP 4118 and GMP 4348 we show H_α images without continuum subtraction convolved with a 2-D Gaussian kernel having FWHM in range $5\ldots7$ pix depending on S/N of input images. For GMP 3176 we show a difference between B and Rc Subaru frames. A spot at the end of the short filament in GMP 4188 pointed by an arrow is a bright Hα source.

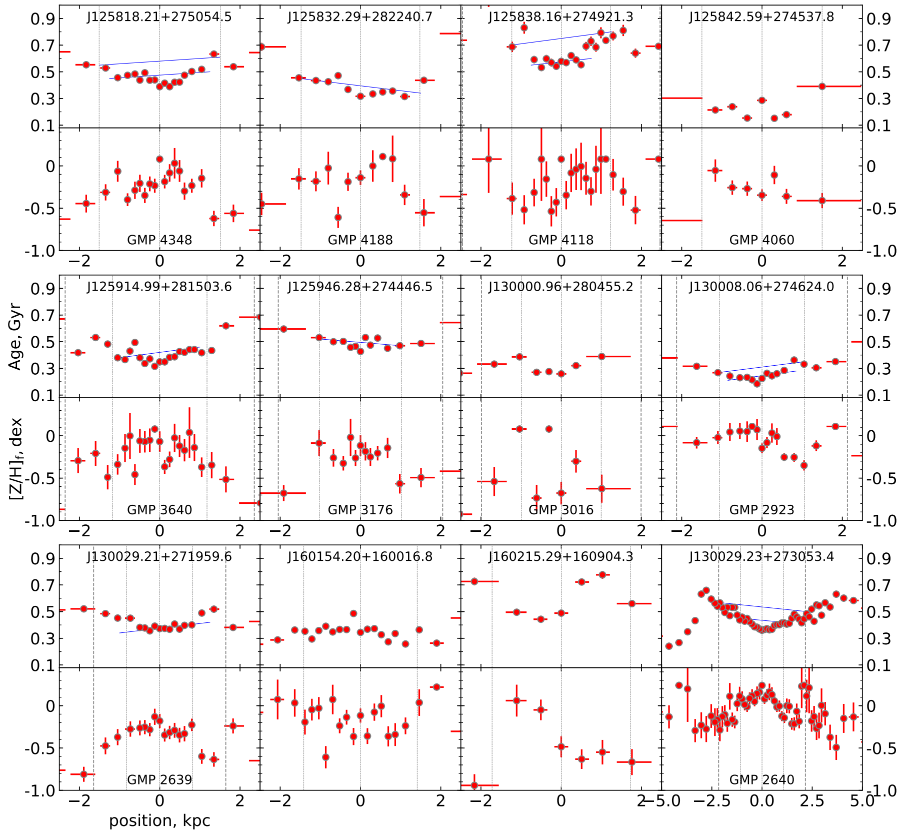

Extended Data Figure 4: Resolved stellar population profiles for the PSGs from the main sample and GMP 3016 obtained from full spectral fitting of long-slit spectra using PEGASE.HR-based templates[28]. We perform the χ^2 minimization varying the truncation age and final metallicity which describes the metallicity of final starburst while other parameters (wind coefficients and SB fraction) are fixed to values derived from the modelling of the co-added 1D spectra with broadband photometry. For galaxies with non-radial age gradients likely caused by the ram pressure stripping, solid blue lines show the gradient trend sometimes over-imposed on the radial gradient illustrating the outside-in quenching. Dotted and dashed lines mark $\pm r_e/2$ and $\pm r_e$ respectively.

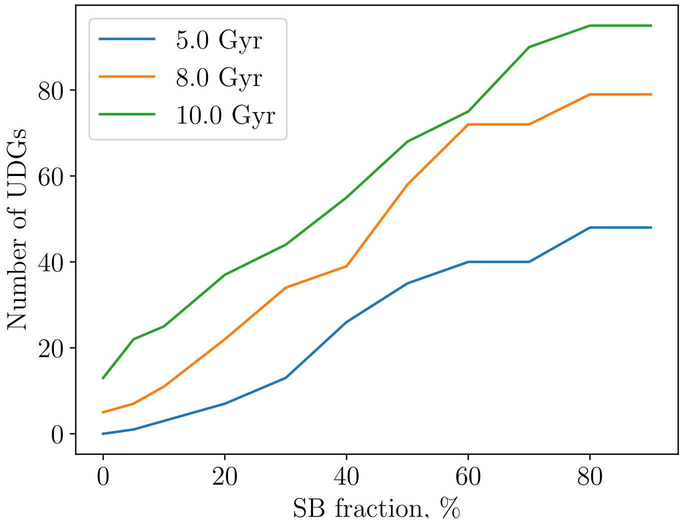

Extended Data Figure 5: A number of UDGs from the Subaru Coma cluster survey[36] that could pass the SDSS spectroscopic selection criteria and satisfy our PSG selection criteria at some moment during their lifetime as a function of a mass fraction of stars born in the final star burst for three different truncation ages: 5, 8, and 10 Gyr.

15. Chilingarian, I. V., Afanasiev, A. V., Grishin, K. A., Fabricant, D. & Moran, S. Internal Dynamics and Stellar Content of Nine Ultra-diffuse Galaxies in the Coma Cluster Prove Their Evolutionary Link with Dwarf Early-type Galaxies. ApJ **884**, 79 (2019).
16. Chilingarian, I. V. *et al.* RCSED - A Value-added Reference Catalog of Spectral Energy Distributions of 800,299 Galaxies in 11 Ultraviolet, Optical, and Near-infrared Bands: Morphologies, Colors, Ionized Gas, and Stellar Population Properties. ApJS **228**, 14 (2017).
17. Abazajian, K. N. *et al.* The Seventh Data Release of the Sloan Digital Sky Survey. ApJS **182**, 543–558 (2009).
18. Poggianti, B. M. *et al.* A Comparison of the Galaxy Populations in the Coma and Distant Clusters: The Evolution of k+a Galaxies and the Role of the Intracluster Medium. ApJ **601**, 197–213 (2004).
19. Yagi, M. *et al.* A Dozen New Galaxies Caught in the Act: Gas Stripping and Extended Emission Line Regions in the Coma Cluster. AJ **140**, 1814–1829 (2010).
20. Smith, R. J. *et al.* Ultraviolet tails and trails in cluster galaxies: a sample of candidate gaseous stripping events in Coma. MNRAS **408**, 1417–1432 (2010).
21. Poggianti, B. M. *et al.* GASP. I. Gas Stripping Phenomena in Galaxies with MUSE. ApJ **844**, 48 (2017).
22. Gullieuszik, M. *et al.* GASP. IV. A Muse View of Extreme Ram-pressure-stripping in the Plane of the Sky: The Case of Jellyfish Galaxy JO204. ApJ **846**, 27 (2017).
23. Kenney, J. D. P. *et al.* Transformation of a Virgo Cluster Dwarf Irregular Galaxy by Ram Pressure Stripping: IC3418 and Its Fireballs. ApJ **780**, 119 (2014).
24. Arrigoni Battaia, F. *et al.* Stripped gas as fuel for newly formed H ii regions in the encounter between VCC 1249 and M 49: a unified picture from NGVS and GUViCS. A&A **543**, A112 (2012).
25. Fujita, Y. & Nagashima, M. Effects of Ram Pressure from the Intracluster Medium on the Star Formation Rate of Disk Galaxies in Clusters of Galaxies. ApJ **516**, 619–625 (1999).
26. Kapferer, W., Sluka, C., Schindler, S., Ferrari, C. & Ziegler, B. The effect of ram pressure on the star formation, mass distribution and morphology of galaxies. A&A **499**, 87–102 (2009).

27. Fabricant, D. *et al.* Binospec: A Wide-field Imaging Spectrograph for the MMT. PASP **131**, 075004 (2019).

28. Grishin, K., Chilingarian, I., Afanasiev, A. & Katkov, I. Reconstructing star formation histories of recently formed ultra-diffuse galaxies. In Valls-Gabaud, D., Trujillo, I. & Okamoto, S. (eds.) *The Realm of the Low-Surface-Brightness Universe*, vol. 355 of *IAU Symposium*, arXiv:1909.13460 (Cambridge University Press, Cambridge, UK, 2019). `1909.13460`.

29. Chilingarian, I. V. & Katkov, I. Y. NBursts+phot: parametric recovery of galaxy star formation histories from the simultaneous fitting of spectra and broad-band spectral energy distributions. In Tuffs, R. J. & Popescu, C. C. (eds.) *The Spectral Energy Distribution of Galaxies - SED 2011*, vol. 284 of *IAU Symposium*, 26–28 (2012). `1112.5191`.

30. Chilingarian, I. V. Evolution of dwarf early-type galaxies - i. spatially resolved stellar populations and internal kinematics of virgo cluster de/ds0 galaxies. MNRAS **394**, 1229–1248 (2009).

31. Cappellari, M. Measuring the inclination and mass-to-light ratio of axisymmetric galaxies via anisotropic Jeans models of stellar kinematics. MNRAS **390**, 71–86 (2008).

32. Safarzadeh, M. & Scannapieco, E. The Fate of Gas-rich Satellites in Clusters. ApJ **850**, 99 (2017).

33. Tremmel, M. *et al.* The formation of ultradiffuse galaxies in the romulusc galaxy cluster simulation. MNRAS **497**, 2786–2810 (2020).

34. Faber, S. M. & Jackson, R. E. Velocity dispersions and mass-to-light ratios for elliptical galaxies. ApJ **204**, 668–683 (1976).

35. Kormendy, J. Brightness distributions in compact and normal galaxies. ii - structure parameters of the spheroidal component. ApJ **218**, 333–346 (1977).

36. Yagi, M., Koda, J., Komiyama, Y. & Yamanoi, H. Catalog of Ultra-diffuse Galaxies in the Coma Clusters from Subaru Imaging Data. ApJS **225**, 11 (2016).

37. Jaffé, Y. L. *et al.* GASP. IX. Jellyfish galaxies in phase-space: an orbital study of intense ram-pressure stripping in clusters. MNRAS **476**, 4753–4764 (2018).

38. Vulcani, B. *et al.* Gasp xxx. the spatially resolved sfr-mass relation in stripping galaxies in the local universe. ApJ **899**, 98 (2020).

39. Jackson, R. A. *et al.* The origin of low-surface-brightness galaxies in the dwarf regime. MNRAS **502**, 4262–4276 (2021).

40. Cramer, W. J. *et al.* Alma evidence for ram pressure compression and stripping of molecular gas in the virgo cluster galaxy ngc 4402. ApJ **901**, 95 (2020).

41. Hunter, D. A. *et al.* Little things. AJ **144**, 134 (2012).

42. Oh, S.-H. *et al.* High-resolution Mass Models of Dwarf Galaxies from LITTLE THINGS. AJ **149**, 180 (2015).

43. van Dokkum, P. *et al.* A High Stellar Velocity Dispersion and ˜100 Globular Clusters for the Ultra-diffuse Galaxy Dragonfly 44. ApJ **828**, L6 (2016).

44. Graham, A. W. & Soria, R. Expected intermediate-mass black holes in the Virgo cluster - I. Early-type galaxies. MNRAS **484**, 794–813 (2019).

45. Chilingarian, I. V. *et al.* Kinematics and stellar populations of low-luminosity early-type galaxies in the abell 496 cluster. A&A **486**, 85–97 (2008).

46. Binggeli, B. & Jerjen, H. Is the shape of the luminosity profile of dwarf elliptical galaxies an useful distance indicator? A&A **333**, 17–26 (1998).

47. Alabi, A. B., Romanowsky, A. J., Forbes, D. A., Brodie, J. P. & Okabe, N. An expanded catalogue of low surface brightness galaxies in the Coma cluster using Subaru/Suprime-Cam. MNRAS **496**, 3182–3197 (2020).

48. van Dokkum, P. G. *et al.* Forming Compact Massive Galaxies. ApJ **813**, 23 (2015).

49. Gu, M. *et al.* Low Metallicities and Old Ages for Three Ultra-diffuse Galaxies in the Coma Cluster. ApJ **859**, 37 (2018).

50. Gannon, J. S. *et al.* On the stellar kinematics and mass of the Virgo ultradiffuse galaxy VCC 1287. MNRAS **495**, 2582–2598 (2020).

51. Gannon, J. S. *et al.* A photometric and kinematic analysis of udg1137+16 (dw1137+16): Probing ultradiffuse galaxy formation in a group environment. MNRAS **502**, 3144–3157 (2021).

52. McConnachie, A. W. The observed properties of dwarf galaxies in and around the local group. AJ **144**, 4 (2012).

53. Bender, R., Burstein, D. & Faber, S. M. Dynamically hot galaxies. I - Structural properties. ApJ **399**, 462–477 (1992).

54. Godwin, J. G., Metcalfe, N. & Peach, J. V. The Coma Cluster - I. A Catalogue of magnitudes, colours, ellipticiesand position angles for 6724 galaxies in the field of the Coma Cluster. MNRAS **202**, 113–124 (1983).

55. Dey, A. *et al.* Overview of the desi legacy imaging surveys. AJ **157**, 168 (2019).

56. Chilingarian, I. V. & Zolotukhin, I. Y. A universal ultraviolet-optical colour-colour-magnitude relation of galaxies. MNRAS **419**, 1727–1739 (2012).

57. Kansky, J. *et al.* Binospec Software System. PASP **131**, 075005 (2019).

58. Bertin, E. Automated Morphometry with SExtractor and PSFEx. In Evans, I. N., Accomazzi, A., Mink, D. J. & Rots, A. H. (eds.) *Astronomical Data Analysis Software and Systems XX*, vol. 442 of *Astronomical Society of the Pacific Conference Series*, 435 (2011).

59. Chilingarian, I. V., Melchior, A.-L. & Zolotukhin, I. Y. Analytical approximations of k-corrections in optical and near-infrared bands. MNRAS **405**, 1409–1420 (2010).

60. Kroupa, P. The initial mass function of stars: Evidence for uniformity in variable systems. *Science* **295**, 82–91 (2002).

61. Chilingarian, I. V. & Asa'd, R. Using Star Clusters as Tracers of Star Formation and Chemical Evolution: The Chemical Enrichment History of the Large Magellanic Cloud. ApJ **858**, 63 (2018).

62. Schmidt, M. The Rate of Star Formation. II. The Rate of Formation of Stars of Different Mass. ApJ **137**, 758 (1963).

63. Pagel, B. E. J. *Nucleosynthesis and Chemical Evolution of Galaxies* (1997).

64. Matteucci, F. Introduction to Galactic Chemical Evolution. In *Journal of Physics Conference Series*, vol. 703 of *Journal of Physics Conference Series*, 012004 (2016). `1602.01004`.

65. Matteucci, F. & Chiosi, C. Stochastic star formation and chemical evolution of dwarf irregular galaxies. A&A **123**, 121–134 (1983).

66. Matteucci, F. *Chemical Evolution of Galaxies* (2012).

67. Matteucci, F., Spitoni, E., Recchi, S. & Valiante, R. The effect of different type Ia supernova progenitors on Galactic chemical evolution. A&A **501**, 531–538 (2009).

68. Barbosa, C. E. *et al.* One Hundred SMUDGes in S-PLUS: Ultra-diffuse Galaxies Flourish in the Field. ApJS **247**, 46 (2020).

69. Martín-Navarro, I. *et al.* Extreme chemical abundance ratio suggesting an exotic origin for an ultradiffuse galaxy. MNRAS **484**, 3425–3433 (2019).

70. Ferré-Mateu, A. *et al.* Origins of ultradiffuse galaxies in the Coma cluster - II. Constraints from their stellar populations. MNRAS **479**, 4891–4906 (2018).

71. Danieli, S., van Dokkum, P., Conroy, C., Abraham, R. & Romanowsky, A. J. Still Missing Dark Matter: KCWI High-resolution Stellar Kinematics of NGC1052-DF2. ApJ **874**, L12 (2019).

72. Trujillo, I. *et al.* A distance of 13 Mpc resolves the claimed anomalies of the galaxy lacking dark matter. MNRAS **486**, 1192–1219 (2019).

73. Danieli, S. *et al.* A Tip of the Red Giant Branch Distance to the Dark Matter Deficient Galaxy NGC 1052-DF4 from Deep Hubble Space Telescope Data. ApJ **895**, L4 (2020).

74. Chilingarian, I., Prugniel, P., Sil'chenko, O. & Koleva, M. Nbursts: Simultaneous extraction of internal kinematics and parametrized sfh from integrated light spectra. In Vazdekis, A. & R. Peletier, R. (eds.) *Stellar Populations as Building Blocks of Galaxies*, vol. 241 of *IAU Symposium*, 175–176 (Cambridge University Press, Cambridge, UK, 2007). `arXiv:0709.3047`.

75. Chilingarian, I. V. & Grishin, K. A. Estimating statistical uncertainties of internal kinematics of galaxies and star clusters derived using full spectrum fitting. PASP **132**, 064503 (2020).

76. Smith, R., Fellhauer, M. & Assmann, P. Ram pressure drag - the effects of ram pressure on dark matter and stellar disc dynamics. MNRAS **420**, 1990–2005 (2012).

77. Miyazaki, S. *et al.* Subaru Prime Focus Camera – Suprime-Cam. PASJ **54**, 833–853 (2002).

78. Miyazaki, S. *et al.* Hyper Suprime-Cam: System design and verification of image quality. PASJ **70**, S1 (2018).

79. Peng, C. Y., Ho, L. C., Impey, C. D. & Rix, H.-W. Detailed decomposition of galaxy images. ii. beyond axisymmetric models. AJ **139**, 2097–2129 (2010).

80. Jeans, J. H. The Motions of Stars in a Kapteyn Universe. MNRAS **82**, 122–132 (1922).

81. Burkert, A. The Structure of Dark Matter Halos in Dwarf Galaxies. ApJ **447**, L25–L28 (1995).

82. Hills, J. G. The effect of mass loss on the dynamical evolution of a stellar system - Analytic approximations. ApJ **235**, 986–991 (1980).

83. Li, P., Lelli, F., McGaugh, S. & Schombert, J. A Comprehensive Catalog of Dark Matter Halo Models for SPARC Galaxies. ApJS **247**, 31 (2020).

84. Mowla, L. *et al.* Evidence of absence of tidal features in the outskirts of ultra diffuse galaxies in the coma cluster. ApJ **851**, 27 (2017).

85. Binney, J. & Tremaine, S. *Galactic Dynamics: Second Edition* (2008).

86. Lisker, T., Weinmann, S. M., Janz, J. & Meyer, H. T. Dwarf galaxy populations in present-day galaxy clusters - II. The history of early-type and late-type dwarfs. MNRAS **432**, 1162–1177 (2013).

Astronomy & Astrophysics manuscript no. output
July 26, 2022

The Galaxy Mass-Size Relation in CARLA Clusters and Proto-Clusters at $1.4 < z < 2.8$: larger cluster galaxy sizes

Anton V. Afanasiev[1]⋆, Simona Mei[1,2], Hao Fu[3], Francesco Shankar[3], Stefania Amodeo[4], Elizabeth Cooke[5], Anthony Gonzalez[6], Gaël Noirot[7], Dominika Wylezalek[8], Carlos De Breuck[9], Nina Hatch[10], Alessandro Rettura[2], Spencer A. Stanford[11], Daniel Stern[2], and Joël Vernet[9]

[1] Université Paris Cité, CNRS, Astroparticule et Cosmologie, F-75013 Paris, France
[2] Jet Propulsion Laboratory, Cahill Center for Astronomy & Astrophysics, California Institute of Technology, 4800 Oak Grove Drive, Pasadena, California, USA
[3] School of Physics & Astronomy, University of Southampton, Highfield, Southampton SO17 1BJ, UK
[4] Université de Strasbourg, CNRS, Observatoire astronomique de Strasbourg, UMR 7550, F-67000 Strasbourg, France
[5] National Physical Laboratory, Hampton Road, Teddington, Middlesex, TW11 0LW, UK
[6] Department of Astronomy, University of Florida, Gainesville, FL 32611-2055, USA
[7] Department of Astronomy Physics, Saint Mary's University, 923 Robie Street, Halifax, NS B3H 3C3, Canada
[8] Zentrum für Astronomie der Universität Heidelberg, Astronomisches Rechen-Institut, Mönchhofstr 12-14, D-69120 Heidelberg, Germany
[9] European Southern Observatory, Karl-Schwarzschildstrasse 2, 85748 Garching, Germany
[10] School of Physics and Astronomy, University of Nottingham, University Park, Nottingham NG7 2RD, UK
[11] Department of Physics, University of California, One Shields Avenue, Davis, CA 95616, USA

Received mmmm dd, yyyy; accepted mmmm dd, yyyy

ABSTRACT

We study the galaxy mass-size relation in 15 spectroscopically confirmed clusters at $1.3 < z < 2.8$ from the Clusters Around Radio-Loud AGN survey. Our clusters span a total stellar mass in the range $11.3 < \log(M_*^c/M_\odot) < 12.6$ (approximate halo mass in the range $13.6 < \log(M_h^c/M_\odot) < 14.6$). Our main finding is that cluster passive early-type galaxies with mass $\log(M/M_\odot) > 10.5$ are systematically ($\gtrsim 3\sigma$) larger then field galaxies from the CANDELS survey. The passive ETG average size evolution with redshift is slower at $1 < z < 2$ when compared to the field. This could be explained by early-epoch differences in the formation and early evolution of galaxies in haloes of different mass, as predicted by models. It does not exclude that other physical mechanisms, such as strong compaction/gas dissipation in field galaxies, followed by a sequence of mergers may have also played a significant role in the field early-type galaxy evolution, but not necessarily in the evolution of cluster galaxies. Our passive ETG mass-size relation show a tendency to flatten at $9.6 < \log(M/M_\odot) < 10.5$, where the average size is $\log(R_e/\mathrm{kpc}) = 0.05 \pm 0.22$, which is broadly consistent with galaxy sizes in the field, and in the local Universe. This implies that the low end of the mass-size relation does not evolve much from $z \sim 2$ to present, and that sizes evolve in the same way in clusters and in the field. Brightest cluster galaxies lie on the same mass-size relation as the satellites, suggesting that their size evolution is not different from the satellites at redshift $z > 2$. Half of the active early-type galaxies, which are 30% of our early-type galaxy sample, follow the field passive galaxy mass-size relation, and the other half the field active galaxy mass-size relation. These galaxies likely went through a recent merger or neighbour galaxy interaction, and would most probably quench at a later epoch and increase the fraction of passive early-type galaxies in clusters. We do not observe a large population of compact galaxies (only one), as is observed in the field at these redshifts, implying that the galaxies in our clusters are not observed in an epoch close to their compaction.

1. Introduction

In the local Universe and up to $z = 3$, the most massive galaxies are also among the largest (Kauffmann et al. 2003; Gadotti 2009; Poggianti et al. 2013; Huertas-Company et al. 2013b; Fernández Lorenzo et al. 2013; Delaye et al. 2014; Belli et al. 2014; van Dokkum et al. 2015). For example, local elliptical galaxies follow a rather tight relation with intrinsic scatter less than 0.3 dex (Nair et al. 2011; Bernardi et al. 2011a,b, 2014). This dependence is called the galaxy mass-size relation (MSR), and provides an insight on the past and present evolution of galaxies.

The first results on the mass-size and size-luminosity relation at $z = 1$ and beyond to $z = 3$ were reported by Trujillo et al. (2004, 2006); McIntosh et al. (2005) who initially did not find strong size differences for massive ($M_* > 2 - 3 \times 10^{10}\ M_\odot$) galaxies at $2 < z < 3$ compared to $z = 0$, but later claimed that galaxies at $z = 2.5$ are on average two times smaller. Later results (Trujillo et al. 2011; Mosleh et al. 2011; Dutton et al. 2011; Szomoru et al. 2012) confirmed that the stellar mass-size relation was already in place at least at $z = 1$, but its normalization increased at low redshift.

The arrival of the new data, such as the Cosmic Assembly Near-infrared Deep Extragalactic Legacy Survey (CANDELS; PI: S. Faber, H. Ferguson; Koekemoer et al. 2011; Grogin et al. 2011), and new observational techniques, such as strong lensing (Yang et al. 2021), confirmed this view. van der Wel et al. (2012, 2014) measured the MSR redshift evolution for both passive and star-forming galaxies in the field in the redshift range $z = 0 - 3$. They demonstrated that the slope of the MSR does not evolve for both populations. However, galaxies become more compact with increasing redshift, which was explained by Carollo et al. (2013) by the fact that the Universe was more dense in earlier times, and the galaxy density evolves approximately as the den-

---

⋆ afanasiev@apc.in2p3.fr

sity of the Universe. Dimauro et al. (2019) analyzed the MSR of bulges and discs, and finds that they follow different MSR. Their MSR weakly depend on the morphology of the host galaxy, and the sizes of disks do not depend on their star-formation activity. They concluded that quenching did not affect disc structures.

The shape of the MSR is consistent with a scenario in which galaxy growth is dominated by star formation due to cold gas accretion up to a certain mass (which is redshift- and size-dependent, corresponding approximately to $M = 10^{11} M_{\odot}$ at $z = 2$ and $R_e = 1$ Kpc) and by galaxy mergers at higher masses (e.g., Shankar et al. 2013; van Dokkum et al. 2015; Zanisi et al. 2020) In fact, hierarchical models could explain the fast size growth of giant elliptical galaxies only by sequential minor dry mergers since $z = 2$ (Naab et al. 2009; Trujillo et al. 2011; Newman et al. 2012; van Dokkum et al. 2015). On the other hand, spiral galaxies do not require minor mergers, since their growth can be attributed to cold gas accretion (Dekel et al. 2009).

It is less clear though if galaxies in clusters and in the field evolved in the same way. Semi-analytical models predict a moderate to strong environmental dependence in the local Universe (Shankar et al. 2014). However, observational results are contradictory. Several works have shown that this relation is independent from environment (e.g., Guo et al. 2009; Weinmann et al. 2009; Cappellari 2013; Huertas-Company et al. 2013b; Mosleh et al. 2018). Others found that cluster early-type galaxies (ETG) are smaller than those in the field (e.g. Poggianti et al. 2013), however they included a large fraction of S0 galaxies which appear to have smaller radii then elliptical galaxies at fixed stellar mass (Bernardi et al. 2013; Huertas-Company et al. 2013a), and different environmental relations (Erwin et al. 2012; Sil'chenko et al. 2018). On the other hand, Huang et al. (2018) found that massive galaxies in clusters are as much as 20%-40% larger than in the field with deep observations with the Hyper Suprime-Cam (see also Yoon et al. 2017).

For spiral galaxies, the environmental dependence of the mass-size relation is even more pronounced: its scatter is much larger (Maltby et al. 2010; Cappellari 2013; Lange et al. 2015) and their disks are smaller in clusters (Kuchner et al. 2017; Demers et al. 2019). This means that dense environment either destroys the disks or inhibits their growth, for example through tidal interactions, ram-pressure and strangulation (Boselli & Gavazzi 2006).

To better understand and confirm which evolutionary physical processes led to the environmental effects observed in the local Universe, it is essential to study the dependence of galaxy size growth on environment through cosmic time.

At $0.4 \lesssim z \lesssim 2$, some works found no differences between galaxies in the field and moderately dense environments (Huertas-Company et al. 2013a; Kelkar et al. 2015) ($\log(M/M_{\odot}) \sim 10.5-11.8$), others found larger quiescent galaxy sizes in clusters in both high (Delaye et al. 2014, $\log(M/M_{\odot}) \sim 10.5 - 11.5$) and low (Mei et al. 2015, $\log(M/M_{\odot}) \sim 9.5 - 10.5$) mass regime. Others report smaller sizes in clusters (Raichoor et al. 2012, $\log(M/M_{\odot}) \sim 10 - 11.5$), in low statistical significant samples. At $z = 2$, Allen et al. (2015) report that cluster star-forming galaxies are larger compared to the field, while quiescent galaxies do not show such a difference being only slightly larger in clusters (in the mass range $\log(M/M_{\odot}) \sim 9-11.5$). This notion is supported by Saracco et al. (2017) at $\log(M/M_{\odot}) \sim 10.3 - 11.3$, who have found no environmental effect on the $z = 1.3$ elliptical MSR, noting that cluster ellipticals tend to be more massive. On the other hand, Chan et al. (2018) find that at $z = 1.4$ passive cluster galaxies ($\log(M/M_{\odot}) \sim 10.2 - 11.5$) are about 30% larger than in the field. Noordeh et al. (2021) also find larger cluster quiescent galaxy sizes at fixed $\log(M/M_{\odot} = 10.7)$ with Sérsic $n > 2$ at $z = 2$. Sazonova et al. (2020) found that $z = 1.5$ bulge-dominated cluster galaxies with $\log(M/M_{\odot} < 10.5)$ are significantly more compact than the field counterparts. Mowla et al. (2019); Marsan et al. (2019) focused at high-mass ($\log(M/M_{\odot} > 11.3)$) passive galaxies, whose MSR was found to be consistent with the lower-mass galaxy MSR and experiencing strong evolution with redshift.

There is also some evidence, that the MSR flattens up at low masses in the local Universe Bernardi et al. (2011b), and up to $z \sim 1$ (Nedkova et al. 2021), as predicted by models (Shankar et al. 2014).

Finally, several studies found high percentages of compact post-starburst (Maltby et al. 2018; Socolovsky et al. 2019; Matharu et al. 2020; Wilkinson et al. 2021) and massive compact galaxies (Lu et al. 2019; Gu et al. 2020; Tadaki et al. 2020) in dense environments at $z = 1.5 - 2$.

In this paper, we extended MSR studies in an unique sample of galaxy clusters at redhift $1.3 \lesssim z \lesssim 2.8$ from the CARLA (Clusters Around Radio-Loud AGN (Wylezalek et al. 2013, 2014) survey. We find that cluster passive early type galaxies are significantly ($> 3\sigma$)larger than in the field at these redshifts, while late-type galaxies have similar sizes. Combining our results with other cluster studies we demonstrate that cluster passive ETG have much slower size evolution than their field counterparts. The Brightest cluster galaxies lie on the same mass-size relation as the satellites. Half of the early-type galaxies with active star-formation lie on the late-type galaxy mass-size relation. The mass-size relation flattens at low mass, and we do not observe large percentages of very compact galaxies in our sample.

The structure of the paper is as follows. We describe our observations in Section 2. The galaxy property measurements are presented in Section 3. Section 4 describes our sample. Our results are presented in Section 5, and discussed in Section 6. Section 7 is the summary of the paper.

Throughout this paper, we adopt a ΛCDM cosmology, with of $\Omega_{\rm M} = 0.3$, $\Omega_{\Lambda} = 0.7$, $\Omega_{\rm k} = 0$ and $h = 0.7$, and assume a Chabrier initial mass function (IMF) (Chabrier 2003). The photometry and structural parameters in this paper were measured adopting the 3D-HST empirical PSF model [1] for the *HST*/WFC3 GOODS-S images in F140W (H_{140}) band. Hereafter, we define galaxies with active star formation as active galaxies.

2. The CARLA survey

2.1. CARLA cluster candidates

CARLA is a 408h Warm *Spitzer*/IRAC survey of galaxy overdensities around 420 radio-loud AGN (RLAGN). The AGN were selected across the full sky and in the redshift range of $1.3 < z < 3.2$. Approximately half of them are radio loud quasars (RLQs) and the other half are radio galaxies (HzRGs). With the aim to detect galaxy cluster candidates, Wylezalek et al. (2013) selected galaxies at $z > 1.3$ around the AGN, using a color selection in the IRAC channel 1 ($\lambda = 3.6\,\mu$m; IRAC1, hereafter) and channel 2 ($\lambda = 4.5\,\mu$m; IRAC2, hereafter). They found that 92% of the selected RLAGN reside in dense environments, with the majority (55%) of them being overdense at a $> 2\sigma$ level, and 10% of them at a $> 5\sigma$ level, with respect to a field sample in the *Spitzer* UKIDSS Ultra Deep Survey (SpUDS, Rieke et al. 2004).

From their IRAC luminosity function, Wylezalek et al. (2014) showed that CARLA overdensity galaxies have probably

---

[1] `https://archive.stsci.edu/prepds/3d-hst/`

quenched faster and earlier compared to field galaxies. Some of the CARLA northern overdensities were also observed in either deep z-band or deep i-band, with Gemini/GMOS, VLT/ISAAC and WHT/ACAM (P.I. Hatch (see below); Cooke et al. 2015). These observations permitted us to estimate galaxy star formation rate histories, and to deduce that, on average, the star formation of galaxies in these targets had been rapidly quenched (Cooke et al. 2015).

The twenty highest CARLA *Spitzer* overdensities candidates were followed by a *Hubble Space Telescope* Wide Field Camera 3 (*HST*/WFC3) observations (P.I. Stern (see below); Noirot et al. 2016, 2018), and sixteen of them were spectroscopically confirmed at $1.4 < z < 2.8$, together with seven spectroscopically confirmed serendipitous structures at $0.9 < z < 2.1$ (Noirot et al. 2018). The structure members were confirmed as line-emitters in Hα, Hβ, [OII], and/or [OIII], depending on the redshift, and have star formation estimates from the line fluxes (Noirot et al. 2018). The galaxy star-formation (for stellar mass $\gtrsim 10^{10} M_\odot$) is below the star-forming *main sequence* (MS) of field galaxies at similar redshift. Star-forming galaxies are mostly found within the central regions (Noirot et al. 2018).

Mei et al. 2022 (hereafter, M22) performed an in-depth study of the morphology, quiescence and merger incidence of CARLA clusters. They found that the galaxy morphology-density and passive-density relations are already in place at $z \sim 3$ and 2, respectively. The cluster ETG and passive fractions depend on local environment and mildly on galaxy mass. Active ETG are 30% of the total ETG population. Cluster merger fractions are significantly higher than in the CANDELS fields, as predicted from previous studies to explain high quiescent fractions at $z \lesssim 1.5$. Their findings confirm that all the spectroscopically confirmed CARLA overdensities have properties consistent with clusters and proto-clusters.

We describe our observations below. More details on the *Spitzer* IRAC, *HST*/WFC3 and ground-based observations, data reduction and results can be found in Wylezalek et al. (2013, 2014), Noirot et al. (2016, 2018), and Cooke et al. (2015), respectively.

2.2. Spitzer Observations

All CARLA clusters were observed with *Spitzer* IRAC1 and IRAC2 (Cycle 7 and 8 snapshot program; P.I.: D. Stern), with total exposure times of 800 s/1000 s in IRAC1 and 2000 s/2100 s in IRAC2, for radio galaxies at $z < 2/z > 2$, which provided a similar depth in both channels. The IRAC cameras have 256 × 256 InSb detector arrays with a pixel size of 1.22 arcsec and a field of view of 5.2 × 5.2 arcmin. Wylezalek et al. (2013) performed the data calibration and mapping with the `MOPEX` package (Makovoz & Khan 2005) and detected sources with SExtractor (Bertin & Arnouts 1996), using the IRAC-optimized SExtractor parameters from Lacy et al. (2005). The final *Spitzer* IRAC1 and IRAC2 mosaic has a pixel size of 0.61 arcsec, after taking into account dithering and sub-pixelation. The 95% completeness limit is obtained at IRAC1=22.6 mag and IRAC2=22.9 mag.

2.3. HST Observations

The *HST*/WFC3 imaging and grism spectroscopy were obtained with the dedicated *HST* follow-up program (Program ID: 13740; P.I.: D. Stern). The program consisted of F140W band (hereafter H_{140}) imaging (with a field of view of 2×2.3 arcmin^2 at a resolution of 0.06 arsec pix^{-1}, after taking into account dithering), and G141 grism spectroscopy (with a thoughtput > 10% in the wavelength range of $1.08\,\mu\text{m} < \lambda < 1.70\,\mu\text{m}$ and spectral resolution $R = \lambda/\Delta\lambda = 130$). This grism was chosen in order to permit the identification of strong emission lines at our target redshift, such as Hα, Hβ, [OII] and [OIII]. Noirot et al. (2016, 2018) performed the data reduction using the `aXe` (Kümmel et al. 2009) pipeline, by combining the individual exposures, and removing cosmic ray and sky signal. They performed the source detection with SExtractor (Bertin & Arnouts 1996), and extracted two-dimensional spectra for each field, based on the positions and sizes of the sources. The redshifts and emission line fluxes were determined using the python version of `mpfit` and are published in Noirot et al. (2018). Our HST image 5σ magnitude limit within an aperture of radius 0.17 arcsec is $H_{140} = 27.1$ mag.

2.4. Ground-based optical observations

Ground-based optical imaging in i or z-band is available for nine of the CARLA clusters (Cooke et al. 2015). Seven clusters were observed in September 2013 - December 2014 using ACAM at 4.2m William Hershel telescope (P.I. Hatch). ACAM has a circular field of view, 8.3 arcmin in diameter with a pixel scale 0.25 arcsec pixel^{-1}. Two other clusters were observed between February and April 2014 with GMOS-S (at Gemini South telescope) using the EEV detectors. The field of view of GMOS-S is 5.5 × 5.5 arcmin with a pixel scale of 0.146 arcsec pixel^{-1}. Exposure times were calculated depending on the actual seeing, in order to reach a consistent depth across all fields. The reduction of the i-band images was performed with the publicly available THELI software (Erben et al. 2005; Schirmer 2013). For the photometric calibration we used either available Sloan Digital Sky Survey photometry or standard stars observed before and after the cluster observations. More details on these observations and image reduction can be found in Cooke et al. (2015). CARLA J2039-2514 has archival imaging observations with VLT/ISAAC (run ID 69.A-0234) in the z-band with 4800s exposure time (see also Noirot et al. 2016).

3. Sample selection and galaxy property measurements

We focus this study on 15 of the 16 CARLA confirmed clusters in Noirot et al. (2018), i.e. those that present enough high overdensity to yield low field galaxy contamination (M22). Details on our cluster and galaxy selection are found in M22, and we describe below the main steps leading to our cluster and galaxy sample selection, and the galaxy property measurements.

3.1. Galaxy photometry and mass measurement

Our photometry was obtained from a joint analysis of IRAC1, IRAC2, H_{140} and, when available, ground-based i-band or z-band images, as described in M22. For an efficient source deblending, we used the T-PHOT software (Merlin et al. 2015, 2016), with the high-resolution *HST* images as priors to derive PSF-matched fluxes in the other lower-resolution bands.

M22 also describe in detail our stellar mass measurements. We measured our CARLA galaxy stellar masses by calibrating our PSF-matched *Spitzer*/IRAC1 magnitudes with galaxy stellar masses from Santini et al. (2015) derived from the Guo et al. (2013) multi-wavelength catalog in the CANDELS WIDE GOODS-S field. The *Spitzer* IRAC1 magnitudes correspond to the rest-frame near-infrared in the redshift range of the CARLA

Table 1. SExtractor parameters used for source detection.

SExtractor	Cold Mode	Hot Mode
DETECT_MINAREA	5.0	10.0
DETECT_THRESH	0.75	0.7
ANALYSIS_THRESH	5.0	0.8
FILTER_NAME	tophat_9.0_9x9	gauss_4.0_7x7
DEBLEND_NTHRESH	16	64
DEBLEND_MINCONT	0.0001	0.001
BACK_SIZE	256	128
BACK_FILTERSIZE	9	5
BACKPHOTO_THICK	100	48

Table 2. Constraints on GALFIT parameters.The constraint on magnitude is relative to the measured SExtractor magnitude.

parameter	description	constraints	units
n	Sérsic index	0.2 : 8	
R_e	effective radius	0.3 : 400	pixel
Q	axis ratio	0.0001 : 1	
m	magnitude	-3 : +3	SExtractor mag

sample, and we expect them not to be biased by extinction. M22 found a very good correlation between these magnitudes and the Santini et al. (2015) mass measurements, with scatters of ≈ 0.12 dex at the redshift of the cluster studied in this paper. Adding in quadrature the scatter of the relation and uncertainties from Santini et al. (2015), we obtained mass uncertainties in the range $\sim 0.4-0.5$ dex, and $\approx 0.2-0.3$ dex for masses larger than $\log_{10}(M/M_{\odot}) > 10.5$. Hereafter, we use the symbol M for the galaxy stellar mass.

3.2. Sample selection

Our sample selection is described in M22. Our selection aims at optimizing the sample completeness and purity. Observations of most of the CARLA clusters and proto-clusters include three (H_{140}, IRAC1 , IRAC2) to five bandpasses (ground based i-band and z-band , H_{140}, IRAC1, IRAC2), and we cannot perform a precise photometric redshift analysis from their spectral energy distribution. Instead, we selected galaxies in color and given spatial regions where we expect a small outlier contamination.

M22 selected galaxies with (IRAC1 − IRAC2) > -0.1, IRAC1 < 22.6 mag, from which we obtained a sample $\sim 90\%$ pure and complete of galaxies at $z > 1.3$. To reduce the contamination from outliers with $z > 1.3$, but not at the cluster redshift, we only selected galaxies hosted by the densest cluster regions, in circles of radius of 0.5 arcmin (~ 0.25 Mpc at our redshifts), in which the background contamination is $\lesssim 20\%$ in most clusters (M22). The scale of these regions corresponds to the scale of the dense cluster cores at $z > 1$ (Postman et al. 2005). van der Wel et al. (2012) and Kartaltepe et al. (2015) showed that morphological classification and the measurement of galaxy structural parameters are dependable only for magnitudes brighter than the WFC3/F160W magnitude $H_{160} = 24.5$ mag, and in this paper we select galaxies brighter than $H_{140} = 24.5$ mag.

Our final sample includes a total of 271 galaxies in the sixteen CARLA confirmed clusters and nineteen overdense regions. In fact, three of our clusters are double structures (CARLAJ1358+5752, CARLAJ1018+0530, and CARLAJ2039-2514; see details in M22), as predicted by cosmological models for clusters assembling at $z = 1.5-3$ (Chiang et al. 2013; Muldrew et al. 2015). Galaxies that were spectroscopically confirmed at a redshift different than the clusters by Noirot et al. (2018) and a recent photo-spectral analysis of CARLAJ1018+0530 by Werner et al. (in preparation) were not considered in this analysis. The details on our galaxy sample selection are in M22.

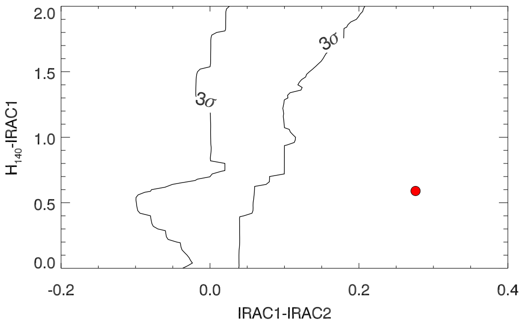

Fig. 1. A two color diagram to separate stars and galaxies. The 3σ locus of the modelled star distribution is shown by a black contour, the unresolved object from our sample is shown in red, and is most probably extragalactic.

3.3. Galaxy morphological classification and Passive and active galaxy selection

The details on our morphological classification and passive and active galaxy selection are provided in M22. Here we reiterate the main points.

M22 performed a galaxy visual morphological classification using two large morphological classes, early-type galaxies (ETG) and late type galaxies (LTG). ETG include spheroid and compact galaxies, and LTG include disks and irregular galaxies. Those correspond to the main morphological classes used in the CANDELS survey (Kartaltepe et al. 2015): (1) Disk. These galaxies have a disk even if they don't show clear spiral arms; (2) Spheroid. These galaxies are resolved spheroids and do not show a disk; (3) Irregular. All galaxies that cannot be classified either as Disk or Speroids; (4) Compact/Unresolved. These are compact or unresolved galaxies; (5) Unclassifiable. The sample used in this paper does not include any *Unclassifiable* galaxy.

For clusters that were observed in four bandpasses, M22 identified passive and active galaxies using color-color diagrams, which correspond to the *UVJ* diagrams used in the literature to separate passive from active dusty galaxies up to a redshift z=3.5 (e.g., Labbé et al. 2005; Wuyts et al. 2007; Williams et al. 2009; Whitaker et al. 2011; Fang et al. 2018).

Passive galaxies were selected as galaxies with specific star formation rate log(sSFR) < -9.5, using the CANDELS Santini et al. (2015) sSFR as the reference "true" sSFR for our selection calibration. This selection permitted us to obtain passive samples that are ~80-85% complete and pure, and includes recently quenched galaxies at $\sim 3\sigma$ below the field star formation main sequence.

3.4. Measurements of galaxy structural properties

We measured galaxy structural parameters using the software GALAPAGOS (Barden et al. 2012), using the high-resolution H_{140} images. The H_{140} channel corresponds to the V-band rest-

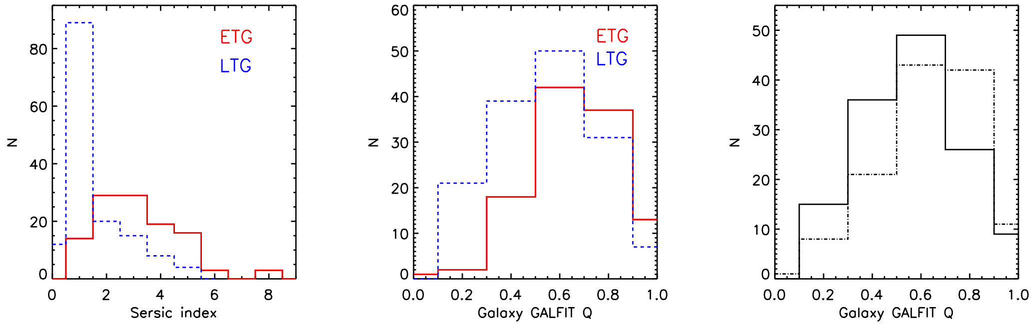

Fig. 2. CARLA cluster structural parameter distribution for our main morphological classes, ETG (red continuous line), and LTG (blue dashed line). Left: Sérsic index distribution; Middle: GALFIT Q distribution; Right: GALFIT Q distribution for asymmetric (continuous line) and symmetric galaxies (dash-dotted line). Our parameters are consistent with the visual morphological classification.

frame for most of our clusters, but the highest redshift one, CARLA J1017+6116, for which H_{140} corresponds to the U-band rest-frame. GALAPAGOS performs the following main steps: source detection; creation of image and noise cutouts for each detected source; estimation of the local background; fit of the surface brightness profile to a Sérsic profile; compilation of all objects in a final output catalog.

The source detection is based on SExtractor (Bertin & Arnouts 1996). Following Barden et al. (2012), we run SExtractor on the H_{140} images in the *cold* and *hot* modes, which are optimized to detect bright and faint objects, respectively. We adopt the same configuration of parameters used for the catalogs released by the Cosmic Assembly Near-IR Deep Extragalactic Legacy Survey (CANDELS, Grogin et al. 2011; Koekemoer et al. 2011), and published by Galametz et al. (2013) and Guo et al. (2013). More specifically, we create a first catalog including all the *cold* sources; then we compare every source detected in the *hot* mode to the first catalog detections, add to the first catalog those whose central position does not lie inside the Kron ellipse of any *cold* source, and discard the others. Table 1 shows the key SExtractor parameters used in our source detection.

The photometric and structural parameter estimation is based on GALFIT (Peng et al. 2002), that fits the surface brightness profile of each detected source to a one-component *Sérsic* model (Sersic 1968), defined by the following free parameters: the total magnitude m, the half-light radius measured along the major axis (effective radius) R_e, the Sérsic index n, the axis ratio Q (the ratio between the model minor and major axis, b/a), the position angle $P.A.$, and the central position. The software uses the Levenberg-Marquardt algorithm to minimise the residual between a galaxy image and the PSF-convolved model by modifying the free parameters.

We use the same GALFIT configuration as van der Wel et al. (2012, 2014) (Table 2). While this CANDELS analysis was not performed in the same observational bandpass as for CARLA, the H_{160} images for the CANDELS "wide" catalog (Koekemoer et al. 2011) have a 5σ magnitude limit of H_{160} = 27.4 mag, which is comparable to the CARLA magnitude limit of H_{140} = 27.1 mag (both were calculated within an aperture with 0.17″radius), when the different filter response functions are taken into account. The conversion to physical length-scale in kiloparsec is performed using the angular distance of each cluster, and assuming that all cluster galaxies have the same redshift as the average redshift of the cluster from Noirot et al. (2018).

We re-run GALFIT on the 22 galaxies for which either GALAPAGOS did not converge or the resulting values had uncertainties greater than the value itself, or the parameters hit the constraints in either R_e, n or q. In those cases, we try different values of the input parameters to find a stable global minimum of the residuals and resolve the problems listed above. We divided our sample in 3 categories: (i) Galaxies with a good quality fit; (ii) QSO, whose effective radii are uncertain due to saturation in the *HST* image (9 objects); (iii) Unresolved galaxies, where GALFIT converged close to the minimum constraint for the effective radius. We exclude QSO from our analysis.

The unresolved galaxy category consists of only one object with an effective radius R_e = 0.5 pix, which is close to the lower limit for the R_e estimate used by van der Wel et al. (2012) ($R_{e,min}$ = 0.018 arcsec or 0.3 pix in WFPC3 image). The objects with such effective radii are essentially indistinguishable from point sources due to PSF, so their R_e is an upper limit, and they might be either a bona-fide extragalactic galaxy, or a Milky Way foreground star. This object is not listed in the Gaia EDR3 catalogue as a star (Gaia Collaboration et al. 2020). We used the TRILEGAL model[2] (Girardi et al. 2005) to obtain a sample of simulated stars with magnitudes $IRAC1 < 26$ mag at the source RA and DEC, and with standard settings for the geometry of the thin disk, the thick disk and the halo of the Milky Way, as well as for their stellar population parameters. We built a (H_{140}-IRAC1) vs (IRAC1-IRAC2) diagram (see Fig. 1), to identify the locus of the synthetic star colors (see Fig. 1). The source does not lie in the star locus and we keep it as a bona-fide extragalactic galaxy.

In Fig. 2, we compare our GALAPAGOS structural parameters with visual morphology from M22. The median Sérsic index for ETG, and LTG, is ∼3 and ∼1, respectively, consistent with what is expected for ETG de Vaucouleur and LTG exponential profiles. The median Q for early, late, asymmetric and symmetric galaxies is ∼ 0.7, 0.55, 0.7, and 0.55, respectively, with early and symmetric galaxies being rounder, as expected.

4. Results

Fig. 3 shows each cluster passive and active galaxy mass-size relation, compared to CANDELS (van der Wel et al. 2014). We

---

[2] http://stev.oapd.inaf.it/cgi-bin/trilegal

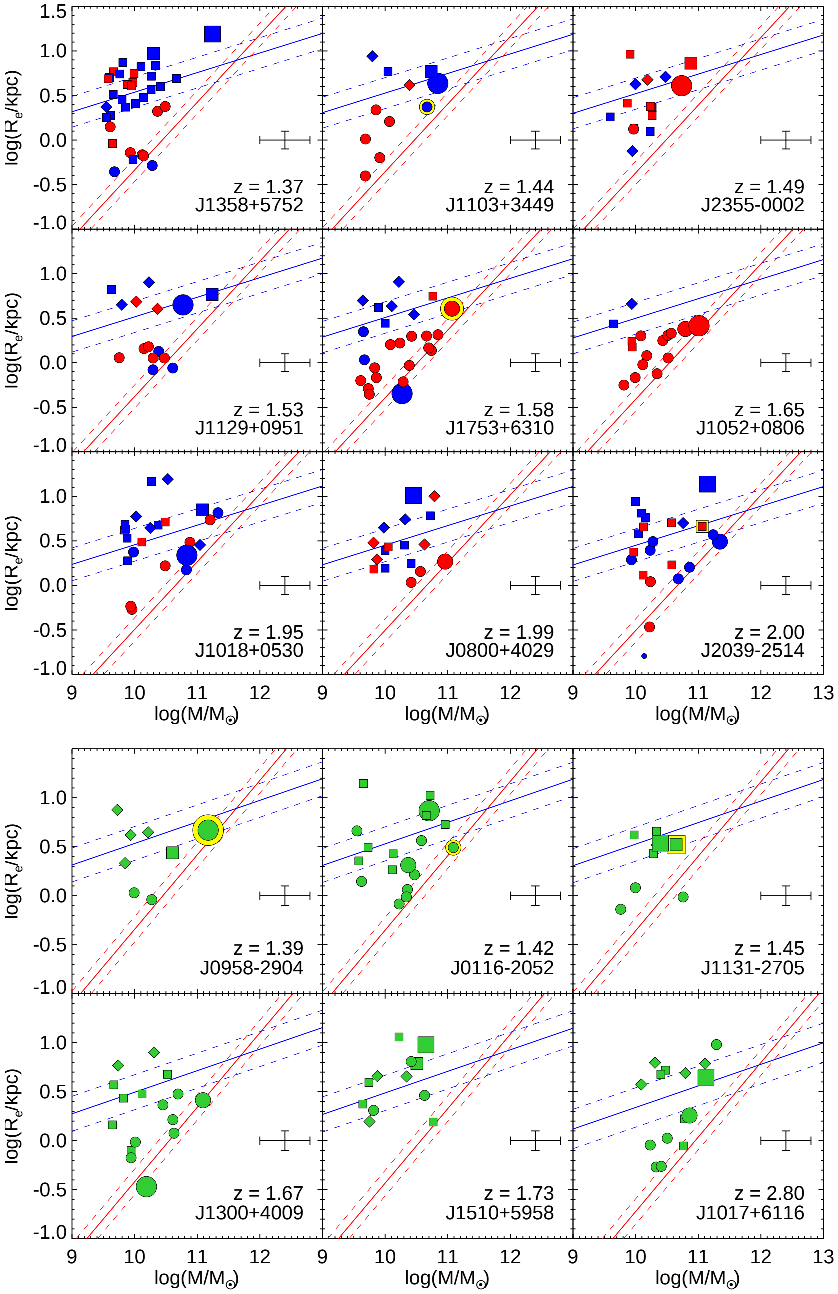

Fig. 3. The mass-size relations for each cluster. Red and blue colors show passive [log(sSFR) < -9.5], and active galaxies, respectively. Green symbols show galaxies for which we could not separate passive from active galaxies. Circles, squares, and diamonds correspond to ETG, LTG and irregulars, respectively. The largest symbols show the BCG, the second largest indicate the second brightest galaxies. The compact galaxy in the J2039-2514 is shown by the smaller symbol. A yellow contour around the galaxy symbol indicates a HzRG. The red and blue solid lines are CANDELS van der Wel et al. (2014)'s mass-size relation for passive and active galaxies respectively, interpolated to the redshift of each cluster. The dashed lines are 1-σ uncertainties of these relations, the average measurement uncertainty is provided on the right-hand side of each box. Cluster active and LTG galaxies lie on the van der Wel et al. (2014)'s active galaxy MSR. Cluster passive ETG have systematically larger sizes than van der Wel et al. (2014)'s passive galaxies.

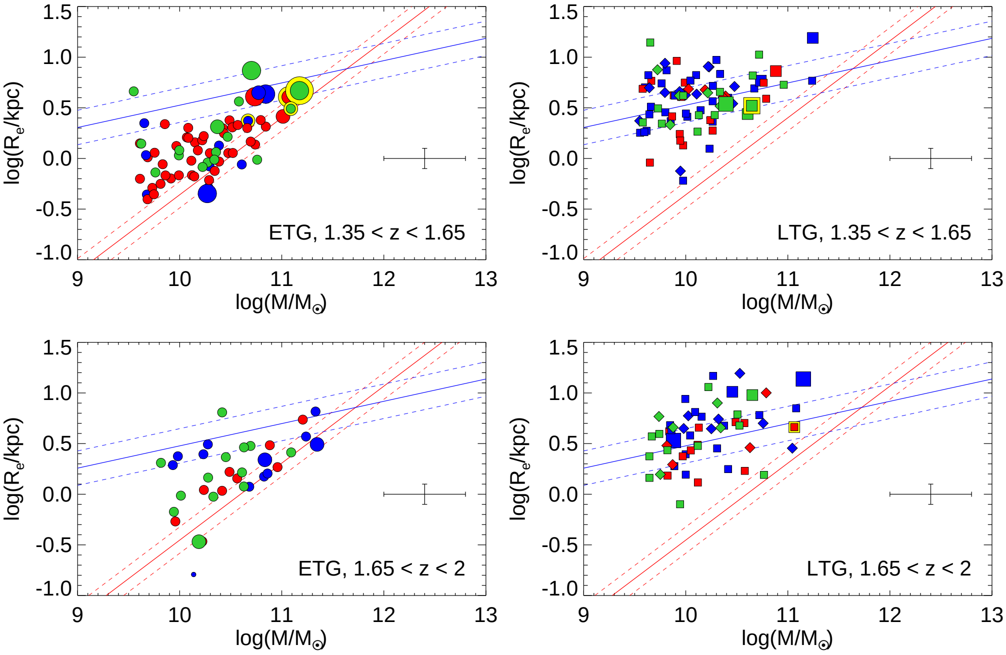

Fig. 4. The mass-size relation in two redshift bins. The symbols are the same as in Figure 3, the van der Wel et al. (2014)'s mass-size relations are shown at the the mean redshift of each bin ($z = 1.47$ and $z = 1.8$). The average measurement uncertainty is provided on the right-hand side of each box. In both redshifts bins, cluster active and LTG galaxies lie on the van der Wel et al. (2014)'s active galaxy MSR. Cluster passive ETG have systematically larger sizes than van der Wel et al. (2014)'s passive galaxies.

interpolated van der Wel et al. (2014)'s relations at each cluster redshift. While the active and LTG distributions lie on the same active galaxy mass-size relation as van der Wel et al. (2014), the passive and ETG population systematically lie above the van der Wel et al. (2014)'s passive galaxy relation. This is also shown in Fig. 4, where we divide the sample in two redshift bins, where we observe a similar behavior. The relation also indicates a tendency to flatten at log(M) $\lesssim 10.5$. About $\sim 30\%$ of the cluster ETG are active, and mostly lie on the LTG galaxy MSR. The bulk of these active ETGs is found in just two clusters (J1018 and J2039, both around $z \sim 2$). The cluster Brightest Cluster Galaxies (BCG) and the second brightest are shown with larger symbols, and lie on the same MSR as the satellites.

Fig 5 shows the evolution of the passive ETG mass-size relation in clusters in the redshift range $0.7 < z < 2$ as compared to the CANDELS (van der Wel et al. 2014)'s mass-size relation. We added to our sample the passive ETG observations from Strazzullo et al. (2013), Delaye et al. (2014), and Newman et al. (2014), which used analyses similar to ours. When authors published circularized effective radii, defined as $R_{e,circ} = R_e\sqrt{(b/a)}$ (e.g., Delaye et al. 2014), we convert their sizes to the Sérsic profile half-light radii along the major axis.

Fig 6 shows the redshift evolution of the mass-normalized radius $R_{10.7}$, defined as (van der Wel et al. 2014) :

$$R_e(\mathrm{kpc}) = R_{10.7}(\mathrm{kpc})\left(\frac{M}{5\times10^{10}M_\odot}\right)^{\beta} \tag{1}$$

In the conversion, we use the slope $\beta \sim 0.74-0.76$ from (van der Wel et al. 2014), interpolated at the redshifts that we are considering. Here we compute the average $\log(R_{10.7}/\mathrm{kpc})$ in each redshift bin for Delaye et al. (2014) and our data, and in each cluster for Strazzullo et al. (2013) and Newman et al. (2014). The Delaye et al. (2014) observations are averaged over the same redshift bins ($0.7 < z < 0.9$; $0.9 < z < 1.1$; $1.1 < z < 1.3$ and $1.3 < z < 1.6$) as in Figure 5. Our CARLA cluster observations are averaged over two redshift bins: $1.35 < z < 1.65$, and $1.9 < z < 2$. The uncertainties on $R_{10.7}$ are calculated using Monte Carlo simulations. For this figure, we only consider galaxies with $\log(M/M_\odot) > 10.5$ for an homogeneous sample comparison.

While the cluster mass-size relation of cluster and field passive ETG is mostly similar in the local Universe (e.g., Huertas-Company et al. 2013a), cluster ETG sizes are systematically higher than field passive galaxies at $\log(M/M_\odot) > 10.5$ and $z > 1$ and their evolution is slower in the range $1 \lesssim z \lesssim 2$. In fact, while the cluster and field MSR are superposed within $\sim 1\sigma$ (Fig. 5), the average normalized radii are clearly different. This is quantified by our fit to the redshift evolution of the cluster $R_{10.7}$ for galaxy mass $\log(M/M_\odot) > 10.5$:

$$\log(R_{10.7}/\mathrm{kpc}) = (-0.16 \pm 0.02)\,(z-1) + (0.44 \pm 0.01) \tag{2}$$

compared to the evolution in the field from van der Wel et al. (2014):

$$\log(R_{10.7}/\mathrm{kpc}) = (-0.32 \pm 0.02)\,(z-1) + (0.33 \pm 0.02) \tag{3}$$

The fit was performed by taking into account the uncertainties on both axes, and the uncertainties are quantified with Monte Carlo simulations. For galaxies with $\log(M/M_\odot) > 10.5$, at $1 < z < 2$, cluster passive ETG are on average $\gtrsim 3\sigma$ larger than the field. At $z = 1.5$ the cluster passive ETG are ~40% larger than those in the field, and at $z = 2$ they are larger by ~120%. The passive ETG fraction in clusters is $\sim 60 \pm 10\%$, compared to $\sim 28 \pm 2\%$ in CANDELS.

At lower mass, $\log(M/M_{\odot}) < 10.5$, the mass-size relation is predicted (Shankar et al. 2013) and observed (Graham et al. 2006; Lange et al. 2015; Li et al. 2018; Hamadouche et al. 2022) to flatten at least up to $z = 2$ (Nedkova et al. 2021).In the range $9.6 < \log(M/M_{\odot}) < 10.5$, where we observe a flattening of the MSR, the average cluster passive ETG size is $\log(R_e/\mathrm{kpc}) = 0.05 \pm 0.22$.

5. Discussion

We observe higher passive ETG sizes in CARLA clusters ($1.4 \leq z \leq 2.8$) when compared to field CANDELS's passive ETG (van der Wel et al. 2014). Larger passive early-type galaxy sizes in clusters at $z > 1$ were also observed by Delaye et al. (2014); Strazzullo et al. (2013); Newman et al. (2014). From these and our results, we obtain the evolution of the mass-normalized radius $R_{10.7}$ as a function of redshift, which shows that passive ETG with $\log(M/M_{\odot}) > 10.5$ and $z > 1$ are systematically larger than field passive ETG galaxies. Their mass growth at $1 \lesssim z \lesssim 2$ is slower than in the field.

5.1. The Mass-size relation at $z \sim 1$

At the lower redshift range $0.86 < z < 1.34$, Matharu et al. (2019) finds that cluster quiescent galaxies with $\log(M/M_{\odot}) \gtrsim 10$ are 0.08 ± 0.04 dex (~ 20 %) slightly more compact than in the field, and also consistent within 1σ with the field MSR, which has an intrinsic scatter $\sigma_{\log(\mathrm{kpc}} = 0.13$ dex. They used a toy model to show that these galaxies will in part merge with the brightest cluster galaxies and in part be tidally destroyed, and new, larger, galaxies will be accreted in clusters from the field, maintaining a similar MSR in field and clusters in the redshift range $0 < z \lesssim 1$. The model considers that galaxies in groups and filaments constantly fall onto the cluster larger haloes with the flow of the cosmic time (progenitor bias; van Dokkum & Franx 1996; Saglia et al. 2010). Because of this accretion, new passive members are added to the original early type passive population. The new passive objects can form either through environmental quenching by ram-pressure (Gunn & Gott 1972), harassment (Moore et al. 1996) or strangulation (van den Bosch et al. 2008), or they can infall already being quenched prior to the entry to the cluster, by group preprocessing (Fujita 2004). In the first case predominantly late-type disky galaxies are mostly transformed into lenticulars and dwarf ellipticals. In the second case, galaxies preprocessed in the group environment are larger. A part of the size growth in the clusters can be attributed to the addition of the group elliptical galaxies and lenticular galaxies that mix with the native cluster ETG population and homogenize the size distribution to that of the field. This is further compounded by results by Matharu et al. (2020), that can be explained by the accretion of old compact ETGs onto BCG or their disruption into the intracluster light. The Matharu et al. (2019)'s results at $1 < z < 1.34$ show larger sizes, and are consistent with Delaye et al. (2014)'s results and our findings in this paper.

5.2. The Mass-size relation at $z \sim 2$: galaxy sizes are larger in clusters than in the field

Field galaxies at $2 \lesssim z \lesssim 3$ (van der Wel et al. 2014; Patel et al. 2017; Marsan et al. 2019) show larger sizes than the extrapolation of the field size evolution at lower redshift (e.g., see the highest redshift field point in Fig 6). This is explained by the transition from the epoch in which galaxy growth is dominated by gas accretion and the epoch in which minor mergers become dominant (Naab et al. 2009). On the other end, cluster galaxies are already larger than field galaxies at $z \sim 2$, then grow more slowly than field galaxies, to reach the same average sizes by $z = 1$ and then evolve to $z \sim 0$ on average in the same way as field galaxies, mainly because of accretion of field larger galaxies and disruption of the cluster more compact galaxies (Matharu et al. 2019).

Our work has highlighted a clear dichotomy in the evolution of the mean passive early-type galaxy sizes of similar stellar mass : galaxies in clusters tend to be larger at $z \gtrsim 1$ than their counterparts in the field, and evolve slowly throughout. Passive ETG in the field are more compact at high redshift, show a faster growth, and eventually show similar MSR as the cluster galaxies at $z \sim 0$, as shown in the works cited above. In other words, passive early-type galaxies of similar stellar mass appear to have a significant environmental (halo) dependence which tends to progressively disappear when approaching the local Universe.

This non-trivial evolution in the size evolution is not easily reconciled with theoretical models. Mergers, especially dry ones, have traditionally often been invoked as the main driver behind the (strong) size evolution of massive galaxies, and in general of all ETG galaxies, as confirmed by a number of cosmological theoretical analytic (e.g., Guo et al. 2011; Shankar et al. 2013, 2014) and numerical (e.g., Naab et al. 2009; Genel et al. 2018; Furlong et al. 2017) studies.

Therefore, one could hypothesize that galaxies in clusters may have undergone a more rapid size increase via mergers before infall into a larger halo. To investigate this hypothesis, we show in Fig 7 the number of expected mergers that a central galaxy of $\log(M/M_{\odot}) > 10.5$ undergoes as a function of host halo mass for different redshifts, making use of the DREAM semi-empirical model by Fu et al. (2022, submitted). DREAM can flexibly compute the number of mergers of any central galaxy at any given redshift and host halo (cluster or field) without limits of mass or volume resolution and for any given input stellar mass-halo mass relation. Fig 7 shows that the number of both major and minor mergers undergone by central galaxies (dashed and solid lines, with thresholds as labelled) is steadily increasing as a function of the host halo mass, at all redshifts. Satellite galaxies with stellar mass $\log(M/M_{\odot}) > 10.5$, which at a given redshift reside in cluster environments with $\log(M_h/M_{\odot}) \sim 14$, were before infall centrals in host haloes with lower mass. In fact, central galaxies with stellar mass $\log(M/M_{\odot}) > 10.5$ typically reside in host haloes of $\log(M_h/M_{\odot}) \gtrsim 12.5$ with a weak dependence on redshift (e.g., Moster et al. 2018; Grylls et al. 2019) Fu et al. 2022, which hardly go through to any major or minor merger according to Fig 7. Even allowing for more massive host haloes for these galaxies, the models predict zero mergers at $z > 2$ up to $\log(M_h/M_{\odot}) \sim 13.7$, thus disfavouring an early size growth via a sequence of minor or major mergers.

Alternatively, progenitor bias could explain the difference between older, more compact and younger, more extended galaxies (e.g., Shankar & Bernardi 2009; Lilly & Carollo 2016), or simply the time a galaxy spends in the main sequence could

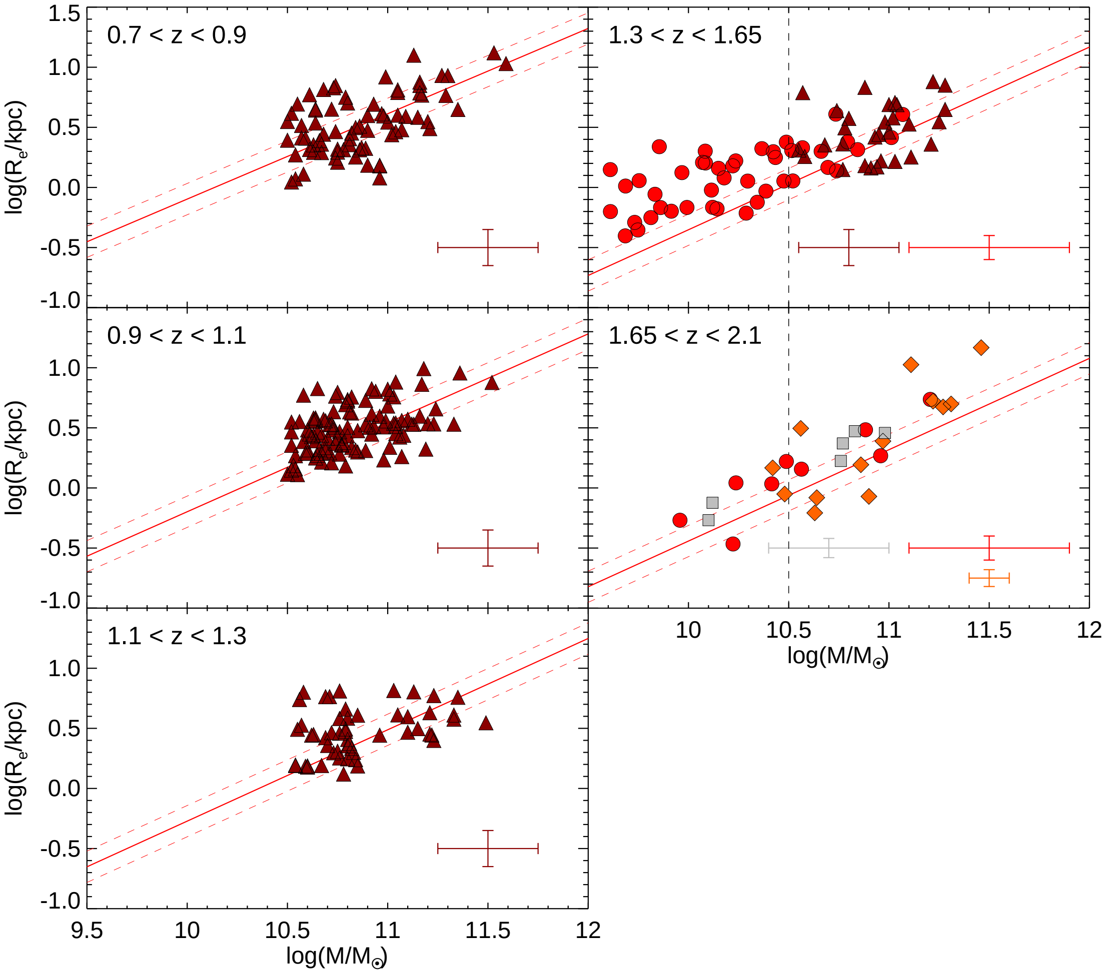

Fig. 5. The evolution of the cluster passive ETG mass-size relation. The red circles are our sample. The brown triangles, grey squares, and orange diamonds are observations from Delaye et al. (2014), Strazzullo et al. (2013), and Newman et al. (2014), respectively. The red continuous line is the van der Wel et al. (2014) CANDELS passive galaxy relation, and the dashed lines show the 1 σ uncertainty. The black dashed line shows the lower limit of our high mass sample. The average data uncertainties are shown in their corresponding color in the bottom-right corner of each sub-plot. Cluster passive ETG are systematically larger than CANDELS galaxies.

make them larger (e.g., Genel et al. 2018). We lack any clear age distributions for our galaxies compared to field counterparts, but galaxies in overdense regions would be, if anything, expected to be older and thus more compact than similar mass galaxies in the field, at variance with our findings.

AGN feedback could induce a rapid puffing up of the host galaxy, if a proportionally significant gas mass is expelled from the central regions (Fan et al. 2008, 2010). However, it is not clear why a strong AGN feedback should act only in those galaxies destined to become satellites in larger haloes and not in all galaxies of similar stellar mass at a given epoch. In addition, we inspected the central surface brightness within 2 kpc of galaxies of similar stellar mass in the field and in clusters, finding no signs of a reduced central density in cluster galaxies (see Fig. 8), which would be expected if AGN feedback has been expanding the central densities (Fan et al. 2010).

Kravtsov (2013) found evidence of a close linear relation between the effective radii of galaxies and their host haloes of the type $R_e = k \times R_{200c}$, where R_{200c} is the host halo radius[3], and the constant of proportionality k equal to a few percent, depending on the exact definition of host halo mass. This relation has also been measured at higher redshifts (e.g., Somerville et al. 2018), confirmed in hydrodynamic simulations (e.g., Rohr et al. 2022), and it has been used in analytic models to show that the size evolution and local size functions of intermediate and massive galaxies can be reproduced (e.g., Stringer et al. 2014; Zanisi

---

[3] defined as the region containing a mass density equal to 200 times the critical density of the Universe

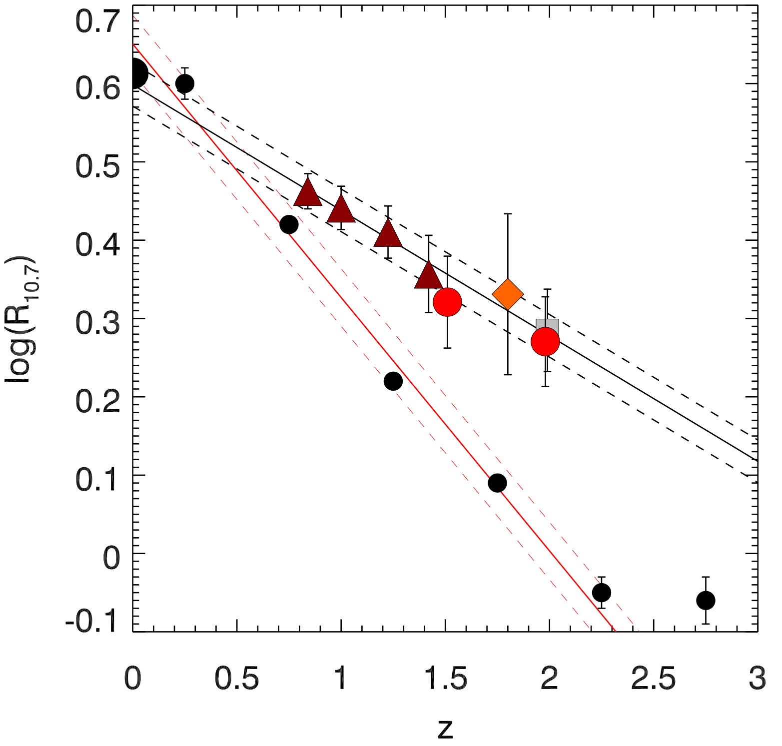

Fig. 6. The size evolution of passive ETG the mass-normalized radius $R_{10.7}$ (see text) with redshift. The red circles are CARLA sample (this study). The brown triangles, grey squares and orange diamonds show observations from Delaye et al. (2014), Strazzullo et al. (2013), and Newman et al. (2014), respectively. The black circles are field ETG sizes taken from Bernardi et al. (2014) and Huertas-Company et al. (2013b) for z = 0, and from van der Wel et al. (2014) for the other redshifts.

et al. 2020, 2021b), along with the environmental halo dependence in the local Universe Zanisi et al. (2021a).

By using DREAM, we have assigned an effective radius to all centrals and satellites galaxies at different epochs living in the field and in clusters as those in our sample ($13.6 < \log(M_{halo}/M_{\odot}) < 14.6$), assuming throughout a constant $R_e = k \times R_{200c}$. The exact value of the constant k assumed in this exercise is irrelevant as we are only interested in the relative difference between the mean sizes of field and cluster galaxies. We found that indeed cluster galaxies have a weaker evolution than field galaxies of similar stellar mass, which catch up with their cluster counterparts at $z < 0.5$, as in the data. However, for both predicted cluster and field galaxies' radii we find an evolution of the type $H[z]^{2/3}$, i.e., as $R_{200c}(z)$ (e.g., Stringer et al. 2014), which is a weaker evolution than the one observed for ETGs (Figure 6) which is closer to $\sim 1/(1+z)^{\alpha}$, with $\alpha \gtrsim 1$ in the field. This apparent discrepancy could be interpreted by the fact that the Kravtsov relation is more appropriate to describe the bulk of the population for a given halo/stellar mass, which is represented by star-forming galaxies with $\log(M/M_{\odot}) \sim 10.5$. We conclude that possibly an imprint in the formation/early evolution of cluster galaxies, as mirrored in the Kravtsov relation, could explain at least in part the systematic difference observed in our sample for cluster and field ETG galaxies, but other factors, such as strong compaction/gas dissipation in field galaxies, followed by a sequence of mergers (e.g., Hopkins et al. 2009 (e.g., Lapi et al. 2018) may have also played a significant role in shaping field, but not necessarily cluster, ETG galaxies.

5.3. BCG sizes

Our cluster BCG and the second brightest lie on the same MSR as the satellite galaxies, in contrast with models that predict them larger due to increased rate of dry minor mergers (e.g., Hopkins et al. 2009; Shankar et al. 2013). On the other hand, there are models that predict that BCG evolve from normal galaxies at z = 2, which then become larger due to different merger history (Zhao et al. 2017). This last wotk also finds that the most massive cluster galaxy at z = 2 is a true progenitor of a z = 0 BCG less than 50% of the time.

Observations show different results, even in the local Universe. For example, in the local Universe, Bernardi (2009) find that BCG are larger than satellite galaxies, while Weinmann et al. (2009) did not size difference between central and satellite ETG.

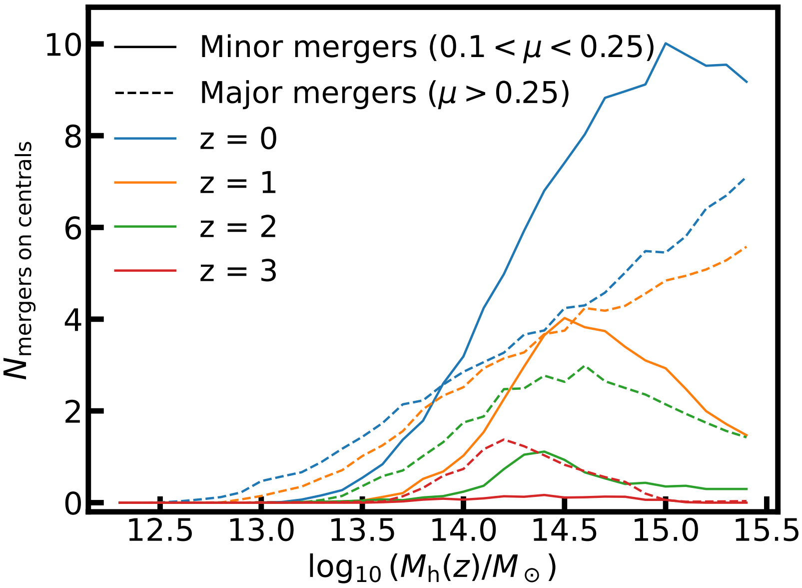

Fig. 7. Number of expected major and minor mergers of mass ratios in the progenitor masses of $\mu > 0.25$ and $0.1 < \mu < 0.25$ (dashed and solid lines, respectively) that a central galaxy of $\log(M/M_\odot) > 10.5$ undergoes as a function of host halo mass at different redshifts, as labelled. The curves are derived from the DREAM semi-empirical model by Fu et al. (2022).

5.4. Star forming ETG

We observe active ETGs that follow the passive ETG MSR in four of our five clusters at $z = 1.5{-}2$. The presence of active ETG in clusters has been observed at $z \sim 0$ (e.g., Sheen et al. 2016) and up to $z \sim 2$ (Ferreras & Silk 2000; Mei et al. 2006, 2015; Jaffé et al. 2011; Mansheim et al. 2017). At $1.35 < z < 1.65$ our active ETG are $20^{+7}_{-5}\%$ of all ETG, of which $45 \pm 18\%$ ($64^{+16}_{-20}\%$ for 2.5σ) lie within 1σ of the passive MSR. At $1.65 < z < 2.05$ active ETG are $55 \pm 13\%$ of all ETG, of which $42 \pm 17\%$ ($58 \pm 17\%$ for 2.5σ) lie within 1σ of the passive MSR.

These galaxies indicate that their morphological transformation happened before quenching Barro et al. (2013, 2014) or that a recent event triggered the star formation again (e.g. Shapiro et al. 2010; Kaviraj et al. 2011).

In the local Universe ($z \lesssim 1$), star forming ETG show evidence for recent gas-rich minor merger events or interactions with gas-rich neighbour galaxies, and are thought to become quiescent when the gas acquired during the merger, and which fuels star formation, will have been exhausted (e.g., Lee et al. 2006; Huertas-Company et al. 2010; George & Zingade 2015; George 2017). If this is true also at the higher redshifts that we probe, these galaxies have gone through a recent merger or neighbour galaxy interaction, and would most probably quench at a later epoch and increase the fraction of passive ETG in the cluster population. This explains why they follow the passive ETG MSR, and not the active galaxy MSR.

5.5. The MSR flattening for $\log(\mathrm{M}) \lesssim 10.5$

Our MSR indicates a tendency to flatten at $\log(M/M_\odot) \lesssim 10.5$. In the range $9.6 < \log(M/M_\odot) < 10.5$, we observe a average cluster passive ETG size of $\log(R_e/\mathrm{kpc}) = 0.05 \pm 0.22$. This is a trend observed in passive ETG in clusters and field in the the local Universe (e.g., Bernardi et al. 2014; Nedkova et al. 2021) and at $z \lesssim 2$ (e.g., Nedkova et al. 2021) for galaxies in the mass range $7 \lesssim \log(\mathrm{M}) \lesssim 10.5$. It is predicted in semi-analytical models (e.g., Shankar et al. 2013), where it occurs at the transitional mass ($\log(\mathrm{M}) \sim 10.5$) below which galaxy growth is dominated by both disk instabilities and mergers, and above which galaxy growth is due to minor mergers. Our average cluster passive ETG size is ~ 0.2 dex smaller than the average size from Nedkova et al. (2021), and consistent within $\sim 1\sigma$. This implies that the low mass end of the MSR does not evolve much from $z \sim 2$ to present.

6. Summary

We studied the mass-size relation of galaxies in a sample of 15 spectroscopically confirmed clusters from the CARLA survey (Wylezalek et al. 2013, 2014; Noirot et al. 2018). Our cluster total stellar mass spans ithe range $11.3 < \log(M_*^c/M_\odot) < 12.6$, which corresponds to an approximate halo mass in the range $13.6 < \log(M_h^c/M_\odot) < 14.6$ (Mei et al., submitted to A&A).

Our main results are:

- Cluster LTG at $1.4 < z < 2.8$ lie on the same MSR as active field galaxies from van der Wel et al. (2014)'s CANDELS

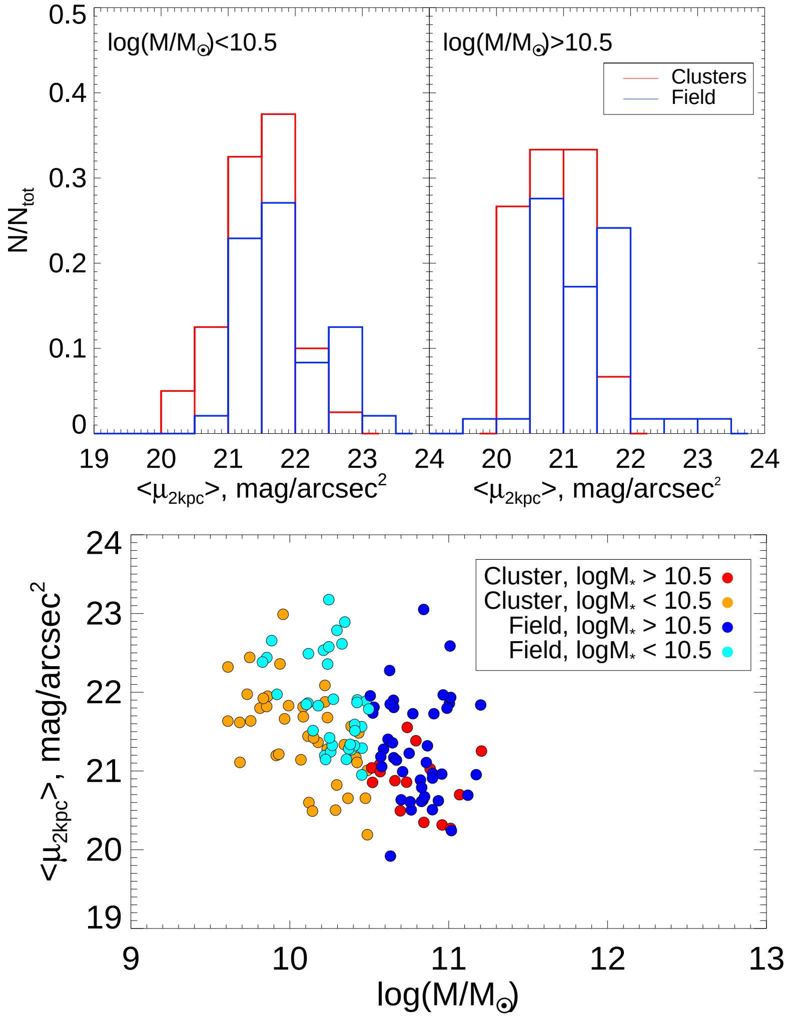

Fig. 8. Top: The histogram of the galaxy average surface brightness within 2 kpc, normalized to the total number of galaxies in each sample. The continuous red and blue lines show cluster and field galaxies, respectively. **Bottom:** The dependence of 2 kpc average surface brightness on galaxy mass in mass bins as shown in the labels. More massive galaxies have on average brighter inner regions. In both cases, the figures show that cluster and field galaxies have similar surface brighness distributions.

analysis, and we do not observe significant differences between field and cluster LTG.

- Cluster ETG at $1.4 < z < 2.8$ show sizes that are $\gtrsim 3\sigma$ systematically higher than passive field galaxies from van der Wel et al. (2014) CANDELS analysis. The evolution of cluster passive ETG sizes is slower at $1 < z < 2$ when compared to the field. We fit the average evolution for the mass-normalized radius as:

$$\log(R_{10.7}/\mathrm{kpc}) = -0.16\,(z-1) + 0.44 \quad (4)$$

compared to the evolution in the field from van der Wel et al. (2014), which is:

$$\log(R_{10.7}/\mathrm{kpc}) = -0.32\,(z-1) + 0.33 \quad (5)$$

- Brightest cluster galaxies lie on the same mass-size relation as the satellites
- Half of the active ETG, which are 30% of our ETG sample, follow the field active galaxy MSR.
- In the range $9.6 < \log(M/M_\odot) < 10.5$, Our passive ETG MSR flattens at $\log(M/M_\odot) < 10.5$, where we obtain an average $\log(R_e/\mathrm{kpc}) = 0.05 \pm 0.22$, which is 0.2 dex smaller, and consistent with galaxy sizes at $z = 0 - 2$ from Nedkova et al. (2021).
- We do not observe a large population of compact galaxies (only one), as it is observed in the field at these redshifts (e.g., Barro et al. 2013).

These results could be explained by similar size evolution for cluster and field galaxies. The systematic difference in size that we observe between cluster and field passive ETG galaxies could most probably be explained by early-epoch differences in the formation and early evolution of galaxies in haloes of different mass, as predicted by models (Kravtsov 2013). However, other physical mechanisms, such as strong compaction/gas dissipation in field galaxies, followed by a sequence of mergers (e.g., Hopkins et al. 2009; Lapi et al. 2018) role in the field ETG galaxy evolution, but not necessarily in the evolution of cluster galaxies.

The brightest cluster galaxies lie on the same MSR as the other cluster galaxies, implying that their size evolution has not be very different from the other cluster galaxies. On the other end, the active ETG that follow the LTG MSR most probably went through a recent merger or neighbour galaxy interaction, and would most probably quench at a later epoch and increase the fraction of passive ETG in the cluster population.

The low mass end of the MSR ($9.6 < \log(M/M_\odot) < 10.5$) did not evolve much between $z \sim 2$ to present and does not show significant environmental dependence. This suggests that the physical mechanisms that govern these low mass galaxies are similar in clusters and field. The lack of compact galaxies implies that the galaxies in our clusters are not observed in an epoch close to their compaction (e.g., Dekel et al. 2009; Barro et al. 2013), which might have happened at higher redshift (e.g., Lustig et al. 2021).

Acknowledgements. This work is based on observations made with the NASA/ESA Hubble Space Telescope, obtained at the Space Telescope Science Institute, which is operated by the Association of Universities for Research in Astronomy Inc., under NASA contract NAS 5-26555. These observations are associated with program GO-13740. Support for program GO-13740 was provided by NASA through a grant from the Space Telescope Science Institute, which is operated by the Association of Universities for Research in Astronomy Inc., under NASA contract NAS 5-26555. HF and FS acknowledge support from the European Union's Horizon 2020 research and innovation programme under the Marie Skłodowska-Curie grant agreement No. 860744. This work is based on observations made with the *Spitzer* Space Telescope, which is operated by the Jet Propulsion Laboratory, California Institute of Technology, under a contract with NASA. We thank Igor Chilingarian, Stefano Andreon, Adriano Fontana, Francoise Combes, Claudia Maraston and Alvio Renzini for useful comments. We thank Sandra Faber and Dave Kocevski for helping with CANDELS templates. We thank Leo Girardi for his help with the model TRILEGAL. We thank Université Paris Cité, which founded AA' s Ph.D. research. SM thanks Jet Propulsion Laboratory, California Institute of Technology, for hosting her in the context of this project. The work of DS was carried out at the Jet Propulsion Laboratory, California Institute of Technology, under a contract with NASA. This work was supported by the French Space Agency (CNES).

References

Allen, R. J., Kacprzak, G. G., Spitler, L. R., et al. 2015, ApJ, 806, 3
Barden, M., Häußler, B., Peng, C. Y., McIntosh, D. H., & Guo, Y. 2012, MNRAS, 422, 449
Barro, G., Faber, S. M., Pérez-González, P. G., et al. 2013, ApJ, 765, 104
Barro, G., Faber, S. M., Pérez-González, P. G., et al. 2014, ApJ, 791, 52
Belli, S., Newman, A. B., & Ellis, R. S. 2014, ApJ, 783, 117
Bernardi, M. 2009, MNRAS, 395, 1491
Bernardi, M., Meert, A., Sheth, R. K., et al. 2013, MNRAS, 436, 697
Bernardi, M., Meert, A., Vikram, V., et al. 2014, MNRAS, 443, 874
Bernardi, M., Roche, N., Shankar, F., & Sheth, R. K. 2011a, MNRAS, 412, 684
Bernardi, M., Roche, N., Shankar, F., & Sheth, R. K. 2011b, MNRAS, 412, L6
Bertin, E. & Arnouts, S. 1996, A&AS, 117, 393
Boselli, A. & Gavazzi, G. 2006, PASP, 118, 517
Cappellari, M. 2013, ApJ, 778, L2
Carollo, C. M., Bschorr, T. J., Renzini, A., et al. 2013, ApJ, 773, 112
Chabrier, G. 2003, PASP, 115, 763
Chan, J. C. C., Beifiori, A., Saglia, R. P., et al. 2018, ApJ, 856, 8
Chiang, Y.-K., Overzier, R., & Gebhardt, K. 2013, ApJ, 779, 127
Cooke, E. A., Hatch, N. A., Rettura, A., et al. 2015, MNRAS, 452, 2318
Dekel, A., Birnboim, Y., Engel, G., et al. 2009, Nature, 457, 451
Delaye, L., Huertas-Company, M., Mei, S., et al. 2014, MNRAS, 441, 203
Demers, M. L., Parker, L. C., & Roberts, I. D. 2019, MNRAS, 489, 2216
Dimauro, P., Huertas-Company, M., Daddi, E., et al. 2019, MNRAS, 489, 4135
Dutton, A. A., van den Bosch, F. C., Faber, S. M., et al. 2011, MNRAS, 410, 1660
Erben, T., Schirmer, M., Dietrich, J. P., et al. 2005, Astronomische Nachrichten, 326, 432
Erwin, P., Gutiérrez, L., & Beckman, J. E. 2012, ApJ, 744, L11
Fan, L., Lapi, A., Bressan, A., et al. 2010, ApJ, 718, 1460
Fan, L., Lapi, A., De Zotti, G., & Danese, L. 2008, ApJ, 689, L101
Fang, J. J., Faber, S. M., Koo, D. C., et al. 2018, ApJ, 858, 100
Fernández Lorenzo, M., Sulentic, J., Verdes-Montenegro, L., & Argudo-Fernández, M. 2013, MNRAS, 434, 325
Ferreras, I. & Silk, J. 2000, ApJ, 541, L37
Fujita, Y. 2004, PASJ, 56, 29
Furlong, M., Bower, R. G., Crain, R. A., et al. 2017, MNRAS, 465, 722
Gadotti, D. A. 2009, MNRAS, 393, 1531
Gaia Collaboration, Brown, A. G. A., Vallenari, A., et al. 2020, arXiv e-prints, arXiv:2012.01533
Galametz, A., Grazian, A., Fontana, A., et al. 2013, ApJS, 206, 10
Genel, S., Nelson, D., Pillepich, A., et al. 2018, MNRAS, 474, 3976
George, K. 2017, A&A, 598, A45
George, K. & Zingade, K. 2015, A&A, 583, A103
Girardi, L., Groenewegen, M. A. T., Hatziminaoglou, E., & da Costa, L. 2005, A&A, 436, 895
Graham, A. W., Merritt, D., Moore, B., Diemand, J., & Terzić, B. 2006, AJ, 132, 2711
Grogin, N. A., Kocevski, D. D., Faber, S. M., et al. 2011, ApJS, 197, 35
Grylls, P. J., Shankar, F., Zanisi, L., & Bernardi, M. 2019, MNRAS, 483, 2506
Gu, Y., Fang, G., Yuan, Q., & Lu, S. 2020, PASP, 132, 054101
Gunn, J. E. & Gott, III, J. R. 1972, ApJ, 176, 1
Guo, Q., White, S., Boylan-Kolchin, M., et al. 2011, MNRAS, 413, 101
Guo, Y., Ferguson, H. C., Giavalisco, M., et al. 2013, ApJS, 207, 24
Guo, Y., McIntosh, D. H., Mo, H. J., et al. 2009, MNRAS, 398, 1129

Hamadouche, M. L., Carnall, A. C., McLure, R. J., et al. 2022, MNRAS, 512, 1262
Hopkins, P. F., Hernquist, L., Cox, T. J., Keres, D., & Wuyts, S. 2009, ApJ, 691, 1424
Huang, S., Leauthaud, A., Greene, J., et al. 2018, MNRAS, 480, 521
Huertas-Company, M., Aguerri, J. A. L., Tresse, L., et al. 2010, A&A, 515, A3
Huertas-Company, M., Mei, S., Shankar, F., et al. 2013a, MNRAS, 428, 1715
Huertas-Company, M., Shankar, F., Mei, S., et al. 2013b, ApJ, 779, 29
Jaffé, Y. L., Aragón-Salamanca, A., De Lucia, G., et al. 2011, MNRAS, 410, 280
Kartaltepe, J. S., Mozena, M., Kocevski, D., et al. 2015, ApJS, 221, 11
Kauffmann, G., Heckman, T. M., White, S. D. M., et al. 2003, MNRAS, 341, 33
Kaviraj, S., Tan, K.-M., Ellis, R. S., & Silk, J. 2011, MNRAS, 411, 2148
Kelkar, K., Aragón-Salamanca, A., Gray, M. E., et al. 2015, MNRAS, 450, 1246
Koekemoer, A. M., Faber, S. M., Ferguson, H. C., et al. 2011, ApJS, 197, 36
Kravtsov, A. V. 2013, ApJ, 764, L31
Kuchner, U., Ziegler, B., Verdugo, M., Bamford, S., & Häußler, B. 2017, A&A, 604, A54
Kümmel, M., Walsh, J. R., Pirzkal, N., Kuntschner, H., & Pasquali, A. 2009, PASP, 121, 59
Labbé, I., Huang, J., Franx, M., et al. 2005, ApJ, 624, L81
Lacy, M., Wilson, G., Masci, F., et al. 2005, ApJS, 161, 41
Lange, R., Driver, S. P., Robotham, A. S. G., et al. 2015, MNRAS, 447, 2603
Lapi, A., Pantoni, L., Zanisi, L., et al. 2018, ApJ, 857, 22
Lee, J. H., Lee, M. G., & Hwang, H. S. 2006, ApJ, 650, 148
Li, H., Mao, S., Cappellari, M., et al. 2018, MNRAS, 476, 1765
Lilly, S. J. & Carollo, C. M. 2016, ApJ, 833, 1
Lu, S.-Y., Gu, Y.-Z., Fang, G.-W., & Yuan, Q.-R. 2019, Research in Astronomy and Astrophysics, 19, 150
Lustig, P., Strazzullo, V., D'Eugenio, C., et al. 2021, MNRAS, 501, 2659
Makovoz, D. & Khan, I. 2005, in Astronomical Society of the Pacific Conference Series, Vol. 347, Astronomical Data Analysis Software and Systems XIV, ed. P. Shopbell, M. Britton, & R. Ebert, 81
Maltby, D. T., Almaini, O., Wild, V., et al. 2018, MNRAS, 480, 381
Maltby, D. T., Aragón-Salamanca, A., Gray, M. E., et al. 2010, MNRAS, 402, 282
Mansheim, A. S., Lemaux, B. C., Dawson, W. A., et al. 2017, ApJ, 834, 205
Marsan, Z. C., Marchesini, D., Muzzin, A., et al. 2019, ApJ, 871, 201
Matharu, J., Muzzin, A., Brammer, G. B., et al. 2020, MNRAS, 493, 6011
Matharu, J., Muzzin, A., Brammer, G. B., et al. 2019, MNRAS, 484, 595
McIntosh, D. H., Bell, E. F., Rix, H.-W., et al. 2005, ApJ, 632, 191
Mei, S., Blakeslee, J. P., Stanford, S. A., et al. 2006, ApJ, 639, 81
Mei, S., Scarlata, C., Pentericci, L., et al. 2015, ApJ, 804, 117
Merlin, E., Bourne, N., Castellano, M., et al. 2016, A&A, 595, A97
Merlin, E., Fontana, A., Ferguson, H. C., et al. 2015, A&A, 582, A15
Moore, B., Katz, N., Lake, G., Dressler, A., & Oemler, A. 1996, Nature, 379, 613
Mosleh, M., Tavasoli, S., & Tacchella, S. 2018, ApJ, 861, 101
Mosleh, M., Williams, R. J., Franx, M., & Kriek, M. 2011, ApJ, 727, 5
Moster, B. P., Naab, T., & White, S. D. M. 2018, MNRAS, 477, 1822
Mowla, L. A., van Dokkum, P., Brammer, G. B., et al. 2019, ApJ, 880, 57
Muldrew, S. I., Hatch, N. A., & Cooke, E. A. 2015, MNRAS, 452, 2528
Naab, T., Johansson, P. H., & Ostriker, J. P. 2009, ApJ, 699, L178
Nair, P., van den Bergh, S., & Abraham, R. G. 2011, ApJ, 734, L31
Nedkova, K. V., Häußler, B., Marchesini, D., et al. 2021, MNRAS, 506, 928
Newman, A. B., Ellis, R. S., Andreon, S., et al. 2014, ApJ, 788, 51
Newman, A. B., Ellis, R. S., Bundy, K., & Treu, T. 2012, ApJ, 746, 162
Noirot, G., Stern, D., Mei, S., et al. 2018, ApJ, 859, 38
Noirot, G., Vernet, J., De Breuck, C., et al. 2016, ApJ, 830, 90
Noordeh, E., Canning, R. E. A., Willis, J. P., et al. 2021, MNRAS, 507, 5272
Patel, S. G., Hong, Y. X., Quadri, R. F., Holden, B. P., & Williams, R. J. 2017, ApJ, 839, 127
Peng, C. Y., Ho, L. C., Impey, C. D., & Rix, H.-W. 2002, AJ, 124, 266
Poggianti, B. M., Calvi, R., Bindoni, D., et al. 2013, ApJ, 762, 77
Postman, M., Franx, M., Cross, N. J. G., et al. 2005, ApJ, 623, 721
Raichoor, A., Mei, S., Stanford, S. A., et al. 2012, ApJ, 745, 130
Rieke, G. H., Young, E. T., Engelbracht, C. W., et al. 2004, ApJS, 154, 25
Rohr, E., Feldmann, R., Bullock, J. S., et al. 2022, MNRAS, 510, 3967
Saglia, R. P., Sánchez-Blázquez, P., Bender, R., et al. 2010, A&A, 524, A6
Santini, P., Ferguson, H. C., Fontana, A., et al. 2015, ApJ, 801, 97
Saracco, P., Gargiulo, A., Ciocca, F., & Marchesini, D. 2017, A&A, 597, A122
Sazonova, E., Alatalo, K., Lotz, J., et al. 2020, ApJ, 899, 85
Schirmer, M. 2013, ApJS, 209, 21
Sersic, J. L. 1968, Atlas de Galaxias Australes
Shankar, F. & Bernardi, M. 2009, MNRAS, 396, L76
Shankar, F., Marulli, F., Bernardi, M., et al. 2013, MNRAS, 428, 109
Shankar, F., Mei, S., Huertas-Company, M., et al. 2014, MNRAS, 439, 3189
Shapiro, K. L., Falcón-Barroso, J., van de Ven, G., et al. 2010, MNRAS, 402, 2140
Sheen, Y.-K., Yi, S. K., Ree, C. H., et al. 2016, ApJ, 827, 32
Sil'chenko, O. K., Kniazev, A. Y., & Chudakova, E. M. 2018, AJ, 156, 118
Socolovsky, M., Maltby, D. T., Hatch, N. A., et al. 2019, MNRAS, 482, 1640
Somerville, R. S., Behroozi, P., Pandya, V., et al. 2018, MNRAS, 473, 2714
Strazzullo, V., Gobat, R., Daddi, E., et al. 2013, ApJ, 772, 118
Stringer, M. J., Shankar, F., Novak, G. S., et al. 2014, MNRAS, 441, 1570
Szomoru, D., Franx, M., & van Dokkum, P. G. 2012, ApJ, 749, 121
Tadaki, K.-i., Belli, S., Burkert, A., et al. 2020, ApJ, 901, 74
Trujillo, I., Ferreras, I., & de La Rosa, I. G. 2011, MNRAS, 415, 3903
Trujillo, I., Förster Schreiber, N. M., Rudnick, G., et al. 2006, ApJ, 650, 18
Trujillo, I., Rudnick, G., Rix, H.-W., et al. 2004, ApJ, 604, 521
van den Bosch, F. C., Aquino, D., Yang, X., et al. 2008, MNRAS, 387, 79
van der Wel, A., Bell, E. F., Häussler, B., et al. 2012, ApJS, 203, 24
van der Wel, A., Franx, M., van Dokkum, P. G., et al. 2014, ApJ, 788, 28
van Dokkum, P. G. & Franx, M. 1996, MNRAS, 281, 985
van Dokkum, P. G., Nelson, E. J., Franx, M., et al. 2015, ApJ, 813, 23
Weinmann, S. M., Kauffmann, G., van den Bosch, F. C., et al. 2009, MNRAS, 394, 1213
Whitaker, K. E., Labbé, I., van Dokkum, P. G., et al. 2011, ApJ, 735, 86
Wilkinson, A., Almaini, O., Wild, V., et al. 2021, MNRAS, 504, 4533
Williams, R. J., Quadri, R. F., Franx, M., van Dokkum, P., & Labbé, I. 2009, ApJ, 691, 1879
Wuyts, S., Labbé, I., Franx, M., et al. 2007, ApJ, 655, 51
Wylezalek, D., Galametz, A., Stern, D., et al. 2013, ApJ, 769, 79
Wylezalek, D., Vernet, J., De Breuck, C., et al. 2014, ApJ, 786, 17
Yang, L., Roberts-Borsani, G., Treu, T., et al. 2021, MNRAS, 501, 1028
Yoon, Y., Im, M., & Kim, J.-W. 2017, ApJ, 834, 73
Zanisi, L., Shankar, F., Bernardi, M., Mei, S., & Huertas-Company, M. 2021a, MNRAS, 505, L84
Zanisi, L., Shankar, F., Fu, H., et al. 2021b, MNRAS, 505, 4555
Zanisi, L., Shankar, F., Lapi, A., et al. 2020, MNRAS, 492, 1671
Zhao, D., Conselice, C. J., Aragón-Salamanca, A., et al. 2017, MNRAS, 464, 1393